Title

Hydrodynamical Simulations of Strong Tides in Astrophysical Systems

Author

Guillochon, James Francis

Publication Date

2013

UNIVERSITY OF CALIFORNIA
SANTA CRUZ

HYDRODYNAMICAL SIMULATIONS OF STRONG TIDES IN ASTROPHYSICAL SYSTEMS

A dissertation submitted in partial satisfaction of the
requirements for the degree of

Doctor of Philosophy

in

ASTRONOMY & ASTROPHYSICS

by

James Guillochon

June 2013

The Dissertation of James Guillochon
is approved:

Professor Enrico Ramirez-Ruiz, Chair

Professor Douglas N. C. Lin

Professor Daniel Kasen

Dean Tyrus Miller
Vice Provost and Dean of Graduate Studies

Table of Contents

List of Figures

List of Tables

Abstract

Hydrodynamical Simulations of Strong Tides in Astrophysical Systems

by

James Guillochon

At the simplest level, gravitational sources are considered to be point-like and in solitude, with a radial force that falls off as r^{-2}. In reality, all astrophysical objects aside from black holes are extended in space, and can be deformed by the tidal forces arising from the proximity of companion objects with large average densities. When these forces are weak, the response of an object to a tide can be through a decomposition into basis functions, but this approach fails when the tide is strong enough to deform an object by a distance equal to its own size. Under these circumstances, a hydrodynamical representation of the object is required to understand the true tidal response.

In this thesis, we present a number of examples of physical systems in which tides dominate the dynamics. First, we consider the case of a star that encounters a supermassive black hole (SMBH) in a deeply penetrating encounter, resulting in a dramatic compression that produces shocks that would be observable in the X-ray. Second, we present the results of hydrodynamical simulations that demonstrate a new mechanism for igniting Type Ia supernovae from binary systems composed of two white dwarfs undergoing Roche-lobe overflow. Third, we investigate the survival prospects of giant planets that have been scattered into highly eccentricity orbits and are exposed to a strong tide applied by their parent star. Fourth, we systematically map the fallback rate resulting from the tidal disruptions of stars by SMBHs. Finally, we use

what we have learned about the feeding rate to model determine the highest-likelihood model for an observed prototypical tidal disruption event.

To my future wife Helen,

and to my mother, father, and step-father,

for their continual support.

Acknowledgments

My successes over the course of obtaining my doctoral degree would never have been realized without the unwaivering support of my advisor Enrico Ramirez-Ruiz, and the wisdom of Douglas Lin, Stephan Rosswog, and Daniel Kasen. I am grateful for the thought-provoking conversations I have had with Doug, and the hospitality extended to me by Stephan, and I am indebted to both of them for the collaboration opportunities they have provided. Dan was especially helpful to me in my early graduate career, and I can only hope that I would eventually be able to make as great of an impact on the astrophysical community as he has. The assistance provided to me by these amazingly generous and brilliant people over the six years I have been at Santa Cruz has been invaluable.

I cannot possibly imagine a better advisor to have than Enrico. Enrico's number one priority is to ensure that his students are successful, and I am exceedingly lucky to have benefited from his endless advocacy, ideas, and friendship. Even in times of great difficultly, Enrico's invincible enthusiasm has never failed to motivate me.

Enrico's group has always felt like a family to me, with support not only coming from Enrico himself, but also from his many students, postdocs, and academic collaborators. In particular, I'd like to thank Laura Lopez for being a great academic "big sister," Morgan MacLeod for being able to provide clarity when I needed it most, and Shawfeng Dong's irreplaceable stewardship of the computing resources at UCSC. This familial environment has encouraged me to return the favor by providing scientific and moral support to others when it is needed, so I am especially proud that I was able to make meaningful contributions to the works of Fabio de Colle, Marius Dan, Cole Holcomb, Shangfei Liu, Morgan MacLeod, and Haik Manukian. I hope that I will be able to continue this tradition of mutual support as I continue along in my academic career.

I am especially fortunate to have been surrounded by the intelligent, friendly, worldly, and approachable graduate students a campus such as UCSC attracts. Particularly, I'd like to thank (in alphabetical order) Jacob Arnold, Edmond Cheung, Claire Dorman, Robert da Silva, Nathan Goldbaum, Javiera Guedes, Anne Meddling, Neil Miller, Mark Mozena, Valery Rashkov, Luke Roberts, and Kevin Schlaufman.

I would also like to thank my mother and step-father for their support. I am especially grateful to my father for encouraging me to pursue science, despite not being a scientist himself, for as long as I can remember. My memories of visiting the library every weekend as a young child with my father are among my happiest. Lastly, I would like to thank my future wife Helen, who is the hardest-working person I have ever met, and yet still has always managed to find the time to love and support me.

The author of this thesis was the primary investigator and first author of all the research presented on the following pages, which are comprised of five publications (four accepted) to the Astrophysical Journal. The author was supported through the David and Lucille Packard Foundation, NASA (NNX07A-L13G, NNX07A-I88G, NNX08A-L41G, NNX08A-M84G), the NSF (PHY-0503584 and AST-0908807), the SciDAC Program (DE-FC02-01ER41176), and the NASA Earth and Space Sciences Fellowship.

Chapter 1

Introduction

Tides have played a critical role in the human experience for millennia, especially to those civilizations that heavily relied upon the oceans for their survival (Cartwright, 1999). Even upon the release of Isaac Newton's *Principia* in 1687, not everyone was convinced that gravitation was the force responsible for inducing Earth's tides. This included Jacques Cassini who ascribed to Descartes' theory for tides which supposes that planetary motion was due to vortices in an "ether," and incorrectly determined that the Earth was elongated at its poles (Figure 1.1). Newton's theory was eventually validated by a polar expedition undertaken by Maupertuis fifty years later (Maupertuis, 1738). When gravitation was accepted as the underlying cause of tides, it was quickly realized that tides are not merely a phenomena particular to Earth, as gravitation is universal and accompanies all massive objects. Since then, tidal theory has been generalized to apply to any self-gravitating object perturbed by the gravitational of a companion body (Press and Teukolsky, 1977), and has been directly observed in objects both large (e.g. the tidal stream of the Tadpole Galaxy) and small (e.g. the disruption of the Shoemaker-Levy 9 comet).

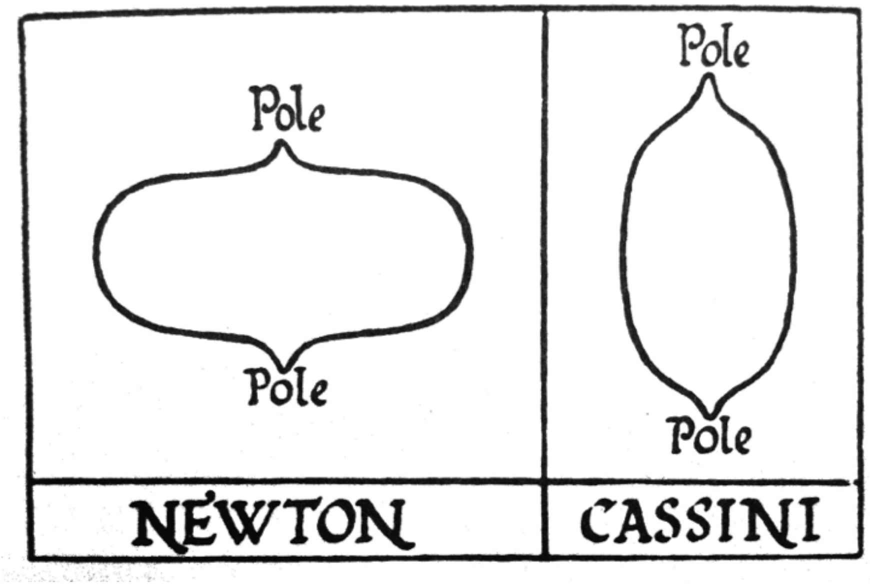

Figure 1.1: Competing geometries proposed by Newton and Cassini for the tide raised by the Moon upon the Earth.

For those objects that are not very close to Earth (as in the case of the comet) or do not subtend a large solid angle (as in the case of galaxies), their distortion and/or disruption by the gravitational field of a companion cannot be imaged. However, the effects of tides have been found to be extremely important in the evolution of many astrophysical systems, and their presence is confirmed by means other than direct imaging. Some definitive examples of tides in action are the large number of binaries actively engaged in Roche-lobe overflow (Thomas, 1977; Verbunt, 1993), the time-dependent deformation of eccentric binary stars (Thompson *et al.*, 2012), and the existence of short-period gas giant planets (Mayor and Queloz, 1995).

In our own solar system, the tides we observe are usually weak, with the most extreme examples being the disruption of objects (such as comets) whose destruction poses little threat to life on Earth. But beyond our solar system the manifestations of tides can be very strong, potentially resulting in the complete destruction of entire stars or planets. In this thesis, we focus on three transient event in which tides are important: The tidal disruption of a main-sequence star by a supermassive black hole (SMBH, Chapters 2, 5, and 6), detonations resulting from mass transfer in double white dwarf systems (Chapter 3), and the survival of giant planets that have been scattered close to their parent stars (Chapter 4).

In Chapter 2 we consider the disruption of main-sequence (MS) stars by SMBHs, which have been discovered in almost all galaxies for which we have searched for them (Kormendy and Ho, 2013). These black holes are orbited by a cluster of stars that interact with one another gravitationally through stochastic encounters. Occasionally, an encounter will shift a star onto an orbit that takes it within its tidal radius, defined as the distance at which the black hole's tidal forces would overcome the star's self-gravity at its surface (Frank and Rees, 1976). When a rapidly changing tidal force starts to compete with the star's self-gravity, the material of the star responds in a complicated way (Rees, 1988; Carter and Luminet, 1983; Bicknell and Gingold, 1983). During a close passage, the star is stretched along the orbital direction, squeezed at a right angle to the orbit, and strongly compressed in the direction perpendicular to the orbital plane.

This phenomenon poses a difficult challenge to computer simulations — three-dimensional gas-dynamical calculations have so far addressed the fate of the bulk of the matter, but key questions relating to the details of tidal disruption had yet to be answered. In particular, very high spatial resolution is needed to model stars passing well within the tidal radius, for which extreme compression is halted by a shock which rebounds and eventually breaks out of the stellar surface. We present a method for performing high-resolution simulations of deeply-penetrating tidal encounters in which these extreme compressions can be resolved. We use the results of our simulation to construct a model for the breakout of shockwaves from a tidally disrupted star, and we apply this model to determine the detectability of these tidal shock breakouts (TSBs) in the local Universe. Our results provide new insights into what happens when stars are strongly shocked as a result of extreme compression and the characteristic properties of such events.

In Chapter 3, we shift gears slightly to consider the effects of strong tides in a different physical system. White dwarfs (WDs), the end point of stellar evolution for most stars, are frequently observed in binary systems with normal stellar companions, and, less frequently, with compact stellar companions. Double degenerate (DD) systems are those in which the companion is another WD. Typically, DD systems are formed via common envelope evolution (Nelemans *et al.*, 2001b,a). Often, the final result of this evolutionary process is a binary consisting of a carbon-oxygen (CO) WD and a lower-mass helium WD companion (Napiwotzki *et al.*, 2007).

Because of the mass-radius relationship of WDs, mass transfer between the two stars is often unstable and can eventually lead to a merger (Marsh *et al.*, 2004; Gokhale *et al.*, 2007). For binary mass ratios close to unity the circularization radius R_{h} drops below the radius of the primary R_1, and thus the accretion stream will directly impact the primary's surface. We present three-dimensional hydrodynamics simulations that demonstrate that explosive phenomena are a likely consequence of the high accretion rates characteristic of the final stages of a merger in a DD system. In some cases, these explosive phenomena may lead to the complete detonation of the CO primary.

In Chapter 4 we consider another astrophysical system in which tides are important, this time the disruption of giant planets by their host stars. The search for planets about other stars has led to the discovery of dozens of planets with unusual properties, including the discovery of many giant planets known colloquially as hot Jupiters and Neptunes, which are thought to have formed far away from their parent stars but were then later transplanted to their observed positions by currently undetermined means. Many of these exoplanets come so close to their parent stars that they toe the line between destruction and survival, with some observed exoplanets in danger of being destroyed on a relatively short timescale (Li *et al.*, 2010). Additionally, the inclination distribution of the hot Jupiters seems to demonstrate significant misalignment between the planet's orbit and the stellar spin axis (Triaud *et al.*, 2010; Schlaufman *et al.*, 2010), a surprising result that may require a dynamical process that acts after the protoplanetary disk dissipates.

One of the primary physical processes that can deposit a planet on an orbit that is very close to its parent star is planet-planet scattering, which can produce both the observed semi-major axis and inclination distributions, and can deposit planets close enough such that tides can circularize the orbits in a time that is less than the system age. Previous hydrodynamical work has only focused on the planet's first close fly-by (Faber *et al.*, 2005, hereafter FRW), and does not investigate how prolonged tidal forcing over many orbits affects a planet's chances for survival. We have performed hydrodynamical simulations of multiple passages of a Jupiter-like planet by a Sun-like star, bridging the gap between numerical and analytical work that have focused on extremely close and extremely grazing encounters respectively. We find that scattering planets into star-grazing orbits is more destructive than previously thought, with Jupiter-like planets being destroyed or ejected at distances no smaller than 2.7 times the tidal radius. This strongly suggests that planet-planet scattering alone cannot explain the complete observed population of close-in Jupiter-like exoplanets.

In Chapter 5 we return to the problem of a main-sequence star being tidally disrupted by a SMBH. The standard model of tidal disruption presumes that the star is completely destroyed, resulting in approximately half of the star's original mass falling back onto the black hole, with the debris possessing a variety of orbital periods resulting from a spread of orbital energy that is "frozen in" at pericenter. Aside from full disruptions, there can also partial stellar disruptions, in which a stellar core survives the encounter and only a fraction of the star's mass becomes immediately bound to the black hole. Additionally, main-sequence stars of different masses will have different density profiles, which can affect the dynamics of the disruption.

We present the results of 43 hydrodynamical simulations at high-resolution representing the disruption of both low-mass and high-mass MS stars. Contrary to what is expected from the freezing model, in which only the distribution of mass at pericenter is considered, the non-linear response of the star to the tidal field is found to play a crucial role in determining the feeding rate. Our simulations show that the simple models previously employed to predict the rate of fallback do not capture the full dynamics of the problem, and are only appropriate for anything other than the full disruption at exactly the tidal radius.

In Chapter 6 we continue to consider a main-sequence star disruption by a SMBH, but now focus on the observational counterpart to the disruption (this time in the optical and UV as opposed to the X-ray, as was the case in Chapter 2). In the event of a full disruption, the star is split into two pieces of nearly-equal mass. One half of the star becomes bound to the black hole after the encounter, and continues along elliptical trajectories with pericenter distances equal to the star's original pericenter distance. The other half of the star gains orbital energy in the encounter, and is placed on hyperbolic trajectories. Determining the fates of these pieces of the star are critical in determining the appearance of the flare that results from the immense gravitational energy that will be released by the accretion disk that eventually forms.

We present three-dimensional hydrodynamical simulations that show that the width of the stream of unbound material is still controlled by the stream's self-gravity in the transverse direction, restricting its width to only be a fraction of the star's original pericenter distance. The surface area of this structure is not significant enough to produce hydrogen emission lines, even for the disruption of a main-sequence (MS) star composed largely of hydrogen. But while we find that the area of the unbound debris has been overestimated, we also find that the area occupied by the accretion disk formed from the bound material has been underestimated. Additionally, we find that significant dissipation occurs when this material returns to pericenter. As the debris stream quickly virializes at pericenter and the density of the material is significantly reduced as compared to the star's original density, self-gravity is suppressed even in the transverse direction. As a result, a fan structure *is* formed once material returns pericenter. But as this material belongs to the fraction of the original star that is strongly bound to the black hole, the radial extent of this material grows at a rate that is significantly smaller than the unbound fraction. We use this information to infer that PS1-10jh is the disruption of a main-sequence star of near-solar composition rather than a relatively rare star composed mostly of helium.

Chapter 2

Shock Breakout from Stars Compressed by Strong Tides

2.1 Introduction

Each star in the vicinity of a supermassive black hole (SMBH) traces out a complicated orbit under the combined influence of all the other stars and the black hole itself. There is a chance that encounters with other stars can send a star onto a nearly radial *loss cone* orbit which brings it very close to the black hole. Exactly how close a star can approach a black hole without suffering distortions is defined by the tidal radius

$$r_{\mathrm{t}} \simeq 7 \times 10^{12} M_6^{1/3} \left(R_*/R_\odot\right) (M_*/M_\odot)^{-1/3} \ \mathrm{cm}, \tag{2.1}$$

where M_6 denotes the mass of the black hole in units of $10^6 M_\odot$. While the tidal radius is defined by average stellar properties, a solar-type star passing within this distance would likely

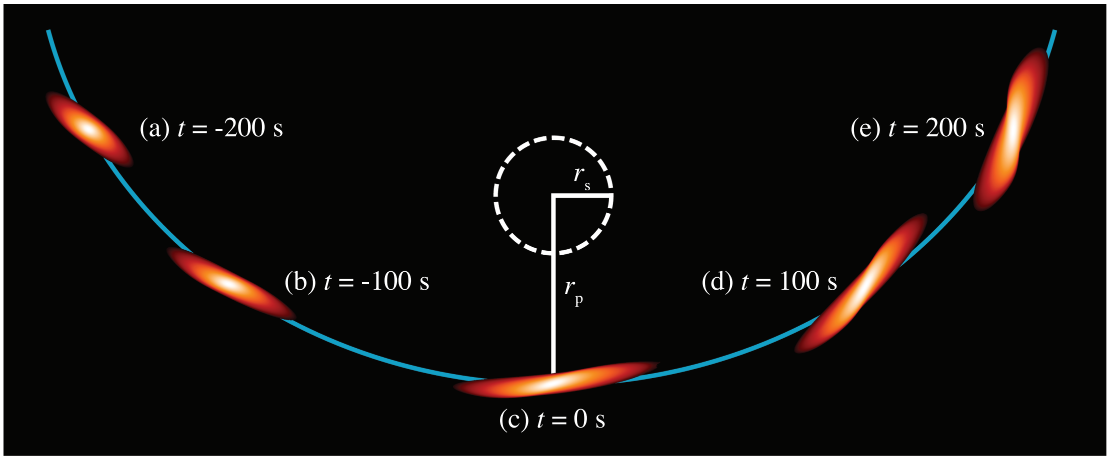

Figure 2.1: Events in the life of a tidally-disrupted solar-type star. The star travels from left to right in the black hole's frame, with $t = 0$ s when $r = r_{\mathrm{p}}$, the pericenter passage distance. The event horizon, which lies a distance r_{s} from the black hole, is shown as a thick dashed line. The orange coloring represents $\log_{10} \rho$, and the light blue line shows the path of the star's center of mass. The encounter is not drawn to scale.

be disrupted in a single flyby.

It is a complicated (although tractable) problem of stellar dynamics to calculate how frequently a star enters this zone of vulnerability (Frank and Rees, 1976). For galaxies with steep density cusps, such disruptions would take place about once every few thousand years (Magorrian and Tremaine, 1999). The exact rate depends on the statistics of the stellar orbits and particularly on how quickly the near-radial loss cone orbits are replenished. When a star is disrupted, the sudden release of gravitational binding energy is bound to produce a burst of radiation. The flares resulting from a disrupted star could be the clearest diagnostic of a black hole's presence.

During a close passage, a star is radically deformed by the black hole's strong tidal field, stretching along the direction of motion while simultaneously being compressed in the other two directions. Encounters that are particularly deep are difficult to simulate because of the extreme degree of compression achieved, with the final height of the star being hundreths or thousandths of its original size (Luminet and Carter, 1986). In this chapter, we present the most highly resolved three-dimensional simulation of the tidal disruption of a solar-type star to date, with voxels $\sim 10^3$ times smaller than previous calculations (Kobayashi *et al.*, 2004; Lodato *et al.*, 2009). We use the results of our simulation to construct a model for the breakout of shockwaves from a tidally disrupted star, and we apply this model to determine the detectability of these tidal shock breakouts (TSBs) in the local Universe.

The structure of this chapter is as follows. A description of the numerical methods and the initial models are summarized in Section 2.2. In Section 2.3, we present a chronological overview of the events in the life of a tidally disrupted star. An analytical treatment of shock breakout in tidally disrupted stars follows in Section 2.4, while estimates for the luminosity and detectability of various TSB events are subsequently presented in Section 2.5. We identify limitations and summarize our results in Section 2.6.

2.2 Numerical Method and Initial Model

Our simulation is carried out using FLASH (Fryxell *et al.*, 2000), an adaptive mesh code that has been used to treat a wide variety of gas dynamics problems. The black hole is initialized as a point mass with $M_{\rm h} = 10^6 M_\odot$, while the progenitor star is initialized as a $1\ M_\odot$, $\Gamma = 3$ polytrope $\left(P \propto \rho^{1+1/\Gamma}\right)$ with $R_* = 7 \times 10^{10}$ cm and central density of 76 g cm^{-3}. During the simulation, the gas obeys a $\gamma_{\rm ad} = 5/3$ equation of state. To ensure that the hydrostatic equilibrium of this configuration is maintained, we ran a control simulation without the presence of the black hole for 10^4 s, roughly the duration of the encounter. We found good stability — density does not change by more than a part in 100 for the inner 99.5% of the star's mass.

The center of the computational domain is fixed to the star's center of mass and is 8×10^{11} cm on a side. We subtract out the gravitational force the black hole exerts on the star's center of mass from every grid cell, leaving just the tidal force, which ensures the star remains centered in our computational domain. Self-gravity is calculated using a multipole expansion of the star's mass distribution with only the monopole and quadrupole moments contributing significantly.

Different refinement levels have different effective viscosities, so it is important that the refinement of cells are chosen to match the symmetry of the problem. We use an adaptive mesh scheme that refines all zones with $\rho > 10^{-4}$ g cm^{-3} to have 8 levels. These zones are refined twice more if they have $|z| \leq 10^{10}$ cm, resulting in a total refinement of 10 levels near the orbital plane where the shock is expected to form. Each block is then divided into 8^3 grid cells, making our smallest cells 2×10^8 cm in width. At pericenter, the star is resolved by 10^8 grid cells.

Because the majority of the stars in the loss cone are on radial orbits (Magorrian and Tremaine, 1999), the orbit is assumed to be parabolic. We begin the simulation at $t = -10^4$ seconds, the star crosses the tidal radius at $t = -10^3$, and reaches pericenter at $t = 0$. At pericenter, the star is brought to within $r_{\rm p} = 10^{12}$ cm of the black hole, which corresponds to an impact parameter $\beta \equiv r_{\rm t}/r_{\rm p} = 7$. Orbital energy is lost to heat and rotation injected into the star during the passage, so we expect some deviation from a parabola. However, for large β the fractional loss of energy is small. At pericenter, the kinetic energy of the star's bulk motion relative to the black hole at is $\beta G M_\odot M_\mathrm{h}/r_\mathrm{t} = 2 \times 10^{53}$ ergs, while our numerical results show only 2×10^{50} ergs are injected as heat and internal motions. Although general relativistic effects do affect the shape of the orbit somewhat for $\beta = 7$, we restrict ourselves to a purely parabolic encounter in Newtonian gravity.

2.3 Hydrodynamics of Stellar Disruption

2.3.1 Initial Approach

A solar-type star on a loss-cone orbit is initially in hydrostatic equilibrium as it advances on a parabolic trajectory towards the black hole, eventually nearing r_t, the distance at which the black hole's tidal forces are comparable to the star's self-gravity. In this region, the velocity and gravitational force vectors $\vec{v}$ and $\vec{F_\mathrm{g}}$ of the star relative to the black hole are almost parallel, resulting in the star being stretched into a prolate spheroid along its direction of travel (Figure 2.1).

As the star continues in its orbit beyond r_t, $\vec{F_\mathrm{g}}$ changes angle with respect to $\vec{v}$, and the star is no longer stretched along its major axis. The angle of the star's major axis at r_t is partially preserved during the passage. As a result, the star is not perfectly aligned with the trajectory of the center of mass. For $\beta \gg 1$, the motion of the fluid after crossing r_t (until reaching r_p) is well-described by the trajectories of a system of collisionless particles. During this phase, the star is vertically compressed by the tidal field, leading to a velocity field that is directed towards the orbital plane and whose magnitude is related to z, the distance above the plane.

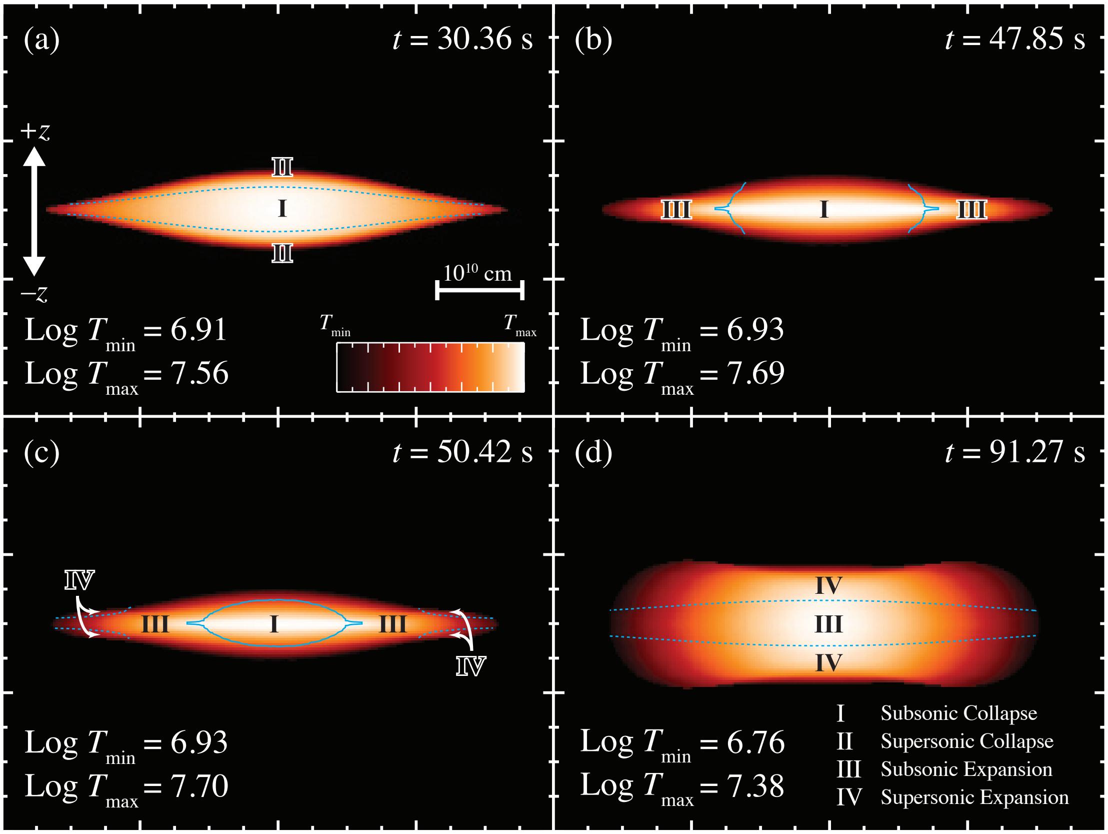

Figure 2.2: The hydrodynamics of shock formation in the core of a tidally compressed star. The snapshots show the progression of gas temperature during the bounce phase of the passage in a slice that passes through the center of mass, is perpendicular to the orbital plane, and parallel to the minor axis of the star. The orange coloring in these figures indicates $\log_{10} T$ where $\rho > 1$ g cm^{-3}. Regions of subsonic/supersonic collapse/expansion are indicated with roman numerals, with solid contours indicating the transition from collapse to expansion. The dashed contour is where $M_z = v_z/c_s = 1$, the mach 1 surface relative to the z direction. The angle of the minor axis to the x-z plane is 126.2° in (a), 127.3° in (b), 127.8° in (c), and 141.9° in (d).

2.3.2 Rebound

In the collisionless approximation, every particle would be expected to cross through the orbital plane shortly after the star's center of mass crossed pericenter. However, as the pressure of the gas in the orbital plane increases, it eventually becomes large enough to overcome the tidal field, which is decreasing as the star moves away from the black hole. When the vertical pressure gradient of the gas at the leading edge of the star becomes larger than the tidal field, the flow reverses and compression waves propagate outwards in all directions. The compression waves perpendicular to the orbital plane travel through a decreasing density gradient and eventually steepen into shock waves. Shock waves that form on the edges of the star are able to reach the surface quickly as the star has little vertical extent in these regions. The first of these shocks form in the leading edge of the star $\sim$30 seconds after pericenter. Subsequent shock formation sweeps across the star (parallel to the star's major axis) at $\sim v_p$, with the edges of the star rebounding before the interior, as illustrated in Figure (2.2).

The largest densities and pressures are reached when the compression wave crosses what was the core of the star prior to the encounter. We find that $P_{\rm max} = 1.3 \times 10^{18}$ dyn cm^{-2} at a density $\rho_{\rm max} = 310$ g cm^{-3}, occurring 53.1 s after pericenter (Figure 2.2, panel c). These conditions persist for only $\sim$10 seconds, and substantial nuclear burning can only be triggered on this timescale for $T \sim 3 \times 10^8$ K and $\rho \sim 10^3$ g cm^{-3} (Champagne and Wiescher, 1992). Comparison with the results presented in Brassart and Luminet (2008) shows that this is substantially lower than the predictions of one-dimensional simulations. This is expected because the density at the leading edge of the star decreases after infall reversal, allowing the pressure build-up at the interior to be relieved by leaking into the newly rarified post-bounce material. The reduction in pressure due to this effect moderates the compression waves that form downstream in denser parts of the star by decreasing the vertical pressure gradient $\partial_z P(x, y, t)$, a feature that is absent from one-dimensional simulations, which assume that all parts of the star collapse at the same time and ignore the effects of neighboring regions.

Additionally, a consequence of simulating tidal disruptions in three-dimensions is

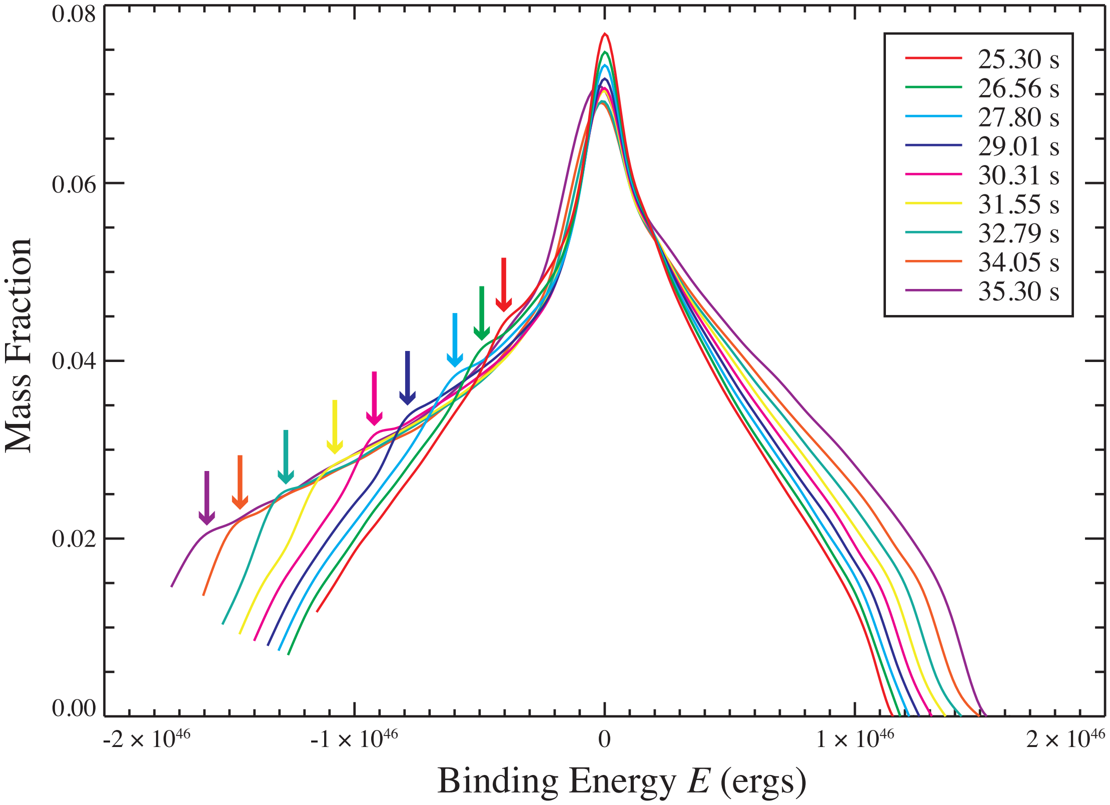

Figure 2.3: Histogram of the energies summed over all fluid elements during maximum compression, $E_i = K_i - U_i$ where $K_i = \frac{1}{2}m_i(\vec{v}_{\rm bulk} + \vec{v}_i)^2$ and $U_i = GM_h m_i/r$. $\vec{v}_{\rm bulk}$ is the star's bulk velocity, while m_i and $\vec{v}_i$ are the ith fluid element's mass and velocity. Energies are distributed among 30 bins and the data is smoothed using a spline fit. Curves are about 1.25s apart in time, with colored arrows indicating effect of the pressure wave propagating through the star.

degraded linear resolution, which reduces the mid-plane pressure by a factor $\chi \sim l^{-1}$, where l is the width of a grid cell. Applying Brassart and Luminet's scaling laws to our progenitor model, we find that they predict a compressed core pressure that is $\chi = 100$ times larger than what is found in our simulation. Because the pressure gradient and resolution effects both lead to a decrease in the mid-plane pressure, we expect that the actual value of the pressure at the mid-plane should fall somewhere between Brassart and Luminet's results and our own.

Shortly after the densest part of the star reaches maximum compression, the trailing edge enters its rebound phase. As the infalling material is halted by internal pressure at the interior, the high pressure wave continues to sweep through the trailing half of the star at velocity $\sim v_p$. Because the compression wave is traveling through a decreasing density gradient, the lighter material piles up on the denser material towards the core, resulting in an increase of velocity of the trailing edge relative to the star's center of mass. This has the effect of binding more material to the black hole (Figure 2.3) because the force is opposite to the direction of the star's motion. As a result about 5% of the mass that was already bound to the black hole becomes more deeply bound after the maximum compression wave has crossed the entire star. One-dimensional models do not replicate this effect mainly because they assume each column of gas collapses independently, neglecting both compression and rarefaction waves that propagate from other regions of the star. The relative speeds between any two parts of the star is proportional to the total spread in velocity $\Delta v \propto v_{\rm p} \propto \beta^{1/2}$ (Rees, 1988). Because the temperature of the star is largely uniform and the sound speed is proportional to β (Luminet and Carter, 1986), a given fluid element will be causally connected with a larger fraction of the star for larger penetration factors, and thus multidimensional effects become increasingly important.

2.3.3 Free Expansion

After the entire star has rebounded, it proceeds to expand and adiabatically degrade its internal energy content. Once again, the star's pressure becomes unimportant in determining its dynamics; as the star leaves the vicinity of the black hole, the effects of tidal stretching begin to dominate. As the leading edge of the star is slightly closer than it would be on a purely parabolic trajectory, the star experiences a torque and slowly rotates counter-clockwise when

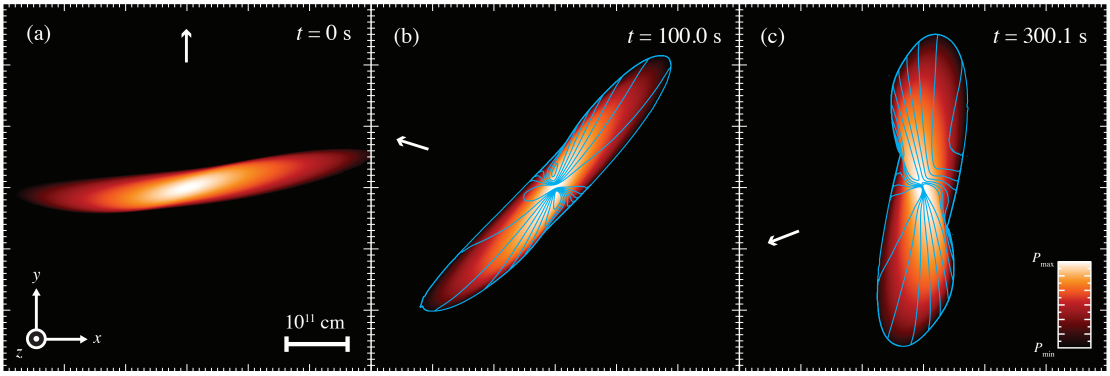

Figure 2.4: Three snapshots showing a slice of the star in the $z = 0$ plane, where t is time after pericenter. The white arrow in each panel indicates the direction to the black hole's center. The orange coloring of the panels indicate $\log_{10} P$ where $\rho > 10^{-3}$, where $P_{\rm min}$ and $P_{\rm max}$ are set to the minimum and maximum pressure in each snapshot. In panels (b) and (c), contours of constant angular velocity $\omega = v_{xy}/|\vec{r}|$ are drawn in cyan showing deviations from rigid-body rotation.

viewed from above (Figure 2.4).

Because different parts of the star lie at different distances to the black hole, they experience slightly different torques and acquire a range of angular velocities. This differential rotation leads to the star folding onto itself, and generates a spiral feature similar to that seen in Figure 2 of Evans and Kochanek (1989).

Eventually, the star leaves the immediate vicinity of the black hole and enters a free expansion phase. As approximately half of the star's mass has a negative binding energy relative to the black hole, the bound material will eventually return to pericenter (Ramirez-Ruiz and Rosswog, 2009), form an accretion disk, and feed an AGN phase for a few months (Rees, 1988). As we will describe in the next section, the rebound of the remnant also produces a clear observable signature, which can be used to predict when a quiescent black hole will become active.

2.4 Shock Breakout

The immediate signatures of tidal disruption will be observable in the X-rays, which correspond to a surface temperature of $\sim 10^7$ K. Because the ratio between the star's vertical extent and its width in the orbital plane is less than 1:10, the light curve produced by shocks propagating perpendicular to the orbital plane should have roughly a $\cos(\psi)$ dependence, where ψ is the angle between the orientation of the orbital plane and the line of sight. Due to the complex nature of the shocks generated by this event, the escaping radiation does not necessary lead to a single burst. In fact, our simulation shows two distinct peaks (Figure 2.5).

Because our simulation only resolves the star out to densities of $\sim 10^{-3}$ g cm^{-3}, our calculated surface lies beneath the true $\tau = 1$ surface for Thomson scattering in a stellar atmosphere. This surface corresponds to densities of $m_{\rm p}/\sigma_{\rm th} l = 10^{-8}$ g cm^{-3} in our simulation, where l is the length of the smallest grid cells. Additionally, the simulation treats the entire star as a $\gamma_{\rm ad} = 5/3$ ideal gas, which is clearly not true in the tenuous outer layers of the star's atmosphere that are radiation pressure dominated for temperatures of $\sim 10^7$ K and densities of $\rho \lesssim 1$ g cm^{-3}. Because of these limitations, we must extrapolate from the conditions at the surface of the simulation to determine the properties of the post-shocked atmosphere.

We define the surface of our simulation to be where $\epsilon_{\rm gas} > 5\epsilon_{\rm rad}$ such that the gas temperature is still representative of the energy content of a given fluid element. As the photons below the $\tau = 1$ surface are trapped on the shock crossing timescale, we can assume the shock has no radiative losses and the properties of the post-shock material are accurately described by the Rankine-Hugoniot jump conditions (Shu, 1992). For a perfect gas of ionized Hydrogen the energy density is $\epsilon_{\rm gas} = 3nk_{\rm b}T$, where n is the number density of atoms and T is the pre-shock gas temperature. Thus, the post-shocked material will have $\epsilon = \frac{\rho}{7}\left(6v_{\rm sh}^2 - k_{\rm b}T/m_{\rm p}\right)$, where $v_{\rm sh}$ is the shock velocity. This expression is controlled by the $v_{\rm sh}^2$ term in the star's outer layers where T is small, and thus the energy density of a post-shocked region is $\propto \rho v_{\rm sh}^2$, the ram pressure of the post-shock material.

If we take the energy density $\epsilon_{\rm s} = 3\rho_{\rm s}k_{\rm b}T_{\rm s}m_{\rm p}^{-1}$ (where the subscript s refers to the surface conditions) to be equal to the post-shock energy density at the base of the atmosphere, we can then calculate the energy density ϵ as a function of height z above this surface by considering the self-similar solutions of a shock propagating through a decreasing density gradient. In such solutions, the evolution of the shock velocity as it moves towards the photosphere is determined by $\gamma_{\rm ad}$ and the dependence of ρ on z, where z is the distance from the base of the atmosphere.

2.4.1 Self-Similar Solutions

Solutions for the post-shock conditions in the strong shock limit of both exponential (Grover and Hardy, 1966; Hayes, 1968; Zel'Dovich and Raizer, 1967) and power-law (Sakurai, 1960) atmospheres are readily available. The outer layers of an $\Gamma = 3$ polytrope are well-described by a power-law distribution with index $1.5 \leq \delta \leq 3$ (Matzner and McKee, 1999); we assume that $\delta = 1.5$ for the remainder of this work. For a power-law atmosphere where z is the distance from the base of the atmosphere and h_0 is the pressure scale height, the density $\rho(z)$ is

$$\rho(z) = \rho_{\rm s}[1 + zh_0^{-1}]^{-\delta}. \tag{2.2}$$

If $v_{\rm sh,s} = \frac{7}{6}\epsilon_{\rm s}/\rho_b$ is the shock velocity at the base of the atmosphere, then $v(z)$ is

$$v(z) = \frac{2v_{\rm sh,s}}{\gamma_{\rm ad}+1}[1+zh_0^{-1}]^{(1-\alpha)/\alpha}. \tag{2.3}$$

Because the post-shock energy density is just equal to the ram pressure in the strong shock limit, the total energy density $\epsilon(z)$ is simply

$$\epsilon(z) = \epsilon_{\rm s}[1+zh_0^{-1}]^{2(1-\alpha)/\alpha-\delta}. \tag{2.4}$$

At the base of the atmosphere thermal pressure dominates, but as the density of the gas decreases with z more rapidly than the temperature, the atmosphere becomes radiation pressure dominated within a couple scale heights and thus $\gamma_{\rm ad} = 4/3$. For our assumed values of δ and $\gamma_{\rm ad}$, Sakurai's method leads to a similarity exponent $\alpha = 0.7774$.

As the atmosphere is strongly compressed by the time-integrated tidal gravitational field, its vertical scale at shock breakout is significantly reduced. To estimate the atmosphere's size at breakout, we assume that collapse is self-similar. Because most of the stretching in a close encounter takes place before the star reaches $r_{\rm p}$, the cross-sectional area A_* should not be a strong function of β, provided that $\beta \gg 1$. Thus, the star's vertical size is directly related to the change in the star's volume

$$\frac{\mathcal{H}_{\rm f}}{\mathcal{H}_{\rm i}} = \frac{V_{\rm f}}{V_{\rm i}}, \tag{2.5}$$

where $\mathcal{H}_{\rm i}\,(=R_*)$ and $\mathcal{H}_{\rm f}$ are the initial and final heights of the star above the orbital plane and $V_{\rm i}$ and $V_{\rm f}$ are the initial and final stellar volumes. The vertical velocity $v_\perp$ of the stellar material just prior to rebound is approximately equal to $\beta c_{\rm s}$ (Carter and Luminet, 1983), and because nearly all of the internal motions during free-fall are vertical, the total kinetic energy of the star can be estimated as

$$\frac{1}{2}M_*v_\perp^2 = \beta^2\frac{GM_*^2}{R_*}. \tag{2.6}$$

At rebound, the kinetic energy of the infalling material is converted into internal energy. Because the star's original internal energy is $U_{\rm i} \simeq GM_*^2/R_*$, the initial and final internal energies are simply related, $U_{\rm f} = \beta^2 U_{\rm i}$. Assuming the compression is adiabatic,

$$V \propto U^{\frac{1}{1-\gamma_{\rm ad}}}, \tag{2.7}$$

and thus

$$\mathcal{H}_{\rm f} = \mathcal{H}_{\rm i}\left(\frac{U_{\rm i}}{U_{\rm f}}\right)^{\frac{1}{1-\gamma_{\rm ad}}} = \mathcal{H}_{\rm i}\beta^{\frac{2}{1-\gamma_{\rm ad}}}. \tag{2.8}$$

For $\gamma_{\rm ad} = 5/3$, Equation 2.8 gives $\mathcal{H}_{\rm f} = \mathcal{H}_{\rm i}\beta^{-3}$. In a self-similar collapse, the scale height $h_{\rm b}$ will be reduced by a factor $\mathcal{H}_{\rm f}/\mathcal{H}_i$, and thus $h_{\rm b} = h_0\beta^{-3}$.

Because the velocity of a given layer is position dependent, Δv is non-zero and the post-shock energy density ϵ is a decreasing function of t. The energy output will therefore be controlled by a balance between photon diffusion and adiabatic expansion, with most of the photons being released from a layer where these two timescales are comparable. Assuming plane-parallel geometry, these timescales can be estimated for a layer at a given z as

$$\tau_{\rm ad} \simeq \left[\mathrm{erf}\left(1/\sqrt{2}\right)^{-1/\gamma_{\rm ad}} - 1 \right] \left(\frac{\partial v(z)}{\partial z} \right)^{-1} \tag{2.9}$$

$$\tau_{\rm diff} \simeq \frac{\tau(z)^2 \rho(z) \sigma_{\rm th}}{c m_{\rm p}}. \tag{2.10}$$

where $\sigma_{\rm th}$ is the Thomson cross-section and $m_{\rm p}$ is the proton mass. Equating these two expressions and solving numerically for z determines $z_{\rm min}$, the deepest layer in the atmosphere that will contribute significantly to the emission.

With the compressed density profile, shock jump conditions, and depth of the emitting region determined, we can calculate the luminosity and spectrum of shock breakout. As the energy density of the post-shocked material is primarily given by the energy density of radiation, we can estimate the photon temperature in the atmosphere as $T_{\rm ph}^4 = \epsilon(z)/a_{\rm b}$, where $a_{\rm b}$ is the Stefan-Boltzmann constant. While the temperature does decrease as z approaches H (the distance from the base of the atmosphere to the photosphere), this decrease is small because $T \propto \epsilon^{1/4}$.

The spectrum of photons near the $\tau = 1$ surface may be significantly non-thermal because the photon spectrum takes a non-neglible amount of time to approach a Planckian distribution (Katz *et al.*, 2009). Additionally, the shock velocity near the surface is $\sim 0.03c$, and special relativistic effects may also contribute to a non-thermal spectrum. While these effects would lead to the production of harder photons that are easier to detect (Band *et al.*, 2008), we conservatively assume that the observed photon spectrum is a combination of blackbodies.

The total energy released by the event can be estimated by integrating the energy density over z and multiplying by twice the cross-sectional of the star at pericenter $2A_* = 2\pi ab$:

$$E_{\rm tot} = 2\pi ab \int_{z_{\rm min}}^{H} \epsilon(z) dz, \tag{2.11}$$

where a and b are the semi-major and semi-minor axes of the star. We can define an effective height parameter Z

$$\begin{aligned} Z &\equiv \int_{z_{\rm min}}^{H} \left(1+\frac{z}{h_{\rm b}}\right)^{2(1-\alpha)/\alpha-\delta} dz \\ &= h_{\rm b} \frac{\alpha}{\alpha(\delta+1)-2} \left(1+\frac{z}{h_{\rm b}}\right)^{\frac{2}{\alpha}-\delta-1} \Bigg|_{z=z_{\rm min}}^{z=H}, \end{aligned} \tag{2.12}$$

which is independent of position on the surface of the star if we assume that the atmosphere is always perpendicular to the orbital plane and that $h_{\rm b}$ and δ are constants. The average luminosity of the event is then given by substituting Z into Equation 2.11 and dividing by the length of time for the star's center of mass to cross pericenter

$$t_{\rm cr} = 2a/v_{\rm p} \simeq \frac{6R_*^{3/2}}{\beta^{1/2} G^{1/2} M_{\rm h}^{1/3} M_*^{1/6}}, \tag{2.13}$$

which yields

$$\bar{L} = \pi v_{\rm p} b \epsilon_{\rm s} Z, \tag{2.14}$$

where we used Equation 2.4 to substitute for $\epsilon(z)$ and our definition for Z. Evaluating Equation (2.14) for the average $\epsilon_{\rm s}$ found at the surface of our simulation, assuming the initial scale height has the solar value of $h_0 \simeq 1.4 \times 10^7$ cm, and using the measured crossing time $t_{\rm cr} = 30$ s, we find $\bar{L} = 3 \times 10^{44}$ ergs s^{-1}.

While our estimation determines the average luminosity $\bar{L}$, calculating the luminosity as a function of time is more difficult because $\epsilon_{\rm s}$ is a function of position on the surface. Because a detailed record of the surface conditions are produced by our simulation, we can calculate what the luminosity and spectrum will look like as a function of time. Most of the luminosity is released from the deepest contributing layer of the atmosphere $\epsilon(z_{\rm min})$, where the diffusion time to the surface is $\sim 10^{-2}$ s. This timescale is significantly shorter than $t_{\rm cr}$, so we approximate each grid cell's contribution to the luminosity as a delta function

$$L(x,y,t) = \frac{Zl^2\epsilon_{\rm s}(x,y)}{\Delta t}\delta[t - t_{\rm b}(x,y)], \tag{2.15}$$

where l is the grid cell size in cm, Δt is the time increment between two data dumps, and $t_{\rm b}(x,y)$ is the breakout time for a given location on the surface. We use $\Delta t = 0.1$s, but the value chosen only affects the smoothness of the resultant light curve so long as $\Delta t \ll t_{\rm cr}$. Because the shock front is not always easy to detect in our simulation due to limited resolution in the perpendicular direction, $t_{\rm b}$ is set by when a given area element's energy density peaks. The luminosity as a function of time is then simply a sum of the individual contributions of the surface grid cells

$$L(t) = \sum_{i}^{N_{\rm cells}} \frac{Zl^2\epsilon_{{\rm s},i}}{\Delta t}\delta(t - t_{{\rm b},i}), \tag{2.16}$$

where $\epsilon_{{\rm s},i}$ and $t_{{\rm b},i}$ are the energy density and breakout time of a given cell, respectively.

Equation (2.16) allows us to generate a light-curve for our disruption event (Figure

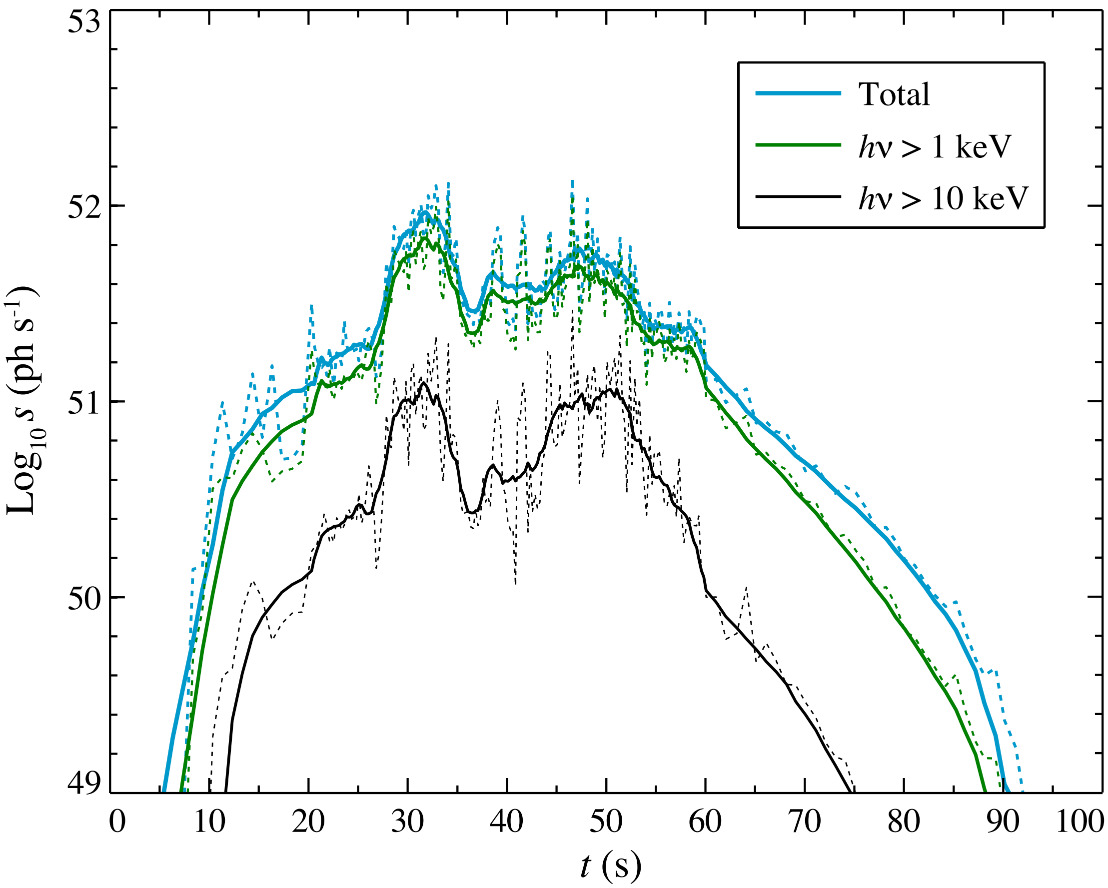

Figure 2.5: Light curve produced by the breakout of shocks across the surface of the disrupted star, where s is the flux in photons per second and t is time since the star's center of mass crossed pericenter. Photons are binned into categories based on energy. The dotted lines show the raw output of the luminosity calculation for a given bin, while the solid lines show a 1 s moving average of the same data.

2.5). We assume that each grid cell produces a blackbody spectrum of photons defined by the photon temperature of that cell, $T_{\mathrm{ph},i} = \epsilon_{\mathrm{s},i}^{1/4} a_{\mathrm{b}}^{-1}$. By summing these spectra, we can obtain a photon distribution at time t. Note that there are two peaks at $\sim$30 and $\sim$50 seconds corresponding to shocks that originate from the limbs of the star. As discussed in §2.3, this double peak feature arises because compression waves that originate near the star's center of mass tend to travel parallel to the orbital plane in the direction of the star's orbital motion into regions that have already begun expanding. This compression moderation results in the non-production of shocks in this region, and thus there is a period of relatively low luminosity as the shocks cross the star's center of mass. The time difference between the two maxima in the light curve is approximately equal to $t_{\rm cr}$ (Equation 2.13).

Our post-shock surface conditions show peak breakout temperatures in excess of 8×10^7 K at densities of 30 g cm^{-3}. Kobayashi *et al.* (2004) estimated that the $\beta = 5$ event will yield photons of energy of 2.2 keV on average, which is in agreement with our mean surface temperature.

2.5 Observability

2.5.1 X-ray Transient

The duration, color, and luminosity of a disruption breakout event depends on β, $M_{\rm h}$, and the parameters of the star being disrupted. Ideally, one would want to construct a predictive model for TSBs by performing a detailed simulation for each possible combination of parameters. However, a thorough exploration of the full parameter space would require many simulations similar in scope to the simulation presented in this work. Fortunately, progress can still be made as our simulation provides an accurate benchmark for the peak luminosity $L_{\rm peak}$ of a deeply-penetrating breakout event. The results of the simulation can then be used together with some simple scaling arguments to construct a function that can describe the features of disruption breakouts for a variety of encounters.

We can gain some insight by considering the scaling of the various parameters that the luminosity (Equation 2.14) depends on. The pericenter velocity is dependent on the black hole mass and the closest-approach distance, which gives a scaling of $v_{\rm p} \propto \beta^{1/2} M_{\rm h}^{1/3}$. For $\gamma_{\rm ad} = 5/3$ (appropriate for the mid-plane), $\rho \propto \beta^3$ and $T \propto \beta^2$ (Luminet and Carter, 1986), which implies that $\epsilon_{\rm s} \propto \rho v_{\rm s}^2 \propto \beta^5$. Because the total height of the atmosphere H scales as β^{-3}, large β events are reduced in output by the decrease in volume of the emitting region. For ultra-close encounters the escape velocity can be comparable to c, and thus the emitted photons are gravitationally redshifted, with the energy of each being divided by a factor of $\left(1 + \frac{1}{2} r_{\rm s}/r_{\rm p}\right)$. Additionally, the passage of time in the star's rest frame is slower than that of an observer for which $r \gg r_{\rm s}$ by a factor of $\sqrt{1 - r_{\rm s}/r_{\rm p}}$, leading to a further decrease in luminosity. Accounting for these effects, the peak luminosity of a TSB roughly scales as

$$L_{\rm peak} \propto \beta^{5/2} M_{\rm h}^{1/3} \frac{\sqrt{1 - r_{\rm s}/r_{\rm p}}}{2 + r_{\rm s}/r_{\rm p}}. \tag{2.17}$$

A more careful calculation considering the detailed properties of the shocked, self-similar atmosphere reveals that L also depends on the choice of δ. The dependence on β and $M_{\rm h}$ still roughly follows the scaling of Equation 2.17, but because the volume of the emitting region depends on where $\tau_{\rm ad} = \tau_{\rm rad}$ (Equations 2.9 and 2.10), the luminosity of a given event must be computed numerically. The full numerical solution for $L_{\rm peak}$ of a $\delta = 1.5$ power-law atmosphere over a range of β and $M_{\rm h}$ is shown in the left panel of Figure 2.6.

We now follow the procedure of Wang and Merritt (2004) to estimate the rate of detectable events. Because the tidal radius grows as $M_{\rm h}^{1/3}$ and the Schwarzschild radius grows as $M_{\rm h}$, disruptions with $\beta > 3$ are only possible for black holes with $M_{\rm h} \lesssim 10^8 M_\odot$. This means a

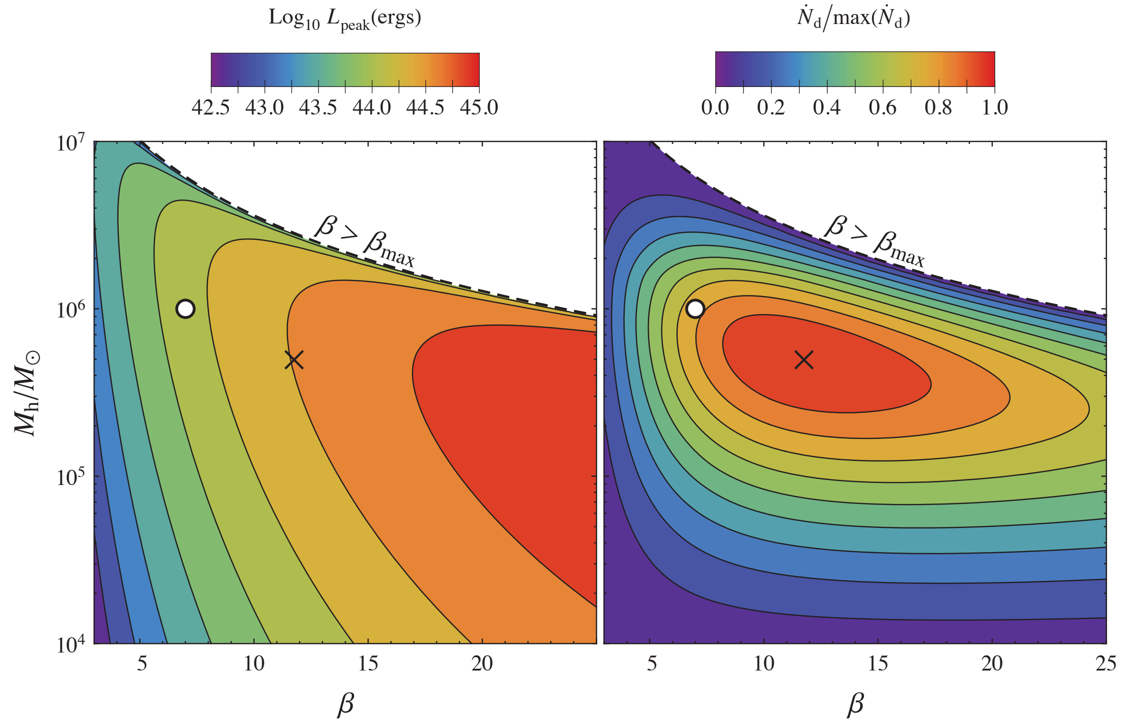

Figure 2.6: Peak luminosity and detectability of events as a function of M_{h} and β, assuming that the outer atmosphere is described by a $\delta = 1.5$ power law. The left panel shows $\log_{10} L_{\text{peak}}$ for a given event, while the right panel shows the number of expected detections by EXIST (Grindlay, 2004) **[update this with active x-ray telescope]** $\dot{N}_{\text{d}}$, normalized to the maximum rate. Our simulation parameters are indicated by the white circles, while the black crosses indicate the location of the events with the largest predicted detection rates. Disruptions are constrained by the $\beta = \beta_{\text{max}}$ curve (shown as a dashed line), which indicates the largest β for a given black hole mass where $r_{\text{p}} > r_{\text{s}}$.

significant detection rate is only obtained when considering the low end of the galaxy luminosity function, as characterized by Trentham and Tully (2002)

$$\begin{aligned} N_{\text{dE}}(\mathcal{M})d\mathcal{M} &= N_{\text{dE},0}\left(10^{-0.4(\mathcal{M}-\mathcal{M}_{\text{dE}})}\right)^{\alpha_{\text{dE}}+1} \\ &\times\ e^{-10^{-0.4(\mathcal{M}-\mathcal{M}_{\text{dE}})}} d\mathcal{M}. \end{aligned} \tag{2.18}$$

In this expression, $N_{\text{dE},0}$ is a normalized dwarf elliptical galaxy number density, $\mathcal{M}_{\text{dE}}$ is the cutoff magnitude for the Schechter function, and $\alpha_{\rm dE}$ describes the faint-end slope. As in Wang and Merritt (2004), we want to write Equation 2.18 as a function of $M_{\rm h}$. We use the scaling relation of Magorrian *et al.* (1998) to write the absolute magnitude $\mathcal{M}$ in terms of bulge mass $M_{\rm bulge}$, which is simply related to $M_{\rm h} = 10^{-2.91} M_{\rm bulge}$ (Merritt and Ferrarese, 2001). We assume that only nucleated dwarf elliptical (dEn) galaxies contain black holes, with the nucleated fraction $F_{\rm n}$ scaling linearly with $\mathcal{M}$. To properly scale $N_{\rm dE,0}$, we assume that the space-averaged dE density is equal to the number of dEs in the Virgo cluster spread into a sphere with radius equal to the distance of the Virgo cluster (approx. 0.2 Mpc^{-3}).

Because we are in the regime where $r_{\rm p} \ll r_{\rm t}$, we know that the disruption rate scales linearly with $r_{\rm p}$ (Rees, 1988), and Wang's expression for the disruption rate becomes

$$\dot{N} = 6.5 \times 10^{-4}\ \mathrm{yr}^{-1} \left(\frac{M_{\rm h}}{10^6\ M_\odot} \right)^{-0.25} \beta^{-1}. \tag{2.19}$$

The maximum distance $R_{\rm d}$ to a detectable event can be expressed as a function of instrumental sensitivity as

$$R_{\rm d} = \sqrt{\frac{\pi L_{\rm peak}}{2\sigma_{\rm b} T_{\rm ph}^4} \int_{\nu_{\rm min}}^{\nu_{\rm max}} \frac{F_{\rm T}^{-1} B_\nu(T_{\rm ph})}{h\nu}\, d\nu}, \tag{2.20}$$

in which $F_{\rm T}(\nu)$ is the burst sensitivity as a function of frequency, the TSB spectrum is given by the Planck function B_ν at a temperature $T_{\rm ph} \propto \beta^{5/4}$, h is Planck's constant, $\sigma_{\rm b}$ is the Stefan-Boltzmann constant, and $\nu_{\rm min}$ and $\nu_{\rm max}$ are the minimum and maximum frequencies accessible

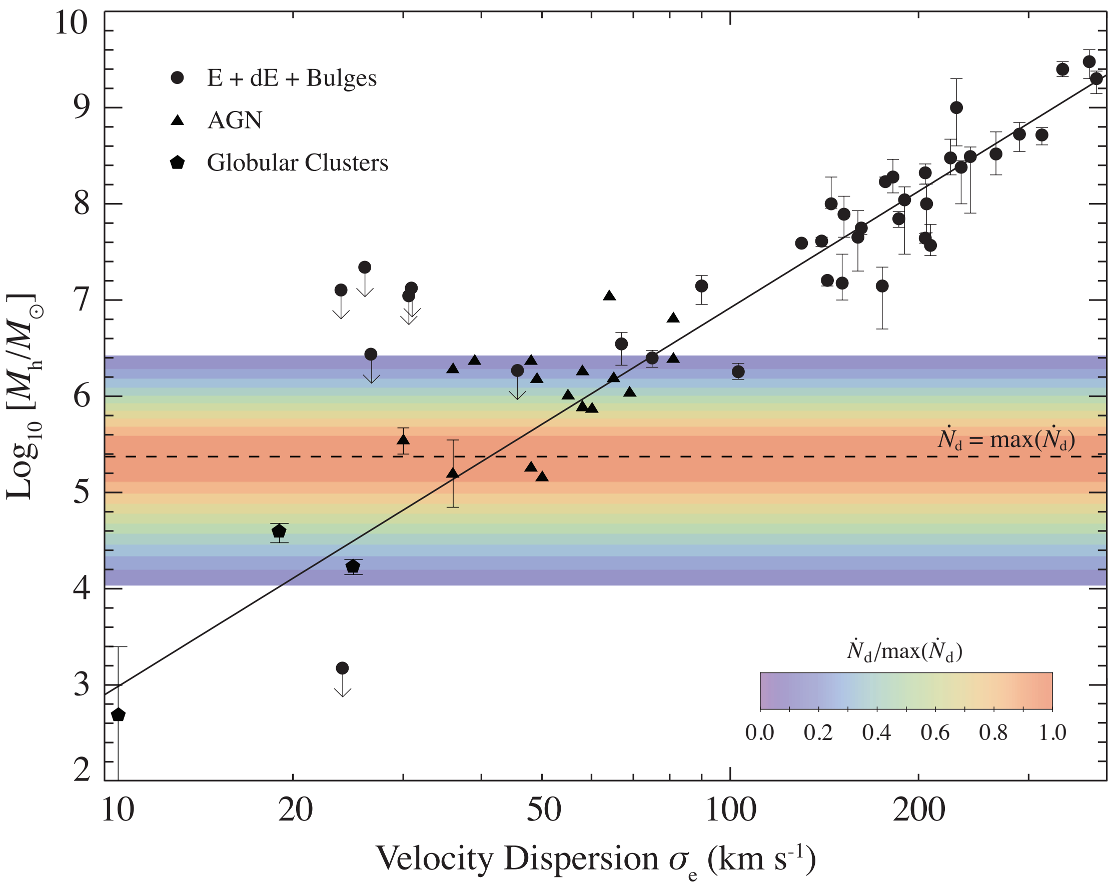

Figure 2.7: Bulge velocity dispersion σ_e vs. BH masses in E, dE, and bulge-dominated spiral galaxies (circles), AGN (triangles), and globular clusters (pentagons). The colored contours represent the detection rate relative to the maximum detection rate as in Figure 2.6, averaged over all β, with the maximum indicated by the dashed line. Plot modified from Geha *et al.* (2002), including the BH masses compiled by Noyola *et al.* (2008).

to the instrument. An instrument is sensitive to all events contained within the volume

$$V_\mathrm{d} = \frac{4}{3}\pi R_\mathrm{d}^3. \tag{2.21}$$

We now have all the pieces needed to determine a detection rate in terms of β and M_h. By multiplying the number density of black holes $N_\mathrm{dE}F_\mathrm{n}$ (Equation 2.18) by the disruption rate

$\dot{N}$ for a black hole of a given mass and penetration factor (Equation 2.19), and by the volume $V_{\rm d}$ in which those events are detectable (Equation 2.21), we obtain the following expression for the total rate of detection

$$\dot{N}_{\rm d} = \frac{\Omega}{4\pi}\int_{3}^{\infty}\int_{M_{\rm min}}^{M_{\rm max}} \dot{N} N_{\rm dE} F_{\rm n} V_{\rm d}\, dM_{\rm h} d\beta, \tag{2.22}$$

in which Ω is the solid angle covered by the instrument's field of view and $M_{\rm max} \equiv \left(c^2 R_{\odot}/4GM_{\odot}\beta\right)^{3/2}$ is the mass at which $r_{\rm p} \leq r_{\rm s}$, the Schwarzschild radius. The integral over β terminates at $\beta = 3$ because shocks have not been seen in one-dimensional calculations for passages with $\beta < 3$ (Brassart and Luminet, 2008). However, our simulation shows that shocks form in the limbs of the star where conditions are substantially different than the core, and thus shocks may still be produced for $\beta < 3$ in some cases.

The detection rate is evaluated using the parameters of the proposed EXIST telescope, which has spectral coverage from 3 to 1000 keV, an average burst sensitivity of $F_{\rm T} = 0.2$ cm^{-2} s^{-1}, and $\sim$ 20% sky coverage (Grindlay, 2004; Band *et al.*, 2008). Using these values, Equation 2.22 predicts that EXIST should detect approximately 1 TSB per year. We can also use the argument of integrals of this equation to generate a map in $(\beta, M_{\rm h})$ space (Figure 2.6, right panel) to predict which events will generate the most detections. Comparison with the left panel of the same figure shows that these events have a characteristic luminosity of $\sim 5 \times 10^{44}$ ergs. Despite being similar to the Eddington value of $10^{44} M_6$ for a SMBH, detection is infrequent because of the short duration of the shock breakout. By integrating Equation 2.22 over all β, we can also determine how black holes of different masses contribute to the detection rate (Figure

2.7), with the peak rate corresponding to a black hole mass of $2 \times 10^5 M_\odot$. The predicted peak in the detection rate is predicated on the assumption that SMBHs obey the black hole to bulge mass relation for $M_\mathrm{h} < 10^6 M_\odot$. Therefore, the detection of TSBs would test the validity of this assumption and potentially provide compelling evidence for SMBHs in low mass galaxies.

2.5.2 Gravitational Wave Signal

In addition to the X-ray breakout signature, gravitational waves are also expected to radiate from the encounter, mostly originating from the changing location of the star relative to the black hole. We can estimate the strength of these waves by approximating the second time derivative of the moment of inertia tensor as $\ddot{I}^{ij} \sim GMR^2/c^4P^2$. If we assume that the period $P \sim r_\mathrm{p}/v_\mathrm{p} = r_p^3/GM_\mathrm{h}$, the length scale of variation $R \sim r_\mathrm{p}$, and the mass $M = M_*$, we find that the gravitational wave amplitude $\bar{h}$ is (Kobayashi *et al.*, 2004)

$$\bar{h} \sim \frac{GM_* r_\mathrm{s}}{dc^2 r_\mathrm{p}} = \frac{\beta G^2 M_*^{4/3} M_\mathrm{h}^{2/3}}{dc^4 R_*}, \tag{2.23}$$

in which d is the distance to the event. For our $\beta = 7$ simulation, we calculate that $\bar{h} \sim 10^{-21}$ for $d = 10$ Mpc. Gravitational waves will also be radiated as the star itself changes shape, but these distortions are far smaller than those generating by the changing quadrupolar moment of the star-SMBH system. Assuming that $R \sim R_*$, the gravitational wave amplitude is

$$\bar{h} \sim \frac{\beta^3 G^2 M_*^2}{dc^4 R_*}. \tag{2.24}$$

Note that this expression is independent of $M_{\rm h}$. For $d = 10$ Mpc, $\bar{h}$ is 10^{-23} for our encounter, beyond LISA's sensitivity range. Because this expression is proportional to β^3, the compression of the star can be a substantial contribution to the gravitational wave signature for very deep passages ($\beta \gtrsim 25$).

If both a gravitational wave signal and a TSB signal are available for the same event, additional information about the encounter can be obtained. While both observational signatures each place upper and lower limits on the properties of the disrupted star, either signature on its own cannot uniquely constrain the star's characteristics. By assuming a stellar mass-radius relationship $M_* = M_0 R_*^{\eta}$, Equation 2.23 can be combined with Equation 2.13 to calculate the mass of the disrupted star

$$M_* \sim \left(\frac{\bar{h} d c^4 t_{\rm cr}^2}{G M_0^{2\eta}} \right)^{\frac{1}{1-2\eta}}, \tag{2.25}$$

in which $t_{\rm cr}$ can be estimated by measuring the distance between the two peaks in the light curve (e.g. Figure 2.5). By determining the masses of disrupted stars, a distribution of stars that occupy the loss cone can be derived. As the IMF in the vicinity of SMBHs is poorly characterized even in our own galaxy (Alexander, 2005), a coincident detection of both the gravitational and TSB signatures would, for the first time, allow us to investigate the IMF in close proximity to extragalactic SMBHs.

2.6 Conclusion

While the simulation presented in this work features the highest resolution of the tidal disruption of star in 3D to date, it still has a few shortcomings. Our model does not have enough linear resolution to resolve the sharp pressure gradients that develop in deeply penetrating encounters, and thus the mid-plane pressure in the rebound phase is certainly underestimated by some factor. In addition, for close passages such as ours, GR effects start to become important. For $5 \lesssim \beta \lesssim 10$, the orbit is better characterized by a Paczynski-Wiita potential, but for $\beta > 10$, a fully general relativistic treatment of the Schwarzschild metric (Frolov *et al.*, 1994) is required. The orbits are then not ellipses, but may have two or more pericenter transversals and, as a result, could lead to the formation of multiple shocks. A full understanding of the compression process in such cases will require detailed GR hydrodynamical simulations.

In this work, we have provided numerical details of how a solar-type star is stretched, squeezed, and strongly shocked during an encounter with a massive black hole. We then calculated the radiation a distant observer might detect as the observational signature of the accompanying shock breakout. If detected, an $L \sim 10^{44}$ erg/s burst that fades within a few minutes and exhibits the predicted double-peaked signature in the soft X-rays would be compelling testimony that a star experiencing an ultra-close encounter with a black hole can be disrupted and compressed to such an extent that shock waves can be triggered.

Chapter 3

Surface Detonations in Roche Lobe Filling Double Degenerate Systems

3.1 Introduction

White dwarfs (WDs), the final state of main-sequence stars with mass $\lesssim 8M_{\odot}$, are extremely common, with about 10^{10} of them residing within the Milky Way (Napiwotzki, 2009). WDs are sometimes observed to have compact stellar companions, with "double degenerate" (DD) systems being defined as those in which the companion is another WD. Most frequently, DD systems are formed via common envelope evolution (Nelemans *et al.*, 2001b,a), and sometimes the final result of this evolutionary process is a binary consisting of a carbon-oxygen (CO) WD and a lower-mass helium WD companion (Napiwotzki *et al.*, 2007).

For decades, Type Ia supernovae (SNe) have been employed as standard candles. Still, even the preferred mechanism exhibits substantial variability (Timmes *et al.*, 2003; Kasen *et al.*, 2009). Complicating this issue further is that WDs may not need to have masses near the Chandrasekhar limit to be capable of exploding; other mechanisms include collisions between WDs in dense stellar environments such as the cores of globular clusters (Rosswog *et al.*, 2009a), tidal encounters with moderately massive black holes (Rosswog *et al.*, 2008a,b, 2009b; Ramirez-Ruiz and Rosswog, 2009), or as we are introducing in this chapter, the accretion of dense material from a He WD companion.

At the distance of tens of WD radii, gravitational radiation can bring two WDs close enough for the less-massive WD (secondary) to overfill its Roche lobe and begin transferring mass to the more-massive WD (primary). Because WDs expand as they lose mass, mass transfer from a WD donor is often unstable and can lead to a merger (Marsh *et al.*, 2004; Gokhale *et al.*, 2007). For binary mass ratios close to unity the circularization radius $R_{\rm h}$ drops below the radius of the primary R_1, and thus the accretion stream will directly impact the primary's surface.

Most studies of dynamically unstable DD systems focus on the evolution of the post-merger object and, assuming that the final object has a mass larger than the Chandrasekhar limit, on how the merged remnant may eventually lead to a Type Ia SNe (Livio, 2000; Yoon *et al.*, 2007). These models all assume that the rapid accretion that precedes coalescence is uneventful. In this chapter, we present three-dimensional hydrodynamics simulations that demonstrate that explosive phenomena are a likely consequence of the high accretion rates characteristic of the final stages of a merger in a DD system. In some cases, these explosive phenomena may lead to the complete detonation of the CO primary.

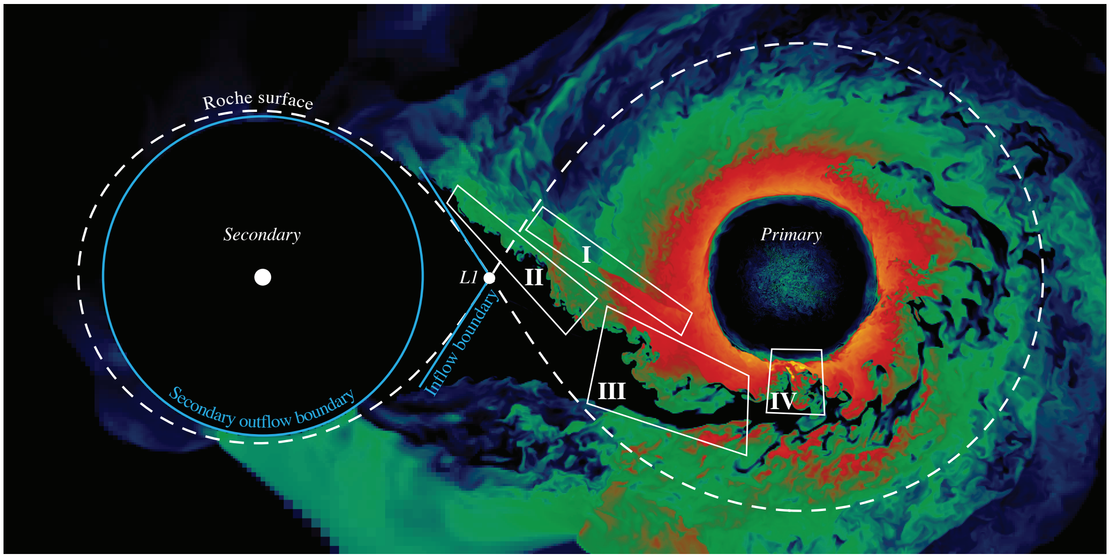

Figure 3.1: Setup of run Ba in FLASH, with several annotated regions of interest. The color scheme shows $\log T$ through a slice of the orbital plane. The cyan circle shows the spherical outflow boundary condition centered about the secondary, while the cyan wedge shows a cross-section of the cone used as the mass inflow boundary. The dashed contour shows the system's Roche surface. The white boxes with labels are described in Section 3.3.

3.2 Numerical Method and Initial Models

The lead-up to the merger has only been studied recently due to the sensitivity of the accretion to the transfer of angular momentum. Several groups have simulated these mergers in three dimensions using particle-based codes (Benz *et al.*, 1990; Rasio and Shapiro, 1995; Segretain *et al.*, 1997; Guerrero *et al.*, 2004; Dan *et al.*, 2009), with the latter being able to resolve the final ~ 100 orbits of the binary prior to coalescence. SPH simulations, with their excellent angular momentum conservation, are well-suited to determine the binary orbital evolution. However, because the SPH particles have a fixed mass and typical accretion rates are $\gtrsim 10^{-5}$ the total mass of the system per orbit, the accretion stream is only resolved by hundreds of particles at best. Consequently, SPH approaches are unable to resolve any of the accretion stream's detailed structure, including how the stream impacts the surface of the primary.

Eulerian codes are able to provide high resolution based on any combination of local and global simulation properties, and thus are ideal for systems where the regions of interest do not overlap with the regions of highest density (New and Tohline, 1997; Swesty *et al.*, 2000). Unfortunately, it is difficult to accurately simulate the overall orbital evolution for many orbits in grid-based codes due to the non-conservation of angular momentum (Krumholz *et al.*, 2004), although a careful choice of coordinate system has led to recent success (D'Souza *et al.*, 2006; Motl *et al.*, 2007). Because the stability of the system depends on the structure of the primary and the secondary, the grid-based simulations that investigate stability must fully resolve both stars, and thus the stream and the primary's surface are less resolved in these simulations.

Here we follow a hybrid approach that combines the strengths of both SPH- and grid-based methods. We follow the impact of the mass transfer onto the orbital evolution by performing an SPH simulation (Dan et al. 2010, in prep.) and use the obtained, time-dependent results for orbital separation and $\dot{M}$ as boundary conditions for FLASH (Fryxell *et al.*, 2000). This combination allows us to realistically determine the dynamic stability of the binary while not sacrificing our spatial resolution of the accretion.

In FLASH, the primary is built under the assumption of spherical hydrostatic equilibrium and a constant temperature of 5×10^5 K, and is mapped into the simulation explicitly. The secondary is *not* mapped directly into the grid and is taken to be a point mass surrounded by a spherical outflow boundary condition. The simulation is performed in a non-inertial frame rotating with angular frequency $\omega = \sqrt{G(M_1 + M_2)/a^3}$ about the barycenter. The primary's gravity is calculated using a multipole expansion of its potential, and because the quadrupolar contribution of the secondary is negligible, we approximate the secondary's gravitational field as a monopole. Because the choice of frame and the presence of the secondary changes the hydrostatic configuration of the primary, we first allow the primary to slowly relax in the presence of the secondary's potential by removing a fraction of its kinetic energy every time-step over many dynamical timescales.

The nuclear composition of the fluid is evolved via the 13 element α-chain network of Timmes (1999) and Timmes *et al.* (2000). Pressures and temperatures are calculated using the Helmholtz equation of state (Timmes and Swesty, 2000). The accretion rate provided by the SPH calculation is used to generate a quasi-hydrostatic inflow boundary condition to replicate the flow of matter from the secondary to the primary (Figure 3.1). The boundary we use is cone-shaped with the apex located at *L1*, and mass is added to the cone under the assumption that the stream is in hydrostatic equilibrium in the direction perpendicular to the barycentric line (Lubow and Shu, 1976). The flow is directed towards the barycenter of the system at velocity $v = c_{\rm s} \sim 10^8$ cm/s, the sound speed within the secondary. In all simulations presented here, the stream is assumed to be pure He. The four simulations that we have performed are summarized in Table 3.1.

3.3 Accretion Stream Instabilities

In a binary system undergoing mass transfer, the fate of the accretion stream is determined by ratio $R_1/R_{\rm h}$. For all three of the binaries we describe $R_{\rm h} < R_1$ and thus the stream would directly impact the surface of the primary assuming the stream was collisionless. How-

Table 3.1: Simulation results.

Run	$t_{\rm evol}$[a]	$l_{\rm min}$[b]	Primary		Secondary		$M_{\rm torus,max}$[c]	Surf.	Mass ejected	Yield ($10^{-3}M_\odot$)	
	s	10^6 cm	$M_\odot$	Type	$M_\odot$	Type	$10^{-2}M_\odot$	det.	$10^{-2}M_\odot$	$20 \le A \le 32$	$A \ge 36$
A	1885	4.9	0.67	CO	0.45	He	14	No	-	-	-
B	434	3.7	0.9	CO	0.45	He	9.7	Yes	5.9	11	1.9
Ba[d]	25	1.8	0.9	CO	0.45	He	11	No	-	-	-
C	335	3.4	0.9	CO	0.6	He/CO	5.0	Yes	6.0	16	5.6

[a] Total evolution time.

[b] Minimum grid cell size.

[c] Maximum mass of the helium torus accumulated during the run; this is either the value just before detonation or at the end of the run if there was no detonation.

[d] Run Ba is initialized from a checkpoint produced by run B at $t = 403s$.

ever, the stream can eventually be deflected by the ram pressure of the thick torus of helium that gradually accumulates on the primary's surface, preventing a direct impact.

As the sound speed within the torus is far smaller than the Keplerian rotation velocity, the collision between the torus and the stream is highly supersonic ($M > 10$), which leads to the development of a standing shock (Figure 3.1, region I). This shock establishes pressure equilibrium across the stream-torus interface. Because of the temperature increase of the material falling from *L1* to the surface of the primary, the torus consists of material heated to a temperature close to the virial temperature of $GM_1 m_{\rm p}/R_1 k_{\rm b} \sim 10^8$ K. Radiation pressure becomes competitive with degeneracy pressure at these temperatures and densities, and as a result the torus has a density smaller than the incoming accretion stream.

Because the accretion stream and the helium torus do not move in the same direction, the difference in velocity at the interface is substantial, $U_1 - U_2 \sim \sqrt{GM_1/r_1}(\sqrt{2} - \cos\theta)$, where θ is the angle between the stream and torus velocities. This shear can lead to the rapid growth of Kelvin-Helmholtz instabilities along the interface between the two regions (Figure 3.1, region II). An important factor in determining which perturbations are unstable is the magnitude of the restoring force perpendicular to this interface. The acceleration g limits the instability to $k > k_{\rm min}$ (Chandrasekhar, 1961)

$$k_{\rm min} = \frac{g\,(\alpha_1 - \alpha_2)}{\alpha_1 \alpha_2\,(U_1 - U_2)^2}, \tag{3.1}$$

where $\alpha_1 \equiv \rho_1/(\rho_1 + \rho_2)$ and $\alpha_2 \equiv \rho_2/(\rho_1 + \rho_2)$. As long as $g > 0$, only perturbations with wavelength $\lambda < \lambda_{\rm max} = 2\pi/k_{\rm min}$ can grow. Within the primary's Roche lobe, g is determined by the combination of the primary's gravity and the Coriolis force

$$g = 2\Omega|\vec{v}| - \frac{GM_1}{|\vec{r}_1|^2}\frac{|\vec{r}_1 \times \vec{v}|}{|\vec{r}_1|\,|\vec{v}|}. \tag{3.2}$$

Because the Coriolis force is always perpendicular to the velocity, its contribution to g is always equal to the magnitude of the force. Only the component of the primary's gravity that is perpendicular to $\vec{v}$ will contribute to g. Near *L1* where the cumulative gravitational forces are parallel to the velocity, the Coriolis term is dominant and is directed away from the primary, and thus g is positive. As the stream falls toward the surface of the primary, $U_1 - U_2$ continually increases, allowing progressively longer wavelengths to become unstable. And because the Coriolis effect is $\propto |\vec{v}| \propto |\vec{r}_1|^{-1/2}$ while the primary's gravity is $\propto |\vec{r}_1|^{-2}$, the primary's gravity eventually becomes the dominant contributor to the restoring force. As the primary's gravity is opposite to the Coriolis force, g eventually changes sign, at which point all wave modes become unstable (Figure 3.1, region III).

The helium torus, which is both clumpy and has a radial density profile, drives the seed vertical displacements in the accretion stream. The torus is highly turbulent, with the largest bulk motions being driven at scales comparable to the width of the accretion stream ($\sim 10^8$ cm) and at speeds that are highly supersonic. Therefore, the power spectrum of the resulting turbulent cascade is given by Burgers turbulence ($E \propto k^{-2}$). Consequently, perturbations with large wavelengths are seeded with large initial amplitudes, giving them a head start over smaller perturbations. Additionally, power is transferred from large k to small k by the tidal stretching of waves as they fall in the primary's gravity. A numerical calculation of the growth rate shows that the largest unstable modes experience a ten-fold increase in amplitude in the time it takes to fall from *L1* to the primary's surface. Because the flow is three-dimensional, instabilities larger than the stream size cannot form, and the end result is that the stream consists of knots of material that are comparable in size to the stream itself (Figure 3.1).

3.4 Surface Detonations

We find that instabilities in the accretion stream are present in all four runs once the helium torus has acquired enough mass to deflect the stream. The material that is compressed against the surface of the primary by the dense knots formed in the stream can be heated to billions of degrees Kelvin (Figure 3.1, region IV). At the onset of mass transfer, the density of the stream is too small to heat the underlying material appreciably. This allows $\sim 1-15\%$ of a solar mass of helium to accumulate on the surface of the primary. As the density of the accretion stream increases with the decreasing separation between the WDs, the temperature of the compressed layer can exceed the temperature required to explosively ignite helium via the

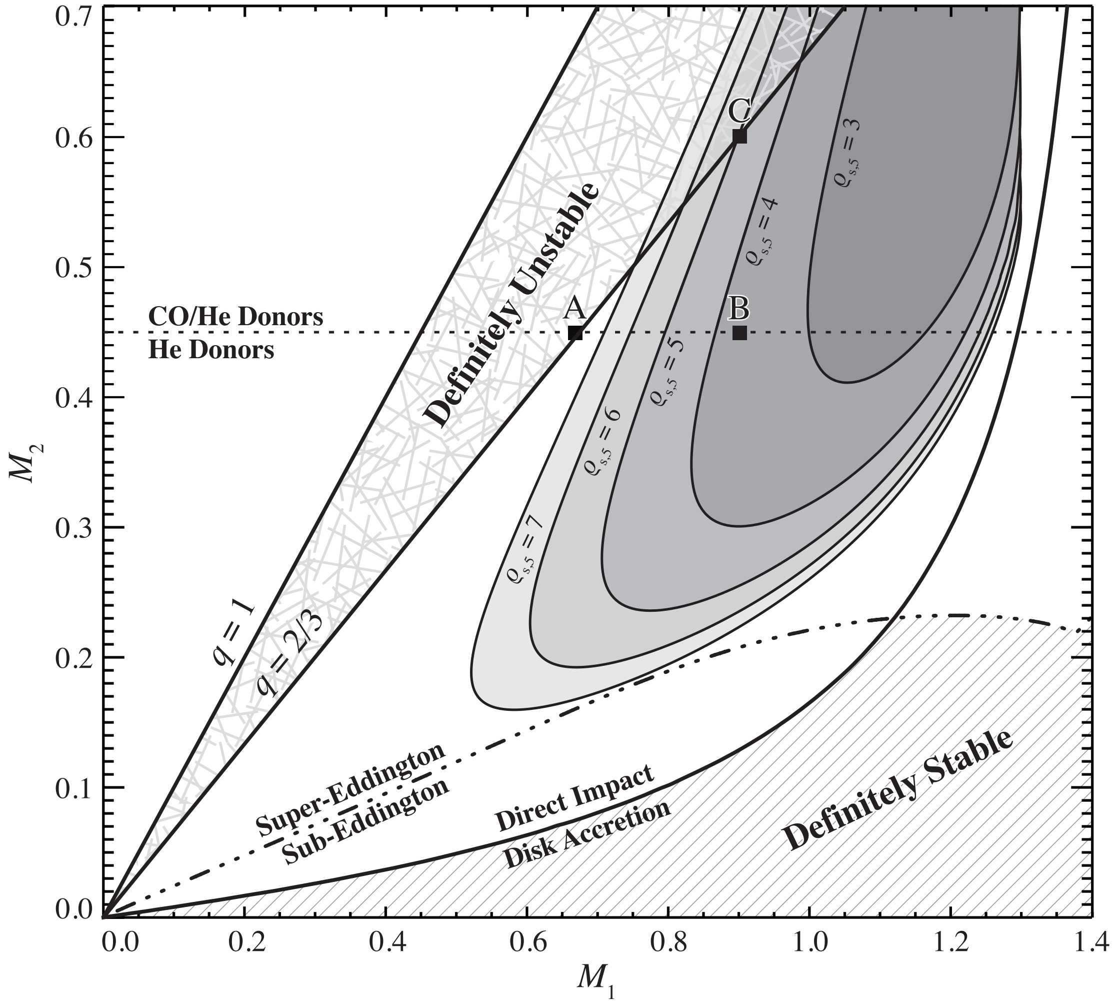

Figure 3.2: The hashed region on the lower right shows systems that are definitely dynamically stable, while the sticked region in the upper left shows systems that are definitely unstable. The thick solid line shows the transition from direct impact to disk accretion, while the dot-dashed curve shows the separation between sub- and super-Eddington accretion in the weak coupling limit (Marsh *et al.*, 2004). The contours show where $\tau_{\rm dyn} = \tau_{3\alpha}$ for different stream densities $\rho_{\rm s,5} \equiv \rho_{\rm s}/10^5$ assuming a torus density of 3×10^5 g cm^{-3}. Surface detonations are likely for systems that accrete with $\rho_{\rm s}$ for which $\tau_{\rm dyn} < \tau_{3\alpha}$ and then experience an increase in $\rho_{\rm s}$ until $\tau_{\rm dyn} > \tau_{3\alpha}$.

triple-alpha process. This leads to a gravitationally confined surface detonation that propagates through the helium torus that wraps around the surface of the primary at approximately the Keplerian velocity (Figure 3.3).

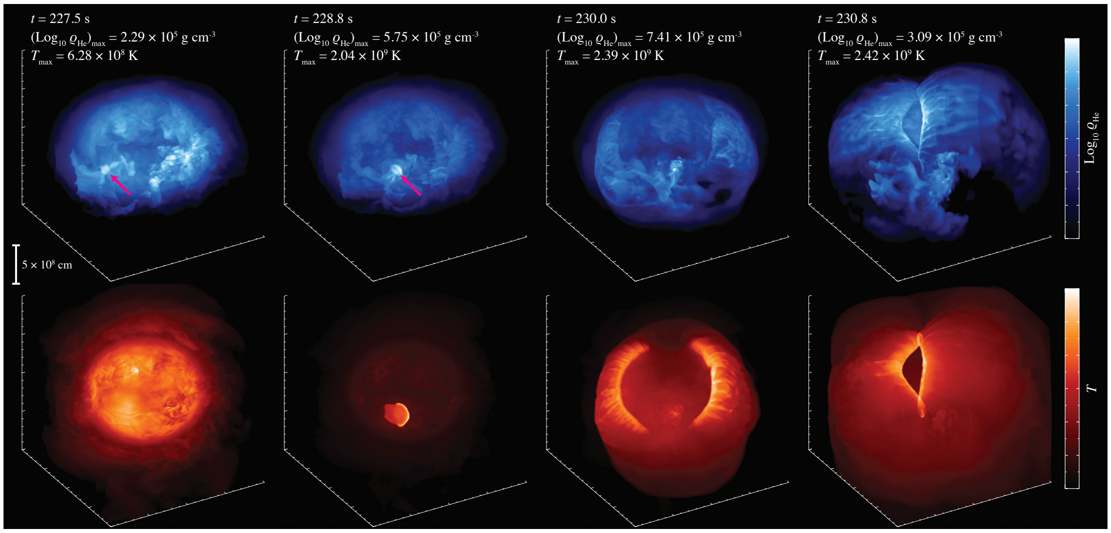

Figure 3.3: Volumetric snapshots showing the temperature T and $\log \rho_{\text{He}} \equiv \rho X_{\text{He}}$ during the explosive event on the surface of the primary in run C. A dense knot of helium that formed through Kelvin-Helmholtz instabilities in the accretion stream is marked by a magenta arrow. The evolution of the surface detonation is described in Section 3.5.

The conditions required for a successful surface detonations are summarized in Figure 3.2. Only systems that are dynamically unstable will ever have accretion rates capable of igniting surface detonations via stream instabilities, and thus the lower-right region of the figure is excluded. The question of whether the surface detonation will occur in a given binary is tricky to answer because the process is highly stochastic; the impact trajectory, density, and geometry of the knots that initiate the detonations vary considerably over the course of the simulations. Nevertheless, we can estimate when surface detonations will occur by comparing the timescale for triple-α reactions $\tau_{3\alpha}$ (Caughlan and Fowler, 1988) to the dynamical timescale $\tau_{\text{dyn}} \simeq R_1/v_{\text{esc},1}$ at the surface of the primary.

For a surface detonation to involve a significant amount of mass, the system must accrete material at a rate for which $\tau_{3\alpha} > \tau_{\text{dyn}}$, and then transition to a rate where $\tau_{3\alpha} \leq \tau_{\text{dyn}}$.

By solving the equations of motion for a test particle released from *L1*, we estimate the two timescales in Figure 3.2 for various stream densities for different primary and secondary masses. The conditions at the He/CO interface are given by $\partial P/\partial r = \partial \phi/\partial r$, where $\phi \simeq GM_1/r_1 - r_1\Omega_{\rm tor}^2$ and $\Omega_{\rm tor}$ is the angular velocity of the torus, which is related to the component of the accretion stream velocity parallel to the primary's surface. Conversely, the ram pressure $P_{\rm ram} \propto \rho v^2$ applied by the accretion stream is dependent on the component of velocity perpendicular to the primary's surface.

The density structure of the torus is approximately fixed as the system evolves towards merger because ϕ only increases slightly due to mass accretion. Meanwhile the stream density continually increases, resulting in the contour of $\tau_{3\alpha} = \tau_{\rm dyn}$ moving leftwards in Figure 3.2. When $\tau_{3\alpha} \lesssim \tau_{\rm dyn}$, the increase in temperature of the torus can no longer be controlled by adiabatic expansion, which results in thermonuclear runaway and a detonation in the helium torus.

3.5 Results and Discussion

Surface detonations are present in both of the longer runs with a 0.9 $M_\odot$ CO primary, although run B detonates much later in its evolution than run C. The geometry and evolution of the detonations are similar in both runs. A small region of the surface helium is heated to a temperature of $\sim 2 \times 10^9$ K, leading to a detonation front that expands outwards from the ignition site along the primary's surface (Figure 3.3, second column). Because the helium layer is toroidal rather than spherical, the front runs out of fuel as it propagates towards the primary's poles. Consequently, the detonation splits into two fronts that run clockwise and counterclockwise around the equator of the primary (Figure 3.3, third column). These detonation fronts eventually run into each other along a longitudinal line that is opposite to the original ignition site (Figure 3.3, fourth column). The highest temperatures are produced in this convergence region.

For run A, the primary's surface gravity is too low to compress the helium layer above the critical temperature necessary for thermonuclear runway. No detonation was observed in run Ba, despite being initialized using a checkpoint from run B just prior to the observed detonation in B. This is because of the stochastic nature of the ignition mechanism — the particular dense knot of material that led to the surface detonation in B has a different shape in Ba, and did not have a favorable geometry for igniting the helium torus. And because Ba has twice the linear resolution of run B, we could only afford to evolve it for a short period of time.

If a helium surface detonation occurs as the result of stream instabilities in a DD system, the resulting transient event could potential resemble a dim Type Ia SNe (Bildsten *et al.*, 2007; Perets *et al.*, 2009; Foley *et al.*, 2009). The results of our simulations shows a large degree of variability which ultimately depends on the geometry of the dense knots when they strike the surface of the primary in the impact zone. However, if the post-detonation temperature is not much larger than 2×10^9 K or the geometry of the detonation fronts are not favorable, it is possible to only synthesize intermediate-mass α-elements (Table 3.1).

The prospect of igniting the CO core itself is attractive because the typical densities of moderate-mass WDs ($M \sim 1.0 M_\odot$) are $\sim 10^6 - 10^7$ g cm^{-3}, comparable to the densities found in the DDT for Type Ia SNe (Khokhlov *et al.*, 1997). Fink *et al.* (2007) (hereafter FHR) show

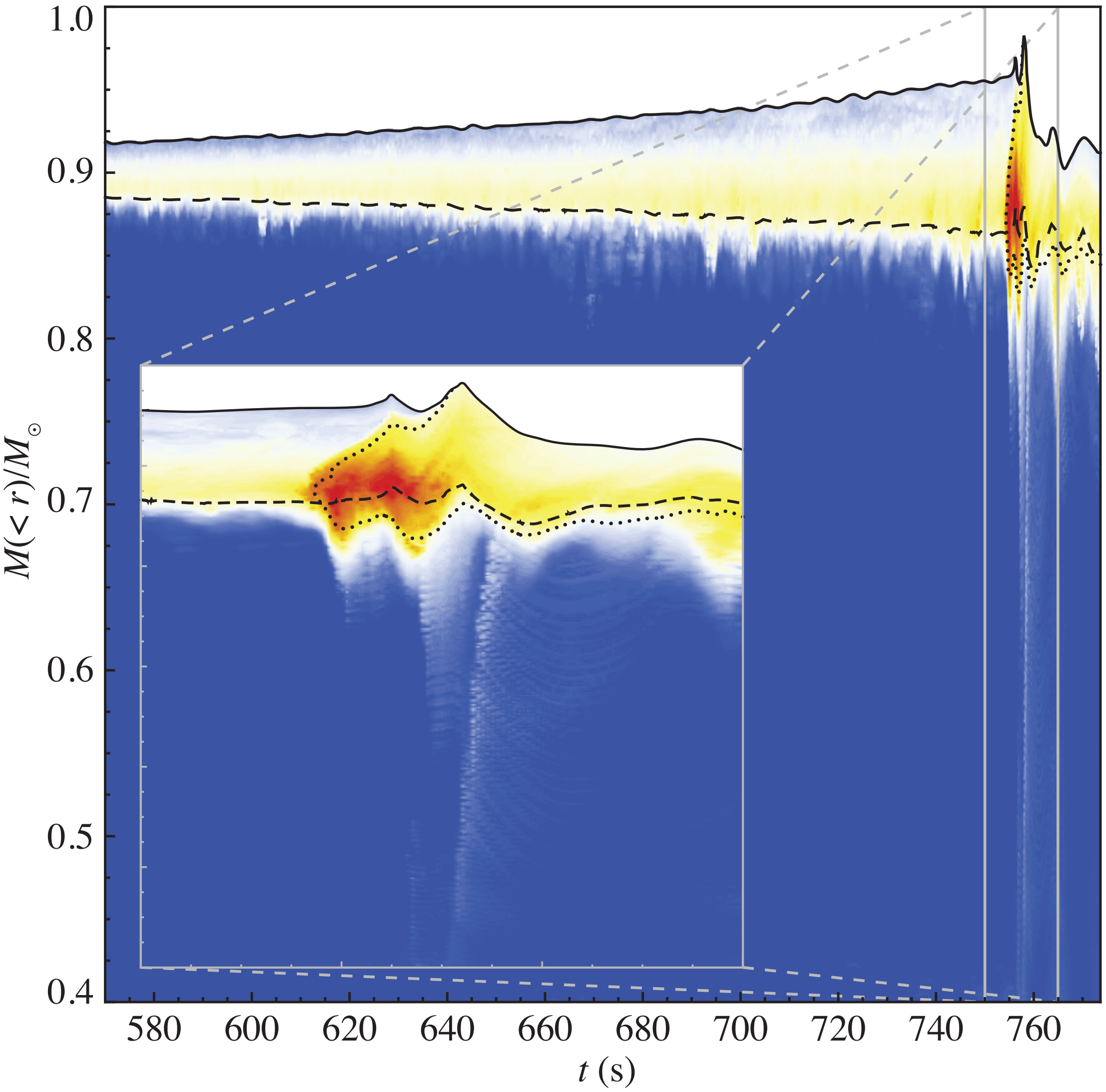

Figure 3.4: Maximum temperature T in a mass shell as a function of interior mass $M(<r)$ and time t for run B. Each shell lies on a surface of equal gravitational potential. The shading is logarithmically binned, with red corresponding to $T_{\max}$ and blue corresponding to $T_{\min} = T_{\max}/10^{1.5}$. The dashed line shows the region where $X_{\mathrm{He}} > 0.02$, while the dotted line shows where $X_{\mathrm{Ne}} > 10^{-3}$. For convenience, we include a zoomed view of the surface detonation as an inset.

that when $0.1M_\odot$ of helium is ignited at the He/CO interface of a moderate-mass WD, strong shocks are launched deep into the CO core, which converge at a focusing point. This focusing produces a region where the temperature and density meet the criteria for explosively igniting carbon (Niemeyer and Woosley, 1997; Röpke *et al.*, 2007; Seitenzahl *et al.*, 2009), thus leading to a full detonation of the CO core.

The linear resolution of our simulations is substantially coarser than the highest-resolution two-dimensional simulations of FHR, and we are certainly under-resolving the true density and temperature peaks. However, FHR's results appear to be rather optimistic when applied to our model for the following reasons. First, FHR assumes perfect mirror symmetry, which dramatically increases the amount of focusing by forcing the shocks to converge at a single point rather than a locus of points. Second, FHR does not use a nuclear network and makes the simplifying assumption that the entire He envelope is burned to Ni, which naturally overestimates the energy injected into the CO core when compared to the more realistic case where burning is incomplete.

Because of these differences, the conditions for double detonation are still not met even in our run with the most favorable shock geometry and strongest surface detonation (run C). In the focusing region of run C, the temperature and density are 2.5×10^8 K and 2.0×10^7 g cm^{-3}, respectively. Conditions for CO core detonation may be more propitious in systems containing a slightly more massive primary, but ultimately the successful detonation of the core depends on the precise distribution of temperature and density within the high-pressure regions of the convergence zone (Seitenzahl *et al.*, 2009).

The mechanism reported here for the detonation of a sub-Chandrasekhar CO WD in a dynamically unstable binary is not tied to a particular mass scale and therefore allows for considerably more diversity. As outlined above, mass transfer between a pure He WD or a

He/CO hybrid and a CO WD before the merger provides a novel pathway to ignite CO WDs. Even if a critical amount of mass is not raised above the conditions required for CO detonation, a peculiar underluminous optical transient should signal the last few orbits of a merging system.

Chapter 4

Tidal Ejection and Disruption of Giant Planets

4.1 Introduction

Both radial velocity and transit surveys are biased towards planets that are both massive and close to their parent stars, the region of parameter space corresponding to planets with a mass larger than that of Neptune and a semi-major axis < 0.1 au is particularly well-explored (Ida and Lin, 2004; Shen and Turner, 2008; Zakamska *et al.*, 2010). This has led to the discovery of many giant planets that are remarkably close to their parent stars, with several examples that orbit so closely that they risk imminent disruption (Li *et al.*, 2010). These planets are also found to be dramatically misaligned with their parent star's spin (Triaud *et al.*, 2010; Schlaufman *et al.*, 2010).

There are three primary physical processes that can deposit a planet on an orbit that is very close to its parent star: disk migration, the Kozai mechanism, and planet-planet scattering. Disk migration can yield hot Jupiters, but as the star collapses from the same cloud as the protoplanetary disk that encircles it, it is difficult to explain the observed orbit misalignments using this mechanism alone (though see Watson *et al.*, 2010; Foucart and Lai, 2011, for discussions regarding star-disk interactions). The Kozai mechanism (Kozai, 1962) can lead to the large eccentricities required to produce close-in planets, but it can only operate in systems in which a massive planet or secondary star are present, and the mechanism may be mitigated by general relativistic effects that become important before tidal dissipation is large enough to circularize the orbit (Takeda and Rasio, 2005; Fabrycky and Tremaine, 2007). Planet-planet scattering can produce both the observed semi-major axis and inclination distributions, and can deposit planets close enough such that tides can circularize the orbits in a time that is less than the system age. Additionally, the object that acts as a scatterer can have approximately the same mass as the scattered object itself and still yield a hot Jupiter in a significant fraction of systems (Ford and Rasio, 2008), negating the need for a non-planetary companion in the system.

Previous hydrodynamical work has only focused on the planet's first close fly-by (Faber *et al.*, 2005, hereafter FRW), and does not investigate how prolonged tidal forcing over many orbits affects a planet's chances for survival. In this chapter we have performed hydrodynamical simulations of multiple passages of a Jupiter-like planet by a Sun-like star, bridging the gap between numerical and analytical work that have focused on extremely close and extremely grazing encounters respectively. We find that scattering planets into star-grazing orbits is more destructive than previously thought, with Jupiter-like planets being destroyed or ejected at distances no smaller than 2.7 times the tidal radius $r_{\rm t}$. As some exoplanets are currently observed to have semi-major axes less than twice this critical value, their initial eccentricities may be required to have been substantially smaller than unity if planet-planet scattering is the mechanism responsible for bringing them so close to their host stars. This strongly suggests that planet-planet scattering alone cannot explain the complete observed population of close-in Jupiter-like exoplanets, and that the process must operate along with one of either the Kozai mechanism, disk migration, or both. These three processes likely act in concert to produce the observed population of hot gas giants, with the relative importance of each process being a function of the system's initial conditions.

If planet-planet scattering is common enough to explain the existence of hot Jupiters, we predict that there should be two signatures of disruption that are readily detectable with today's instruments. Firstly, we find that the parent star can have its spin significantly altered by the accretion of material removed from the planet as a result of the disruption, producing a star that can be significantly misaligned relative to any remaining planets. Secondly, we find that most planet disruption events lead to the planet's ejection from the host system prior to the planet being completely destroyed, and that this ejected planet can remain almost as bright as its host star for centuries.

In this chapter we focus on the results of numerical hydrodynamical simulations that have been used to attempt to ascertain the true radii of destruction and ejection for Jupiter-like exoplanets, and the consequences of these planet-removing processes on their stellar hosts. In Section 4.2 we review the history of the analytical and numerical work done to characterize the orbital evolution of a planet that comes within a few tidal radii of its host star, and then we detail our particular numerical approach to modeling tidal disruption. We report the results of our simulations in Section 4.3. In Section 4.4 we discuss the implications of our results, with special attention paid to the viability of various mechanisms for producing hot Jupiters, and the

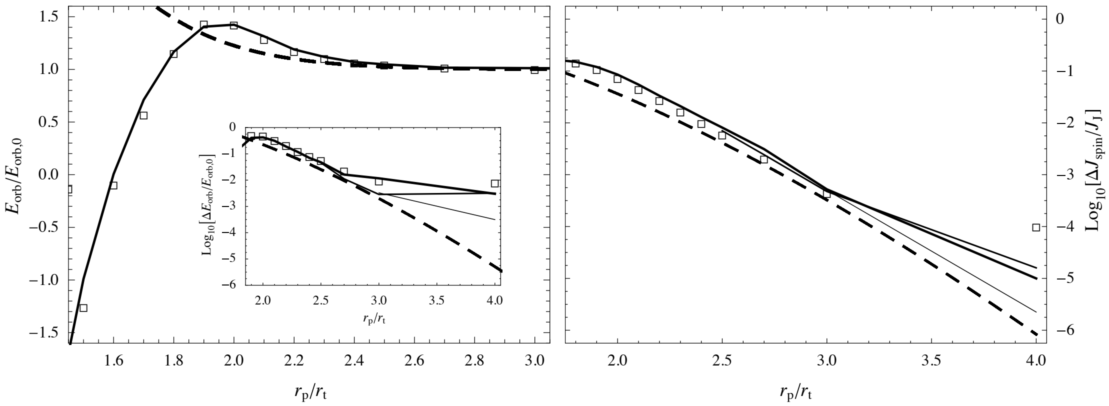

Figure 4.1: Final orbital energy $E_{\rm orb}$ scaled to the initial orbital energy $E_{\rm orb,0}$ (left panel), change in orbital energy $\Delta E_{\rm orb} \equiv E_{\rm orb,0} - E_{\rm orb}$ scaled by $E_{\rm orb,0}$ (left sub-panel), and spin angular momentum $J_{\rm spin}$ scaled by the characteristic angular momentum of Jupiter $J_{\rm J}^2 \equiv GM_{\rm J}^3 R_{\rm J}$ (right panel) as functions of periastron distance $r_{\rm p}$ after a single near-parabolic encounter between a $M_{\rm P} = M_{\rm J}$ Jupiter-like planet and a $M_* = 10^3 M_{\rm J}$ star. The solid lines show the results from this work, with decreasing thickness corresponding to increasing maximum refinement, square markers show the results of FRW, and the dashed lines shows the prediction of PT using FRW's analytical $n = 1$ solutions for T_l and S_l. Note that our results and that of FRW are consistent for $r_{\rm p} \leq 2.5 r_{\rm t}$. At the highest resolution, our results are consistent with that of PT until $r_{\rm p} \geq 4 r_{\rm t}$.

observational signatures of planetary disruption and ejection. We summarize the shortcomings of our models and the possible fates of a Jupiter-like exoplanet in Section 4.5. Appendix A is provided to detail our algorithm used to simulate multiple orbits and for presenting tests of the algorithm's conservative properties.

4.2 Modeling Planetary Disruption

4.2.1 Previous Disruption Models

Tidal encounters between a point mass and an extended, initially spherical object have been described with progressively more detailed analytical models and simulations. The first analytical models of tidal dissipation were laid out in Press and Teukolsky (1977) (hereafter

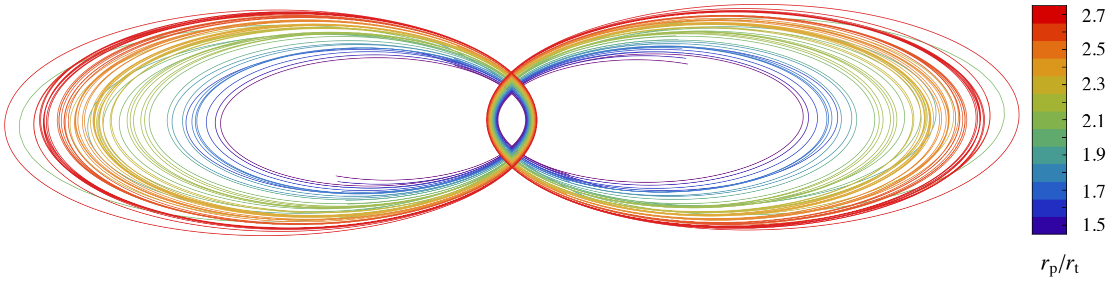

Figure 4.2: The double rainbow curves show orbital trajectories for both the planet (left) and star (right) during the encounter for different values of the periastron distance r_p. The star's trajectory is magnified by a factor of $M_*/M_\mathrm{P} = 10^3$ to make its motion apparent. While the orbits do precess slightly over the course of the simulations, this plot shows the orbits with the precession removed. Note that the $r_p = 2.1$ run (light green) experiences a particularly ejective encounter on its 2nd periastron passage.

PT), which assumes that the tidally excited body retains its spherical shape and that the motions induced by the encounter can be described with spherical harmonics. This model works quite well for encounters where tides are weak, i.e. more than a few tidal radii away from the perturbing body, where the assumption of sphericity is valid. If mode-mode coupling is weak, the initially excited modes have no mechanism to share energy with each other during the encounter itself, and the PT formalism can accurately predict the amount of energy injected into the extended object.

In the PT formalism, the amount of energy and angular momentum injected into an object is derived by taking the convolution of the object's modes of oscillation and the frequency decomposition of the tidal field, which drops the time-dependence from the governing equations. However, if the incoming object is already oscillating, the phase of these oscillations relative to the time of periastron is important, which by construction cannot be resolved by the time-independent PT formalism. The absence of time-dependence also requires that the base-state is cylindrically symmetric relative to the line connecting the extended object to the perturber, which can only be accomplished for an initially non-rotating object by using a spherical geometry. As the amplitude of the mode oscillations approaches the size of the object itself, the body must become highly non-spherical and therefore the PT formalism must break down.

These two shortcomings lead to the development of the "affine" model for tidal encounters (Carter and Luminet, 1983, 1985), which allows the initially spherical object to deform into a triaxial ellipsoid during and after the encounter. One axis of the ellipsoid is fixed to be perpendicular to the orbital plane, with the other two axes lying within the plane at a right angle to each other and with arbitrary orientation angle relative to the first axis. This feature allows for the object to be followed dynamically, which means that the incoming state of the object's oscillations can affect the object's response to future encounters.

Because the excitation of normal modes in a dynamically inert object can only yield an increase in the object's energy and angular momentum budgets, an initially spherical object would always find itself in a more-tightly bound orbit after the encounter. An important facet of the problem that the affine model can investigate is how the fundamental modes excited in previous encounters are de-excited in future encounters, which can lead to a positive change in the orbital energy. The inclusion of de-excitation of modes adds a chaotic component to the problem, with the orbital evolution behaving as a "random-walk" process (Kochanek, 1992; Mardling, 1995a).

While mass loss has been included in a nested-ellipsoid version of the affine model presented by Ivanov and Novikov (2001), asymmetrical mass loss is not treated as the models assume mirror symmetry. Asymmetric mass loss is expected in real disruptions as the tidal field is stronger on the side of the object facing the point mass. This is due to the steep power-law dependence of the strength of the tidal field ($\propto r^{-3}$) and the non-linear evolution of the tide raised on the object, with both the velocity and amount of mass lost being larger on the side of the object closest to the point mass. Numerical simulations by FRW show that this asymmetric mass loss leads to a substantial deviation from the nested-ellipsoid treatment, especially when the closest approach distance is $\lesssim 2r_{\rm t}$. Within this distance, the asymmetric removal of mass can lead to a positive increase in the orbital energy, which can cause the object to be completely ejected from the system if $E_{\rm orb} \equiv -GM_*M_{\rm P}/2a \sim E_{\rm obj}$.

The disruption of polytropes in highly eccentric encounters has been investigated numerically by both Lagrangian (Nolthenius and Katz, 1982; Bicknell and Gingold, 1983; Evans and Kochanek, 1989; Kobayashi *et al.*, 2004; Faber *et al.*, 2005; Rosswog *et al.*, 2008b, 2009b; Ramirez-Ruiz and Rosswog, 2009; Lodato *et al.*, 2009) and Eulerian methods (see Chapter 2, also see Khokhlov *et al.*, 1993b,a; Frolov *et al.*, 1994; Diener *et al.*, 1997; Guillochon *et al.*, 2009), with the principle focus being on stars or compact objects that are disrupted by point-like gravitational sources. However, most hydrodynamic simulations that have focused on the long-term survival of these systems only consider when the two objects have a mass ratio close to unity (Lee *et al.*, 2010; Lorén-Aguilar *et al.*, 2009), or for non-disruptive encounters (Rathore, 2005). Recently, Antonini *et al.* (2010) performed low-resolution multiple-passage simulations in the context of the galactic center, allowing the exploration of a large parameter space at the expense of accuracy.

To summarize, most analytical models of tides in an astrophysical context focus on objects which do not lose any mass at their closest approach, and conversely most numerical work has focused on encounters where the object is completely destroyed. The intermediate regime, where objects lose some mass but are not completely destroyed in their first passage, is largely uncharacterized. If the planet survives the initial encounter, some of the mass that is removed from the planet can become bound to the planet again as it recedes from periastron to a region with a weaker tidal field. The return and subsequent re-accretion of this material is not treated at all in analytical models. As we will describe in Section 4.3.2, the structure of the planet can be significantly altered by the re-accretion of the planetary envelope, and the inclusion of this re-accretion into tidal disruption theory is necessary to determine if a planet will ultimately survive.

4.2.2 Our Approach

While Lagrangian codes are well-suited for treating problems where a hydrostatic object moves rapidly with respect to a fixed reference frame, their relatively poor scalability makes it difficult to follow the evolution of an object for many dynamical timescales with sufficient spatial resolution. On the other hand, maintaining near-hydrostatic balance in rapidly advecting frames using Eulerian methods can also be quite challenging. Robertson *et al.* (2010) show that performing Eulerian simulations in a boosted frame with unresolved pressure gradients leads to a spurious viscosity term that tends to damp out instabilities. This has been colloquially referred to as the non-Galilean invariance (GI) of the Riemann problem (Tasker *et al.*, 2008; Springel, 2010). While Robertson *et al.* showed that GI issues can be avoided with increased resolution, the requisite spatial resolution can be impractical for three-dimensional simulations that are evolved over thousands of dynamical timescales, or for when the bulk velocities are many times larger than the internal sound speeds within the simulation. The problem is compounded in the outermost layers of Jupiter-like planets, which exhibit particularly steep pressure gradients.

To side-step the GI issues, our simulations are performed in the rest-frame of the planet, which limits the typical fluid velocities to the planet's sound speed for tidal disruption calculations (see Chapter 2 and Guillochon *et al.*, 2009). We model the planet as an $n = 1$, $\Gamma = 2$ polytrope, with the fluid being described by a polytropic equation of state ($P \propto \rho^{\gamma}$), where the adiabatic index $\gamma = \Gamma$. This gives a reasonable approximation to the interior structure of Jupiter-like planets (Hubbard, 1984), as long as the core is not a significant fraction of the planet's mass. Our simulations are constructed within the framework of FLASH (Fryxell *et al.*, 2000), an adaptive-mesh, grid-based hydrodynamics code. We treat the star as a point-mass because the distortion of the star itself contributes negligibly to the planet's orbital evolution in the case where $M_{*} \gg M_{\rm P}$ (Matsumura *et al.*, 2008). The relative positions of the star and the planet are explicitly tracked over the course of the simulation using two virtual particles $\mathbf{x}_{\rm S}$ (star) and $\mathbf{x}_{\rm P}$ (planet), which are evolved alongside the hydro calculation using a Burlisch-Stoer integrator (Press *et al.*, 1986) with maximum error constrained to be less than 10^{-12}. The planet's self-gravity is calculated using a multipole $O(l_{\rm max}^2 N)$ expansion of the fluid, where we take $l_{\rm max} = 12$.

The flux-calculation step in any hydro code depends on the time-dependent force applied to the fluid over the duration of the step. Because the gravitational field is applied as a source term in most multi-dimensional hydro codes that include self-gravity, conservation of energy is not explicitly achievable when self-gravity is included, as the potential at timestep $m+1$ is unknown and must be estimated. In the case of self-bound objects in hydrostatic equilibrium, small perturbations can lead to a systematic drift in the total energy of the system. For hydrostatic objects, we find that an increase in spatial resolution reduces this drift by an amount that approximately scales with the number of voxels used to resolve a given region. This is because the relative forces acting on neighboring cells decrease as the voxels are more closely packed together, and because the sharp density gradients present in the 1D hydrostatic profile are better resolved.

The potential at $m+1$ must be estimated because the value of ϕ^{m+1} depends on ρ^{m+1}, which is not known until the hydro step has been completed. This extrapolation is one of the main sources of error in the code because the obtained acceleration is only an estimate based on the previous evolution of ϕ. And because the extrapolation is only first-order accurate in time, smaller time-steps do not improve the accuracy of the results (Springel, 2010). The error can be somewhat reduced by using a higher-order extrapolation that includes N previous time-steps, but our tests show that including the $m-2$ time-step only leads to a few percent reduction in error relative to the first-order approximation. Additionally, it imposes additional memory and disk overhead to save the full potential field from the previous N time-steps.

For cases where the object is nearly in hydrostatic equilibrium the gravitational field does not rapidly change with time. However, a tidal disruption can lead to variations in the gravitational field of order unity over a fraction of the planet's dynamical timescale. As a result, the default method used by FLASH to apply the gravitational field can lead to substantial changes in the total energy. Motivated by this, we implement a novel method where the potential contribution from the fluid and from tidal forces are separated, negating much of the error associated with the extrapolation of the potential. Details of this algorithm are provided in Appendix A.

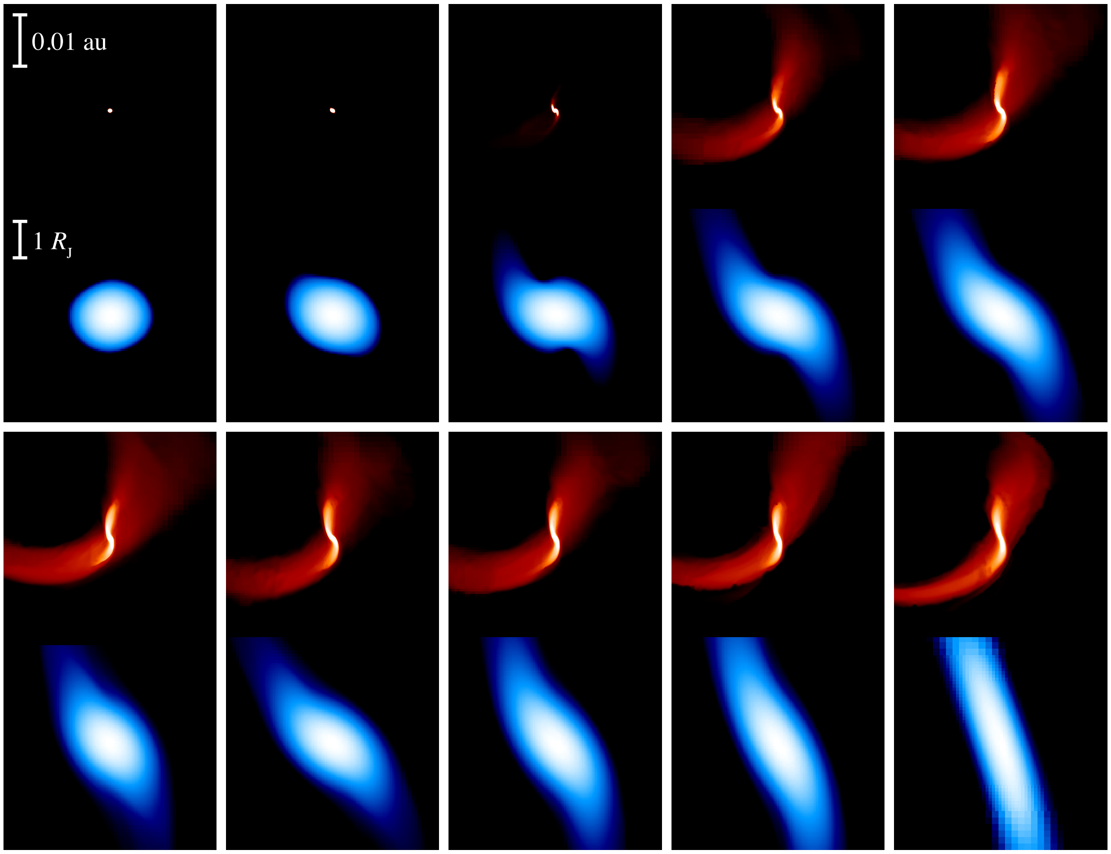

Figure 4.3: Slices through the orbital plane shortly after each periastron passage for the simulation where $r_p = 2.7r_t$. All plots show log ρ. The upper, red color-coded figures show a wide view of each encounter, with white corresponding to $\rho = 10^{-2}$ g cm^{-3} and black corresponding to $\rho = 10^{-7}$ g cm^{-3}, while the lower, blue color-coded figures show a close-up view of the core, with white corresponding to the maximum density $\rho_{\max}$ and black corresponding to $\rho = 10^{-2}$ g cm^{-3}.

4.3 Simulation Results

4.3.1 Single Passage Encounters

For comparison purposes, we first ran a suite of simulations with physical initial conditions identical to that of FRW. The planet is assumed to have a radius $R_P = R_J$ and mass $M_P = M_J$, where R_J and M_J are the radius and mass of Jupiter. The planets are disrupted by a

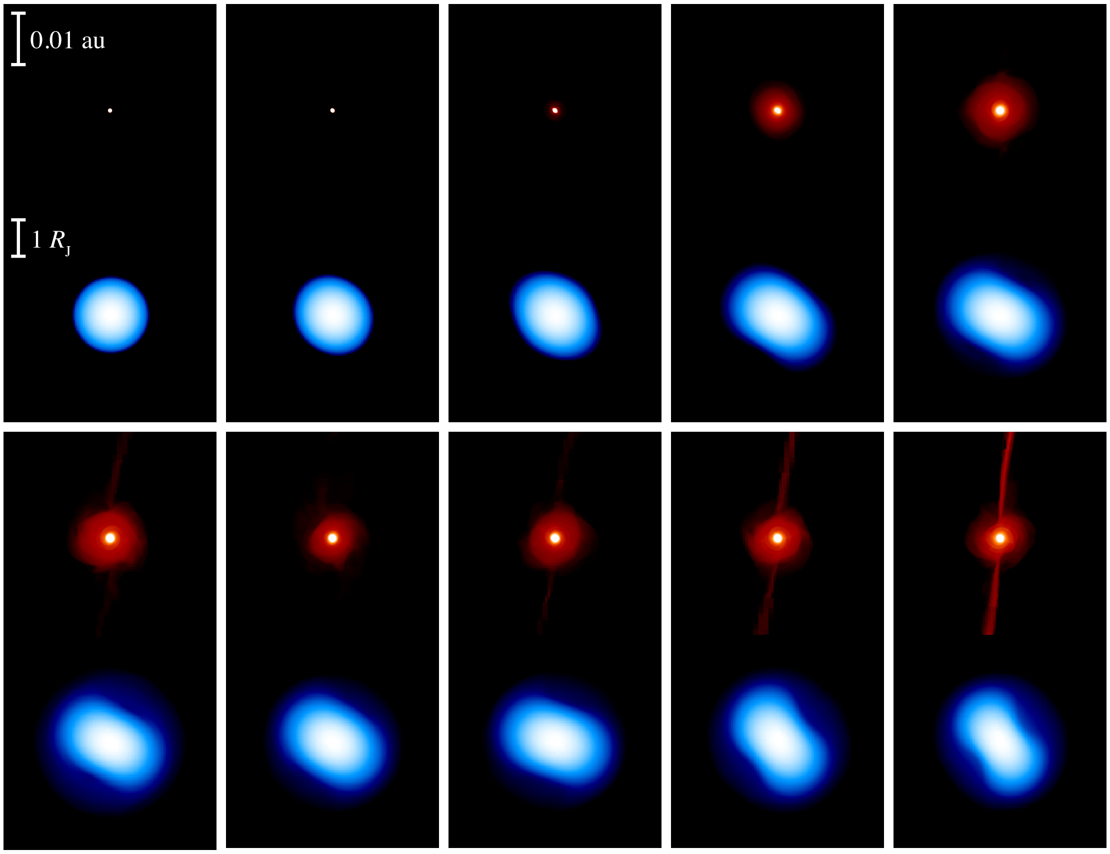

Figure 4.4: Same as Figure 4.3, but with frames 2-10 corresponding to apastron. The first frame shows the initial conditions.

star with $M_* = 10^3 M_J$, with the orbits of incoming planets are set to have an apastron separation $r_a = 10^4 R_J$. Our lowest-resolution models have maximum spatial resolutions of $s = 0.02 R_J$, where s is the width of the smallest grid cells, corresponding to $N^3 \simeq 10^6$, slightly better than the peak spatial resolution of FRW. Our results agree very well with FRW's results for periastron passage distances $r_p \leq 2.5 r_t$ (Figure 4.1).

Because the amount of energy stored in the oscillations is $\Delta E \sim E_J (\Delta R / R_J)^2$ where E_J is the binding energy of Jupiter and ΔR is the amplitude of the mode, the simulations converge to the analytical solution only when the spatial resolution is fine enough to resolve ΔR. As is evident in both FRW and our lower-resolution runs, the measured amount of energy dissipation is larger than the analytical predictions of PT when the oscillatory amplitude is smaller than the minimum grid scale. To test for convergent behavior, we ran higher-resolution simulations with double and quadrupole the resolution of our fiducial test for the more grazing encounters. For the $r_{\rm p} = 2.7 r_{\rm t}$ and $r_{\rm p} = 3 r_{\rm t}$ runs, the improved spatial resolution allows us to recover the analytical solution. It is also apparent that our $r_{\rm p} = 4 r_{\rm t}$ simulation is closer to convergence than the lower-resolution models, but the estimated resolution required for true convergence ($l \sim 10^{-3} R_{\rm J}, N^3 = 10^{10}$) means that recovering the predicted results of PT for such a grazing passage is currently beyond our computational ability.

As in FRW and Khokhlov *et al.* (1993b), we also find that the change in $E_{\rm orb}$ and $J_{\rm spin}$ is slightly larger than what is predicted by the analytical models, even in the simulations that have surely converged and have minimal mass loss (i.e., $2 r_{\rm t} \leq r_{\rm p} \leq 2.7 r_{\rm t}$). This is almost certainly due to the dynamical tide effects neglected by the PT model. Comparing the hydrodynamic results to that of a dynamical treatment of tides shows better agreement for this range of pericenter distances (Lai *et al.*, 1994), but note that these dynamical models only include the $l = 2$ f-mode of oscillation, and thus do not account for energy transferred to higher-order f-modes or p-modes. For grazing encounters, the dynamical tide is much less important, and thus we expect that the change in orbital energy and angular momentum should converge to the PT prediction for an inviscid planet.

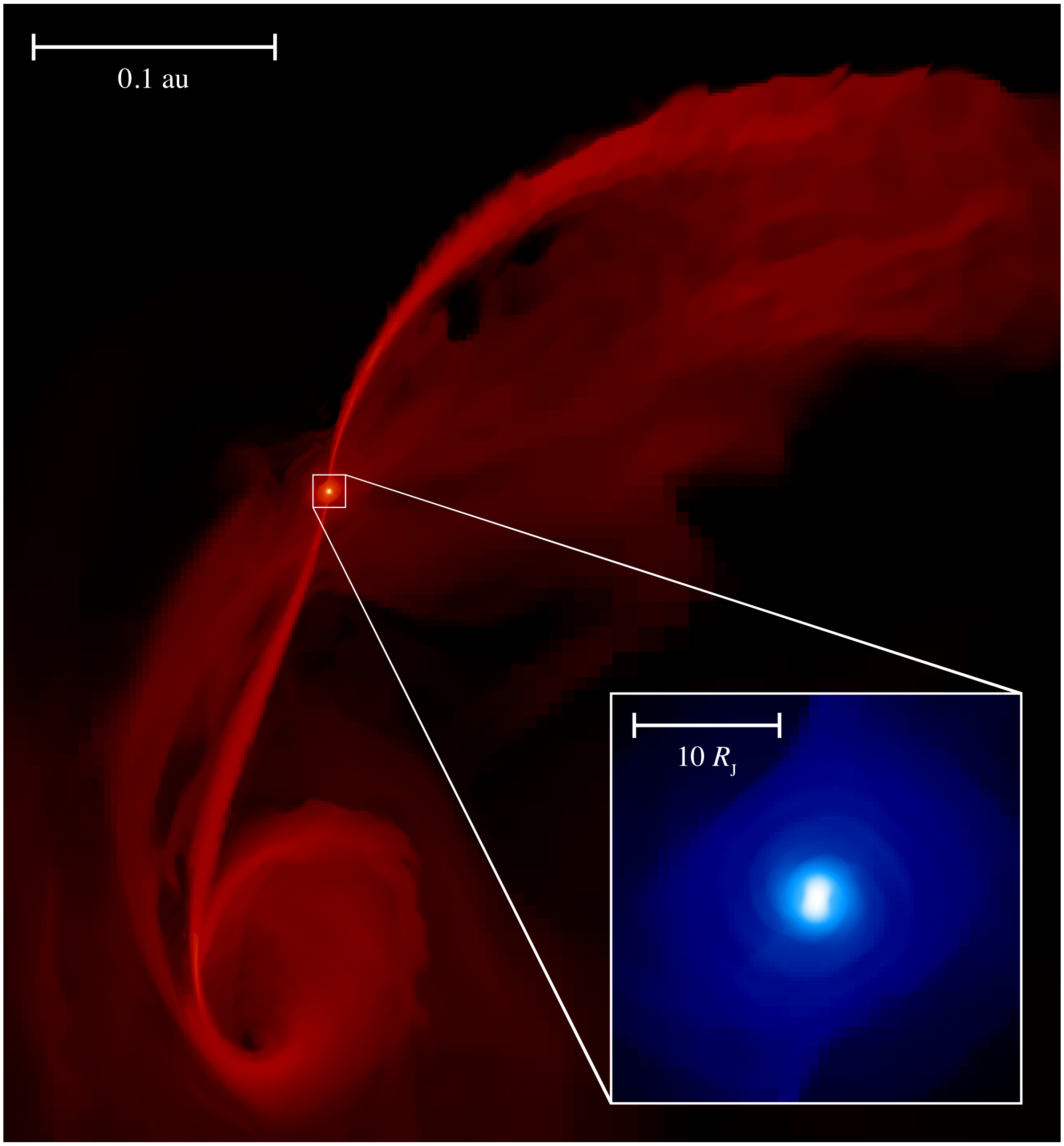

Figure 4.5: Fallback accretion stream formed as the result of the 8th encounter between a 1 $M_\odot$ star and 1 M_J planet with initial $r_p = 2.7r_t$. The large, red color-coded image shows a wide-view of the disruption, while the inset blue color-coded figure shows a close-up of the surviving planetary core.

4.3.2 Multiple Passage Encounters

The initial conditions of FRW are not appropriate for investigating multiple-passage encounters as the orbital timescale is many thousands of times longer than the dynamical timescale. Thus, for our second set of simulations in which we explore multiple passages, we assume that the planets are initially on $e = 0.9$ orbits (Figure 4.2). Depending on the initial pericenter distance, the planets are destroyed in as few as one and as many as ten orbits (Figures 4.3 and 4.4), where a planet is considered to be destroyed once it has lost more than 90% of its original mass.

To ensure that our assumption of a less eccentric orbit is valid, we consider the effects of varying e when $e \approx 1$. For nearly-parabolic orbits, the shape of the orbit in the vicinity of periastron changes very little with changing e, with the main effect being that the average strength of the tidal force is slightly stronger for smaller e before and after pericenter. This means that the critical distance for which a planet is destroyed or ejected is very slightly larger than our setup for single encounters described in the previous section where $e \simeq 1$. To estimate the magnitude of this effect, we calculate the ratio of the distances at fixed true anomaly for two orbits with eccentricities e_1 and e_2, assuming both orbits have the same $r_{\rm p}$

$$\frac{r_2}{r_1} = \frac{e_1(e_2+1)r_{\rm p}}{(e_1-e_2)r_1+(e_1+1)e_2 r_{\rm p}} \tag{4.1}$$

As the strength of the tidal force is $\propto r^{-3}$, the difference in the strength of the tidal force between the two orbits with respect to the tidal force experienced at pericenter is

$$\frac{F_1 - F_2}{F_{r_\mathrm{p}}} = r_\mathrm{p}^3 \left(r_1^{-3} - r_2^{-3} \right) \tag{4.2}$$

$$= \frac{3\,(e_1 - e_2)}{e_2\,(e_2 + 1)} \frac{r_\mathrm{p}^3}{r_1^3} \left(\frac{r_1}{r_\mathrm{p}} - 1 \right) + O(2) \qquad : e_1 - e_2 \rightarrow 0. \tag{4.3}$$

This expression is maximized at $r_1 = \frac{3}{2} r_\mathrm{p}$, where the force difference between an $e_1 = 0.9$ and $e_2 = 1.1$ encounter evaluates to 4%. For all other values of r_1, the force differences are much smaller than this maximum. Thus, our hydrodynamical treatment of tides in a $e = 0.9$ orbit is directly applicable to all orbits with $0.9 \lesssim e \lesssim 1.1$.

After an orbit in which the planet sheds mass, some of the material that is removed from the planet's surface remains marginally bound to the planetary core. The majority of this material is then re-accreted by the planet over a few dynamical timescales. When the free-falling material encounters the surviving planetary remnant, its kinetic energy is converted to internal energy in a standing accretion shock, which results in the planet possessing a hot outer layer with temperature close to the virial temperature (Figure 4.5). Additionally, the material striking the remnant leads to some heating of the remnant's outer mass shells. This effect is predominantly important in determining the envelope's temperature early in the accretion history before the pressure of the growing hot atmosphere becomes comparable to the ram pressure and is able to halt the flow before it can reach the core's surface (Frank *et al.*, 2002).

Because the re-accreted material is marginally bound to planet, the orbital trajectories characterizing the accretion streams have apocenter distances comparable to the planet's Hill sphere $r_\mathrm{H} \equiv r_\mathrm{p}(M_\mathrm{P}/3M_*)^{1/3}$ and follow highly eccentric orbits. As the re-accreted material returns on a Keplerian trajectory (Kochanek, 1994; Ramirez-Ruiz and Rosswog, 2009), it carries a substantial amount of specific angular momentum. This leads to a rapid spin-up of the planetary remnant's outer layers. In encounters with little or no mass loss, the planets spin slowly post-encounter as the angular momentum carried by the normal modes is almost equally distributed between rotating and counter-rotating regions (Figure 4.6). The process of re-accretion produces a planet that has a lower average density and more mass at larger radii, which makes the planet easier to destroy on subsequent passages.

As the re-accreted material has a temperature comparable to the virial temperature, radiative cooling may be able affect the atmosphere's structure, an effect that we do not account for in our simulations. However, as the planet can only thermally evolve for one orbital period, the atmosphere does not have much time to cool down before it has another strong tidal encounter with the star. While the outer layers of the planet may cool relatively rapidly and lead produce a brief transient visible in the UV (see Section 4.4.3), the denser regions of the planet's hot atmosphere component contains much more mass and is too optically thick to cool significantly before returning to pericenter. Assuming Thomson scattering, this corresponds to a mass of the hot atmosphere component $M_{\rm atm} \sim 10^{-5} M_{\rm J}$. This means that we expect that the thermal evolution of the reaccreted material is unimportant in determining the planet's density profile interior to the most tenuous outer layers. Thus, we expect that the dynamically relevant distribution of mass within the planet should remain relatively unchanged between encounters with the star, even for values of e significantly closer to 1 than what we use in our simulations.

This allows us to use the change in orbital energy and angular momentum from our simulations to calculate the orbital evolution for orbits with semi-major axes of several au. The change in orbital energy as a result of each encounter is shown in Figure 4.7. For grazing encounters with little mass loss, the change in orbital energy is negative; the planet becomes progressively more bound to the star after each encounter. The magnitude of this change is related to the state of the dynamical tide on the planet at pericenter, where the interaction between the oscillation of the fundamental modes can interact with the tidal field to reduce the amount of energy removed from the orbit, or even change its sign (see Section 4.3.3). As the mass loss per orbit exceeds $\sim 10\%$, the trend in orbital energy change becomes positive, and planets become progressively less bound on each subsequent encounter. This is primarily a result of the asymmetrical mass loss, although the interaction with the normal modes is important for encounters where the mass loss is on the order of a few percent.

For orbits with $a \sim a_{\rm ice}$, where $a_{\rm ice} = 2.7(L_*/L_\odot)^{1/2}$ au (Ida and Lin, 2008) is the ice line, the total orbital energy is small relative to the self-binding energy of the planet, and a positive ΔE can lead to the surviving planet becoming unbound from the host star. The number of orbits completed by a planet before it becomes unbound is shown in Figure 4.8. All Jupiter-like planets that come within $r_{\rm p} \leq 2.7 r_{\rm t}$ are expected to be ejected if $e \gtrsim 0.97$, and destroyed otherwise. For the most grazing encounters and smallest eccentricities, we find that the planet can survive for as many as ten orbits before being destroyed by the host star. The general trend is that planets that come closer to their parent stars tend to be ejected or destroyed in fewer orbits, but the consequences of the encounter seem to depend heavily on the orientation of the planet's long axis at pericenter, which as we will show in the next section is quite difficult to predict.

4.3.3 The Role of Chaos

As the planet continues in its orbit after its first encounter with the parent star, the planet exhibits both rotation and oscillation. Both the magnitude and sign of the orbital energy change is related to the phase of the planet's dynamical tide at periastron. Because the tidal forces strongly excite the $l = 2$ modes, the coherence or decoherence of these modes at periastron can greatly change the effects of that particular encounter (Kochanek, 1992; Mardling, 1995a,b; Usami and Fujimoto, 1997). As the ratio of the orbital period to the break-up rotation period for a Jupiter-like planet scattered in from the ice line is $\sim (M_{\rm J}/M_*)^{1/2}(a_{\rm ice}/R_{\rm J})^{3/2} \sim 10^5$, even a very small change in the orbital parameters introduces a dramatic variability in the amount mass lost and the change in orbital energy.

For our simulations where $e = 0.9$, the planet completes hundreds revolutions between periastron passages, which means extremely fine sampling of $r_{\rm p}$ would be required to completely describe the problem. To explore the chaotic behavior we ran another multiple disruption simulation with $r_{\rm p} = 2r_{\rm t}$, with the only difference being that the initial eccentricity is set to $e = 0.90012$, corresponding to an orbital period that is one free-fall timescale $t_{\rm ff} \equiv (R_{\rm J}^3/GM_{\rm J})^{1/2}/2\pi$ longer than the corresponding $e = 0.9$ simulation. As shown in Figure 4.9, multiple outcomes are possible for even slight changes in the initial conditions, with the planet surviving for a different number of orbits in the two simulations. The chaotic behavior is also evident for our multiple disruption simulation where $r_{\rm p} = 1.8r_{\rm t}$, which is destroyed on its fourth periastron passage, whereas both the $r_{\rm p} = 1.7r_{\rm t}$ and $r_{\rm p} = 1.9r_{\rm t}$ runs are destroyed on their third passages. This chaotic behavior arises because the angle of the major axis of the oscillating planetary core can range from being perpendicular to parallel to the true anomaly at periastron, which dramatically affects the ability of a planet to survive on any particular orbit.

As the principle component of the tidal field are the $l = 2, m = \pm 2$ harmonics, the only way to avoid chaotic behavior is to somehow remove energy from these modes before the planet returns to periastron. For fully-convective, Jupiter-like planets, this can be potentially achieved through three types of mechanisms: Viscosity (either microscopic or turbulent), coupling to other oscillatory modes, or the increase in entropy associated with sound waves steepening into shocks at either the surface of the planet or within its interior. It should be emphasized that most of the work investigating these energy-sharing mechanisms have concentrated on systems where the oscillations can be treated linearly, and thus the results of these studies can only give us a rough idea to their importance when applied to partially-disruptive encounters.

The two main differences between the linear models and the survivors of a partially-disruptive encounter are the amplitude of the oscillations, which are close to unity, and the presence of a hot, optically thick envelope that accumulates after the disruption and sits on top of the oscillating core. We know that in order for a particular mechanism to result in significant damping of the $l = 2$ modes, the damping timescale has to be at least on the order of the orbital period P, if not shorter. As all of the mechanisms for removal of energy from the $l = 2$ modes result in a cascade to microscopic scales, systems with effective damping will experience inflation of the core, inflation of the envelope, or inflation of both regions. This inevitably leads to reduced survivability on subsequent passages.

We now briefly discuss the applicability and viability of each of these proposed mechanisms. For Jupiter-like planets, the microscopic and turbulent fluid viscosities seem to be too small to produce any significant damping on an orbital timescale (Guillot *et al.*, 2004). Perhaps a more promising mechanism is the coupling of the primary $l = 2$ modes to higher-order "daughter" modes, which then couple to "grand-daughter" modes, etc., in a cascade resembling the cascade of energy from large scales to small scales in turbulent fluids (Kumar and Goodman, 1996). In the linear regime, the fundamental mode normally couples to the low frequency g-modes, with the degree of coupling being related to the amplitude of the primary perturbation relative to the size of the object, $\Delta R/R$. But for Jupiter-like planets, which are fully convective and have a negligible luminosity, the polytropic index Γ is equal to the adiabatic index γ, which makes their interiors incapable of supporting g-modes (Cowling, 1941). Coupling can still occur through p-modes, which have higher frequencies than the fundamental mode, but the coupling is only effective for large displacements where the behavior becomes non-linear and for which the rate of energy-sharing is highly uncertain (Kumar and Goodman, 1996).

Inertial waves may be an effective means of dissipating the $l = 2$ modes given low-frequency tidal forcing (Ivanov and Papaloizou, 2010), but the efficiency of this dissipation as the forcing frequency approaches the characteristic frequency is not well understood. And because inertial waves are most effective when the planet spin frequency is comparable to the orbital frequency, they may not be important during the first few passages before syncronicity is established. Additional dissipation may occur via the interaction between inertial waves and Hough waves (Ogilvie and Lin, 2004), in which effective coupling is achieved when the wavelength of the inertial modes is comparable to the size of the radiative zone. As scattered planets tend to have large eccentricities, stellar insolation is unlikely to be important for these planets prior to circularization, but as the hot envelope produced by partially disruptive events is radiative, effective dissipation via Hough waves may still be possible.

In our simulations, we do not find that the $l = 2$ modes decay appreciably between periastron passages, despite the fact that the planet oscillates thousands of times in the course of each orbit. We do find, however, that the re-accretion of loosely-bound material moderates the chaotic behavior somewhat. As the density in this region is $\gtrsim 10^3$ times smaller than the core, the tidal radius for the hot envelope component is $\gtrsim 10$ larger than the core's initial tidal radius, which results in the hot envelope being easily removed on subsequent encounters. And unlike the core, the hot envelope has a large sound-crossing time relative to the periastron passage time, and thus no fundamental modes that could affect the interaction on future passages are excited in this region. This leads to the result that as the envelope becomes a larger fraction of the planet's total mass, the behavior becomes notably less chaotic.

Even if the mode energy is completely damped before the planet again passes through periastron, interactions with other planets in the system can potentially lead to major changes in the planet's orbit, which adds another element of chaos to the planet's orbital evolution. While the scattered planet has a possibility of strongly interacting with any other planets with orbital periastrons smaller than its own apastron, its most probable interaction partner is the planet that originally scattered it. If we optimistically assume that the orbits are co-planar and that the scattered planet's apastron lies within the path of the scatterer's orbit, the change in angular momentum ΔJ under the impulse approximation is $GM_1 M_2 / b v_{12}$, where M_1 and M_2 are the masses of the two planets, b is their separation at closest approach, and v_{12} is the difference in their orbital velocities. The probability that the scatterer can result in relative change in the orbital angular momentum $\Delta J / J_{\rm orb}$ is then proportional to the fraction of time the scatterer is within a window of size b at the time the scattered planet crosses its orbit, or

$$\frac{1}{8\pi}\frac{J_{\rm orb}}{\Delta J}\frac{M_1+M_2}{M_*}\left(\frac{a_{\rm ice}}{r_{\rm p}}\right)^{1/2} \text{ per orbit.} \tag{4.4}$$

As $M_* \sim 10^3(M_1+M_2)$ and $a_{\rm ice} \sim 10^3 r_{\rm p}$, the typical value of $\Delta J/J_{\rm orb}$ is small, $\sim 10^{-2}$. Like the chaotic behavior related to the phase of the planet's oscillatory modes, these changes in $J_{\rm orb}$ can change the number of orbits a planet may survive, but does not affect the overall survival rate of scattered planets as $\Delta r_{\rm p} \propto \sqrt{\Delta J}$ is much smaller than $r_{\rm p}$. Additionally, future encounters with the original scatterer become progressively less probable as a changes in response to the scattered planets changes in orbital energy, as $\Delta E \sim E_{\rm J} \gg E_{\rm orb}(a_{\rm ice})$.

4.3.4 Debris Accreted by the Star

The amount of mass removed on the first few orbits can vary over many orders of magnitude for a relatively small range of $r_{\rm p}$. For our closest simulated encounters, nearly half the planet ends up being bound to the host star after the first passage, while our most grazing encounters show almost no mass loss at all (Figure 4.10). However, as the initial passages excite fundamental modes of oscillation, and the returning debris leads to additional heating in the planet's outer layers, the amount of mass removed geometrically increases with each subsequent passage. This leads to the result that approximately 20-50% of the planet's initial mass is accreted by the host star by the time the planet has been completely disrupted, with slightly less material being accreted when the initial encounter is grazing.

The reason closer disruptions lead to more mass accreted by the central star has to do with the asymmetry of the tides; the force resulting from the inner tide (closest to the star) at pericenter is

$$\frac{\left(2r_{\rm p}-R_{\rm P}\right)\left(R_{\rm P}+r_{\rm p}\right)^2}{\left(2r_{\rm p}+R_{\rm P}\right)\left(R_{\rm P}-r_{\rm p}\right)^2} \simeq 1+\frac{3R_{\rm P}}{r_{\rm p}} \text{ as } r_{\rm p} \to \infty \tag{4.5}$$

times larger than the outer tide (furthest from the star). And while the effective size of the planet increases due to the excitation of oscillations and the loss of mass, subsequent passages yield diminishing returns as material has already been removed on previous encounters.

As the mass lost by the planet from a series of partially disruptive encounters is highly stochastic, the exact amount of mass accreted by the star for any given multiple-orbit encounter is difficult to predict. To parameterize the average mass accreted by the star, we consider two limiting cases. If the planet is scattered into an orbit with $a \ll a_{\rm ice}$, the planet will be completely destroyed before it is ejected. On the other hand, if a planet is scattered from the ice line, $E_{\rm orb}$ is much smaller than the planet's binding energy and the planet will be ejected on the orbit for which $\Delta E_{\rm orb} > E_{\rm orb}$. A fit of ΔM_* for these two limiting cases yields

$$\Delta M_*(\beta) = \begin{cases} 1.26 \exp\left[-0.79\beta^{-1}\right] M_{\rm J} & : a_0 \ll a_{\rm ice} \\ & \\ 9.62 \exp\left[-2.59\beta^{-1}\right] M_{\rm J} & : a_0 \sim a_{\rm ice}, \end{cases} \tag{4.6}$$

for $0.37 \leq \beta \leq 0.83$. For the case where the planet is completely destroyed, the amount of mass accreted is nearly constant, with a slight decrease with decreasing β. The decrease is substantially steeper for the incomplete disruptions, as planets on grazing orbits are less likely to transfer much mass to their parent stars prior to being ejected.

Table 4.1: Hot Jupiters

Planet	$r_{\mathrm{p}}/r_{\mathrm{t}}$	$r_{a,\max}/a_{\mathrm{ice}}$	$\tau_{\mathrm{age,L}}$[a] (Gyr)	$\tau_{\mathrm{age,U}}$[a] (Gyr)	$Q_{*,\max}$[b] (Gyr)	$\tau_{\mathrm{life,max}}$[b]	$\tau_{\mathrm{life,max}}/\tau_{\mathrm{age}}$
CoRoT-1 b	4.8	0.044	1.0	14.0	2×10^6 — 3×10^7	0.4 — 6	0.4
HAT-P-23 b	5.0	0.052	4.0	6.0	5×10^7 — 8×10^7	2.0 — 3	0.6
OGLE-TR-56 b	4.2	0.014	1.9	4.2	1×10^7 — 3×10^7	0.4 — 0.9	0.2
OGLE-TR-113 b	5.0	0.083	10.8	14.0	1×10^7 — 2×10^7	6.2 — 8.0	0.6
Qatar-1 b	4.6	0.043	4.0	14.0	3×10^6 — 1×10^7	1.5 — 5.3	0.4
TrES-3 b	5.1	0.10	0.1	3.7	9×10^5 — 3×10^7	0.07 — 2.7	0.7
WASP-4 b	4.5	0.028	2.0	9.0	7×10^6 — 3×10^7	0.6 — 2.6	0.3
WASP-12 b	4.1	0.011	1.0	3.0	1×10^7 — 4×10^7	0.2 — 0.6	0.2
WASP-19 b	3.2	0.0080	1.0	14.0	2×10^6 — 2×10^7	0.03 — 0.5	0.03

[a] The τ_{age} values shown are as compiled by (Schlaufman, 2010), except for CoRoT-1 b (no measured age information available), WASP-19 b (Hellier *et al.*, 2011), Qatar-1 b (Alsubai *et al.*, 2010), and HAT-P-23 b (Bakos *et al.*, 2010). All other data was taken from the Extrasolar Planets Encyclopaedia (`http://exoplanet.eu`) on January 24, 2011.

[b] Assuming $r_{\mathrm{p},0} = 2r_{\tau,\mathrm{sim}}$, $a_0 = a_{\mathrm{ice}}$. The minimum and maximum values are calculated using $\tau_{\mathrm{age,L}}$ and $\tau_{\mathrm{age,U}}$, the lower and upper limits on the host star's age.

4.4 Discussion

4.4.1 The Jupiter Exclusion Zone

As discussed in Section 4.3, there exists an exclusion zone with radius $r_\tau = 2.7r_{\mathrm{t}}$ within which all Jupiter-like planets are either ejected or destroyed. For our simulations we used a polytropic model of a gas giant, with a mass and radius equal to present-day Jupiter. As some gas giant planets may not have had much time to cool before being disrupted, it is likely that disrupted Jupiter-like planets are larger than our fiducial cold Jupiter model (Bodenheimer *et al.*, 2001). This is confirmed by observations, many of the known hot Jupiters are observed to be inflated, with larger radii and lower densities as a result of the injection of entropy via stellar insolation (Fortney *et al.*, 2007; Miller *et al.*, 2009; Li *et al.*, 2010), and potentially also other dissipative mechanisms (Ogilvie and Lin, 2004; Laine *et al.*, 2009; Arras and Socrates, 2010). But this means that the tidal radii for these planets must be *larger* than what we use in our calculations, translating to planets that are more easily disrupted than cold gas giants. And while the core mass of Jupiter-like planets is uncertain, all plausible models include cores that compose such a small fraction of the planet's total mass that they are unimportant in determining the structure of the gas envelope, and thus the dynamics of the disruption. The value of $r_{\mathcal{T}}$ calculated in this chapter is thus a lower limit for Jupiter-like planets. For gas giants with masses more similar to Neptune, the affect of an increased core mass may allow these planets to survive closer to their parent stars due to the increase in average density. We stress that our model should only be applied to planets of $M \gtrsim 0.25 M_{\rm J}$.

Because the spatial resolution required to resolve grazing passages becomes computationally prohibitive beyond $\sim 3 r_{\rm t}$, the true value of $r_{\mathcal{T}}$ may lie beyond what we have been able to calculate for even cold Jupiter-like planets. Thus, the exclusion zone radius determined by our simulations $r_{\mathcal{T},\rm sim}$ is a lower bound on the size of exclusion zone for Jupiters scattered from the ice line. However, the true cutoff value probably lies no further than the current periastron distance of WASP-19 b (denoted as $r_{\mathcal{T},\rm obs}$), the exoplanet with the smallest known value of $r_{\rm p}/r_{\rm t}$ (Hellier *et al.*, 2011), which appears to be quite inflated (Hebb *et al.*, 2010) and possesses a tidal radius that is likely larger than a cold gas giant of the same mass. Hence, we can only constrain $r_{\mathcal{T}}$ to lie within the range $r_{\mathcal{T},\rm sim} \leq r_{\mathcal{T}} \leq r_{\mathcal{T},\rm obs}$, or $2.7 \leq r_{\mathcal{T}}/r_{\rm t} \leq 3.20$, where the upper bound is derived by assuming WASP-19 b's radius at the time of scattering is equal to its cold radius.

Because specific orbital angular momentum is very nearly conserved during even strong tidal encounters (Figure 4.2), the currently observed semi-major axes of hot Jupiters is at most 2 $r_{\rm p,0}$, where $r_{\rm p,0}$ is the planet's initial pericenter distance after being scattered into a disruptive orbit. As the exclusion radius $r_\mathcal{T}$ is larger than the $a/2$ for many known exoplanets, there exists a maximum initial apastron distance from which a planet could have been scattered without having been destroyed or ejected

$$r_{\mathrm{a,max}} = \frac{a_{\mathrm{obs}}\left(1-e_{\mathrm{obs}}^2\right) r_\mathcal{T}}{a_{\mathrm{obs}}\left(e_{\mathrm{obs}}^2-1\right)+2r_\mathcal{T}}, \tag{4.7}$$

where a_{obs} and e_{obs} are the currently observed semi-major axis and eccentricity. This maximum apastron value is illustrated for the currently known hot Jupiters in Figure 4.11. Because a planet that is scattered into a disruptive orbit from the ice line possesses $e \sim 1$, the maximum allowed apastron is a highly sensitive function of $r_\mathcal{T}$ for $r_{\mathrm{a}} \gtrsim 0.1a_{\mathrm{ice}}$. Thus, if the current distance of an exoplanet from its host star is less than $2r_\mathcal{T}$, it is highly likely that its initial orbit prior to scattering must have been significantly closer to the star than the ice line. This means that no Jupiter-like planets would be observed for initial pericenter distances smaller than this value if they were scattered from the ice line to their present-day orbits.

Nine of the currently known hot Jupiters (CoRoT-1 b, HAT-P-23 b, OGLE-TR-56 b, OGLE-TR-113 b, Qatar-1 b, TrES-3 b, WASP-4 b, WASP-12 b, and WASP-19 b) with $M > 0.25M_{\mathrm{J}}$ have observed semi-major axes $a_{\mathrm{obs}} > 2r_{\mathcal{T},\mathrm{sim}}$, corresponding to $r_{\mathrm{a,max}} \ll a_{\mathrm{ice}}$ (Table 4.1), indeed for all nine planets the maximum initial apastron distance is less than 0.1 a_{ice}. As all Jupiter-mass planets are thought to form beyond a_{ice}, these planets could not have been *directly* scattered to their current locations. This implies that a migration process that resulted in a dramatic decrease in a must have occurred either before or after these planets were scattered. If the true value of $r_\mathcal{T}$ for cold Jupiter-like planets lies closer to the maximum possible value set by WASP-19 b ($r_{\tau,\mathrm{obs}}$), as many as 12 of the currently known hot Jupiters with $M > 0.25 M_\mathrm{J}$ could not have survived the scattering event that deposited them at their current locations.

As both planet-planet scattering and the Kozai mechanism do not radically alter a planet's semi-major axis, disk migration would be required to explain how close-in planets would have initial apastrons that are significantly smaller than a_ice (Lin *et al.*, 1996; Ida and Lin, 2004, 2008). As many of the currently known exoplanets have $r_{a,\mathrm{max}} < a_\mathrm{ice}$, this would imply that the migration timescale in these systems must have been substantially shorter than the disk lifetime if the planets migrated prior to the scattering event. For the misaligned systems, a dynamical process (either planet-planet scattering or the Kozai mechanism) may need to occur after the migration or while the gas disk dissipates (Matsumura *et al.*, 2010) to produce the observed misalignment.

Alternatively, the planets may have migrated after the scattering event. For this to be the case, the scattering event had to bring the planet close enough to its parent star such that the tide raised on the star can alter the planet's orbit in a time shorter than the system age, but not too close that the planet is destroyed or ejected by the star. Suppose that a planet is scattered from beyond a_ice such that $r_{\mathrm{p},0} > r_\tau$. After circularization the pericenter distance doubles to $2r_\tau$, and the planet's semi-major axis evolves via the interaction between the planet and the tide it raises on the surface of the star (Hut, 1980; Eggleton *et al.*, 1998). At this distance, the orbital period of the planet is almost always shorter than the spin-period of the star, except perhaps for stars with ages $\lesssim 650$ Myr (Irwin and Bouvier, 2009). This results in a spin-up of the star, which tries to "catch up" to the Keplerian frequency imposed by the planet's orbit, and an inward migration of the planet.

As the planet is likely to be tidally locked even prior to circularization, the timescale for evolution of the planet's semi-major axis is entirely determined by the star's properties and the orbital frequency ω (Dobbs-Dixon *et al.*, 2004),

$$\frac{a}{\dot{a}} = \frac{1}{9} Q_* \left(\frac{M_*}{M_{\rm P}}\right) \left(\frac{a}{R_*}\right)^5 (\omega - \Omega_*)^{-1}, \tag{4.8}$$

where R_* is the star's radius, Q_* is the star's tidal quality factor, and Ω_* is its rotation frequency. The fastest inward migration occurs when a star is not rotating, e.g. $\Omega_* \to 0$. As planet-planet scattering seems to be rare after 10^8 yr (Matsumura *et al.*, 2008), we can set $a/\dot{a}$ equal to the system age $\tau_{\rm age}$ to determine $Q_{*,\rm max}$, the maximum tidal quality factor for which a planet can migrate from $2r_\mathcal{T}$ to $a_{\rm obs}$

$$\begin{aligned} Q_{*,\rm max} = 1.7 \times 10^6 &\left(\frac{M_{\rm P}}{M_{\rm J}}\right)^{8/3} \left(\frac{M_*}{M_\odot}\right)^{-8/3} \left(\frac{R_{\rm P}}{R_{\rm J}}\right)^{-5} \\ &\times \left(\frac{r_\mathcal{T}}{2.7 r_{\rm t}}\right)^{-5} \left(\frac{P_0}{2\ \rm days}\right)^{-1} \left(\frac{\tau_{\rm age}}{\rm Gyr}\right), \end{aligned} \tag{4.9}$$

where P_0 is the initial orbital period. When setting $r_\mathcal{T} = r_{\mathcal{T},\rm sim}$, all of the known hot Jupiters with $a_{\rm obs} < 2r_\mathcal{T}$ yields values for $Q_{*,\rm max}$ that are consistent with those expected for stars (Table 4.1).

If the true radius of disruption lies closer to $r_{\mathcal{T},\rm obs}$, the measured values of $Q_{*,\rm max}$ are more restrictive, meaning that higher dissipation rates would be required to enable planet-planet scattering to viably produce hot Jupiters with $a < 2r_\mathcal{T}$. This would also imply that most observed hot Jupiters would only exist a short while longer before being destroyed by their parent star. This remaining lifetime can be calculated by solving Equation (4.8) using present-day values for a, ω, and Ω_* (denoted $\tau_{\rm life,max}$ in Table 4.1). As $Q_{*,\rm max}$ is extremely sensitive to the exact value of $r_\mathcal{T}$, only a slight increase in $r_\mathcal{T}$ is required to eliminate direct scattering as a possible genesis mechanism for a significant fraction of the hot Jupiters. If it can be shown that $r_\mathcal{T}$ is substantially larger than what we have calculated in this work (i.e. $r_\mathcal{T} \simeq r_{\mathcal{T},\rm obs}$), $Q_{*,\rm max}$ can put definitive constraints on the mechanism responsible for producing hot Jupiters.

4.4.2 Stellar Spin-Up from Planetary Disruption

As discussed in Section 4.3.4, the star acquires a substantial injection of angular momentum from the disrupted planet. Our simulations give us an empirical determination of $\Delta M_* \left(\beta, M_{\rm P} = M_{\rm J}, M_* = 10^3 M_{\rm J}\right)$, the amount of mass gained by a star with $M_* = 10^3 M_{\rm J}$ from the disruption of a Jupiter-mass planet given the impact parameter β (Figure 4.10). The angular momentum acquired by the star is simply equal to the specific angular momentum at the star's radius multiplied by the amount of mass accreted, $\Delta J_* = \Delta M_* \sqrt{G M_* R_*}$. Note that this is not the same as the total angular momentum content of the disk formed from the debris as claimed by Jackson *et al.* (2009), as the accretion stream does not intersect the star's radius unless the planet's original orbit has $r_{\rm p} < R_*$ (Kochanek, 1994).

If all disrupted Jupiter-like planets are approximately the same size and $e \sim 1$, all disruptions can be treated using our fiducial model and the inclusion of the simple scaling associated with the increase in the orbital angular momentum. This is because the only difference that arises from changing the mass of the planet and the star is the degree of asymmetry of the tides, which is third-order in the force expansion and is $(R_{\rm J}/\beta r_{\rm t})^2 \sim 10^{-2}$ times smaller than the tidal force itself. Thus, in the event that the planet is completely destroyed by the star, we expect that the amount of angular momentum acquired by the star should simply scale with M_* and $M_{\rm P}$

$$\Delta J_*(\beta, M_{\rm P}, M_*) = \left(\frac{M_*}{M_\odot}\right)^{1/2} \left(\frac{M_{\rm P}}{M_{\rm J}}\right)^{3/2} \times \Delta J_*(\beta, M_{\rm J}, 10^3 M_{\rm J}). \tag{4.10}$$

However, our results show that a substantial fraction of planets are ejected from the system before they can be fully destroyed by the star. This reduces the amount of mass ΔM_* accreted by the star, and thus ΔJ_*. Therefore ΔJ_* for any given encounter should depend on which particular orbit a planet is ejected $N_{\rm ej}$. This parameter depends on the orbital energy $E_{\rm orb}$, and the change in orbital energy associated with each encounter, which as we explain in Section 4.3.2 should also should scale simply with the masses of the planet and the star. Thus our expression for ΔJ_* becomes

$$\Delta J_*(\beta, M_{\rm P}, M_*) = \left(\frac{M_*}{M_\odot}\right)^{1/2} \left(\frac{M_{\rm P}}{M_{\rm J}}\right)^{3/2} \times \Delta J_*(\beta, M_{\rm J}, 10^3 M_{\rm J}, N_{\rm ej}) \tag{4.11}$$

$$\Sigma_{N=1}^{N_{\rm ej}} \Delta E_{\rm orb} > -E_{\rm orb}, \tag{4.12}$$

where $N_{\rm ej}$ is equal to the lowest value of N for which Equation (4.12) is satisfied. While this gives us the amount of angular momentum acquired by the star for a set of encounter parameters, we must know the distribution of β in order to estimate the probability for which a star will possess a total angular momentum J_* and obliquity ψ_* after a number of planetary disruptions

N_d.

The integrated rate of scattering (i.e., all encounters with β greater than some value) has been evaluated numerically by a number of authors. (Jurić and Tremaine, 2008) show that up to 20% of planets present at the end of phase I of planetary formation can collide with the host star, e.g. $r_\mathrm{p} < R_*$. (Ford and Rasio, 2008) show that up to 16% of planets in a 3-body system can be thrown into a "star-grazing" orbit, which they define as $r_\mathrm{p} < 10^{-2} a_\mathrm{init}$. Nagasawa *et al.* (2008) show that planet-planet scattering events tend to induce transitions between Kozai states (with the duration of each state being $\sim 10^6 - 10^7$ yr) until a planet is ejected from the system or until the eccentricity of the innermost planet is damped by tides. Nagasawa *et al.* note that most of the close-in planets seem to be driven to their closest approaches via the Kozai mechanism, which gently drives the planets into the region where they can be circularized, as opposed to being directly scattered into such orbits. None of the models presented above include the precession associated with general relativity that would normally quench the Kozai mechanism.

Because the numerical scattering experiments do not include a hydrodynamical treatment of tides, the fates of planets that are either scattered or driven by the Kozai to $r_\mathrm{t} \leq r_\mathrm{p} \leq r_\mathcal{T}$ are not accurately represented. What the scattering experiments *do* reveal is the total rate of planet-planet interactions as a function of the number of gravitating bodies in the system, and the distribution of orbits that arises from numerous planet-planet interactions. And despite the simplistic treatment of tides or the neglect of tides altogether, different prescriptions of tidal dissipation do not seem to strongly affect the distribution of the remaining planets in the system (Nagasawa *et al.*, 2008), which means that the orbit distributions these models predict should still be appropriate to use as inputs for our post-disruption stellar spin estimates.

For systems that are not dynamically stable after the gas disk dissipates, or for systems which are driven to instability by an external perturber (Zhou *et al.*, 2007; Malmberg *et al.*, 2011), the models indicate that the eccentricity distribution of planets quickly evolves to a Rayleigh distribution (Jurić and Tremaine, 2008)

$$dN = \frac{e}{\sigma_e^2} \exp\left(\frac{-e^2}{2\sigma_e^2}\right) de \tag{4.13}$$

As the relaxation to this distribution is mainly driven by strong two-body planet-planet interactions, the new eccentricity e of a planet after a scattering event should also be drawn from the above distribution. Because we are interested in objects that may be unbound from the system after the encounter, objects with e initially larger than 1 should be included when calculating the number of events at each e. Using our definition of β,

$$e = 1 - \frac{2}{\beta r_{\rm t}/r_{\rm a} + 1}, \tag{4.14}$$

and by making a change of variable from e to β, Equation (4.13) becomes

$$dN = \frac{2 r_{\rm a} r_{\rm t} (r_{\rm a}\beta - r_{\rm t})}{(r_{\rm t} + r_{\rm a}\beta)^3 \sigma_e^2} \exp\left[-\frac{(r_{\rm t} - r_{\rm a}\beta)^2}{2(r_{\rm t} + r_{\rm a}\beta)^2 \sigma_e^2}\right] d\beta. \tag{4.15}$$

When $r_{\rm a} \gg r_{\rm p}$, as is the case in planet disruption, the above expression simplifies to

$$dN \simeq \frac{2 r_{\rm t}}{r_{\rm a} \sigma_e^2} \exp\left[-\frac{1}{2\sigma_e^2}\right] \frac{d\beta}{\beta^2}, \tag{4.16}$$

which when integrated yields a disruption probability that scales inversely with β (Rees, 1988). Because we are including hyperbolic encounters, β can assume both positive and negative values, with $r_{\rm t}/r_{\rm a} < |\beta| < \infty$. To first order, the value of the integrand is equal for both positive and negative values of β, and the total number of events where $\beta > \beta'$ is given by

$$N = 2\int_{\beta'}^{\infty} \frac{dN}{d\beta} d\beta. \tag{4.17}$$

This implies that equal numbers of planets will be scattered into prograde and retrograde orbits. Under these assumptions and given our empirically determined lower limit for ejection $r_{\rm p} = 2.7r_{\rm t}$, it is immediately clear that the rate of collisions with the central star is lower than the combined rate of ejections and disruptions by at least a factor $r_{\mathcal{T}}/R_* - 1 = 1.78$, assuming solar and Jovian values.

Now that we have a model for the expected initial distribution of giant planets in a dynamically relaxed system, we can use Equation (4.15) to evaluate the expected values of J_* and ψ_* after $N_{\rm d}$ planetary disruptions for a star of $M_* = M_\odot$ (Figure 4.12). Here we consider the scattered objects to be cold, Jupiter-like planets with $M_{\rm P} > 0.25M_{\rm J}$, resulting in a nearly-constant planetary radius $R_{\rm P}$. This assumption is only valid if the system is older than $\sim 10^8$ yr and if the planet's initial orbit is far enough from its parent star to have negligible insolation, but note that including these effects would only act to increase the amount of mass removed from the planet per orbit. We also assume that the planets are distributed uniformly in log a from $r_{\mathcal{T}}$ to $10a_{\rm ice}$, and in log $M_{\rm P}$ from 0.25 to 10 $M_{\rm J}$, with Rayleigh distributions in e and i with $\sigma_e = 0.3$ and $\sigma_i = 10^\circ$. For simplicity, we assume that any angular momentum acquired by the star through a disruption is shared equally with all parts of the star.

For a single planet disruption in a system where the star possesses initial angular momentum equal to the Sun, ψ_* exceeds 30° in 15% of the stellar hosts, and 90° (i.e. the star rotates retrograde to the invariable plane) in 8% of systems. The spin rate of the star also tends to increase, with 10% of stars possessing $3J_\odot$ after the disruption. If disruptions are very common ($N = 5$), the probability of $> 10/ > 90°$ increases to 47/22%, and 41% of stars have $J_* > 3J_\odot$. The probability for enhanced values of J_* and ψ_* are all slightly smaller if we restrict disruptions to come from $a > a_{\rm ice}$, as the amount of mass the star acquires from disruptions is slightly less on average, Equation (4.6). However, the effect is minor, with changes in the cumulative probabilities being on the order of a few percent.

If a star is unable to share the angular momentum deposited in its outer layers in a time less than its age, the star may be observed to have larger values of Ω_* or ψ_* than what would be expected given complete mixing. The timescale τ_ν for sharing angular momentum across the tachocline in the Sun is known to be only $\sim$3 Myr (Gough and McIntyre, 1998), with the timescale decreasing for increasing rotation rates in the convective region. The timescale for sharing angular momentum across the tachocline appears to increase significantly as the size of the convective zone shrinks for rapidly rotating stars (Barnes, 2003; Barnes and Kim, 2010), but this may be moderated by a fingering instability made possible by the larger molecular weight of the disruption debris (Garaud, 2010; Rosenblum *et al.*, 2011). A disruption in a system where the host star never has a thick convective zone could effectively erase the star's original spin rate and obliquity, with ψ_* being pulled from the inclination distribution of planetary orbits.

4.4.3 Observational Signatures

If we assume that the pressure profile of the hot atmosphere that accumulates on the planet has a pressure profile $P = P_{\rm ram}$ at all radii (Frank *et al.*, 2002), the initial Kelvin-Helmholtz cooling timescale given a total atmosphere mass $M_{\rm atm}$ is approximately

$$\tau_{\rm KH} \simeq 1.2 \left(\frac{M_{\rm atm}}{0.1 M_{\rm J}}\right) \left(\frac{M_{\rm P}}{M_{\rm J}}\right) \left(\frac{R_{\rm P}}{R_{\rm J}}\right)^{-1} \times \left(\frac{R_{\rm atm}}{3 R_{\rm J}}\right)^{-2} \left(\frac{T_{\rm vir}}{10^5\,{\rm K}}\right)^{-4} {\rm days}, \tag{4.18}$$

where $T_{\rm vir}$ is the virial temperature, $M_{\rm atm}$ is the mass of the atmosphere and $R_{\rm atm}$ is the radius of the atmosphere. Because $T_{\rm vir}$ is initially very large, the atmosphere is at first completely ionized. At this temperature, $\tau_{\rm KH}$ is a few days, leading to a rapid thermal evolution of the planet's outer layers shortly after most of the sundered mass returns to the planet. During this phase, the planet can briefly outshine its parent star with $L_{\rm bol} \sim 10^{36}$ erg s^{-1}, with most of the radiation being emitted in the UV. As the atmosphere cools it shrinks back down onto the planet's surface until $R_{\rm atm} \sim R_{\rm P}$. We can then estimate the temperature at which the planet radiates for the majority of its orbit by setting P equal to $\tau_{\rm KH}$, which yields a temperature of a few 10^4 K. This indicates that the planet's outer layers will still be somewhat inflated before the planet returns to pericenter, and thus will be easily removed on subsequent passages.

For planets that are ejected from their host stars, the thermal evolution of their outer layers continues until the temperature reaches a few thousand Kelvin, at which point hydrogen begins to recombine, which acts as a thermostat to maintain the temperature at a relatively constant value. The recombination timescale is

$$\tau_{\rm rec} \simeq 150 \left(\frac{X_{\rm H}}{0.7}\right) \left(\frac{M_{\rm atm}}{0.1 M_{\rm J}}\right) \left(\frac{R_{\rm P}}{R_{\rm J}}\right) \text{ years,} \tag{4.19}$$

where $X_{\rm H}$ is the Hydrogen fraction. As a result of this relatively long time-scale, these ejected planets could remain quite bright ($L_{\rm bol} \sim 0.1 L_\odot$) for an extended period of time, even without additional tidal forcing. If we assume that one in ten planet-hosting stars ejects a Jupiter-like planet via a partial disruption, and adopting an average star formation rate of $1 M_\odot$ per year, at least one ejected planet in the recombination phase should be visible in the galaxy at any one time.

4.5 Conclusions

4.5.1 Limitations and Future Directions

The principle assumptions that we have made in this chapter is that Jupiter-like planets are represented accurately by a polytropic model of its structure. One advantage of this model is that disruption simulations are trivially scalable to planets of a different size by a simple correction to β, assuming that the planet's mass interior to a given radius $M_{\rm P}(< r)$ scales self-similarly and that the fluid γ remains unchanged. An $n = 1$ polytrope reproduces the mass profile of coreless 1 $M_{\rm J}$ planet relatively well, with the difference in $M_{\rm P}(< r)$ never exceeding 10% throughout the planet's interior (N. Miller, private communication).

The inclusion of a core of a few tens of $M_\oplus$ affects $M_{\rm P}(< r)$ out to a few times the core radius, for which $M_{\rm P}(< r) \sim 0.4M(R_{\rm P})$. Beyond this radius, the structure of the planet is nearly identical to the coreless/polytropic models. This means that our simulations should be an accurate representation for disruptions where $\lesssim 70\%$ of the planet's mass is removed for Jupiter-like planets. For Neptune-like planets, where the core mass can be larger than the gas mass, the difference in $M_{\rm P}(< r)$ is substantial all the way to the planet's outermost layers, and thus our simulation results should not be directly applied. As the average densities of Neptune-like planets is larger than Jupiter-like planets, $r_\mathcal{T}$ for Neptunes should assume a smaller value.

Additionally, we assume that $\gamma = 2$ throughout the simulation volume, even for regions of very low density where the fluid is completely ionized and should behave as an ideal gas ($\gamma = 5/3$) or even a radiation pressure dominated fluid ($\gamma = 4/3$) in the lowest-density regions. This transition to different values of γ should affect the structure of the hot envelope that forms from the re-accreted debris that surrounds a partially disrupted planet, which is dynamically unimportant but may affect the planet's observable signature. This is not to say that a more realistic equation of state would not affect the mass loss itself. As the process of ripping material from the planet involves rapid fluid decompression, a decrease in γ may result in slightly altered disruption dynamics.

Ideally, one would like to extend the models we have presented here to include a more physical equation of state that can treat all components of the pre- and post-disrupted planet realistically. As the resolution required to determine $r_\mathcal{T}$ for multiple-orbit encounters beyond what we have presented here is prohibitive, it seems that the exploring the affects of using a more-complete equation of state with a realistic initial planet model is the next natural step for future studies. In the case of planets with a substantial core, these modifications are necessary to determine $r_{\mathcal{T}}$ with any confidence.

4.5.2 The Fates of Scattered Jupiters

The fate of a Jupiter-like planet after a strong scattering event is a function of the strength of the tidal forces it experiences at periastron. In this chapter, we have determined the disruption radius $r_{\mathcal{T}}$ for Jupiter-like planets which sets the boundary between long-term survival and rapid tidal disruption. Below, we summarize the various post-scattering outcomes in order of decreasing distance, using $r_{\mathcal{T}}$ and the tidal radius $r_{\rm t}$ as points of reference.

Stalled $\left(r_{\rm p} \gtrsim 6r_{\rm t}\right)$: The planet is deposited into an orbit where the rate of tidal dissipation is too small to result in a change in semi-major axis over the lifetime of the system. This planet may be in a Kozai state driven by a third body in the system, or could experience another strong scattering event, which may lead to an increase of eccentricity and subsequent circularization.

Circularization/Migration $\left(r_{\mathcal{T}} < r_{\rm p} < 6r_{\rm t}, e \lesssim 0.9\right)$: In this region, the planet is close enough to its parent star that tidal dissipation is effective, and the planet can circularize in 10^9 yr or less for moderate values of e. For near-radial orbits, circularization may still be longer than the stellar age, but again the Kozai mechanism or scattering could lead to a more rapid orbital evolution. All currently observed hot Jupiters are either stalled, in the process of circularizing, or already have circular orbits. If the planet is close enough to its parent star and $Q_* \lesssim 10^7$, the planet will raise a tide on the star and migrate inwards due to the transfer of angular momentum.

Ejection $\left(r_{\rm p} < r_{\mathcal{T}}, e \gtrsim 0.97\right)$: A planet that passes within the exclusion zone will be ejected from the system if its initial orbit is radial enough such that its orbital energy $E_{\rm orb}$ is significantly smaller than the self-binding energy $E_{\rm p}$ of the planet. Slightly less than half of the planet's initial mass remains bound to the central star, carrying with it a large reservoir of angular momentum that can significantly alter the host star's spin rate and axis of rotation. The ejected planet will remain as bright or brighter than its host star for a few years, eventually plateauing via hydrogen recombination as an object with a fraction of solar luminosity for a century. All Jupiter-like planets that scatter in from beyond $a_{\rm ice}$ such that $r_{\rm p} < r_{\mathcal{T}}$ will be ejected from the system.

Complete disruption $\left(r_{\rm p} < r_{\mathcal{T}}, e \lesssim 0.97\right)$: For planets that are deep within their parent star's potential well, the planet cannot soak the change in energy required to significantly alter the orbit, which eventually leads to its complete disruption. Approximately half of the planet's mass accretes onto the stellar host, carrying the same specific angular momentum as in the ejection case, leading to even more pronounced effects on the stellar spin. Only planets that have migrated close to their stars prior to being scattered are destroyed before they are ejected.

Collision with the central star $\left(r_{\rm p} < R_*\right)$: The planet strikes the surface of the star directly. Anywhere from half to all of the planet's mass is absorbed by the star, with the angular momentum being carried by this material potentially being smaller than that carried by the debris from a disruption, depending on how direct the impact is. These events are approximately twice as uncommon as ejections/disruptions.

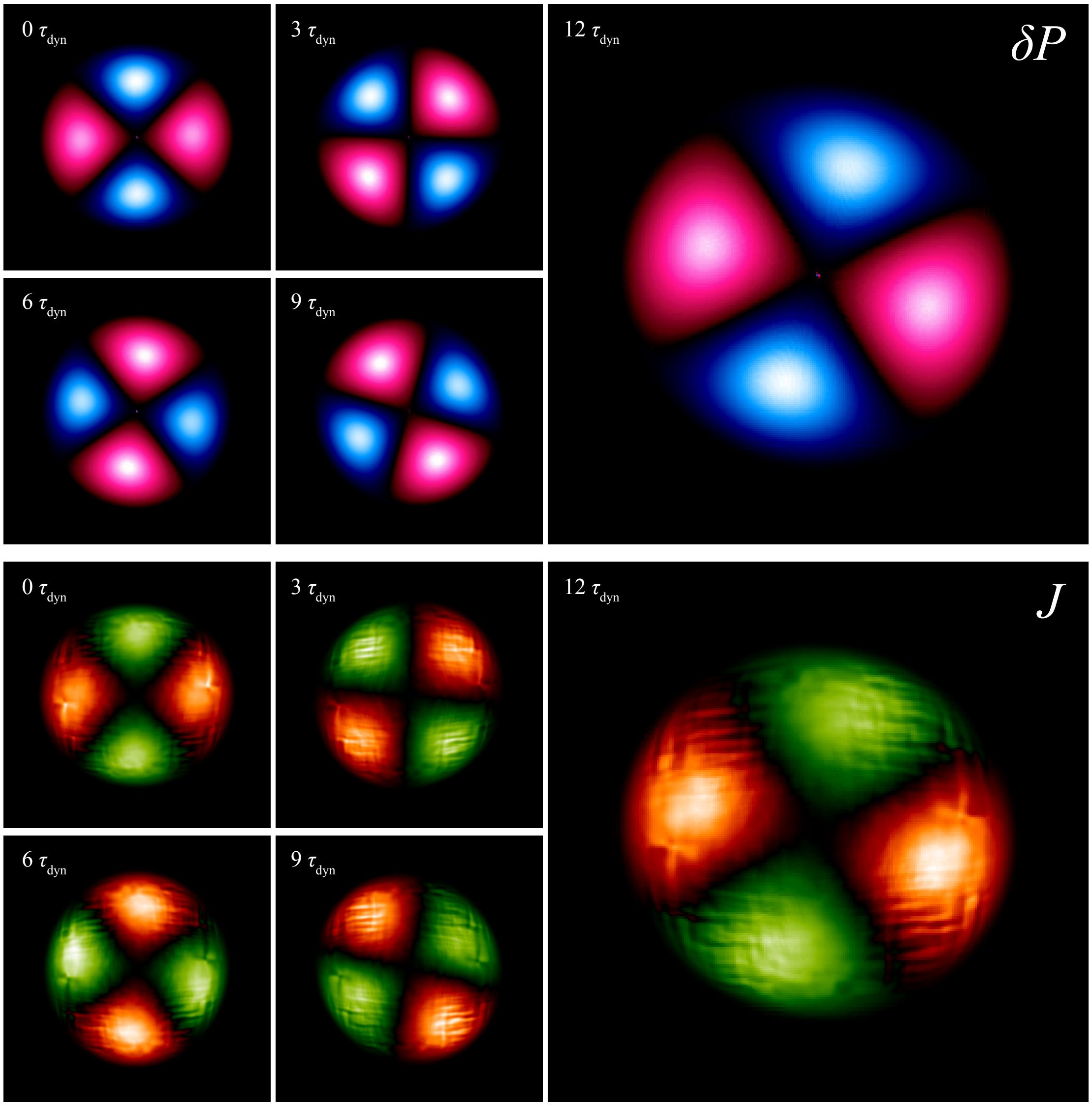

Figure 4.6: Pressure perturbations and spin excited by a grazing encounter with $r_{\rm p} = 3r_{\rm t}$. The upper five panels show the pressure perturbation δP over several $\tau_{\rm dyn}$, with blue corresponding to regions of lower pressure and pink corresponding to regions of higher pressure relative to the base state. The lower five panels show the fluid's angular momentum relative to $\mathbf{r}_{\rm c}$ (Equation (A.2)), with green representing clockwise rotation and orange representing counter-clockwise. Note that while the object appears to be rotating rapidly, the presence of rotating and counter-rotating regions leads to almost an exact cancellation of the total angular momentum J. The illusion of rapid rotation is in fact related to the pattern speed of the $l = 2$, $m = \pm 2$ normal modes. Because the angular momentum carried by this mode is related to the tangential component of the expansion and contraction of the planet as it oscillates, the fluid vacillates back and forth at the mode frequency. As can be seen in the figure, the fluid with $J > 0$ possess slightly more total angular momentum than the fluid with $J < 0$. This leads to a spin frequency $\omega = \sum J/I$ that is actually very small.

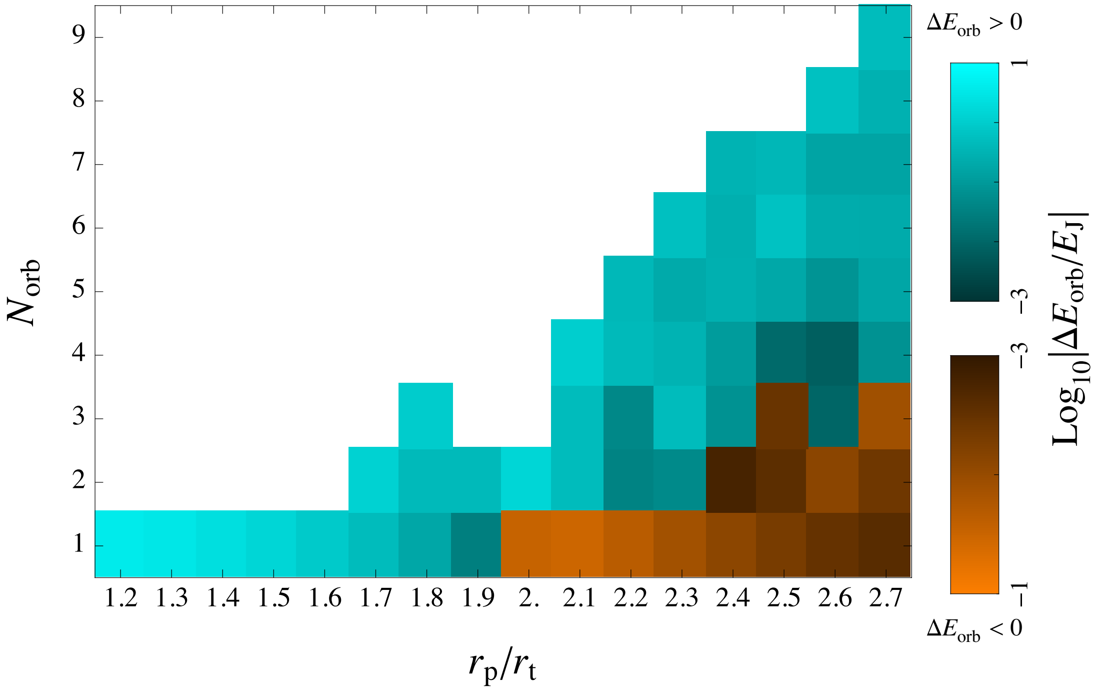

Figure 4.7: Change in orbital energy E_{orb} attributed to each passage as a function of r_{p} and orbit number N_{orb}. The orange regions show decreases in E_{orb} (more bound), while the cyan regions show increases in E_{orb} (less bound). The height of each r_{p} column shows the number of orbits a planet survives before being destroyed.

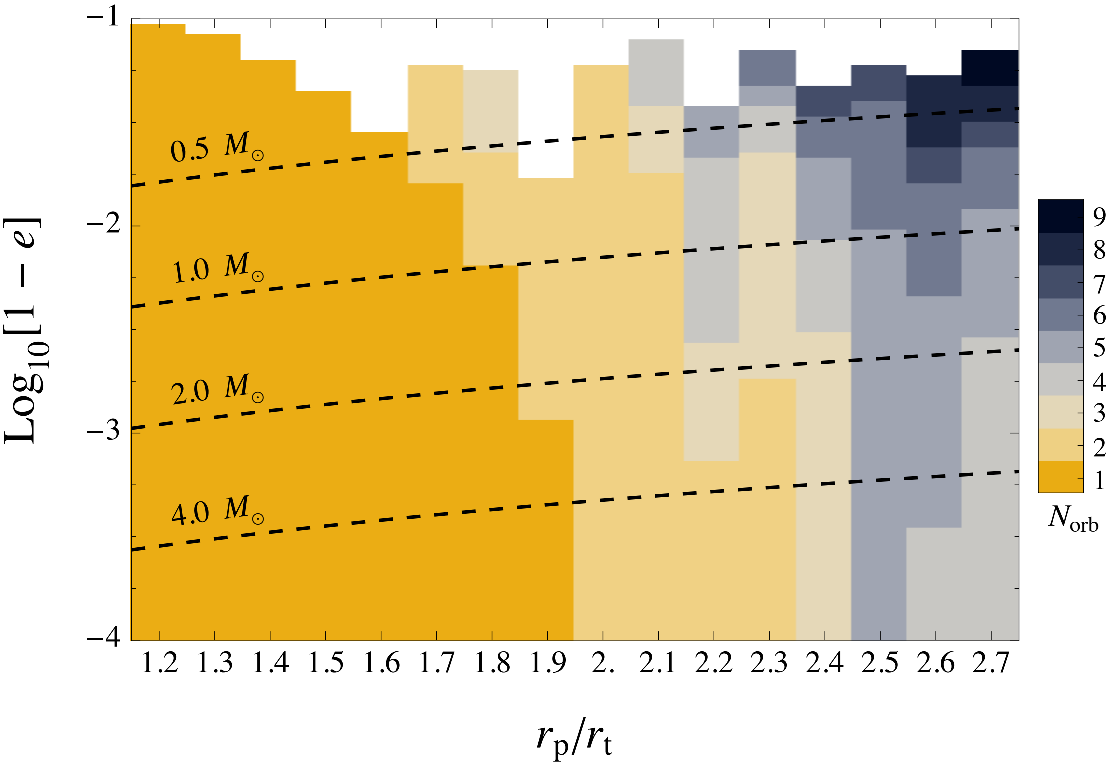

Figure 4.8: Criteria leading to planet ejection given an initial periastron passage distance r_p and eccentricity e. The colored regions correspond to the number of orbits before a planet is ejected by its interaction with the parent star. The dashed lines show the value of e given an apocenter distance equal to the ice line a_{ice}, assuming that $L_* \propto M_*^{3.9}$. For all values of r_p shown and for $e \lesssim 0.97$, planets are ejected before they are totally disrupted. Note that the region bounding the planets that are ejected on the first orbit has a monotonic dependence on r_p, while all other regions exhibit more complicated structure. This is because the first passage involves a planet with no internal motions, and thus no relation between phase and the excitation or de-excitation of fundamental modes. All future passages for $N > 1$ involve a planet that is both differentially rotating and oscillating, resulting in a large variance in the amount of energy added or removed from the orbit.

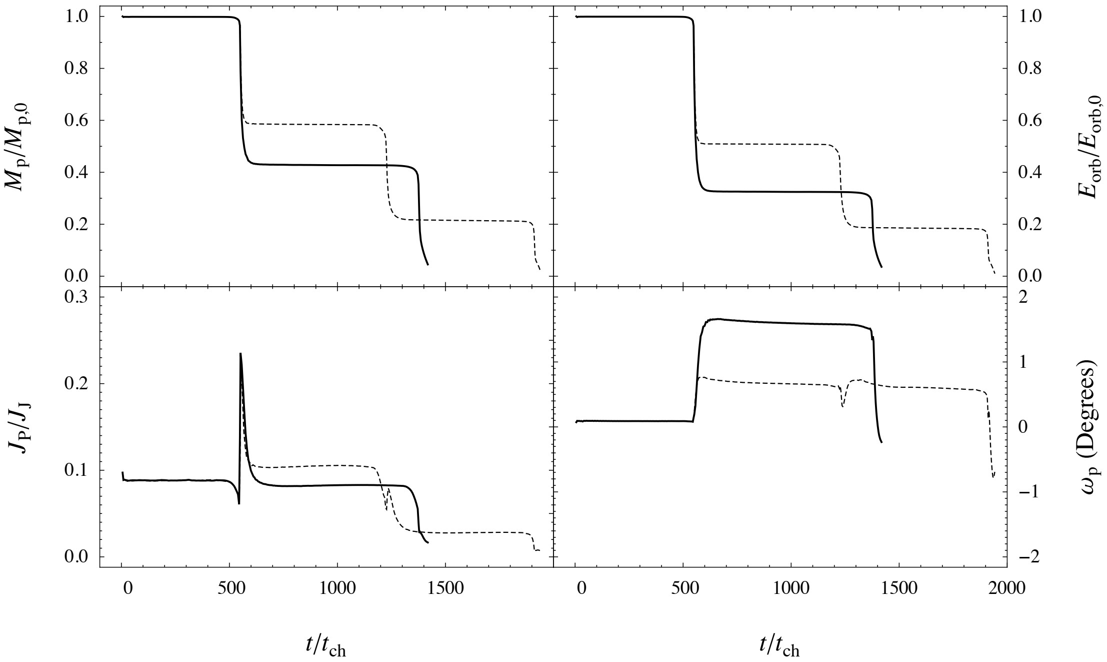

Figure 4.9: The evolution of two multiple encounter simulations with almost identical initial conditions. Both simulations use the same initial conditions as the rest of the multiple encounter simulations presented in this chapter, with $r_p = 2r_t$. The only difference between the two simulations is the initial eccentricity: The solid curves show the outcome for initial eccentricity $e = 0.9$, while the dotted curves show the outcome for $e = 0.90012$, which corresponds to an orbital period that is one free-fall time-scale t_{ff} longer than the $e = 0.9$ case. The four plots show the planetary mass M_P, orbital energy E_{orb}, spin angular momentum J_P, and precession of the orbit ω as functions of t/t_{ch}. Note that while the outcome of the first encounter at $t = 0$ is almost completely identical in both simulations, the behavior diverges on the second encounter, which leads to the planet on the $e = 0.9$ orbit being destroyed in three orbits, whereas the planet on the $e = 0.90012$ is destroyed in four. This divergence is a result of the phase difference between the two simulations introduced by the slight difference in initial orbital period.

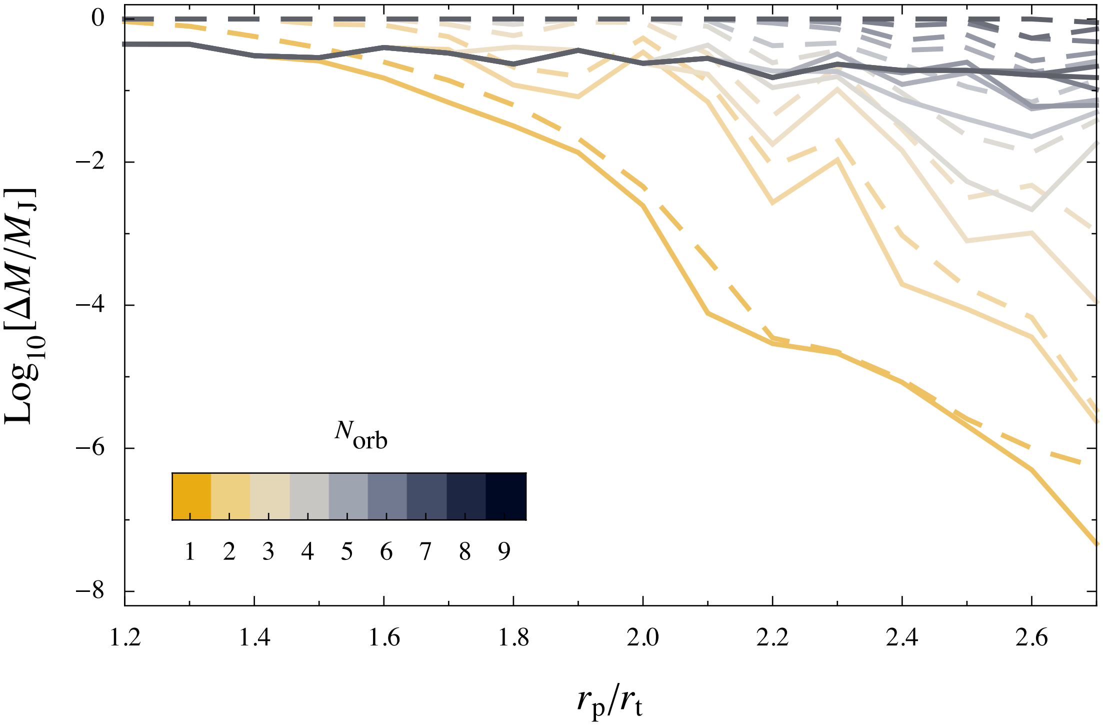

Figure 4.10: Mass loss history of multiple passage encounters for different initial values of r_p. Each curve is color-coded to correspond to a particular orbit number. The solid lines show the aggregate mass accreted by the star, while the dashed lines show the total mass lost from the planet.

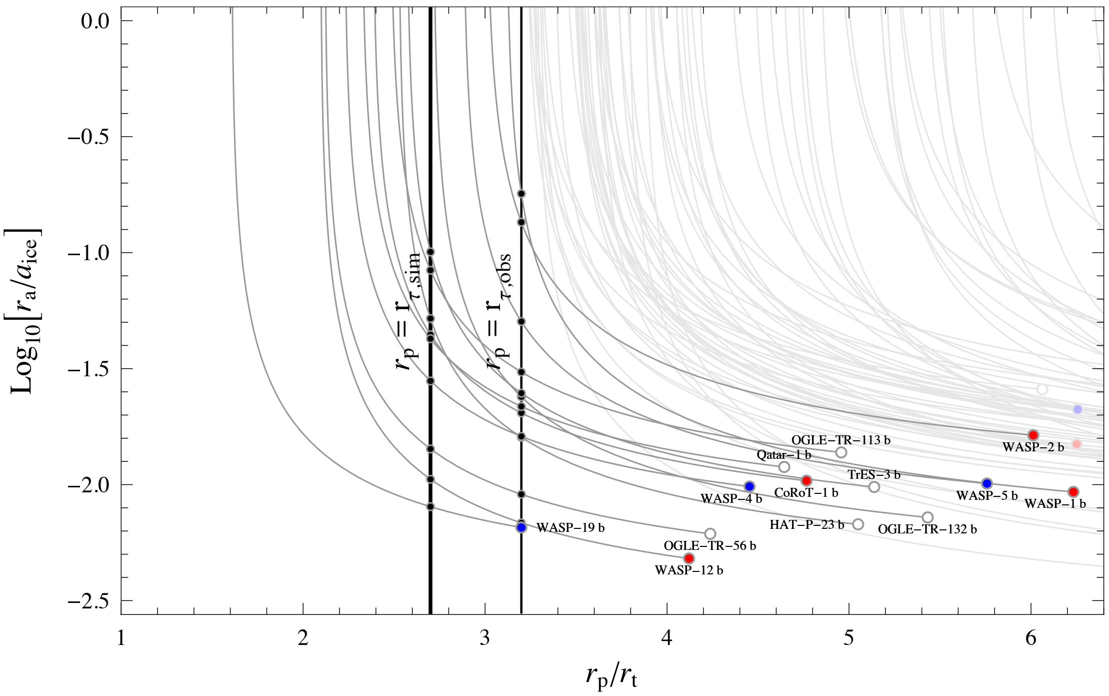

Figure 4.11: Possible apastrons r_a for the known hot Jupiters with $M_P > 0.25M_J$. Each arc shows the apocenter of an orbit with pericenter r_p, assuming that the angular momentum of the initial orbit is equal to the orbital angular momentum observed today. The open circles show each planet's currently observed r_p and r_a, scaled to the tidal radius r_t and the ice line a_{ice} respectively, which are determined by the planet/host star properties at the time of scattering. For the planet's radius at the time of scattering, we use the cold, coreless Jupiter models of (Fortney *et al.*, 2007) at 300 Myr. Blue-filled circles are planets that are thought to be aligned with their host stars, red-filled circles are thought to be misaligned (either via direct measurement or because they have observed to have statistically inconsistent rotation rates, see Schlaufman, 2010), and white-filled circles show systems with unknown orientations. The thick vertical line (labeled $r_{\tau,sim}$) shows the minimum possible value of r_τ corresponding to the Jupiter exclusion zone, which is determined through our numerical simulations for Jupiter-like planets to be $2.7r_t$, while the thinner vertical line (labeled $r_{\tau,obs}$) shows the maximum possible value for r_τ, which is defined by the planet that is currently observed to be closest to its classically defined tidal radius, WASP-19 b. Filled black circles show the intersection between the r_τ lines and each of the arcs of constant angular momentum shows the maximum apastron distance $r_{a,max}$ a planet could have been scattered from without being destroyed on its subsequent encounters with the host star. Only planets for which $r_{a,max} < a_{ice}$ assuming $r_\tau \leq r_{\tau,obs}$ are labeled, hot Jupiters that do not meet this criteria are left unlabeled and are greyed out. Note that the typical $r_{a,max}$ values are significantly smaller than a_{ice}, which indicates that those planets must have migrated prior to being scattered if planet-planet scattering brought them to their current positions. All data taken from the Extrasolar Planets Encyclopaedia (`http://exoplanet.eu`) and René Heller's Holt-Rossiter-McLaughlin Encyclopaedia (`http://www.aip.de/People/RHeller/`) on January 24, 2011.

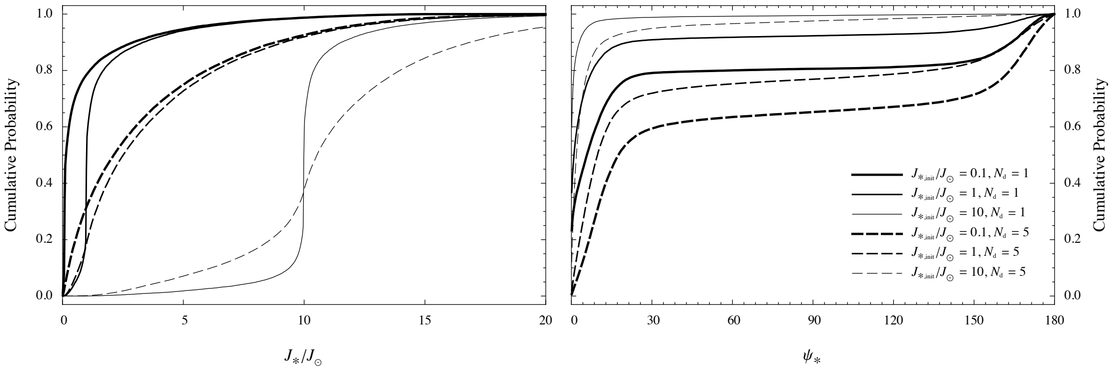

Figure 4.12: Changes to the stellar spin as a result of accreting tidally disrupted planets. The curves show the cumulative probability that a star will possess a given angular momentum J_* and spin inclination ψ_* after 1 (solid) or 5 (dashed) planetary disruptions $N_{\rm d}$ for different initial stellar angular momentum $J_{*,\rm init}$. Planets are assumed to have a logarithmic distribution in mass ($0.25M_{\rm J} \leq M \leq 10M_{\rm J}$) and semi-major axes ($r_\tau \leq a \leq 10a_{\rm ice}$), where r_τ is the minimum distance for which a planet won't be tidally disrupted and $a_{\rm ice}$ is the ice line. The eccentricity e and inclination i relative to the invariable plane are assumed to follow Rayleigh distributions, with $\sigma_e = 0.3$ and $\sigma_i = 10°$.

Chapter 5

The Importance of the Impact Parameter and Stellar Structure for the Tidal Disruption of Stars

5.1 Introduction

Supermassive black holes (SMBHs) have been found to reside at the centers of most galaxies. These black holes are surrounded by a dense stellar cluster which will occasionally deposit a star into an orbit that takes it within its tidal radius. A fraction of the star's mass then becomes bound to the black hole, and proceeds to fall back towards the star's original pericenter, eventually forming an accretion disk that results in a luminous flare with a luminosity comparable to the Eddington luminosity.

The standard model of tidal disruption presumes that nothing remains of the star after the encounter, resulting in approximately half of the star's original mass falling back onto the black hole, with the debris possessing a variety of orbital periods resulting from a spread of orbital energy that is "frozen in" at pericenter. First described in Rees (1988), the rate of fallback has been estimated both through increasingly sophisticated numerical simulations and analytical models. While previous results have provided reasonable models for the fallback resulting from the complete disruptions of stars at the tidal radius $r_{\rm t}$, where M_* and R_* are the mass and radius of the star and $M_{\rm h}$ is the mass of the black hole, they completely neglect partial stellar disruptions, in which a stellar core survives the encounter and only a fraction of the star's mass becomes immediately bound to the black hole. These events are likely to be much more common than their complete disruption counterparts, both for the reason that the rate of encounters interior to the pericenter distance $r_{\rm p}$ scales as $r_{\rm p}$ (Hills, 1988), and also that the disrupted star may return on subsequent orbits and be subject to disruption and/or further tidal dissipation. Additionally, many previous studies have focused on stars of a single structural profile, usually selected to match the familiar profile of our own Sun. However, standard stellar mass functions predict that low-mass main sequence (MS) stars are more common (e.g. Kroupa *et al.*, 1993), and thus may contribute significantly to the overall disruption rate. These stars are significantly less centrally concentrated than their solar mass brethren.

The dynamics of stellar tidal disruption have been modeled by many authors using simple analytical arguments (Rees, 1988; Phinney, 1989; Lodato *et al.*, 2009; Kasen and Ramirez-Ruiz, 2010), increasingly complex dynamical models (Luminet and Marck, 1985; Carter and Luminet, 1985; Luminet and Carter, 1986; Diener *et al.*, 1995; Ivanov and Novikov, 2001), and hydrodymical simulations utilizing either an Eulerian (see Chapter 2, also see Evans and Kochanek, 1989; Khokhlov *et al.*, 1993a,b; Diener *et al.*, 1997; Guillochon *et al.*, 2009) or Lagrangian (Nolthenius and Katz, 1982; Bicknell and Gingold, 1983; Laguna *et al.*, 1993; Kobayashi *et al.*, 2004; Rosswog *et al.*, 2008a; Lodato *et al.*, 2009; Ramirez-Ruiz and Rosswog, 2009; Rosswog *et al.*, 2009b; Antonini *et al.*, 2011) approaches. Very few of these studies have presented the effect varying $r_{\rm p}$ on the amount of mass lost by the star, ΔM, or the effect on $\dot{M}$, the rate at which the mass liberated from the star returns to pericenter. Given that the viscous time is expected to be significantly shorter than the period of the returning debris, this $\dot{M}$ is expected to track the luminosity $L(t)$ closely. As the number of observed disruptions increases, and as the cadence and quality of data improves, it becomes increasingly more important to improve models of $\dot{M}$ for disruptions of all kinds.

In this chapter, we present the results of 43 hydrodynamical simulations at high-resolution representing the disruption of both low-mass and high-mass MS stars. This provides, for the first time, a complete picture of the feeding of SMBHs by the disruption of MS stars. While the expected trend of smaller mass accretion rates for progressively more grazing encounters is reproduced, our study reveals several surprises on how disruptions work, particularly on the effect of stellar structure and how the fallback rate scales for both grazing and deep encounters. Contrary to what is expected from the freezing model, in which only the distribution of mass at pericenter is considered, the non-linear response of the star to the tidal field is found to play a crucial role in determining $\dot{M}$. Our simulations show that the simple models previously employed to predict the rate of fallback do not capture the full dynamics of the problem, and are only appropriate for anything other than the full disruption at exactly the tidal radius.

We find that the decay rate of $\dot{M}$ does not settle to a constant value until a few months after the disruption for all disruptions by black holes with $M_{\rm h} > 10^{6} M_{\odot}$, implying that the range of characteristic decay rates used to identify tidal disruption flares should be widened to include events that may not follow the fiducial $t^{-5/3}$ decay rate. For partial disruptions, the decay rate at a few years after the disruption depends crucially on the hydrodynamical evolution of the debris stream. This means that simulations must cover more than a few stellar dynamical timescales after the disruption, with the final functional form of $\dot{M}$ not being established until the star is many hundreds of tidal radii away from the black hole. And while we do find that there are differences between the fallback functions calculated for the disruptions of profiles characteristic of low- and high-mass stars, the mass-radius relationship of MS stars results in a family of fallback curves that are difficult to distinguish from one another for stars of $0.3M_{\odot} \gtrsim M_{*} \gtrsim 1.0M_{\odot}$ without considering secondary features related to the shape of the fallback curves themselves, such as the decay rate of $\dot{M}$, characterized by a time-dependent power-law index $n(t)$.

This chapter is organized as follows. We describe our numerical method, initial models, and method for calculating ΔM and $\dot{M}$ in Section 5.2. The results of these simulations and how they improve our understanding of stellar tidal disruptions is described in Section 5.3. A discussion of the general trends and their effect on the observable features of tidal disruptions is presented in Section 5.4. Finally, we provide fitting formula to four characteristic variables describing disruptions of stellar profiles characteristic of low- and high-mass stars in Appendix B.

5.2 Method

Our simulations of tidal disruption are performed in `FLASH` (Fryxell *et al.*, 2000), an adaptive-mesh grid-based hydrodynamics code which includes self-gravity. The standard hydrodynamical equations are solved using the directionally split piecewise-parabolic approach (Colella and Woodward, 1984) as provided by the `FLASH` software, which has a small numerical viscosity and diffusivity as compared to the available unsplit solvers Therefore, the principle source of entropy generation is via shocks, if they are present. The solution to the Riemann problem is sensitive to the velocity of the frame in which the problem is solved, and poor solutions can be returned in regions where the velocity of the frame is many times larger than the sound speed (Tasker *et al.*, 2008; Robertson *et al.*, 2010; Springel, 2010). As stars that are disrupted by SMBHs are traveling at a fraction of the speed of light c, we perform our simulations in the rest-frame of the star where the velocities are $\sim \sqrt{c_{\rm s} v_{\rm p}}$, where $c_{\rm s}$ is the sound speed within the star and $v_{\rm p}$ is the velocity at pericenter.

Our method for this chapter is very similar to what is presented in Chapter 4, except that we now utilize version 4.0 of the `FLASH` software, which has a greatly improved multipole gravity solver[1]. A key parameter of the multipole gravity solver is the maximum angular number of the multipole expansion $l_{\rm m}$. A test simulation setting $l_{\rm m} = 10$ showed multiple recollapse points for a nearly-complete disruption, which is not expected to occur in disrupted stars (as described in Section 5.3.1). We suspected this behavior was a consequence of the large aspect ratio of the debris stream, which results in gravity being under-resolved if the multipole expansion is truncated at small $l_{\rm m}$. With $l_{\rm m}$ set to 20, only a single recollapse occurs, as is expected.

---

[1] See http://flash.uchicago.edu for details

For $l_{\rm m} = 40$, we found no significantly difference in any quantities of interest as compared to $l_{\rm m} = 20$, except for cases in which a very small remnant survives the disruption. In these cases, the error is in the mass of the surviving object, which is difficult to resolve for marginally surviving stars (see Section 5.3.1). The results presented in this work all use $l_{\rm m} = 20$ for optimal runtime efficiency.

Additionally, we add a truncation density parameter $\rho_{\rm damp}$ that is set to 10^{-18} g cm^{-1}, a factor of 10 larger than the fluff density. Material with density less than this value is not included in the multipole expansion, nor are any gravitational forces applied to this material. This is necessary as the domain is extremely large as compared to the initial star, and so even $10^{-11} M_{\odot}$ of material can introduce a significant error in the calculated position of the center of mass. We also only include material with a density greater than 10% of the star's original peak density when calculating the location to use as the multipole expansion point; however all material with density greater than $\rho_{\rm damp}$ is included when calculating the magnitude of each of the multipole terms. This is done because the total center of mass does not always spatially coincide with the peak density, which can result in a multipole expansion that is a poor representation of the underlying density distribution.

5.2.1 Parameter Study

Ignoring general relativistic effects and stellar rotation, it may seem that a complete study of tidal disruptions would require an exhaustive study of the various combinations of six parameters: M_*, R_*, $M_{\rm h}$, the orbital eccentricity e, the polytropic index γ, and $\beta \equiv r_{\rm t}/r_{\rm p}$. As an exhaustive search of a six-dimensional parameter space is prohibitive, we wish to reduce the

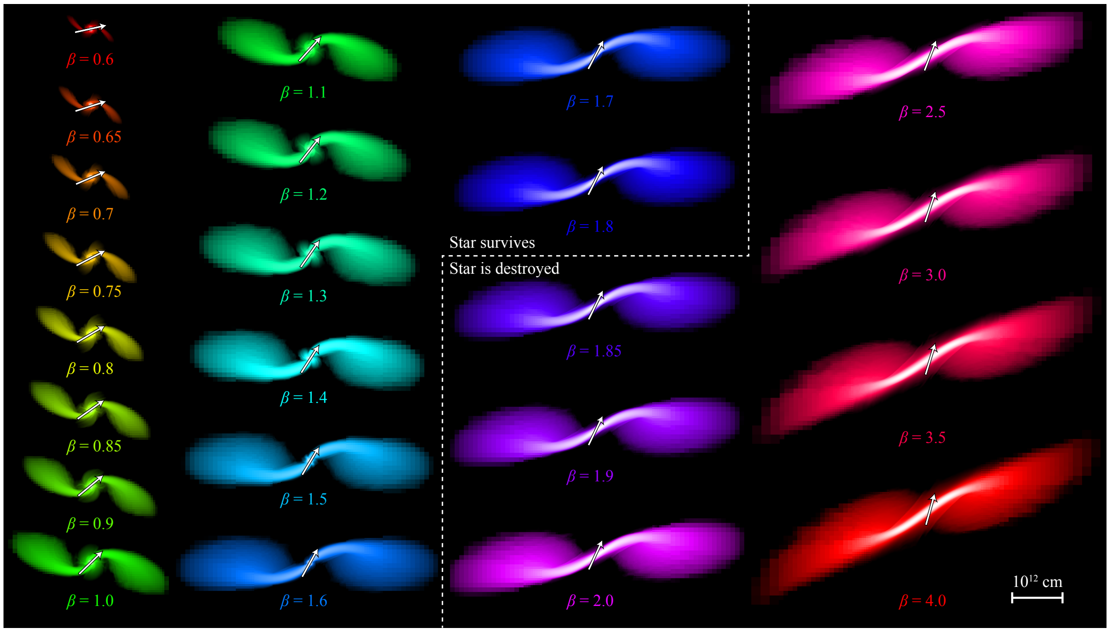

Figure 5.1: Snapshots of the density $\log \rho$ for all $\gamma = 4/3$ simulations at $t = 4 \times 10^4$ s after the start of each simulation, with white corresponding to the maximum density and black corresponding to 10^{-6} g cm^{-1}. Each snapshot is labeled with the ratio of the tidal radius to the pericenter distance β. The white arrows indicate the angle of the velocity vector at the time of each snapshot. The white dashed line separates simulations in which a core survives the encounter; although not visible here, recollapse does occur for the β = 1.7 and 1.8 simulations, but for $t > 4 \times 10^4$ s.

number of free parameters to a more manageable number. For fixed β, both $r_{\rm p}$ and $v_{\rm p}$ scale as $M_{\rm h}^{1/2}$, and thus the pericenter crossing time $t_{\rm p}$ is independent of $M_{\rm h}$. Additionally, as the mass ratio approaches infinity, the asymmetry of the tidal field becomes progressively less important as $R_* \ll r_{\rm t}$, with the difference in the strength of the tidal field at pericenter between the near-side and the far-side for a $10^6 : 1$ encounter being $\simeq 3\%$ (see Equation 4.5). And as most of the stars that are scattered into disruptive orbits originate from the sphere of influence or beyond (Magorrian and Tremaine, 1999; Wang and Merritt, 2004), the orbital eccentricity of almost all

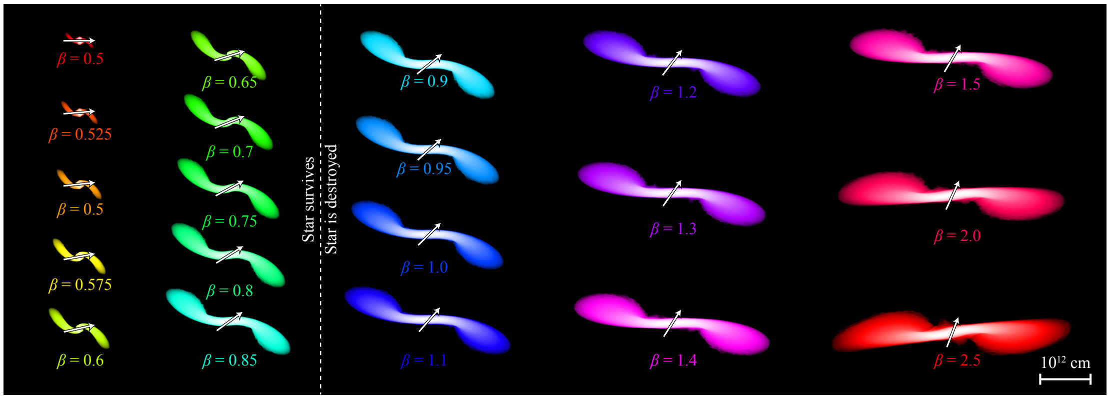

Figure 5.2: Snapshots of $\log \rho$ for all $\gamma = 5/3$ simulations at $t = 4 \times 10^4$ s, colors and annotations are the same as in Figure 5.1. Although not visible here, recollapse does occur for the $\beta = 0.75$ – 0.85 simulations, but for $t > 4 \times 10^4$ s.

disrupted stars is approximately unity[2].

It then follows that as the ratio of the time of the encounter $t_{\rm p}$ to the star's dynamical time $t_{\rm dyn} = \sqrt{R_*^3/GM_*}$, shape of the orbit (which depends on e), and asymmetry of the tides are nearly identical for all encounters of interest for a fixed β, the tidal force applied to the star as a function of time is independent of $M_{\rm h}$, e, M_*, and R_*. Thus, we find that the vast majority of stellar disruptions by SMBHs can be described by just two parameters: β and γ, with all other parameters obeying simple scaling relations. While previous numerical studies have considered the effect of varying γ on $\dot{M}$(Rosswog *et al.*, 2009b; Lodato *et al.*, 2009; Ramirez-Ruiz and Rosswog, 2009), the present work is the first to explore the effect of varying β on $\dot{M}$ in cases ranging from no mass loss to deeply penetrating encounters[3].

To explore this reduced but physically motivated parameter space, we run a series of simulations assuming $M_* = M_\odot$ and $M_{\rm h} = 10^6 M_\odot$. Our stars are constructed as polytropes,

---

[2] See (Madigan *et al.*, 2011) for a discussion of resonant relation processes that may produce a different distribution of eccentricities for stellar disruptions.

[3] Note that Laguna *et al.* (1993) do present $\dot{M}$ from low-resolution simulations for three different β values, two of which are very deeply penetrating ($\beta \geq 5$).

with the polytropic γ being set to either 5/3 or 4/3, representative of both low- and high-mass stars, respectively. During the simulation, the stars are evolved hydrodynamically according to a $\Gamma = 5/3$ equation of state, with the difference between γ and Γ for high-mass stars being a consequence of the radiation transfer within the star (Chandrasekhar, 1939). These one-dimensional profiles are then mapped to the three-dimensional grid, with initially uniform refinement across the star. The star is then relaxed for 10^4 s at the center of a cubical domain, which is 4×10^{14} cm on a side. The domain is initially composed of a single 8^3 block, which is then bisected into smaller 8^3 blocks as many as 15 times, resulting in a minimum cell size of 3×10^9 cm, or approximately 2% of the star's original diameter. Our refinement criteria is solely dependent on the density relative to the initial central density, with a factor of two reduction in resolution for each factor of a hundred in density. Regions within the simulation that are within 1% of the peak density are always maximally refined.

We ran simulations for 23 different impact parameters β ranging from 0.6 to 4.0 for $\gamma = 4/3$, and 20 different β ranging from 0.5 to 2.5 for $\gamma = 5/3$. Two additional simulations were run at $\beta = 0.5$ for $\gamma = 4/3$ and $\beta = 0.45$ for $\gamma = 5/3$; as less than $10^{-6} M_{\odot}$ is observed to be removed from the stars in these two borderline cases, we conlude that no mass is lost for values of β less than the above quoted ranges in β. Snapshots from each simulation recorded shortly after pericenter are shown in Figures 5.1 and 5.2.

5.2.2 Calculation of ΔM and $\dot{M}$

Our hydrodynamical simulations enable us to calculate the binding energy of the material to the black hole dM/dE. This function can be used to determine the feeding rate as a function of time through Kepler's third law,

$$\dot{M} = \frac{dM}{dE}\frac{dE}{dt} = \frac{2\pi}{3}\left(GM_{\mathrm{h}}\right)^{2/3}\frac{dM}{dE}t^{-5/3}. \tag{5.1}$$

For full disruptions, the entirety of the star's original mass is included in the calculation of dM/dE, approximately half of which will have specific orbit energy $E > 0$ and is thus unbound from the black hole. For partial disruptions, the criteria for determining which material to include in the determination of dM/dE is less straightforward, as what will be accreted by the black hole is only the material that the star's gravity is unable to retain. As the star is on a parabolic orbit, the distance from the black hole changes rapidly as a function of time, and thus the star's Hill radius $a_{\mathrm{H}}(t) \equiv r(M_{\mathrm{bound}}(t)/M_{\mathrm{h}})^{1/3}$ is also time-dependent, introducing some ambiguity into the determination of the self-bound mass $M_{\mathrm{bound}}(t)$.

In principle, the distance of matter from the surviving star can be compared to $a_{\mathrm{H}}(t)$ to determine what mass is bound to the star. However, the continual reaccretion of matter means that the star is extended, non-spherical, and dynamically unrelaxed for many dynamical timescales, and thus the appropriate mass to use in the calculation of a_{H} is uncertain. To circumvent this, we choose an iterative energy-based approach that we find converges quickly to a solution. First, we calculate the material that remains bound to the star, where the initial reference point is taken to be at the location of the star's peak density, which has a velocity $\mathbf{v}_{\mathrm{peak}}$. The specific binding energy of material in a given cell is calculated as

$$E_{*,i} = \frac{1}{2}\left(\mathbf{v}_i - \mathbf{v}_{\mathrm{peak}}\right)^2 - \phi_*, \tag{5.2}$$

where ϕ_* is the gravitational self-potential as calculated by the multipole solver. The center of momentum $\mathbf{v}_{\rm cm}$ is then determined by summing over all mass elements for which $E_{*,i} < 0$

$$\mathbf{v}_{\rm cm} = \frac{\sum_{E_{*,i}<0} \mathbf{v}_i \rho_i V_i}{\sum_{E_{*,i}<0} \rho_i V_i}, \tag{5.3}$$

where ρ_i and V_i are the cell density and volume. Equation (5.2) is then re-evaluated with $\mathbf{v}_{\rm peak}$ being replaced by $\mathbf{v}_{\rm cm}$. This process is repeated until $\mathbf{v}_{\rm cm}$ (and thus $M_{\rm bound}$) converges to a constant value. While this approach yields a value for $M_{\rm bound}$ in most cases, the question of whether an object is completely destroyed is somewhat complicated by the fact that the tidal force formally approaches zero as $\Delta r \to 0$, and thus there is always some material for which $\mathbf{v}_i = \mathbf{v}_{\rm cm}$, resulting in a infinitesimal, but non-zero $M_{\rm bound}$ even as the time since disruption $t - t_{\rm d} \to \infty$.

Figure 5.3 shows how the maximum density within a simulation $\rho_{\rm max}$ compares to the star's initial maximum density $\rho_{\rm max,0}$ for six simulations (three for $\gamma = 4/3$ and three for $\gamma = 5/3$). Two of the simulations shown for each γ exhibit a continuous decrease in $\rho_{\rm max}$, showing no signs of recollapse, whereas the third simulation for each γ shows an increase in density sometime after pericenter, eventually settling to a constant value as the collapsed object dynamically relaxes. As a check on the convergence of $M_{\rm bound}$ for all the simulations presented in this work, we compute the quantity $\mathcal{F} \equiv \left|\dot{M}_{\rm bound}/M_{\rm bound}\right| (t - t_{\rm d})$, which expresses the fractional change in $M_{\rm bound}$ since the time of disruption. Disruptions in which a self-bound core forms asymptote quickly to a constant $M_{\rm bound}$, and thus small values of $\mathcal{F}$, whereas disruptions in which $\rho_{\rm max}$ consistently decreases show $\mathcal{F} \sim 1$ at all times. The only disruptions in which the

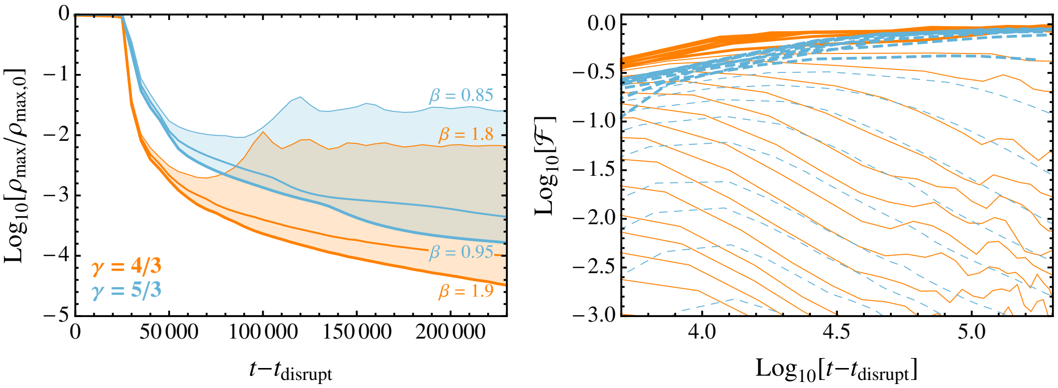

Figure 5.3: Evolution of maximum density ρ_{max} and bound mass M_{bound} as a function of time since disruption. In the left panel, the evolution of the ratio of ρ_{max} to the original maximum density $\rho_{\mathrm{max,0}}$ is shown for six simulations (filled regions), three for $\gamma = 4/3$ (orange, solid lines) with $\beta = 0.85$, 0.9, and 0.95, and three for $\gamma = 5/3$ (light blue, dashed lines) with $\beta = 1.8$, 1.85, and 1.9. In the right panel, the parameter $\mathcal{F} \equiv |\dot{M}_{\mathrm{bound}}/M_{\mathrm{bound}}|(t - t_{\mathrm{d}})$ is shown for all simulations, demonstrating the convergence of the calculate M_{bound} for all the simulations presented in this work (see Section 5.2.2 for details). When the value of this quantity is close to unity, M_{bound} is still changing by order unity over that timescale, indicating that the final bound mass cannot yet be determined at that t. The thick lines show simulations for which the star is considering to be destroyed after the encounter, whereas the thin lines show simulations for which a surviving core forms.

final core mass has not completely converged are the borderline survival cases (e.g. β slightly less than β_{d}). However, while the fractional error in M_{bound} is large for the borderline cases, the definition of $\Delta M = M_* - M_{\mathrm{bound}}$ means that the amount of mass lost from the star (and also the amount of mass bound to the black hole) is well-determined.

Once $\mathbf{v}_{\mathrm{cm}}$ has been determined, all material for which $E_{*,i} < 0$ is excluded, and the binding energy to the black hole E is calculated. This data is then binned in E, the result of which is used to determine dM/dE. The values of ΔM and $\dot{M}$ presented in the figures in the subsequent sections are all generated from snapshots that are produced at $t = 2.5 \times 10^5$ s after the start of each simulation (unless otherwise noted), or approximately 100 dynamical times after pericenter.

5.3 Hydrodynamics of the tidal disruption of MS stars

Many assumptions about the way partial and full disruptions work have never been tested beyond analytical approximations. Quantities that have been estimated include the time of return of the most bound material $t_{\rm most}$, the time of peak accretion rate $t_{\rm peak}$ and the magnitude of this rate $\dot{M}_{\rm peak}$, and the amount of mass bound both to the star and to the black hole after the encounter. Additionally, it has always been presumed that the late-time evolution of the fallback converges to the $t^{-5/3}$ decay law, whereas this is not necessarily true in partial disruptions where the surviving core may affect the binding energy of this material. We empirically measure these quantities from our calculations of dM/dE, and find that while some of the commonly-held assumptions are reasonably accurate, many are not. Most of these assumptions arise from how the problem was originally formulated, in which the star's self-gravity is viewed as inconsequential, and only the spread in binding energy across the star at pericenter is relevant in determining the features of the resulting $\dot{M}$. We find that the star's self-gravity is critical in determining the resulting $\dot{M}$, even for encounters with pericenters that are many times deeper than the tidal radius.

5.3.1 The Boundary Between Survival or Destruction

A collection of non-interacting particles in the presence of a point mass potential will all follow Keplerian orbits, provided that no outside force acts upon them. This means that once both the star's gravity and pressure become unimportant at a time close to the star's closest approach to a black hole, the position and velocity of each mass element can be recorded, and the future orbits of each part of the debris stream can be determined. It has been presumed that this condition is satisfied at $r_{\rm t}$, the distance at which the tidal force is greater than the self-gravitational force at the object's surface. This assumption is flawed in that the tidal radius as classically defined does not denote the distance at which the tidal force dominates self-gravity for any point within the star, but rather only at its surface. The conditions necessary for a polytrope to lose mass due to the presence of an external tidal force have been previously determined in the context of the Roche problem, which considers when the tidal force at the surface of an object exceeds the self-gravitational force in a circular orbit (Aizenman, 1968; Chandrasekhar, 1969). However, again, this limit only informs us as to when we expect the object to begin losing mass, and not the distance at which the object is completely destroyed. Additionally, the Roche limit is evaluated under the assumption of hydrostatic equilibrium, and presumes that the orbital velocity is equal to that of a circular orbit $v_{\rm c}$, resulting in a different dynamical response than for parabolic encounters in which the pericenter velocity is $\sqrt{2}v_{\rm c}$.

The question of whether a star survives depends not on the ability of tidal forces to remove some mass, but on whether these forces are overwhelming enough to disrupt the star's densest regions. Furthermore, even if a star experiences a seemingly complete disruption, the star may be capable of recollapse into a self-bound object after the encounter under the proper conditions. It has been shown that gamma-law equations of state stiffer than $\Gamma = 2$ can result in the recollapse of material within expanding thin streams for infinitesimally small masses (Chandrasekhar, 1961; Lee and Ramirez-Ruiz, 2007). As stars are well-approximated by $\Gamma \leq 5/3$ equations of state, these instabilities are not expected to appear in stellar disruptions, and thus recollapse is not guaranteed for all β.

The affine model, as introduced in Carter and Luminet (1985), improved upon the initial estimates provided by the Roche approach by including the effects of the dynamical tide, but while this approach is able to evaluate the distance at which distortions become non-linear, it is not capable of determining the actual distance at which disruptions occur. Later, Diener *et al.* (1995) extended the affine approach to calculate the critical impact parameter for full disruption $\beta_{\rm d}$, finding $\beta_{\rm d} = 1.12$ for $\gamma = 4/3$ and $\beta_{\rm d} = 0.67$ for $\gamma = 5/3$ polytropes, where $\beta_{\rm d}$ is the critical impact parameter at which complete disruption ensues. More recently, the affine formalism was improved upon further by modeling the star as a nested set of ellipsoids, each of which respond dynamically to the external tidal field (Ivanov and Novikov, 2001; Ivanov *et al.*, 2003). While this model is the first analytical approach to provide estimates for ΔM, the simplifying assumptions made regarding the treatment of self-gravity, pressure, and geometry does not guarantee that the true solution can be recovered via this approach.

In Figure 5.4 we show the amount of mass lost $\Delta M = M_* - M_{\rm bound}$ (measured at the end of each simulation) as a function of β for both $\gamma = 4/3$ and $\gamma = 5/3$, with comparisons to Ivanov and Novikov (2001) shown in black. Remarkably, the model of Ivanov and Novikov comes quite close to predicting the critical β value as measured by these simulations, despite the assumptions made, and is able to recover reasonable values for ΔM, although the scaling between ΔM and β is somewhat steeper than what is observed in the simulations. In particular, we find that stars can survive encounters for larger values of β than the nested affine model predicts. We speculate that the method presented in Ivanov and Novikov could be extended to

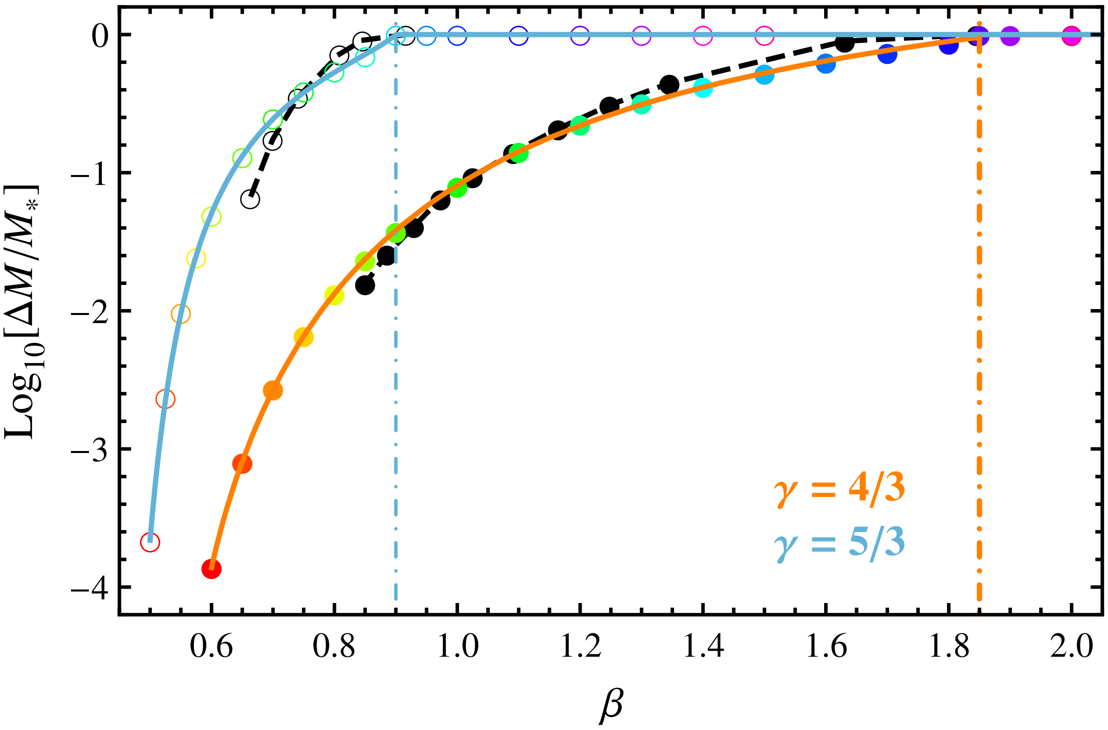

Figure 5.4: Fits to ΔM, with the fits to the $\gamma = 4/3$ models being shown by the solid colored circles, and fits to the $\gamma = 5/3$ models being shown by the open colored circles. Predictions of ΔM from Ivanov and Novikov (2001) for both $\gamma = 4/3$ and $\gamma = 5/3$ are represented by the black symbols/curves. The color coding matches that of Figures 5.1 and 5.2, with the impact parameters $\beta_{\rm d}$ beyond which stars are considered to be destroyed being denoted by the colored dot-dashed lines.

calculate $\dot{M}$ if the time at which each ellipsoid becomes unbound were recorded, which given the low computational burden of this approach could be used to perform more extensive parameter space studies.

We observe that while some stars appear initially to be completely destroyed, with their cores being disrupted along with their envelopes (Figures 5.1 and 5.2), the debris stream can often recollapse many dynamical timescales after the encounter, resulting in a small yet self-bound remnant. The mass of the remnant that results is roughly equal to the amount of

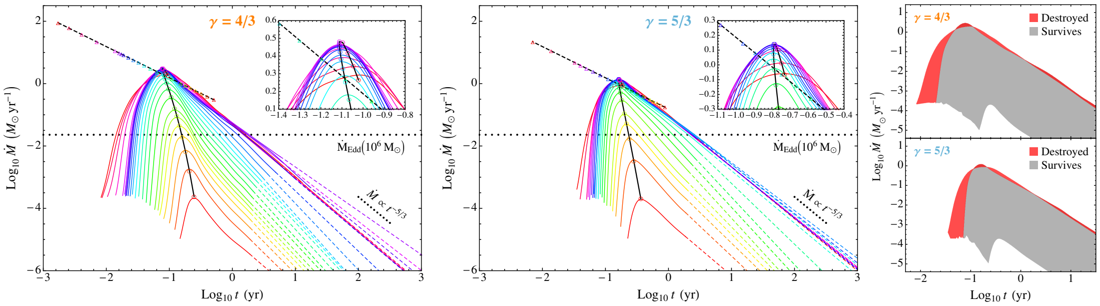

Figure 5.5: Fallback accretion rate $\dot{M}$ onto a $10^6 M_\odot$ black hole from the disruption of a 1 $M_\odot$ star as a function of γ and β. The colored curves in the left two panels show $\dot{M}$, with the color of each curve corresponding to the color coding scheme presented in Figures 5.1 and 5.2. The dashed portions of each curve are extrapolations based on the slope of the $\dot{M}$ immediately prior to the extrapolated region, which accounts for the fact that the late-time slope can only be determined exactly if the simulations are run for a prohibitive amount of time (see Figure 5.10). The dotted line shows the Eddington limit for a $10^6 M_\odot$ black hole assuming an accretion efficiency $\epsilon = 0.1$. The open triangles connected by the gray dashed line show the peak fallback rate $\dot{M}_{\rm peak}$ and time of peak $t_{\rm peak}$ as predicted by the energy-freezing model, in which the period of the return of materials scales as β^3 (Evans and Kochanek, 1989; Ulmer, 1999; Lodato *et al.*, 2009). The open circles connected by the black line show the fits to $M_{\rm peak}$ and $t_{\rm peak}$ as given by Equations B.1 and B.2 respectively. The right two panels shows the same data as the left two panels, with the filled regions showing the range of $\dot{M}$ curves resulting from full disruptions (red) and from disruptions in which the star survives (gray).

mass contained within a sphere centered at the recollapse point and with a radius equal to the cylindrical radius of the debris stream S.

For collapsing gaseous cylinders, spurious condensations as the result of the accumulation of numerical error may develop if the Jeans length is not properly resolved (Truelove *et al.*, 1997), with the source of that error being exacerbated by an inexact determination of the gravitational potential (Jiang *et al.*, 2013). Truelove *et al.* found that no spurious gravitational collapse occurs if the ratio J of the grid scale to the Jeans length $\lambda_{\rm J} \equiv \sqrt{\pi c_{\rm s}^2/G\rho}$, where $c_{\rm s}$ is the sound speed and ρ is the density, is always less than 0.25 in all grid cells at all times. In all of our simulations, the width of the debris stream is comparable to the star's initial size, and the resolution in the densest portion of the stream as it condenses is equal to the resolution used to resolve the original star (~ 50 grid cells). Therefore, in the case in which a recollapse marginally occurs (i.e. $J/S \sim 1$), $J \simeq 0.02$, satisfying the Truelove criteria.

For $\gamma = 4/3$, we find that stars are destroyed for $\beta \geq \beta_{\rm d} = 1.85$, i.e. no self-bound stellar remnant is produced. To verify that we are adequately resolving the boundary between survival and destruction, we ran a single $\gamma = 4/3, \beta = 1.8$ simulation at double the linear resolution, and found a recollapse that results in a bound remnant of only a few percent of a solar mass, slightly smaller than what is found using our fiducial resolution. As the mass of the surviving star nears zero, the resolution requirements become progressively more restrictive, as even slight changes in the cylindrical density profile or gravitational potential can alter the time of recollapse, and thus the final bound mass. For $\gamma = 5/3$, we find that stars are destroyed for $\beta \geq \beta_{\rm d} = 0.9$.

Numerical challenges aside, the exact boundary between survival and destruction for real stars is likely to be slightly different than what is predicted here, as the central densities of stars on the MS depend on rotation, metallicity, and age (Maeder, 1974; Wagner, 1974). Notably, our own Sun has a central density approximately twice that of the standard $\gamma = 4/3$ polytrope used to model it. This may allow the cores of somewhat evolved MS stars to survive for slightly larger values of β, although their gravitational influence is likely small as the helium-enriched cores of evolved MS stars are no larger than 10% of the star's mass (Schönberg and Chandrasekhar, 1942).

5.3.2 Characteristic features of $\dot{M}$

Figure 5.5 shows the family of $\dot{M}$ curves as a function of β for both $\gamma = 4/3$ and $\gamma = 5/3$. Immediately evident is the strong dependence between $\dot{M}_{\rm peak}$ and β for $\beta < \beta_{\rm d}$, and the similarity of the $\dot{M}$ curve family for $\beta \geq \beta_{\rm d}$. The result that deeper encounters do not produce more rapid flares is in direct conflict with the analytical prescription presented in Lodato *et al.* (2009) (hereafter LKP), in which the binding energy dM/dE is equivalent to the spread in mass over distance (modulo a constant), dM/dx, at pericenter. In this model (hereafter referred to as the "freezing model"), the binding energy is given by

$$E = GM_{\rm h}x/r_{\rm p}^2, \tag{5.4}$$

and thus deeper encounters always result in faster-peaking transients. Because the binding energy $E \propto r_{\rm p}^{-2}$, the scaling between β and $t_{\rm peak}$ is expected to be $t_{\rm peak} \propto \beta^3$ (Ulmer, 1999).

We definitively find that this is not the case, as the two separate functional forms of the parametric pair $\left[t_{\rm peak}(\beta), \dot{M}_{\rm peak}(\beta)\right]$ indicate a separate set of assumptions are appropriate for the two cases $\beta < \beta_{\rm d}$ and $\beta > \beta_{\rm d}$, neither of which match the functional form advocated by LKP (Figure 5.5, triangles). For encounters in which $\beta < \beta_{\rm d}$, $t_{\rm peak}$ and $\dot{M}_{\rm peak}$ are approximately related to one another by a power law, with the best fit model having $\dot{M}_{\rm peak} \propto t_{\rm peak}^{-7.4}$ for $\gamma = 4/3$ and $\dot{M}_{\rm peak} \propto t_{\rm peak}^{-10.5}$ for $\gamma = 5/3$. The steepness of this relation means that the difference in $t_{\rm peak}$ is only a few tenths of a dex between an event in which $10^{-4} M_{\odot}$ is lost and a full disruption. For $\beta > \beta_{\rm d}$, the trend between $t_{\rm peak}$ and $\dot{M}_{\rm peak}$ reverses for increasing β, with deep encounters resulting in both slightly longer duration flares and slightly lower typical accretion rates.

For fully-disruptive encounters, we find that $\dot{M}$ varies little with increasing β. An assumption of the freezing model is that the distance at which the dynamics of the debris can be described by Kepler's laws is when the star is at pericenter. In fact, the star's self-gravity becomes unimportant *before* the star comes this close to the black hole for encounters where $\beta > \beta_{\rm d}$. This suggests that the binding energy distribution of the material should be determined shortly after the star crosses the full disruption radius $r_{\rm d} \equiv r_{\rm t}/\beta_{\rm d}$, and not at its closest approach, unless the encounter is grazing enough such that $r_{\rm p} < r_{\rm d}$.

This can be understood by considering the local reaction time of each layer of the star's structure as compared to the passage timescale. The dynamical timescale for a particular layer is $\tau_{\rm dyn} \simeq \sqrt{1/G\bar{\rho}_{\rm x}}$, which is approximately equal to the time between when the star is at a distance where the tidal force is capable of removing that layer and the time of pericenter,

$$\begin{aligned} \tau_{\rm tidal} &= r_{{\rm t},x}/v_{{\rm t},x} \simeq \sqrt{\frac{r_{{\rm t},x}^3}{GM_{\rm h}}} = \sqrt{\frac{x^3}{GM_x}} \qquad (5.5) \\ &\simeq \sqrt{1/G\bar{\rho}_x}, \qquad (5.6) \end{aligned}$$

where the subscript x refers to quantities defined by the mass interior to x. Thus, regardless of the distance at which the tidal force begins to dominate the self-gravitational force, material is removed from the star at or near the full disruption radius $r_{\rm d}$. This means that the effective radius that should be used in the denominator of Equation 5.4 is $r_{\rm eff} = \max(r_{\rm d}, r_{\rm p})$. However, as the degree of balance between the tidal and self-gravitational forces continuously evolves over the encounter, the actual radius at which mass is removed can be larger or smaller than $r_{\rm eff}$, and thus the relationship between E and x is more complicated than outlined here.

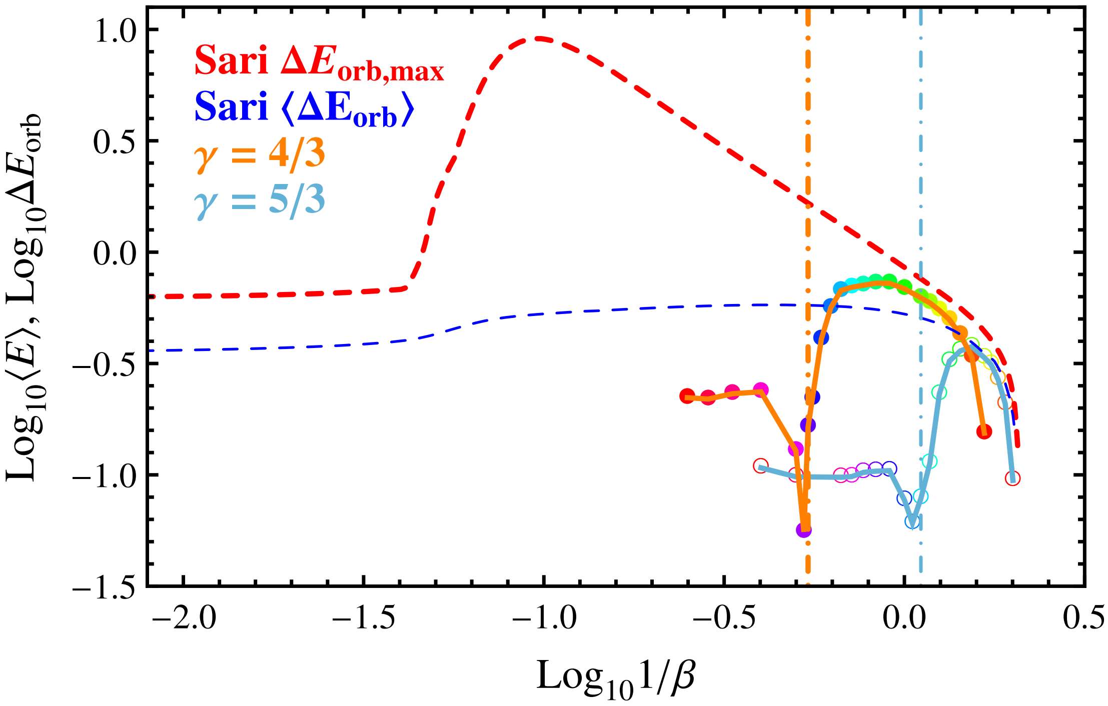

Figure 5.6: Average spread of matter post-disruption as compared to the change in orbital energy for binary disruptions (Sari *et al.*, 2010). The solid curves show $\langle E\rangle$ (the mass-averaged binding energy of the bound debris post-disruption) for both $\gamma = 4/3$ (light blue, open circles) and $\gamma = 5/3$ (orange, filled circles) stars, whereas the dashed curves show the change in orbital energy ΔE_{orb} for prograde binary encounters, where we have presumed that each star has mass $M_{\odot}$. The impact parameters β_{d} beyond which stars are considered to be destroyed being denoted by the colored dot-dashed lines. The red dashed curve shows the maximum change in orbital energy $\Delta E_{\mathrm{orb,max}}$ at a particular β, whereas the blue dashed curve shows E_{orb} averaged over binary phase. The binary disruption energies are scaled by $(GM_*/a)(M_{\mathrm{h}}/M_{\odot})^{1/3}$, where a is the initial binary separation, whereas the stellar disruption curves are scaled by $(GM_*/R_*)(M_{\mathrm{h}}/M_{\odot})^{1/3}$.

Additionally, while the binding energy is effectively frozen-in once the star crosses r_{d}, the assumption that the orbital energy can be reliably recorded at this point is only valid if the pressure gradient that develops within the star during maximum compression is not large enough to affect dM/dE. As shown in Carter and Luminet (1983), the pressure component of the Lagrangian does build significantly shortly after pericenter, and eventually dominates the

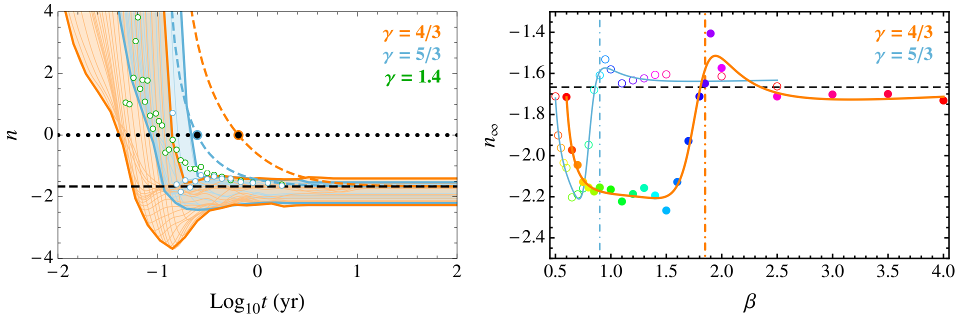

Figure 5.7: The left panel shows the power-law index n, with orange corresponding to $\gamma = 4/3$ stars and light blue corresponding to $\gamma = 5/3$ stars. The filled regions show the convex hull of n over all values of β; the lightly-weighted curves within the filled regions represent individual simulations for specific values of β. The horizontal dotted and dashed black curves show $n = 0$ (i.e. the peak of the accretion rate) and $n = -5/3$ (the canonical value for constant dM/dE), respectively. The dashed colored curves are produced using the analytical formulae of Lodato *et al.* (2009) for $\beta = 1$ encounters for both values of γ. For 1 $M_\odot$ stars, the analytical formulae predict a faster rise to peak for $\gamma = 4/3$ (orange-bordered point) than for $\gamma = 5/3$ (blue-bordered point), and fail to reproduce the steeper power law index that is found shortly after peak for $\gamma = 4/3$. The open colored circles show the numerical results of Lodato *et al.* (2009) for $\beta = 1$, where we include their $\gamma = 1.4$ case (dark green) in addition to $\gamma = 5/3$ and note that their simulations set $\Gamma = \gamma$. The right panel shows the asymptotic power-law index n_∞ as a function of β, with the color coding scheme identical to that of Figures 5.1 and 5.2, where the filled circles show n_∞ for $\gamma = 4/3$, and the open circles for $\gamma = 5/3$. A best fit for both values of γ are shown by the solid colored curves, and the impact parameters $\beta_{\rm d}$ beyond which stars are considered to be destroyed are denoted by the colored dot-dashed lines.

tidal component for sufficiently deep encounters. However, while this build-up can lead to the production of shocks whose breakouts may be observable as short X-ray transients (see Chapter 2 and Guillochon *et al.*, 2009), we find that the gradient of pressure within the orbital plane primarily acts to redistribute the most highly-bound material for ($t \lesssim t_{\rm peak}$), and not the material that determines the behavior of the decay phase (see Figure 3 of Guillochon *et al.* and Figure 5 of LKP). The tangible effect of this pressure build-up on the shape of $\dot{M}$ is the spreading of some material that would have otherwise accreted at $t_{\rm peak}$ to more highly-bound orbits, thus reducing the rate of accretion at peak, shifting $t_{\rm peak}$ to later times, and leading to an increased feeding rate at early times.

This behavior is analogous with what is found for binary star disruptions, in which the change in orbital energy $\Delta E_{\rm orb}$ of the stars is independent of the impact parameter for sufficiently deep encounters (Sari *et al.*, 2010). In Figure 5.6, we compare $\Delta E_{\rm orb}$ calculated by Sari *et al.* for binary disruptions to the mass-averaged spread in the binding energy $\langle E \rangle$ of the material that becomes bound to the black hole. As is found in binary disruption calculations, the change in energy initially increases with increasing β, then a transition point is reached where the binary's gravity (or star's gravity, in our case) no longer affects the dynamics, and finally the change in energy approaches a constant. A single star disruption and the disruption of a binary system are conceptually quite similar. A full disruption is analogous to an equal-mass binary disruption with separation distance $a \sim R_*$, where the mass of each "star" is equal to the mass liberated from each Lagrange point, $M_1 = M_2 = M_*/2$. A partial disruption is analogous to an unequal mass "trinary" system, in which the three masses correspond to the surviving self-bound core with mass $M_* - \Delta M$, and the bound/unbound debris streams with mass $\Delta M/2$, all with initial separation $a \sim R_*$. As the results presented in Sari *et al.* are independent of mass, the normalized ΔE for disruptions still map closely to those seen for binary disruptions, despite the variance in mass of the two (or three) interacting objects.

A caveat in our comparison to binary systems is that binaries can have an arbitrary orientation upon arrival at pericenter. This leads to an increase in the potential maximum energy change, and the β value at which it occurs. This comes as the result of stars in a binary being able to come arbitrarily close to one another during an encounter for favorable binary phases at pericenter ($\Delta E_{\rm orb,max}$ in Figure 5.6), which permits them to interact gravitationally for longer.

In effect, the binary can become "denser," decreasing the size of its effective tidal radius. For a stellar disruption in which the star is not initially rotating, the mass interior to a given radius cannot increase in the same way, and thus its self-gravity ceases to be important interior to its original tidal radius. This results in the near–constant spread in energy as described above, and is visually evident from simulation snapshots (Figures 5.1 and 5.2), in which the debris distributions are almost identical for $\beta \gtrsim \beta_{\rm d}$. We speculate that for rapidly rotating stars that this same effect that can yield large ΔE for certain binary phases may also apply, as stellar rotation can permit stars to penetrate more deeply before dM/dE is set (Stone *et al.*, 2012).

Figure 5.7 shows both the power-law slope $n(t)$ over the full $\dot{M}$ curve (left panel), and the asymptotic power-law slopes n_∞ (right panel), as produced by our disruption simulations. The behavior of the curves is more complicated than what is implied by the freezing model, in which $n \geq -5/3$ for all t. The qualitative behavior of the $\dot{M}$ curves can be characterized by three phases: A *rise* phase, in which $n > 0$, a *drop* phase, in which $n < 0$ (and potentially even < -5/3), and an *asymptotic* phase, in which $n_\infty \equiv n(t \to \infty)$ assumes a constant value. The rise phase is somewhat similar to what is predicted by the freezing model, although the evolution of n is somewhat more rapid within the simulations. The drop phase exhibits particularly steep downward slopes for $\gamma = 4/3$ stars, with $n \sim -4$ shortly after peak, but n for $\gamma = 5/3$ stars is closer to the predicted asymptotic value. Despite the disagreement between our simulations and the analytical model presented in LKP, we do find we reproduce the simulation results of LKP for $\gamma = 5/3$ stars at the same β (Figures 5.7 and 5.13).

The discrepancy between the simulation results and the prediction of the freezing model can be understood by considering what material becomes bound to the black hole in the case that the star is not completely destroyed. The binding energy E of material a distance x from the center of the star is $\propto x/\max(r_{\rm d}, r_{\rm p})^2 \propto x\beta^2$ (assuming $x \ll r_{\rm p}$). The value of x that corresponds to the material that determines the asymptotic behavior of $\dot{M}$ can be estimated by considering the deepest point within the star during the encounter in which tidal forces are capable of overcoming the star's self-gravitational force, the exact functional form of which is dependent upon the hydrodynamical response of the star during the encounter. While this functional form can only truly be determined through hydrodynamical simulation, it is clear that the effective x must decrease with increasing β, as the tidal forces remove an ever-increasing fraction of the star's mass. This implies that the scaling between E and β must be weaker than β^2, and thus $t_{\rm peak}$ should show less evolution for progressively deeper, but not completely disruptive encounters.

The asymptotic phase exhibits a more complicated behavior that depends on β, and shows four distinct behaviors depending on the depth of the encounter for both $\gamma = 4/3$ and $\gamma = 5/3$ stars. For extremely grazing encounters in which a small fraction of the star's mass is lost, $n_\infty \simeq -5/3$. In these encounters, all of the mass is removed near pericenter, resulting in an energy spread that only depends on x, the distance to the star's center of mass (in agreement with the freezing model).

When a significant fraction of the star's mass is removed in an encounter, n_∞ steepens to values as large as $\simeq -2.2$. This behavior arises from the influence of the star's core (Figure 5.8). As the outermost layers of the star are removed prior to pericenter, the core is able to partially counter the black hole's tidal force, keeping material closer to the star's core, and thus reducing the effective x at which the material is no longer strongly affected by the core's

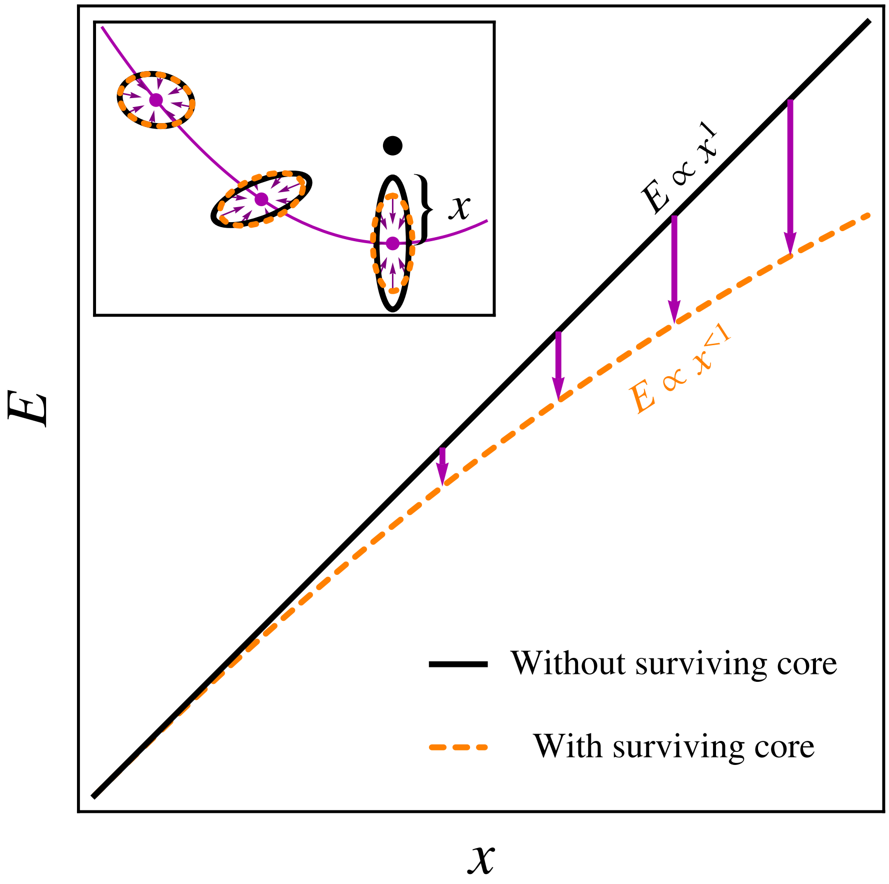

Figure 5.8: Cartoon showing the gravitational effect of a surviving core on the dynamics of material that is removed from the star during a partially-disruptive encounter. The inset diagram in the upper left demonstrates how the restoring force provided by a surviving core can alter the structure of the outer layers. For encounters in which the core plays little role, the binding energy to the black hole E scales linearly with x (black solid curve), the distance from the star's center of mass (Lodato *et al.*, 2009). If a core survives the encounter, its gravity prevents material from moving as quickly away from the star, resulting in a weaker relationship between E and x (orange dashed curve). This consequently results in a more-steeply declining $\dot{M}$. If the core itself is close to destruction, its gravitational influence is minimal, and the canonical $\dot{M} \propto t^{-5/3}$ decay law is recovered.

gravity. This results in a sub-linear relationship between E and x. As $E \propto t^{-2/3}$, and $E \propto x^m$,

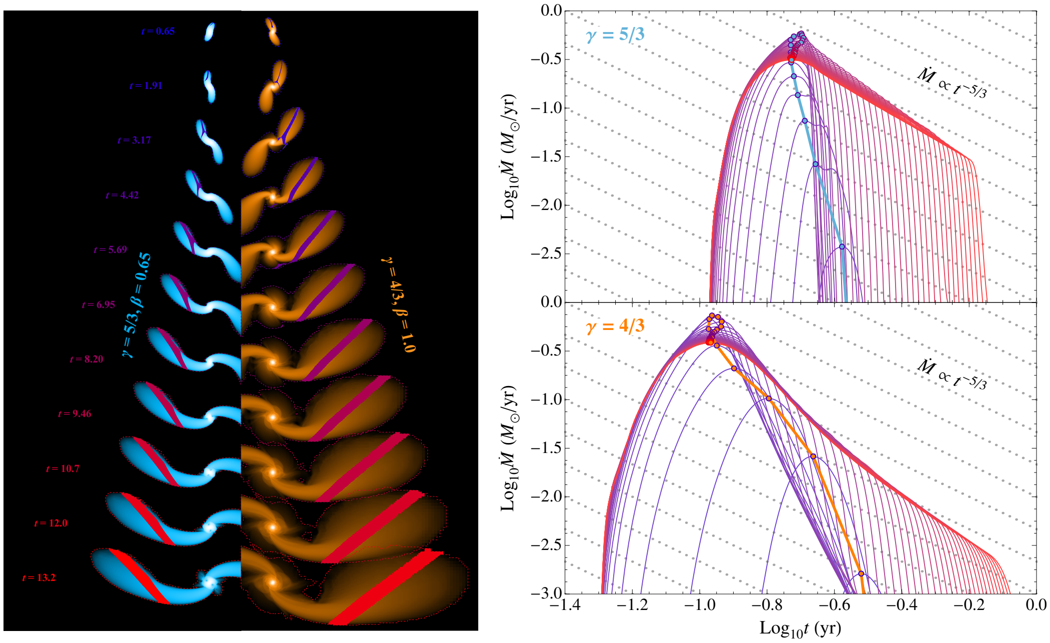

Figure 5.9: The left panel shows a collage from two simulations of the regions that contain the mass that contributes to $\dot{M}_{\rm peak}(t)$, super-imposed over the density distribution of the each snapshot. The fill and outline color denotes the time of the snapshot after pericenter, with blue corresponding to $t = t_{\rm p}$, and red corresponding to $t = t_{\rm p} + 2 \times 10^4$. Snapshots are shown from two different disruption simulations that have similar values of ΔM, with light blue showing the disruption of a $\gamma = 5/3$ star for $\beta = 0.65$, and orange showing the disruption of a $\gamma = 4/3$ star for $\beta = 1.0$. Each fill region shows the material that contributes to the part of $\dot{M}$ that is within 90% of $\dot{M}_{\rm peak}(t)$. The right panel shows the values of $\dot{M}$ derived from these two simulations (one curve per snapshot), with the colors of each curve corresponding to the color of the fill regions of each snapshot. The solid lines correspond to $\gamma = 5/3$, and the dashed lines corresponding to $\gamma = 4/3$, with the thick light blue and orange lines being fitted to $\dot{M}_{\rm peak}(t)$.

where $m \leq 1$, the resulting asymptotic power-law is

$$n_\infty = \frac{2}{3m} - \frac{7}{3} \tag{5.7}$$

where $n_\infty = -5/3$ is recovered for the standard linear relationship. If $m < 0$, this implies that E actually decreases with x, and thus the most bound material would initially lie interior to the least bound. As the most bound material would have to cross beyond the least bound, we expect that any $m < 0$ relationship would be quickly flattened to at least $m = 0$ by pressure gradients, resulting in a limit on the asymptotic slope of $n_\infty \geq -7/3$.

For disruptions that are just deep enough to destroy the star (i.e. $\beta = \beta_{\rm d}$), n_∞ can be somewhat less steep than -5/3. This implies that $m > 1$; the relationship between E and x is super-linear. For this borderline case only, the release of material that eventually composes the decay tail of $\dot{M}$ is moderated by the slow shrinkage of the stellar core, which is not fully destroyed until after the star has passed pericenter. For these encounters, r and x are somewhat dependent, with the material being released at the smallest x being launched at large r, and thus the quantity x/r^2 can be $\propto x^{>1}$.

Finally, for deep encounters, n_∞ again seems to be consistent with -5/3. Unlike the borderline case where a core persists long after pericenter, here the core is rapidly destroyed, and the energy is again set at a fixed r. As there is no core to resist the tidal force, the energy spread is simply given by the spread in potential energy across the star, à la the freezing model.

5.3.3 The Influence of Stellar Structure

A seemingly counter-intuitive result in the context of the freezing model is the fact that less-centrally concentrated stars, which have more mass at larger radii, result in transient events that peak at later times than their more centrally concentrated brethren, even for events that yield the same ΔM. As shown in Section 5.3.1, the distance at which total disruption occurs is significantly deeper for centrally concentrated stars, which may explain some of the discrepancy. Consider what happens to a star in the approach to pericenter for two extreme

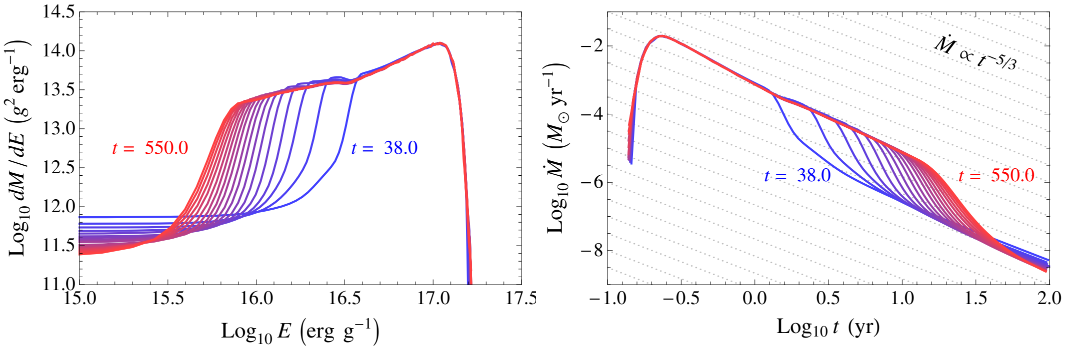

Figure 5.10: Evolution of dM/dE (left panel) and $\dot{M}$ (right panel) for the disruption of a star with polytropic index $\gamma = 5/3$ and impact parameter $\beta = 0.55$. The measured mass distribution in both plots is shown as a function of time relative to the time of pericenter, with the blue curves indicating early times and the red curves showing late times. The right-hand plot is overlaid on a series of dotted gray lines showing the fiducial $\dot{M} \propto t^{-5/3}$ evolution. While the early-time $\dot{M}$ can be determined shortly after the disruption, the rate of fallback still evolves for $t \gtrsim 10$ yr even after the simulation has been allowed to run for many hundreds of dynamical timescales.

cases: A case in which most of the star's mass is concentrated at its center, and a case in which the star has near-constant density. In the centrally-concentrated example, the star's outer layers will find that their dynamics are partly determined by the tidal force at early times, but also partly determined by the core, which remains initially undisturbed (Figure 5.8). The influence of any surviving core on the dynamics of the matter can thus affect the final binding energy E.

The left panel of Figure 5.9 shows that one of the fundamental assumptions of the freezing model, that the binding energy E and the distance from the star's core x are linearly related, is not correct, and matter that contributes to a particular E is drawn from a range in x that spans nearly the entire star. In Figure 5.9 we compare two disruptions with nearly identical ΔM for $\gamma = 4/3$ and $\gamma = 5/3$. The left panel shows the time evolution of the material that determines the peak of $\dot{M}$, with the contour colors corresponding to the same times after pericenter. The filled contours show the regions that contribute to $\dot{M}_{\rm peak}$ within each snapshot. The expectation under the freezing approximation would be that all mass that possesses a given energy E comes from a cylindrical cross-section of the star, but as illustrated in Figure 5.9 the geometry of the debris that contributes to $\dot{M}_{\rm peak}$ is clearly not cylindrical. The right panel shows the $\dot{M}$ that correspond to these snapshots. For the earliest snapshots (light blue-filled contours), the material in the $\gamma = 5/3$ simulation appears to have a head-start over the centrally-concentrated case, despite the fact that the $\gamma = 4/3$ encounter is 50% deeper ($\beta = 1.0$ for $\gamma = 5/3$ versus $\beta = 0.65$ for $\gamma = 4/3$). However, as the encounter progresses, the peak of $\dot{M}$ for $\gamma = 4/3$ moves to progressively earlier times relative to $\gamma = 5/3$, eventually settling to a value that results in a faster transient.

This implies that the binding energy of these layers relative to the black hole should not be recorded assuming the star has preserved its original spherical shape and size. While less material is positioned near the black hole when comparing the centrally-concentrated case to the constant density case, the core of the star continues to interact with the debris, and effectively "carries" material to larger E before E has been fixed. For constant density stars, the tidal force and the self-gravitational force scale to the same power in x, and the core is disrupted at approximately the same time as the outer layers, which is consequently why these stars are destroyed at a distance that more closely matches the classical Roche result. In this case, the assumption that E can be determined by considering the star's original size and shape is more appropriate, as little stellar material is carried closer to the black hole, as is found in the centrally-concentrated case.

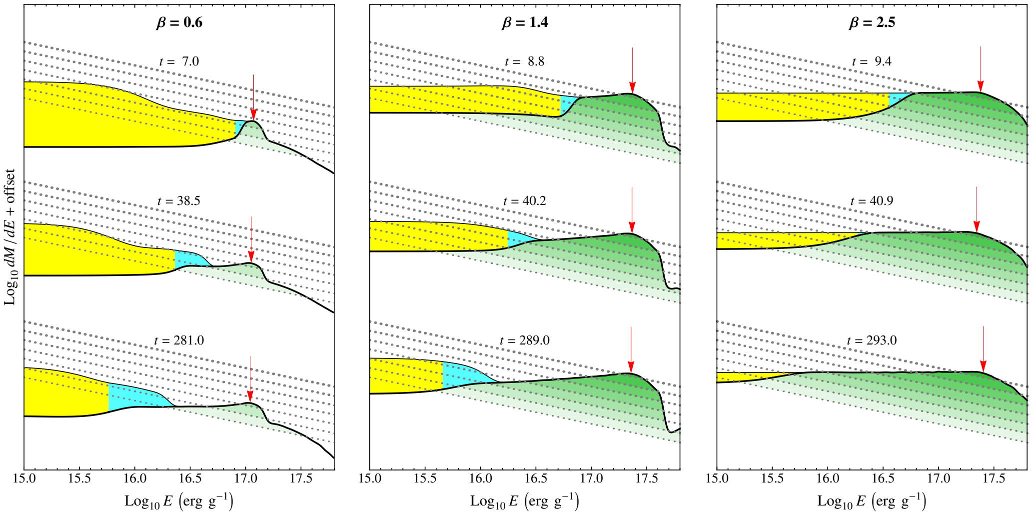

Figure 5.11: Distribution of mass as a function of binding energy E for three different simulations of a $\gamma = 4/3$ disruption for $\beta = 0.6$, 1.4, and 2.5. Shown in each panel is a sequence of mass distributions in time, with the evolution in time progressing from top to bottom, where the yellow regions show all material that remains bound to the black hole, and the green regions show material bound to the black hole but *not* bound to the star. The cyan region shows material that is bound to the star, but whose semi-major axis larger than the distance defined by the surviving core's time-dependent Hill sphere, $a_{\rm H}(t)$. The green regions are separated by the gray dotted curves into sub-regions where the resulting accretion rate $\dot{M}$ exceeds, from lowest to highest, 10^{-6}, 10^{-5}, 10^{-4}, 10^{-3}, 10^{-2}, 10^{-1}, and 1 $M_{\odot}$/yr. The red arrows show the location within the material bound to the black hole which determines the peak accretion rate $\dot{M}_{\rm peak}$.

5.3.4 Long-term evolution of $\dot{M}$

While the peak of the accretion rate is determined within tens of stellar dynamical timescales, the tail of $\dot{M}$ continues to evolve for hundreds of dynamical timescales. Most notably, a large "cavity" in $\dot{M}$ is present for accretion times $t > t_{\rm peak}$ (Figure 5.10), which gradually fills from left to right as additional material in the tidal debris tails satisfies the simple energy criteria applied to determine if matter is bound to the black hole. An example of the long-term evolution of $\dot{M}$ arising from this interaction is shown in Figure 5.10, where $\dot{M}$ is not determined for $t \gtrsim 10$ years until 550 dynamical timescales after the disruption. As the star recedes from the black hole, the evolution of $\dot{M}$ slows (as indicated by the decreasing space between the curves in Figure 5.10), implying that progressively longer simulation times are required to determine $\dot{M}$ much beyond $t_{\rm peak}$.

The cavity arises from the exclusion of material within the debris stream that remains bound to the stellar core after the encounter, with the evolution coming as a result of the continued interaction between either the stellar core (if the star survived the encounter) or a mildly self-gravitating debris stream (if it did not) and the black hole. An examination of the pressure of the debris tails reveals that the debris is free-streaming, even in the vicinity of the Hill sphere. In other words, the pressure gradients present within the stream are small enough to be incapable of modifying the material's trajectory. Thus, the interaction between the stream, black hole, and surviving core is purely gravitational.

In Figure 5.11 we show dM/dE for disruptions of a $\gamma = 4/3$ star for three values of β. As material that is considered to be bound to the star (yellow) crosses the time-dependent Hill sphere, it becomes bound to the black hole (green). We find that there is always some mass in the vicinity of the time-dependent Hill sphere $a_{\rm H}(t)$ (cyan) for encounters in which a core survives, whereas full disruptions do not show this behavior, mostly because the self-bound mass shrinks drastically as progressively less material satisfies the criteria for being self-bound.

As the star moves away from the black hole, the Hill radius grows, but by a rate that is a factor $(M_*/M_{\rm h})^{1/3}$ smaller than the rate at which the star recedes from the black hole. This implies that any material that retains a positive velocity relative to the surviving core after the encounter has the potential to be removed from the star, even if it is technically bound to the core (i.e. $v^2 < 2GM_{\rm core}/r$) at an earlier epoch. Much of the observed evolution of dM/dE may be due

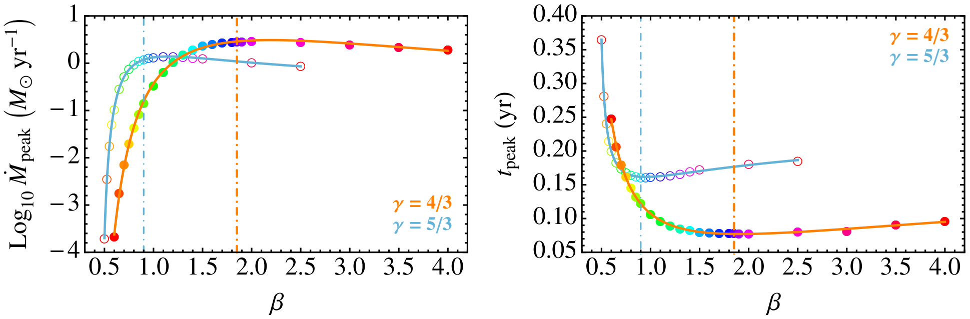

Figure 5.12: Fits to $\dot{M}_{\rm peak}$ and $t_{\rm peak}$, with the fits to the $\gamma = 4/3$ models being shown by the solid colored circles, and fits to the $\gamma = 5/3$ models being shown by the open colored circles. The color coding matches that of Figures 5.1 and 5.2, with the impact parameters $\beta_{\rm d}$ beyond which stars are considered to be destroyed being denoted by the colored dot-dashed lines.

to our definition for what is considered to be "bound" to the surviving core after the encounter (Section 5.2). Our calculation presumes that the energy budget of material with respect to the star is sufficient to determine what inevitably remains bound to the star; in reality the question of whether a given particle remains bound or not amounts to solving the restricted elliptical three-body problem, for which no closed-form solution exists. The Jacobi constant, which has a fixed value in the restricted circular three-body problem and can be used to determine the zones within which a particle of a given initial position and velocity can occupy (Murray and Dermott, 1999), is not constant once the orbit is non-circular (Hamilton and Burns, 1992).

However, while the energy balance approach may not be capable of immediately determining the mass that will eventually become bound to the black hole, the distribution only remains uncertain for material that is accreted far beyond $t_{\rm peak}$. In the limit that $t \to \infty$, the distance of the star to the black hole increases as $t^{2/3}$, and thus E for material leaving the Hill sphere is $GM_{\rm h}a_{\rm h}/r^2 \propto t^{-2/3}$. This explains the observed slowing of the evolution of $\dot{M}$.

The material that fills in the cavity assumes a distribution in E that is not entirely flat,

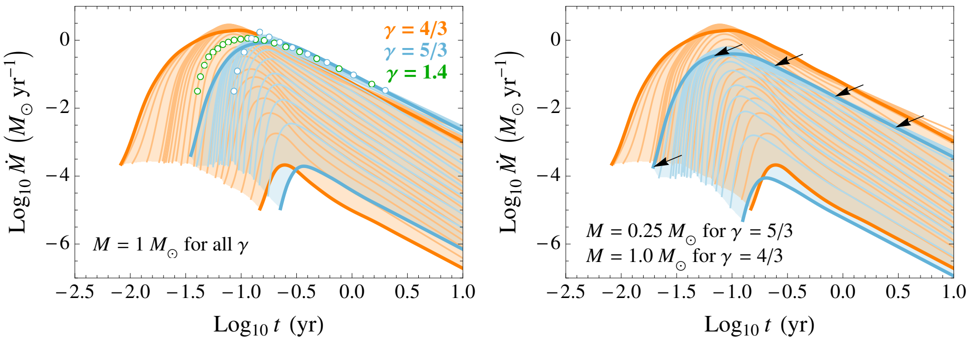

Figure 5.13: Comparison of the families of $\dot{M}$ curves for $\gamma = 4/3$ (orange) and $\gamma = 5/3$ (light blue). The left panel shows $\dot{M}$ derived from the simulations presented here as solid lines, assuming that the stars for both γ have mass $M = 1M_{\odot}$. The open circles show the numerical results of (Lodato *et al.*, 2009) for $\beta = 1$ and $\gamma = 1.4$ (dark green) and $\gamma = 5/3$ (light blue). The right panel shows the shift in $\dot{M}$ (black arrows) if the mass and radius of star that is expected to have a structure described by $\gamma = 5/3$ is taken into account (Tout *et al.*, 1996).

resulting in a fallback rate that scales to a power slightly steeper than the canonical $t^{-5/3}$. This energy distribution is likely set near pericenter, where the pressure component is comparable to the tidal component. As the star recedes from the black hole, the pressure component of the force decreases more quickly than the tidal component (Kochanek, 1994), and thus the debris is expected to evolve purely gravitationally. However, the conditions under which material is launched across the time-dependent Hill sphere may depend somewhat on the pressure gradient, no matter how small, as the net gravitational force is zero (Lubow and Shu, 1975).

5.4 Discussion

The results of our extensive parameter study produce a number of unexpected trends as compared to the predictions presented by previous work. In the previous section we attempted to explain the observed scalings, and how these features arise as a result of the interaction between the black hole and a potentially surviving stellar core. In what follows, we explain how these newly discovered features can be used to constrain the type of disrupted star and how it was disrupted.

5.4.1 Can γ and β be determined a posteriori?

Given our predicted $\dot{M}$, is it possible to determine either the stellar structure or the impact parameter from the light curve produced by a tidal disruption event? The conversion efficiency between mass accreted by the black hole and the light emitted is somewhat uncertain, and depends on factors such as the black hole's spin and how the accretion rate compares to $\dot{M}_{\rm Edd}$ (Ulmer, 1999; Beloborodov, 1999; Strubbe and Quataert, 2009; Lodato and Rossi, 2010). However, as the efficiency cannot be larger than unity, and as flares are typically observed in the decay phase, we can only place lower limits on the amount of mass accreted by a black hole to produce a given flare (Gezari *et al.*, 2008). Thus, at the very least, our predicted ΔM (Figure 5.4) can be used to exclude events for β less than some critical value, given the mass of the star.

Figures 5.7 and 5.12 present four additional quantities that enable us to classify tidal disruptions based on the properties of observed tidal disruption flares. Two of these quantities, $\dot{M}_{\rm peak}$ and $t_{\rm peak}$, are only available to us for flares in which the peak of the accretion rate is clearly observed (Gezari *et al.*, 2012), but both $n(t)$ and n_∞ are measurable for flares that are observed long after peak (Komossa and Greiner, 1999; Komossa *et al.*, 2004; Gezari *et al.*, 2006, 2008; Cappelluti *et al.*, 2009; van Velzen *et al.*, 2011; Cenko *et al.*, 2012). If the mass of the black hole is known with some certainty, one may be able to infer both M_* and β by simply measuring $\dot{M}_{\rm peak}$ and $t_{\rm peak}$ and comparing to our resultant $\dot{M}$, which at first glance appear to form distinct sequences for $\gamma = 4/3$ and $\gamma = 5/3$ stars (Figure 5.13, left panel). However, this is only true assuming that centrally concentrated stars have the same mass and radius as stars of near constant density. The transition from stars that are well-modeled by a $\gamma = 4/3$ polytrope to a $\gamma = 5/3$ polytrope is also accompanied by a decrease in radius such that all stars with mass $0.25M_\odot < M_* < M_\odot$ have the same central density (Kippenhahn and Weigert, 1990). Adjusting the radii and mass of our $\gamma = 5/3$ models to the mass and radius of a $0.25M_\odot$ star (Tout *et al.*, 1996), we find that the sequence of $\dot{M}$ functions for $1.0M_\odot$ and $0.25M_\odot$ stars lie on top of each other (Figure 5.13, right panel), making the determination of the disrupted mass of a star somewhat degenerate with its structure.

This motivates us to look for other features of $\dot{M}$ that may uniquely identify either γ or β. If we consider the power-law of the rate of decline n after peak, we find that there is a distinguishing feature between $\gamma = 5/3$ and $\gamma = 4/3$ models at ~ 0.5 dex after $t_{\rm peak}$. Whereas $\gamma = 5/3$ stars quickly converge to $n \simeq -5/3$, $\gamma = 4/3$ models show a characteristic drop, with n being as large as -4 for some encounters (Figure 5.7, left panel). This feature is most prominent for intermediate β in which $\sim 50\%$ of the star's mass is removed during the encounter, and represents the strong influence of the dense stellar core, which acts to drag material deeper within the black hole's potential before tidal forces are capable of removing it.

In addition to being more centrally-concentrated to begin with, an additional component that likely contributes to this observed drop is the adiabatic response of the surviving core. For $\gamma = 5/3$ stars, the removal of mass results in the inflation of the star, whereas $\gamma = 4/3$ exhibit the opposite behavior, shrinking dramatically in response to the loss of mass (Hjellming and Webbink, 1987). This enhances the core's influence during the encounter in the phase where the core's mass is changing, slowing the reduction in the core's effective gravity, and thus pulling even more matter to higher binding energies. The recently observed flare PS1-10jh presented in Gezari *et al.* (2012) shows a clear drop in the accretion rate with respect to the canonical $t^{-5/3}$ decline rate expected from the freezing model. In the freezing model, it is impossible to produce a decline feature steeper than $t^{-5/3}$ within any part of $\dot{M}$, as we explained in Section 5.3.2. As many tidal disruption flares may show this characteristic drop in $\dot{M}$, a clearly-resolved peak can be used to compare to the subsequent decay phase for a precise determination of $n(t)$.

For events in which the peak is not clearly observed, and for which the signal-to-noise is too small to permit an accurate determination of $n(t)$, the asymptotic slope n_∞ of $\dot{M}$ can still provide additional information about the star that was disrupted. As shown in the right panel of Figure 5.7, n_∞ can be used to distinguish between partial and full disruptions. The fact that n_∞ assumes values that are significantly steeper than -5/3 may indicate that additional tidal disruption flares have been found observationally, but subsequently discarded and/or ignored due to the mismatch between the measured n and $-5/3$ (van Velzen *et al.*, 2011). This implies that some supernovae that have been observed at the centers of galaxies may in fact be misidentified partial tidal disruptions.

5.4.2 Future work

As found in previous work (see Chapter 4, also see Faber *et al.*, 2005; Guillochon *et al.*, 2011), there is a change in surviving star's orbital energy after the encounter, with the change in energy being comparable to the star's initial self-binding energy. This change in energy, combined with the star's initial orbital energy, leads to a shift in the entire dM/dE distribution, which can affect the fallback of material for $E \sim \Delta E_{\rm orb}$, or for $t \gtrsim M_{\rm h} R_*^{3/2} G^{-1/2} M_*^{-3/2} \sim$ 100 years, given that $\Delta E_{\rm orb} \sim GM_*/R_*$. As the star's initial orbital energy may not be zero and can be comparable to ΔE itself, and thus the final binding energy of the star depends on its initial orbital energy, we have presented our dM/dE and $\dot{M}$ curves with this change in energy removed. As a result, our plots show the fallback rate that would be expected if the final star were to remain on a parabolic trajectory, as our initial conditions assume. While these kicks that are typically of the order of star's own escape velocity may be important in determining the further fate of the star and whether it will suffer additional disruptions, they are not expected to affect the first century of a flare's evolution, of which only the first few years are accessible to currently available transient surveys.

Even if $\dot{M}$ is directly related to the properties of the star being disrupted, the luminosity of the accretion disk L may not directly follow $\dot{M}$. The primary factors that affect the link between $\dot{M}$ and the bolometric L are the viscous evolution of the disk and the size of the disk (Ramirez-Ruiz and Rosswog, 2009), although other processes may strongly affect the amount of light observed in a single band, especially in the optical/UV where dust extinction can play a vital role. Disk viscosity can only affect L for $t \lesssim \tau_{\rm visc}$, in which its primary affect is to delay emission at early times. However, once $t > \tau_{\rm visc}$, L is expected to track $\dot{M}$ closely. As the material is delivered to the disk at $r \simeq r_{\rm p}$, the ratio of $\tau_{\rm visc}$ to $t_{\rm peak}$ is

$$\frac{\tau_{\rm visc}}{t_{\rm peak}} = 3.2 \times 10^{-2} \beta^{-3} \left(\frac{B_\gamma(\beta)}{0.1} \right)^{-1} \times \left(\frac{M_{\rm h}}{10^6 M_\odot} \right)^{-1/2} \left(\frac{\alpha}{0.1} \right)^{-1} \left(\frac{M_*}{M_\odot} \right)^{1/2}, \tag{5.8}$$

where B_γ is a fitted parameter derived from our simulations, ($B_\gamma \sim 0.1$ for most β, see Appendix B) and α is the parameterized α-disk scaling coefficient, where we have taken the scale-height ratio $h/r = 1$. If $\tau_{\rm visc}/t_{\rm peak} \gtrsim 1$, the accretion is spread over longer timescales, resulting in a power-law decay index $n = -1.1$ (Cannizzo *et al.*, 1990). This may affect the light curve shape in the earliest phases of the fallback (prior to peak) where $t \ll \tau_{\rm visc}$, and thus the early evolution of $L(t)$ may not follow the functional forms of $\dot{M}$ presented here for $t \ll t_{\rm peak}$. But as observations of tidal disruption flares in the decay phase seem to be consistent with the canonical $n = -5/3$ decay law, it is clear that $\dot{M}$ and $L(t)$ must be closely coupled on year-long timescales.

An ingredient that the set of simulations presented in this chapter do not include is the inclusion of general relativistic effects, which become important for very deeply penetrating encounters. Qualitatively, for both spinning and non-spinning black holes, general relativity is expected to result in more mass loss and a spreading of mass in dM/dE as compared to Newtonian encounters, as its primary effect is to bend the star's path such that it spends a larger fraction of time near the black hole where tidal forces are important (Luminet and Marck, 1985; Kobayashi *et al.*, 2004). The only numerical provenance for how the metric may affect the feeding rate comes from low-resolution simulations performed by Laguna *et al.* (1993), which find a slight increase in $\dot{M}_{\rm peak}$ for increasing β, but much less than the predicted β^3 scaling. If the black hole has non-zero spin, the resulting dM/dE depends on the orientation of the star's angular momentum vector as compared to the black hole's spin vector (Haas *et al.*, 2012).

A spinning black hole permits deeper encounters that don't result in the star being immediately swallowed (Kesden, 2012b), provided that the two angular momentum vectors are aligned, and also should affect the final binding energy distribution, with co- and counter-rotational encounters resulting in smaller and larger ΔM, respectively (Diener *et al.*, 1997; Ivanov and Chernyakova, 2006; Kesden, 2012a). However, as the fraction of disruptions in which non-Newtonian metrics can affect the dynamics is $\sim r_{\rm s}/r_{\rm t}$, which is $\sim 5\%$ for a $10^6 M_\odot$ black hole and $\sim 20\%$ for a $10^7 M_\odot$ black hole, the majority of tidal disruption events are well-represented by a Newtonian approximation to the black hole's gravity.

Lastly, the absence of hydrogen in spectra taken of the tidal disruption event PS1-10jh (Gezari *et al.*, 2012) strongly suggests that the disruption of stars that are not on the MS may contribute significantly to the overall rate of tidal disruption. As we show, the structure of the star that is disrupted is clearly imprinted upon $\dot{M}$, providing valuable additional information that can be used to distinguish between candidate disruption victims. We explore the disruption of post-MS stars in a companion paper using a method similar to what is presented here (MacLeod *et al.*, 2012).

The discovery of flaring black hole candidates in nearby galaxies will continue to elucidate the demography of the AGN population (De Colle *et al.*, 2012). Whereas AGN are supplied by a steady stream of fuel for hundreds or even thousands of years, tidal disruptions offer a unique opportunity to study a single black hole under a set of conditions that change over a range of timescales. There are, of course, rapidly varying stellar-mass black hole candidates in

X-ray binaries within our own Galaxy. But for SMBHs, tidal disruption events offer the firmest hope of studying the evolution of their accretion disks for a wide range of mass accretion rates and feeding timescales. The simulations and resultant $\dot{M}$ curves presented here are crucial for determining the properties of the black hole itself, as an incomplete model of a stellar disruption can result in much uncertainty in how the black hole converts matter into light. For a disruption with a well-resolved light curve, our models permit a significant reduction of the number of potential combinations of star and black hole properties, enabling a better characterization of SMBHs and the dense stellar clusters that surround them.

Chapter 6

PS1-10jh: The Case for the Disruption of a Solar-Type Star

6.1 Introduction

The tidal disruption of a star by a supermassive black hole (SMBH) splits the star into either two or three ballistically distinct masses. In the event of a full disruption, the star is split into two pieces of nearly-equal mass. One half of the star becomes bound to the black hole after the encounter, and continues along elliptical trajectories with pericenter distances equal to the star's original pericenter distance. The other half of the star gains orbital energy in the encounter, and is placed on hyperbolic trajectories. For a partial disruption, a third mass in the form of a surviving stellar core emerges from the encounter, with the absolute value of its orbital energy comparable to its own binding energy (see Chapter 4, also see Faber *et al.*, 2005; Guillochon *et al.*, 2011; MacLeod *et al.*, 2012; Liu *et al.*, 2013).

Determining the fates of these pieces of the star are critical in determining the appearance of the flare that results from the immense gravitational energy that will be released by the accretion disk that eventually forms. Previously, it has been assumed that the unbound material, which was thought to be a wide "fan," was the primary contributor to the broad emission lines that are produced as the result of a tidal disruption (Strubbe and Quataert, 2009; Kasen and Ramirez-Ruiz, 2010; Clausen and Eracleous, 2011). For the tidal disruption event (TDE) PS1-10jh, it was assumed that hydrogen, which is ejected to large distances within the wide debris fan generated by the disruption, can recombine more quickly than the rate at which it is ionized by the central source (Gezari *et al.*, 2012, hereafter G12). This would ensure that the vast majority of the hydrogen is neutral, and thus any ionizing radiation incident upon the fan would produce an emission feature. The absence of any hydrogen emission features was used to derive an upper limit on the amount of hydrogen present, implying that helium is five times more common than hydrogen by mass with the disrupted star.

In this chapter, we present three-dimensional hydrodynamical simulations that show that the assumption that this debris fan intercepts a significant fraction of the light is incorrect. As noted by Kochanek (1994), the width of the stream of unbound material is still controlled by the stream's self-gravity in the transverse direction, restricting its width to only be a fraction of the star's original pericenter distance. Through numerical simulations of fully-disruptive encounters with mass ratios $q \equiv M_{\rm h}/M_{\odot} = 10^3$ and 10^6, we verify that the transverse containment of the stream's width does indeed occur (Figure 6.1). As a result, the stream only grows in the radial direction, and thus the total volume and surface area increase only slightly more steeply than $v_{\rm p}$. The surface area of this structure is not significant enough to produce hydrogen emission lines, even for the disruption of a main-sequence (MS) star composed largely of hydrogen.

But while we find that the area of the unbound debris has been vastly overestimated, we also find that the area occupied by the accretion disk formed from the bound material has been vastly underestimated. Our numerical simulations confirm the prediction that material that returns to pericenter is ballistically launched to very large distances from the black hole, hundreds of times $r_{\rm p}$. Additionally, we find that significant dissipation occurs when this material returns to pericenter. As the debris stream quickly virializes at pericenter and the density of the material is significantly reduced as compared to the star's original density, self-gravity is suppressed even in the transverse direction. As a result, a fan structure *is* formed once material returns pericenter. But as this material belongs to the fraction of the original star that is strongly bound to the black hole, the radial extent of this material grows at a rate that is significantly smaller than the unbound fraction.

As the region in which Hα is produced in steady AGN is on the order of a few light days from the black hole (Peterson, 2006), we show that it is very unlikely that the debris ejected by the disruption has traveled the distance necessary to produce an Hα line for PS1-10jh. Through comparison with the processes responsible for producing the broad line regions (BLRs) of steadily-accreting AGN, we predict that the helium lines that are observed in PS1-10jh are produced much closer to the black hole (Bentz *et al.*, 2010), and the debris has sufficient time to reach this distance by the time the first spectrum was observed. Motivated by the results of our hydrodynamical simulations, we model the accretion disk structure and use a Markov-Chain Monte Carlo (MCMC) procedure to determine the combinations of parameters with the highest-likelihood, and we find that the highest-likelihood models involve the disruption of a low-mass main-sequence star with mass $\sim 0.5 M_{\odot}$ by a $M_{\rm h} = 10^7 M_{\odot}$ black hole.

In Section 6.2 we describe our method for running hydrodynamical simulations to characterize the behavior of the debris stream after a disruption, and describe the maximum likelihood analysis we employed to estimate the parameters of PS1-10jh. In Section 6.3 we present a physical interpretation of the results of our hydrodynamical simulations. Bearing these results in mind, we develop our generalized model for the time-dependent, broadband light that would accompany the disruption of a star in Section 6.5. We then apply this model specifically to PS1-10jh in Section 6.6. Finally, we review additional evidence as to why the disruption of a helium-rich star is unlikely to have produced PS1-10jh in the first place, and look towards the future when TDEs will be regularly observed.

6.2 Method

6.2.1 Hydrodynamical Simulations

The black hole at the center of our own galaxy is estimated to be $\simeq 4 \times 10^6 M_{\odot}$ (Ghez *et al.*, 2008), and is one of the smallest known massive black holes (Gültekin *et al.*, 2009). As the mass of an average main-sequence star is $\sim 0.1 M_{\odot}$ (Kroupa *et al.*, 1993), the majority of stellar tidal disruptions will have $q \gtrsim 10^6$. For such disruptions, the timescale of return of the most bound debris is on the order of days to weeks (Rees, 1988), with the peak fallback rate occurring approximately one month after the time of the disruption (see Chapter 5, also see Evans and Kochanek, 1989; Lodato *et al.*, 2009; Guillochon and Ramirez-Ruiz, 2013).

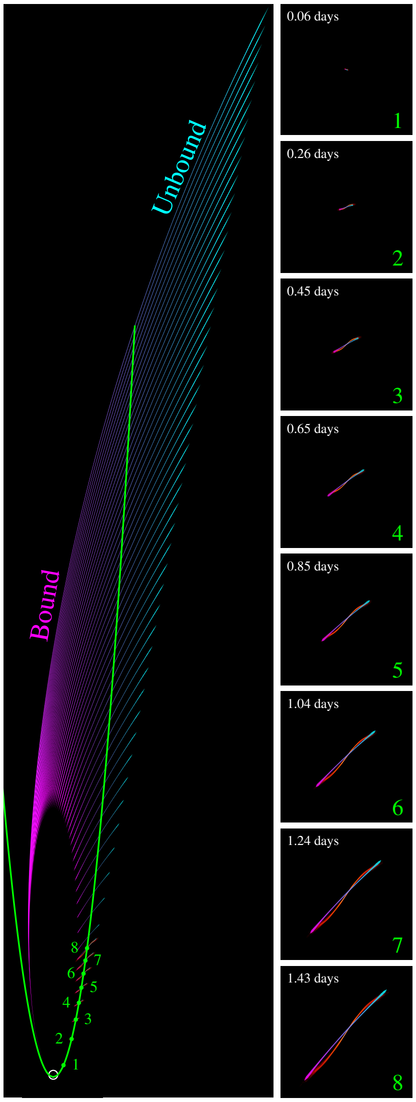

Figure 6.1: Snapshots from a tidal disruption simulation with $M_* = M_\odot$, $M_\mathrm{h} = 10^6 M_\odot$, and $\beta = 1.8$, as compared to a simple model of a tidally-confined debris stream with self-gravity, where we assume that the width of the stream scales as $r^{1/4}$ (Kochanek, 1994). The left panel shows a superposition of the debris stream at different times, with the longest stream depicting the time when the most bound material returns to pericenter at $t = 42$ days. The color along the stream indicates whether it is bound or unbound from the SMBH, with magenta corresponding to bound and cyan corresponding to unbound. The green line shows the original path of the star, and the green circles show the locations of the surviving core corresponding to the eight snapshots shown on the right-hand side of the figure. In each of the right-hand panels, the simple model of the debris stream is shown atop the results from the simulation.

For hydrodynamical simulations of TDEs, the main limiting factor is the sound-crossing time of the star, which for a solar mass star is approximately one hour. Given an initial stellar model that occupies 100^3 grid cells, each hydrodynamical time-step translates to only one minute of physical time. Thus, the simulation of the tidal disruption of a solar mass star by a $10^6 M_\odot$ black hole that includes the time at which the fallback rate is at a maximum requires $\sim 10^5$ time-steps. Additionally, the debris stream resulting from the disruption must be fully resolved in both length and in width. As the stream is self-gravitating (as described in Section 6.3.1), it mains a very narrow profile, with the aspect ratio of the stream when the first material returns to pericenter being $q^{1/3}(t_{\rm peak}/t_{\rm p})^{1/2} \sim 10^3$, where $t_{\rm peak}$ is the time where $\dot{M}$ reaches a maximum, and $t_{\rm p}$ is the pericenter crossing time. If the number of grid cells across the stream is forced to be at least 20, which is necessary to satisfy the Truelove *et al.* (1997) criteria, then 10^6 grid cells would be required to be evolved for 10^5 time-steps.

This means that a complete simulation of the full problem within a single simulation is very computationally expensive. Instead, we run two separate simulations that are each well-equipped to describe the behavior of the debris stream at two different epochs. To determine the fate of the debris liberated from a star during a tidal disruption, we used two similar simulation setups, differing only in the mass ratio q. The first simulation sets $q = 10^6$ and solely focuses on the evolution of the debris stream as it expands away from pericenter after the star's initial encounter with the black hole. Because of the computational expense, the return of the debris to pericenter is not followed in this simulation. The second simulation sets $q = 10^3$, and follows the return of the debris to pericenter well beyond the peak in the accretion rate $\dot{M}_{\rm peak}$. In these encounters, the peak accretion rate is realized only one day after pericenter, and we follow the evolution of the returning debris for a total of 5×10^5 seconds (about one week). Our hydrodynamical simulations were performed in a module written for the `FLASH` adaptive mesh refinement code, the details of which can be found in Chapters 2, 4, and 5 (also see Guillochon *et al.*, 2009, 2011; Guillochon and Ramirez-Ruiz, 2013).

The initial conditions of the simulation are similar to those presented in Chapter 4, with the polytropic Γ that describes the star's structure being set to 5/3, and the impact parameter β being set to 2. The star is placed on a parabolic trajectory at an initial position that is several times further than $r_{\rm t}$, and is initially resolved by 50 grid cells across its diameter. As realistic equations of state are only sensical at the full-scale of the problem, the hydrodynamics of the gas are treated using a simple adiabatic polytrope $P \propto \rho^{\gamma}$, where γ is the adiabatic index. The code utilizes the adaptive-mesh functionality of the `FLASH` software in different ways for the two simulations. In the $q = 10^3$ simulation, regions which are less than 10^{-1} times as dense as the current peak density are derefined, but maximum refinement is maintained within $4r_{\rm p}$ at all times. For the $q = 10^6$ simulation, each refinement level is assigned to a single decade in ρ, using the star's original central density $\rho_{\rm c}$ as a baseline, with the exception of the first refinement threshold which is set to $\rho = 5 \times 10^{-3}\rho_{\rm c}$.

As both the timescales and the length scales of a $q = 10^3$ disruption are different from those of the more typical $q = 10^6$ disruption, care must be taken when interpreting the results from these simulations and attempting to scale them up to what would be realized for larger mass ratios. As we will describe in Section 6.3.2, the dissipation processes that are observed in the scaled-down simulation are analogous to other dissipation mechanism that operate for larger values of q, given the proper scaling.

6.2.2 Fitting TDE Observations

For fitting our models for tidal disruptions to observed events, we have developed the code `TDEFit`, which performs a maximum likelihood analysis using an affine-invariant MCMC (Goodman and Weare, 2010; Foreman-Mackey *et al.*, 2013). The code is written in Fortran and utilizes the parallel variant of the algorithm presented in Foreman-Mackey *et al.*. We have designed the software to be flexible in the model parameters it accepts as inputs, any free parameter (either discrete or continuous) can be included in the parameter space exploration by simply listing it and its range of acceptable values within a parameter file. In the same way, both trivial and non-trivial priors can be specified at runtime for single or combinations of input parameters.

As the solutions can often be multi-modal, with small regions of acceptable parameter space separated by large voids of poor parameter space, it can sometimes be difficult to find the deepest global minimum using the vanilla affine-invariant algorithm. We have improved upon this algorithm by performing simulated annealing (SA, Press *et al.*, 1986) on a fraction F of the walkers every N timesteps during a "bake-in" period, where both F and N are adjustable. Each walker that is selected to anneal is used to seed an amoeba whose points are randomly drawn a small distance away from the original walker, these "frackers" then run through a full SA cycle in which the temperature is gradually reduced until they are unable to improve upon their local solution.

This enables the depths of local minima to be found more quickly, and in tests we have found that this improves the time of convergence to the global solution by orders of magnitude.

Additionally, we anneal the ensemble of walkers themselves during the bake-in period, using the temperature schedule proposed in Hou *et al.* (2012), and periodically compare the scores of walkers to the best so far, removing those that fall below a pre-determined threshold that depends on the current annealing temperature. After the bake-in period, the algorithm reverts to the vanilla affine-invariant MCMC and run for several autocorrelation times, ensuring that detailed balance is maintained.

As inputs to this method, we use the full functional forms of the fallback rate (parameterized as $\dot{M}_{\rm sim}$, see Figure 5.5) for $\gamma = 4/3$ and $\gamma = 5/3$ polytropes. We assume that as the mass ratio $q \gg 1$, the dependence of $\dot{M}$ on $M_{\rm h}$, M_*, and R_* is self-similar,

$$\dot{M} = M_{\rm h,6}^{-1/2} M_{*,\odot}^{2} R_{*,\odot}^{-3/2} \dot{M}_{\rm int}(\beta), \tag{6.1}$$

where $10^6 M_{\rm h,6} = M_{\rm h}$, $M_\odot M_{*,\odot} = M_*$, $R_\odot R_{*,\odot} = R_*$ and $\dot{M}_{\rm int}$ is an interpolation of $\dot{M}_{\rm sim}$, defined below. We can eliminate R_* in this expression by using known mass-radius relationships (e.g. Tout *et al.* 1996 for MS stars or Nauenberg 1972 for white dwarfs). For MS stars, we presume that all objects with $M_* \leq 0.1 M_\odot$ have the radius of a $0.1 M_*$ star. With these relations, $\dot{M}$ is solely a function of $M_{\rm h}$, M_*, and β.

As the simulations of Chapter 5 are only run for specific values of β, we determine intermediate β solutions by rescaling neighboring simulations in β-space to the same scaled time variable $x \equiv (t - t_{\rm min})/(t_{\rm max} - t_{\rm min})$, where $t_{\rm min}$ and $t_{\rm max}$ are the minimum and maximum times for each $\dot{M}_{\rm sim}$ curve, and then interpolating linearly between the two solutions,

$$\lfloor \beta \rfloor = \min \{ B \in \beta_{\rm sim} \mid B \geq \beta \} \tag{6.2}$$

$$\lceil \beta \rceil = \max \{ B \in \beta_{\rm sim} \mid B \leq \beta \} \tag{6.3}$$

$$\begin{aligned} \dot{M}_{\rm int}(\beta, x) = {} & \dot{M}_{\rm sim}(\lfloor \beta \rfloor, x) \\ & + \frac{\beta - \lfloor \beta \rfloor}{\lceil \beta \rceil - \lfloor \beta \rfloor} \left[\dot{M}_{\rm sim}(\lceil \beta \rceil, x) - \dot{M}_{\rm sim}(\lfloor \beta \rfloor, x) \right], \end{aligned} \tag{6.4}$$

where $\beta_{\rm sim}$ is the set of all β for which a simulation is available, and where $\lfloor \beta \rfloor$ and $\lceil \beta \rceil$ return the values of $\beta_{\rm sim}$ that bracket β. We find this preserves the overall shape of the $\dot{M}$ curves well for values of β for which a simulation is not available, as long as the sampling in $\beta_{\rm sim}$ is sufficiently dense to capture the overall trends.

The objective function used within `TDEFit` when comparing our models to the data is the maximum likelihood function,

$$\ln \mathcal{L}_{\rm LC} = \sum_{i=1}^{n} \left[\frac{\left(V_{{\rm obs},i} - V_{{\rm mod},i} \right)^2}{\left(\sigma_{{\rm obs},i}^2 + \sigma_{\rm v}^2 \right)} + \ln \left(\sigma_{{\rm obs},i} + \sigma_{\rm v}^2 \right) \right], \tag{6.5}$$

where n is the number of datapoints, $V_{{\rm obs},i}$ and $V_{{\rm mod},i}$ are respectively the AB magnitude at the ith datapoint for the observation and the model, $\sigma_{{\rm obs},i}$ is the measurement error associated with the ith datapoint, and $\sigma_{\rm v}$ is the intrinsic variability of the source, assumed to be a constant that scales with black hole mass (see Section 6.5.1).

6.3 Hydrodynamics of Post-Disruption Debris

6.3.1 Debris Stream with Self-Gravity

Determining the fate of the various pieces of the star after a disruptive encounter is critical in determining the appearance of the flare that results from the immense gravitational energy that will be released by the accretion disk that eventually forms. Previously, it has been assumed that self-gravity of the disrupted star is unimportant, and therefore the spread in energy imparted to the debris at pericenter leads to a spread in angle as well as semi-major axis (Strubbe and Quataert, 2009; Kasen and Ramirez-Ruiz, 2010). Under this assumption, the unbound debris is a homologously expanding structure, which occupies a constant solid angle and whose volume increases proportional to $v_{\rm p}^3$.

However, Kochanek (1994) showed that the stream can be in fact gravitationally confined in the transverse direction by self-gravity and forms a very thin structure (Figure 6.1), with a width Δ and height H that scale as $\tilde{r}^{1/4}$ for $\gamma = 5/3$, where $\tilde{r} \equiv r/r_{\rm t}$. For general γ,

$$H^2 \Lambda^{\frac{2-\gamma}{\gamma-1}} \propto \text{constant} \tag{6.6}$$

where Λ is the mass per unit length (Ostriker, 1964), which we define to be $\Lambda = M_*/2R_*$ at $t = t_{\rm d}$. Assuming that $\Lambda \propto r^{-1}$ (Kochanek, 1994),

$$H = R_* \tilde{r}^{\frac{2-\gamma}{2\gamma-2}}, \tag{6.7}$$

where we recover $H \propto \tilde{r}^{1/4}$ for $\gamma = 5/3$.

In the right eight panels of Figure 6.1, we superimpose the results of our hydrodynamical simulations of the disruption of a star by a black hole with mass ratio $q = 10^6$ with this simple prescription. We find excellent agreement between the prediction of Kochanek and our results over the time period in which we ran the simulation. The thinness of the stream is also noted in other hydrodynamical simulations in which the mass ratio is large (Rosswog *et al.*, 2009b; Hayasaki *et al.*, 2012).

The surface area of this structure for $\gamma = 5/3$ is

$$\begin{aligned} A_{\rm s} &= \frac{2\pi R_*^2 q^{1/3}}{\beta}\int_1^{r_{\rm u}/r_{\rm p}} \tilde{r}^{1/4} d\tilde{r} \\ &\simeq 1.4\times 10^{-2} M_6^{1/3}\beta^{7/8}\left(\frac{t}{t_{\rm ff}}\right)^{5/4} {\rm AU}^2, \end{aligned} \tag{6.8}$$

where $r_{\rm u} \simeq r_{\rm t}\beta^{1/2}(t/t_{\rm ff})$ is the distance to which the most unbound material has traveled (Strubbe and Quataert, 2009), and $t_{\rm ff} \equiv \pi\sqrt{R_*^3/GM_*}$ is the star's free-fall time. At the peak time of $\sim$100 days, PS1-10jh emits $\sim 10^{45}$ erg s^{-1} of radiation with an effective temperature of a few 10^4 K, implying a photosphere size of $\sim 10^{15}$ cm with area $\sim 10^5$ AU^2. By contrast, the area occupied by the stream is only comparable to this value when $t \approx 10^5 t_{\rm ff} \approx 10$ yr for $q = 10^6$ and $\beta = 1$. Kasen and Ramirez-Ruiz (2010) calculated that this component would contribute at most 10^{40} ergs s^{-1} of luminosity for the disruption of a solar mass star. However, we believe that this represents an upper limit as the self-gravity of the stream was not included in that work, resulting in an artificially fast rate of recombination.

Because the evolution of the stream is adiabatic, but not incompressible, the stream is resistant to gravitational collapse in both the radial direction perpendicular to the stream, and in the axial direction along the cylinder. Collapse can only occur in the radial direction when $\gamma < 1$, as it becomes energetically favorable to collapse radially (McKee and Ostriker, 2007), and can only occur axially for $\gamma > 2$, where the fastest growing mode has a non-zero wavelength and leads to fragmentation (Figure 4 of Ostriker, 1964; Lee and Ramirez-Ruiz, 2007).

In a thin stream, the tidal force applied by the black hole results in the density ρ scaling as r^{-3} (Kochanek, 1994). As the distance $r \propto t^{2/3}$ when $t \to \infty$ for parabolic orbits, this implies that $\rho \propto t^{-2}$. For cylinders, the time of free-fall $t_{\rm ff}$ is proportional to $\rho^{-1/2}$, the same as it is for spherical collapse (Chandrasekhar, 1961), and thus $t_{\rm ff} \propto t$. Therefore, a segment of the stream within which $t_{\rm ff}$ ever becomes greater than t will not experience recollapse at any future time, as the two timescales differ from one another only by a multiplicative constant. It is also evident that self-gravitating cylinders can be bound whereas a self-bound sphere will not, as the Jeans length progressively decreases in size for structures that are initially confined in fewer directions (Larson, 1985). This implies that the cylindrical configuration may not remain self-bound if sufficient energy is injected into the star via a particularly deep encounter in which the core itself is violently shocked, which only occurs for $\beta \gtrsim 3$ (see Chapter 2, also see Kobayashi *et al.*, 2004; Guillochon *et al.*, 2009; Rosswog *et al.*, 2009b), approximately 10% of disruption events. Additional energy can also be injected by nuclear burning (Carter and Luminet, 1982; Rosswog *et al.*, 2008a), again only for events in which β is significantly larger than 1. For most values of β, the amount of energy injected into the star at pericenter is insufficient counteract gravitational confinement in the transverse direction at $t = 0$, and thus from the timescale argument given above the unbound stream would forever be confined.

Given this result, and given the computation burden of resolving a structure with such a large aspect ratio for the number of dynamical timescales necessary for the material to begin accreting onto the black hole, we presume that the gravitational confinement continues to hold at larger distances than we are capable of resolving, and show how the profile of the debris stream would appear if the simulation were followed to the point of the material's return to pericenter in the left panel of Figure 6.1.

By contrast, the bound material travels a much shorter distance from the black hole before turning around. For the material that remains bound to the hole, it has been assumed that the material circularizes quickly after returning to pericenter, resulting in an accretion disk with an outer radius equal to $2r_{\rm p}$, where $r_{\rm p}$ is the pericenter distance (Cannizzo *et al.*, 1990; Ulmer, 1999; Gezari *et al.*, 2009; Lodato and Rossi, 2010; Strubbe and Quataert, 2011). This is actually a vast underestimate of the distance to which the debris travels, which can be found via Kepler's third law for the orbital period of a body and dividing by two to get the half-period, and then solving for the semi-major axis a,

$$r_{\rm o} = 2\left(\frac{GM_{\rm h}t^2}{\pi^2}\right)^{1/3}, \tag{6.9}$$

where we have made the assumption that $r_{\rm o} \simeq 2a$, appropriate for the highly elliptical orbits of the bound material (The most-bound material has eccentricity $e = 1 - 2q^{-1/3} = 0.98$ for $q = 10^6$). As this material is initially confined by its own gravity, the return of the stream to pericenter mimics a huge β encounter, which as we explain in the following section can yield a impressive compression ratio.

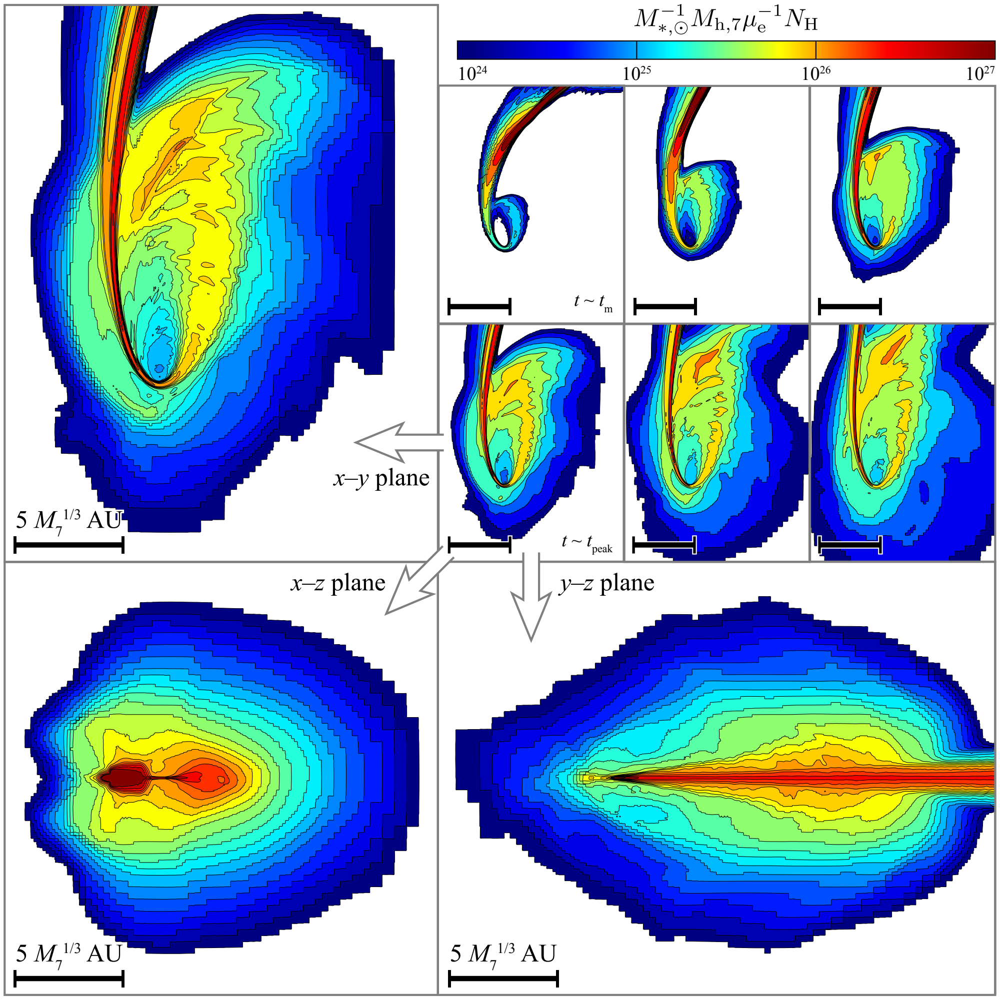

Figure 6.2: Column density contours of the debris resulting from the disruption of a $M_* = M_\odot$ star by a $M_{\mathrm{h}} = 10^3 M_\odot$ black hole. The column density shown in all panels is scaled to the value that would be expected for a disruption by a $M_{\mathrm{h}} = 10^7 M_\odot$ black hole, which is $10^{-3.5}$ smaller than what is expected for $M_{\mathrm{h}} = 10^3 M_\odot$. The six mini-panels in the upper right show the evolution of the column density in the *xy*-plane with time, with the upper left mini-panel showing the column density at the time of return of the most bound material t_{m}, and lower left mini-panel showing the column density at the time of peak accretion t_{peak}. The three large panels show the column density as viewed from the *x*–*y*, *x*–*z*, and *y*–*z* planes at $t = t_{\mathrm{peak}}$.

6.3.2 Dissipative Effects within the Nozzle

There are a combination of potentially active mechanisms that can provide the required dissipation for any given event, with each mechanism dominating for particular combinations of M_{h} and β. To quantify the effect of each of these mechanisms, we define the ratio $\mathcal{V} \equiv (\partial E/\partial t)(T/E)$, where T is the orbital period. $\mathcal{V}$ represents the fraction of gravitational binding energy that is extracted per orbit, with $\mathcal{V} = 1$ indicating a mechanism that fully converts kinetic to internal energy within a single orbit. To have $\dot{M}$ and L trace one another over the duration of a flare, $\mathcal{V}$ must have a value $\gtrsim t_{\mathrm{m}}/t_{\mathrm{peak}}$, where t_{peak} is the time at which the accretion rate peaks and t_{m} is the time at which the most bound debris returns to pericenter. For partially disruptive encounters, the ratio between these two times is ~ 3, but then increases as β^3 for deep encounters in which t_{m} varies more quickly than t_{peak} (see Chapter 5 and Guillochon and Ramirez-Ruiz, 2013).

In the following sections we provide a brief description of the dissipation mechanisms that are expected to operate in a TDE. Only the first mechanism (hydrodynamical dissipation) is present within our calculations, as we do not include magnetic fields or the effects of a curved space time. Regardless of the origin of the dissipation, we expect that the dissipation observed in our simulations is likely to be quite analogous to the other dissipative process that operate.

6.3.2.1 Hydrodynamical dissipation

As described in Section 6.3.1, self-gravity within the debris stream sets its width and height to be equal to $R_* \tilde{r}^{1/4}$, and thus when the stream crosses the original tidal radius, its height is approximately equal to the size of the original star. If the return of the material to pericenter behaved in the same way as the original encounter, the maximum collapse velocity $v_\perp$ would be equal to the sound speed at $r_{\rm t}$ multiplied by β, yielding a dissipation per orbit $\mathcal{V} = q^{-2/3}/\beta$, equal to 2% for $q = 10^3$ and $\beta = 2$ (Carter and Luminet, 1983; Stone *et al.*, 2012). In our hydrodynamical simulations for $q = 10^3$, we find that $\approx$ 10% of the total kinetic energy of the debris is dissipated upon its return to pericenter through strong compression at the nozzle (Figure 6.2). This is a factor of a few larger than the expected dissipation.

However, as the star has been stretched tremendously, the sound speed within the stream has dropped by a significant factor, meaning that the distance from the black hole at which the stream's sound-crossing time is comparable to the orbital time (i.e., where the tidal and pressure forces are approximately in balance) is not the star's original tidal radius, but is instead somewhat further away.

For two points that are separated by a distance dr within the original star, their new distance dr' upon returning to pericenter is related to the difference in binding energy between them, which remains constant after the encounter and is equal to

$$\frac{dE}{dr} \simeq \frac{E(r_{\rm p})}{r_{\rm p}} = \frac{GM_*}{R_*^2} q^{1/3} \tag{6.10}$$

As angular momentum is approximately conserved, the two points will cross pericenter at the same location they originally crossed pericenter, but at two different times t separated by a time dt owing to their different orbital energies. Assuming that the star originally had approached on a parabolic orbit, and that all the bound debris are on highly elliptical orbits, the distance from the black hole is

$$r' = \left(\frac{9}{2}GM_{\rm h}t^2\right)^{1/3}, \tag{6.11}$$

and thus

$$\frac{dr'}{dt} = \left(\frac{4GM_{\rm h}}{3t}\right)^{1/3}. \tag{6.12}$$

If we set $t = 0$ to be the time when the first point re-crosses pericenter, the difference in time is simply the difference in orbital period, and thus we can use Kepler's third law to derive dE/dt. Using Equations 6.10 and 6.12, we can use the chain rule to determine dr'/dr,

$$\frac{dr'}{dr} = \frac{dE}{dr}\frac{dt}{dE}\frac{dr'}{dt} = \left(\frac{3\pi}{2}\right)^{2/3}\left(\frac{t}{t_{\rm m}}\right)^{4/3} q^{2/3}. \tag{6.13}$$

For $q = 10^3$, this implies that the material has been stretched by a factor $\gtrsim 10^2$ at all times beyond the time the most-bound material begins accreting, and for $q = 10^6$ this factor is $\gtrsim 10^4$. The change in volume is then given by the change in cross-section of the stream multiplied by the change in length given by Equation 6.13,

$$\frac{dV'}{dV} = \frac{dr'}{dr}\tilde{r}^{\frac{2-\gamma}{\gamma-1}} \tag{6.14}$$

where we have used Equation 6.7 to estimate the width and height of the stream.

The density of the stream ρ as it returns to pericenter can be approximated by assuming that $dM/dr = \Lambda$, although in reality this distribution can be determined more exactly from the numerical determination of $\dot{M}$ by a change of variables from E to r. Under this assumption, the change in density is simply related to the change in volume alone. As the tidal radius is proportional to $\rho^{1/3}$, the ratio of the effective tidal radius of the stream $r_{\rm t,s}$ to $r_{\rm t}$ is then

$$\begin{aligned}\frac{r_{\rm t,s}}{r_{\rm t}} &= \left(\frac{dV'}{dV}\right)^{1/3}\\ &= \left(\frac{3\pi}{2}q\right)^{\frac{2}{3}\frac{\gamma-1}{4\gamma-5}} \left(\frac{t}{t_{\rm m}}\right)^{\frac{4}{3}\frac{\gamma-1}{4\gamma-5}} \equiv \frac{\beta_{\rm s}}{\beta} \end{aligned} \tag{6.15}$$

where we have substituted $r_{\rm t,s}/r_{\rm t}$ for $\tilde{r}$, and where we have presumed that the time until the stream reaches pericenter from $r_{\rm t,s}$ is small compared to the time since disruption.

Under the assumption that the stream expands adiabatically and its pressure is governed by ideal gas pressure, this results in a reduction in the sound speed $c_{\rm s} = \sqrt{dP/d\rho} \propto V^{(1-\gamma)/2}$, where γ is the adiabatic index of the fluid. At $r = r_{\rm t,s}$, the ratio of the sound speed within the stream $c_{\rm s,s}$ to the star's original sound speed $c_{{\rm s},*}$ is

$$\begin{aligned}\frac{c_{\rm s,s}}{c_{{\rm s},*}} &= \left(\frac{dV'}{dV}\right)^{\frac{1-\gamma}{2}}\\ &= \left(\frac{3\pi}{2}q\right)^{\frac{(\gamma-1)^2}{5-4\gamma}} \left(\frac{t}{t_{\rm m}}\right)^{\frac{2(\gamma-1)^2}{5-4\gamma}} . \end{aligned} \tag{6.16}$$

Analogous to the original star, the maximum collapse velocity of the stream $v_{\perp,{\rm s}}$ is equal to the sound speed at $r_{\rm t,s}$ multiplied by the stream's impact parameter $\beta_{\rm s} \equiv \beta r_{\rm t,s}/r_{\rm t}$, $v_{\perp} = \beta_{\rm s} c_{\rm s,s}$. As the majority of the dissipation comes through the conversion of the kinetic energy of the vertical collapse via shocks, the fractional change in the specific internal energy is

$$\begin{aligned}\mathcal{V}_{\rm H} &= \frac{\beta_{\rm s}^2 c_{\rm s,s}^2}{v_{\rm p}^2} \\ &= \left(\frac{3\pi}{2}q\right)^{-\frac{2}{3}\frac{(\gamma-1)(3\gamma-5)}{4\gamma-5}} \left(\frac{t}{t_{\rm m}}\right)^{-\frac{4}{3}\frac{(\gamma-1)(3\gamma-5)}{4\gamma-5}} \beta q^{-2/3}.\end{aligned} \tag{6.17}$$

As $r_{\rm t} \propto \rho^{1/3}$, and $c_{\rm s} \propto \rho^{-1/3}$ for $\gamma = 5/3$, Equations 6.15 and 6.16 are inverses of one another in the adiabatic case,

$$\frac{r_{\rm t,s}}{r_{\rm t}} = \frac{c_{{\rm s},*}}{c_{\rm s,s}} = 60 M_6^{4/15} \left(\frac{t}{t_{\rm m}}\right)^{8/15} \tag{6.18}$$

and thus 6.17 simplifies to $\mathcal{V}_{\rm H} = \beta q^{-2/3}$, identical to the amount of dissipation experienced by the original star. One key difference exists between the original encounter and the stream's return to pericenter: While the original encounter may only result in the partial shock-heating of the star, even for relatively deep β (Guillochon *et al.*, 2009), the fact that the collapse of the stream is highly supersonic ($\beta_{\rm s} \sim 60\beta$) guarantees that shock-heating will occur upon the material's return to pericenter.

For our $q = 10^3$ simulation, the amount of dissipation expected per orbit predicted by Equation 6.17 is 4×10^{-2}, and for our $q = 10^6$ simulation the expected dissipation would only be 4×10^{-4}. Thus, the conversion of kinetic energy to internal energy via shocks at the nozzle point is inefficient for all but the lowest mass ratios and/or the largest impact parameters, and would be incapable of circularizing material on a timescale that is shorter than the peak timescale of PS1-10jh (Figure 6.3). This suggests that a viscous mechanism that involves an unresolved hydrodynamical instability, or a mechanism that is beyond pure hydrodynamics, is responsible for the circularization of the material for this event.

An additional complication that is not addressed here is recombination. As the stream expands, its internal temperature drops below the point at which hydrogen and helium begin to recombine, flooring its temperature to $\sim 10^4$ K (Roos, 1992; Kochanek, 1994). This implies that the ratio between the initial and final sound speeds is somewhat smaller than when assuming adiabaticity holds to arbitrarily-low stream densities, and depends on the initial temperature of the fluid, which is $\sim 10^4$ K in the outer layers of the Sun, but $\sim 10^7$ K in its core. This also causes the stream to expand somewhat due to the release of latent heat. However, as the material returns to pericenter, the compression of the material will reionize it. Given these complications, it is unclear if this process would lead to more or less dissipation at the nozzle.

6.3.2.2 Dissipation through General Relativistic Precession

For orbits in which the pericenter is comparable to the Schwarzschild radius $r_{\rm g}$, the orbital trajectory begins to deviate from elliptical due to precession induced by the curved space-time. The precession time in the inner part of the disk is (Valsecchi *et al.*, 2012):

$$\dot{\gamma}_{\rm GR} = \left(\frac{2\pi}{T}\right)^{5/3} \frac{3G^{2/3}}{c^2} \frac{M_{\rm h}^{2/3}}{1-e^2}, \tag{6.19}$$

where T and e are respectively the period and eccentricity of the stream. As the debris resulting from a tidal disruption has a range of pericenter distances ($r_{\rm p} \pm R_*$), there is a gradient in precession times of the returning debris. This precession causes the orbits to cross one an-

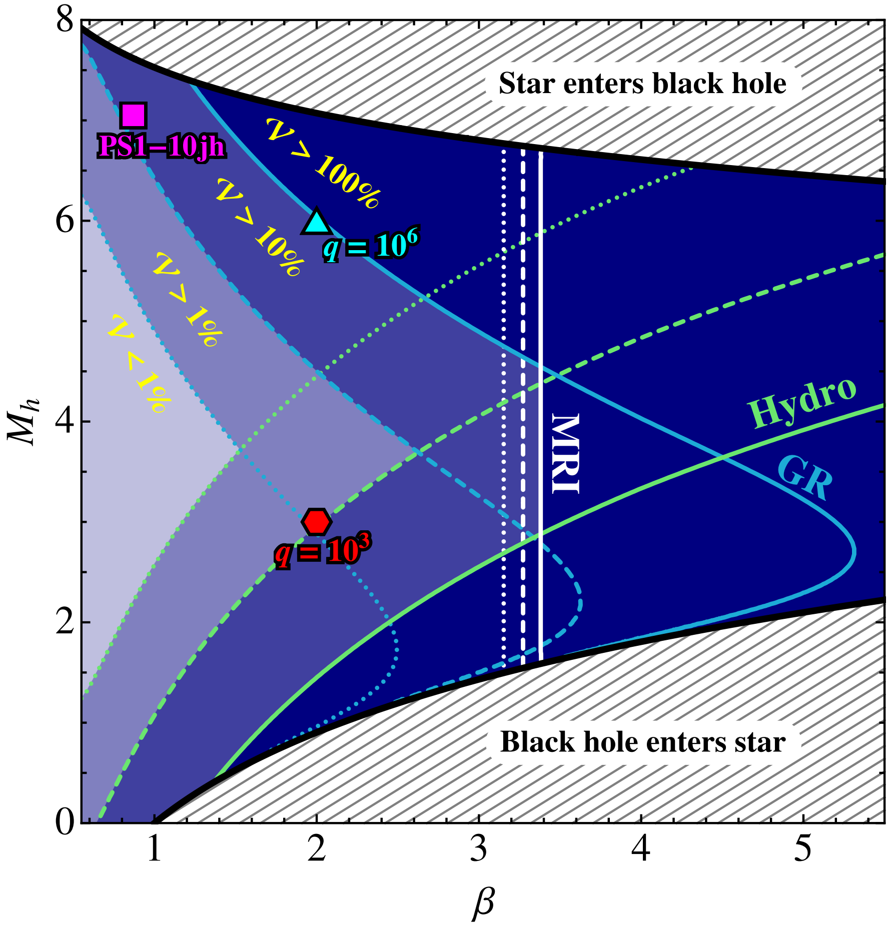

Figure 6.3: Fraction of binding energy dissipated at $t = t_{\rm peak}$ for three mechanisms that may contribute to the circularization of material after a tidal disruption, with light green corresponding to hydrodynamical shocks at the nozzle point, light blue corresponding to dissipation through GR precession (presuming $\gamma = 5/3$), and white corresponding to the MRI mechanism. For each mechanism, three contours of $\mathcal{V}$ are shown, with solid corresponding to 100%, dashed corresponding to 10%, and dotted corresponding to 1%. If all three mechanisms operate, the shaded blue regions represent zones in which $\mathcal{V}$ adopts the values specified by the unions of the regions enclosed by the three sets of contours, with the lightest/darkest corresponding to the least/most dissipation. In order for L and $\dot{M}$ to trace one another closely, $\mathcal{V} \sim 100\%$. For reference, our two hydrodynamical simulations are shown by the cyan triangle and the red hexagon, and the highest-likelihood fit returned by our maximum likelihood analysis (Section 6.6.3) is shown by the magenta square.

other, dissipating energy (Eracleous *et al.*, 1995). When compared to the standard α viscosity prescription, the timescale of this precession is comparable to the viscous time,

$$t_{\rm prec} = 10^{-1.7} M_6 T_5^{-1/2} (1+e) \left(\frac{r_{\rm p}}{r_{\rm g}} \right)^2 \text{ yr}, \tag{6.20}$$

where $T_5 \equiv 10^5 T$ is the local disk temperature. In a tidal disruption, the most-bound material is also the material with the shortest precession time, and it is this timescale that sets the overall rate of dissipation. By setting T and e in Equation 6.19 to $t_{\rm m} \equiv \sqrt{q/2}\beta^{-3} t_{\rm ff}$ and $e_{\rm m} \equiv 1 - 2\beta q^{-1/3}$, the period and eccentricity of the most-bound material, and by assuming that precession through an angle 2π would lead to complete dissipation, the dissipation due to relativistic precession for the material that corresponds to the peak in the accretion rate is

$$\mathcal{V}_{\rm GR,peak} = \frac{t_{\rm peak}}{t_{\rm m}} \left(\frac{2\pi}{t_{\rm m}} \right)^{2/3} \frac{3G^{2/3}}{c^2} \frac{M_{\rm h}^{2/3}}{1 - e_{\rm m}^2}. \tag{6.21}$$

In general, the period of the most-bound material tends to smaller values for larger q and β, resulting in more dissipation, except in the case that $r_{\rm p}$ and R_* are comparable (Figure 6.3, cyan curves). If none of the other dissipation mechanisms are effective, this means that disruptions by massive black holes, in which $r_{\rm p}$ and $r_{\rm g}$ are closer to one another in value, would be the only cases in which $\dot{M}$ and L follow one another closely.

As we will show in Section 6.6, the highest-likelihood models of PS1-10jh seem to be consistent with a relativistic encounter with the central black hole. If no other dissipative mechanisms are able to operate effectively in tidal disruption accretion disks, the possibility exists that only those events in which $r_{\rm p}$ and $r_{\rm g}$ are comparable will have L and $\dot{M}$ trace one another closely.

6.3.2.3 Super-Keplerian, Compressive MRI

The magnetic field in the bound stellar debris is likely to be amplified by compression and by strong shearing within the nozzle region. The effects of magnetic shearing, the magneto-rotational instability (MRI; Balbus and Hawley, 1998), is expected to lead to the rapid exponential growth of the magnetic field with a characteristic timescale of order the rotational period. This instability has been routinely studied in the context of accretion disks and we argue here that it is likely to operate within the nozzle although its exact character is difficult to constrain given that the boundary conditions are constantly changing and the material is never in steady-state.

The MRI is present in a weakly magnetized, rotating fluid wherever

$$\frac{d\Omega^2}{d\ln r} < 0. \tag{6.22}$$

The ensuing growth of the field is exponential with a characteristic time scale given by $t_{\rm MRI} = 4\pi|d\Omega/d\ln r|^{-1}$ (Balbus and Hawley, 1998). For a (super-)Keplerian angular velocity distribution $\Omega \propto r^{-3/2}$, this gives $t_{\rm MRI} = (4/3)\Omega^{-1}$. Exponential growth of the field on the timescale Ω^{-1} by the MRI is likely to dominate over other amplification process such as field compression within the same characteristic time. While a variety of accretion efficiencies are reported in numerical realizations of magnetically-driven accretion disks, which depend on the geometry, dimensionality of the simulation, and included physics, essentially all models find that the strength of the magnetic field amplifies to the point that it is capable of converting fluid motion into internal energy. From global simulations of the MRI, the build-up of the magnetic field strength is confirmed to be exponential, resulting in a dissipation rate that is a constant multiple of the orbital period. In Stone *et al.* (1996), this constant is found to be 3. Once the magnetic field strength is saturated, the resulting angular momentum transport will be governed by the turbulence and is therefore expected to take place over longer timescales. A simple estimate of the saturation field can be obtained by equating the characteristic mode scale, $\sim v_{\rm A}(d\Omega/d\ln r)^{-1}$, where $v_{\rm A}$ is the Alfvén velocity, to the shearing length scale, $\sim dr/d\ln\Omega$, such that $B_{\rm sat} \sim (4\pi\rho)^{1/2}\Omega r$. This saturation field is achieved after turbulence is fully developed, which in numerical simulations takes about a few tens of rotations following the initial exponential growth (Hawley *et al.*, 1996; Stone *et al.*, 1996).

For the Sun, the initial interior magnetic field energy at the base of the convective zone $E_{B,0} \sim 10^{-10} E_{\rm g}$ (Miesch and Toomre, 2009), although larger initial fields are possible in general (Durney *et al.*, 1993). As the tidal forces stretch the star into a long stream, the volume of the fluid increases by a factor $\beta_{\rm s}^3$ (Equation 6.15) prior to returning to pericenter, reducing the magnetic field strength further. However, when the stream returns to pericenter, it experiences a dramatic decrease in volume by a factor $\beta_{\rm s}^{2/(\gamma-1)}$ (Luminet and Carter, 1986). Assuming the frozen flux approximation, the new magnetic energy density is

$$E_B = E_{B,0}\beta_{\rm s}^{\frac{3\gamma-5}{\gamma-1}} \tag{6.23}$$

$$= \left(\frac{3\pi}{2}q\right)^{\frac{2}{3}\frac{3\gamma-5}{4\gamma-5}} \left(\frac{t}{t_{\rm m}}\right)^{\frac{4}{3}\frac{3\gamma-5}{4\gamma-5}} \tag{6.24}$$

For $\gamma = 5/3$, the dependence on $\beta_{\rm s}$ disappears, i.e. the magnetic field strength upon return to pericenter is identical to the star's initial interior field. Assuming that the magnetic field within the debris has strength E_B relative to the local gravitational binding energy $E_{\rm g}$ upon returning to the nozzle, $\mathcal{V}_{\rm MRI}$ adopts a simple form (Figure 6.3, white curves),

$$\mathcal{V}_{\rm MRI,peak} = \frac{E_B}{E_{\rm g}} \exp\left[\frac{t_{\rm peak}}{3t_{\rm m}}\right]. \tag{6.25}$$

6.3.3 Is the Debris Disk Dissipative Enough?

In order for the emergent luminosity L to follow the feeding rate $\dot{M}$ closely, the dissipation must be effective enough such that material returning to pericenter can circularize on a timescale $t_{\rm c}$ that is at most the time since disruption $t_{\rm d}$. In Figure 6.3 we show the three sources of dissipation that we estimated above. We find that while significant dissipation is expected for large β encounters, or for encounters in which $r_{\rm p} \sim r_{\rm g}$ (as is the case for our best-fitting model for PS1-10jh), that there are many combinations of β and q that may not have the required dissipation necessary to ensure the direct mapping in time of $\dot{M}$ to L. In our $q = 10^3$ hydrodynamical simulation, we found somewhat more dissipation than what is expected from a simple analytical calculation, but the resolution at which we resolved the compression at pericenter was only marginally sufficient to resolve the strong shocks that form there.

One potential resolution to this issue is the adiabatic index of the fluid γ, which in the above calculations we have assumed $= 5/3$, although the real equation of state within the stream is likely softer due to the influence of recombination. With a softer equation of state, the cancelations that occur for $\gamma = 5/3$ and eliminate the dependence on $\beta_{\rm s}$ for the hydrodynamical (Equation 6.17) and MRI (Equation 6.25) dissipation mechanisms would no longer apply, yielding both increased compression and magnetic field strengths, and thus additional dissipation.

While the initial dissipation of the stream may indeed come as the combination of the three previously described mechanisms, it is likely that the mechanism responsible for the accretion onto the black hole once the material has been assembled into a disk is the MRI mechanism, as is suspected for steadily-accreting AGN. Given the computational challenge of simultaneously resolving the nozzle region and the full debris stream, it is clear that local high-resolution magnetohydrodynamic simulations are required to determine the true dissipation rate $\mathcal{V}$ at the nozzle.

6.4 The Relationship Between Steadily-Accreting AGN and TDE Debris Disks

Within the debris structure formed from a tidal disruption, the same mechanisms that operate in steady-state AGN may continue to operate. There are a number of differences between the structure of a debris disk resulting from tidal disruption and the structure of steadily-accreting AGN, but we will argue that similar processes are responsible for the appearance of both structures. In this section, we will make continued reference to the highest-likelihood model of PS1-10jh, which is determined in Section 6.5.

6.4.1 The Conversion of Mass to Light

For steadily-accreting AGN, energy is thought to be released by the viscous MRI process at all radii. The amount of energy available at a particular radius depends on the local gravitational potential, and thus the vast majority of the energy emitted by accreting black holes is produced within a few times the Schwarzschild radius $r_{\rm g}$. The temperature profile that results from this release in energy within the accretion disk is given by the well-known expression presented in Shakura and Sunyaev (1973), and scales as $r^{-3/4}$, resulting in a sum of blackbodies with a continuum slope $F_\nu \propto \nu^{1/3}$ (Pringle and Rees, 1972; Gaskell, 2008). AGN are divided into two primary categories: Compton-thick AGN, which are obscured by $\sim 10^{24}$ cm^2 of column and thus making them optically thick to Compton scattering (Treister *et al.*, 2009), and thermal AGN, which have column densities significantly less than this value, enabling the black hole's emission to be directly observed. However, all thermal AGN show an excess in the blue known as the "big blue bump" (Shields, 1978; Lawrence, 2012), and the slopes of their continuum $F_\nu \propto \nu^{-1}$ (Gaskell, 2009). This is more consistent with the notion that the light emitted from the central parts of the disk is intercepted by intervening gas before it is observed, with nearly one hundred percent of the light emitted by the disk being reprocessed in this way. This implies that a significant fraction of the mass that may eventually be accreted by the black hole is suspended some distance above the disk plane, where it can intercept a large fraction of the outgoing light.

For the accretion structure that forms from the debris of a tidal disruption, the dissipation at the nozzle point provides a means for lifting material above and below the orbital plane, resulting in a sheath of material that surrounds the debris and is very optically thick for

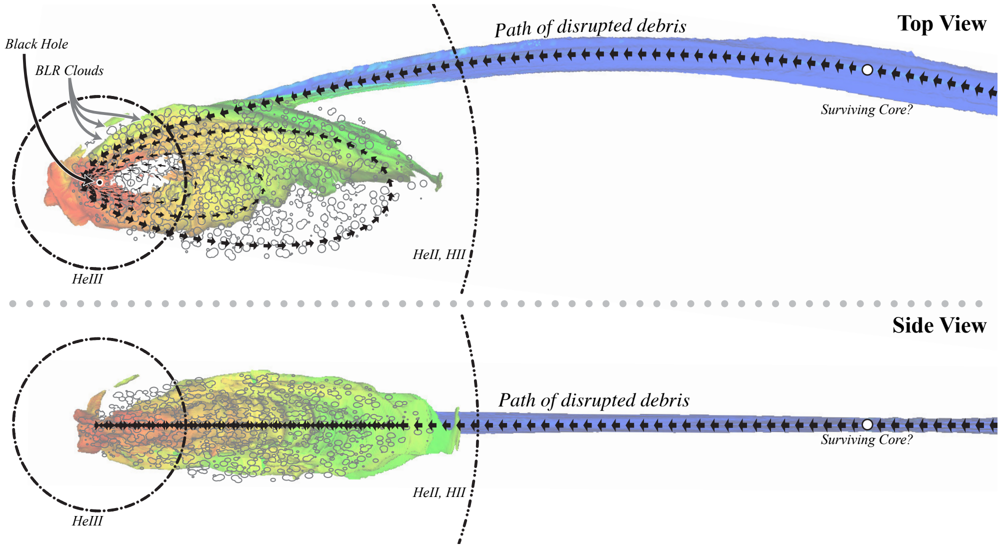

Figure 6.4: Schematic figure from our $q = 10^3$ simulation demonstrating the geometry of the debris resulting from a tidal disruption at $t - t_{\rm d} = 4.3 \times 10^5$ s, shown from the top (top image) and the side (bottom image). The three-dimensional isodensity contours are colored according their temperature, with red being hot and blue being cold. Super-imposed on these contours are a line of arrows showing the path of the circularizing debris as return to the black hole (black disk), inside which a surviving stellar core may reside (white disk). The dot-dashed and double-dot-dashed lines respectively show the regions interior to which helium is doubly-ionized and hydrogen/helium are singly ionized within the BLR. The region in which BLR clouds may form is super-imposed using the gray contours, although we note that the BLR may instead be in the form of a diffuse wind.

certain lines of sight (Figure 6.2). However, as the spread in energy at the nozzle point does not completely virialize the flow, the resulting distribution of matter is flattened, allowing the central regions of the accretion disk to be visible through material that is close to the Compton-thick limit. The time-series presented in the upper six panels of Figure 6.2 show that despite the continually active dissipation process at the nozzle-point, the region directly above the central parts of the accretion disk remain relatively evacuated of gas before, during, and after the time of peak accretion. For the toy simulation presented here, the optical depth to Thomson scattering directly above the black hole and perpendicular to the orbital plane of the debris is ~ 1, depending on the electron fraction of debris (assumed to be pure hydrogen in Figure 6.2). For more massive black holes, the debris is spread over a larger volume, as the tidal radius grows as $M_{\rm h}^{1/3}$, and thus $N \propto M_{\rm h}^{-1}$. If the dissipation rate were the same independent of black hole mass, it would be expected that the disruption of stars by more massive black holes would yield more lines of sight for which $\tau \sim 1$.

6.4.2 Source of Broad Emission Lines

Broad line emission is visible in many AGN, being thought to be produced by gas above and below the disk plane at distances on the order of light days away from the black hole. For other AGN, this region is not directly observable, which has been attributed to a torus at large radii that can obscure the broad line region for lines of sight that run within a few tens of degrees of the disk plane (i.e. the AGN unification model, Antonucci, 1993). The emission lines produced within this region have been successfully used to measure black hole masses (Peterson and Wandel, 1999; Peterson *et al.*, 2004) based on measurements of the time lag in the response of line luminosity to variations in the output of the central engine. It is still debated whether this material is in the form of an optically-thick disk wind (Trump *et al.*, 2011) or optically-thick clouds (Celotti and Rees, 1999), but in either case the material that constitutes the BLR is likely bound to the black hole (Proga *et al.*, 2008; Pancoast *et al.*, 2012).

In a steady-accreting AGN, material accretes from very large distances ($\gtrsim 10^3 r_{\rm g}$), and the emission from this region is often manifest as an IR bump in Type II AGN (Koratkar and Blaes, 1999). At such distances, the ionizing flux originating from the black hole is not sufficient to maintain a large ion fraction within the disk's emitting layer. The closer one gets to the central black hole, the greater the incident flux of ionizing radiation on the BLR wind/clouds that generate the observed emission lines. The fraction of atoms in an excited state X_+ relative to the state directly below it X_0 is approximately (Frank *et al.*, 2002)

$$\frac{n_{X_+}}{n_{X_0}} \sim \frac{a(\nu_{\rm ion})}{\alpha_B(X_0) h\nu_{\rm ion}} \frac{Q(X_0)}{4\pi r^2 n_e}, \tag{6.26}$$

where $Q(X_0)$ is the flux in photons capable of ionizing the lower state. This expression shows that that as the distance from the central engine increases, the number of atoms in the high state decreases, assuming that the electron density n_e decreases with radius more slowly than r^{-4} (as $Q \propto r^{-2}$), and also shows that species with larger ionization potentials will have less atoms in the high state than species with smaller ionization potentials. This leads to a hierarchy of ions in the disk, with those with the highest ionization potential being predominant in the inner regions of the disk. In a steadily-accreting AGN, the flux in ionizing photons is large enough to fully ionize iron (as evidenced by the existence of Fe K lines, Fabian *et al.*, 2000), and given that atoms at large radii are mostly neutral, all ionic species of all elements exist at some distance from the central engine. Reverberation mapping supports this basic photoionization picture, as $R_{\rm BLR} \sim L^{1/2}$ (Bentz *et al.*, 2010, 2013). In particular, the optical wave band hosts several lines from the Balmer series of hydrogen and lines from both singly-ionized and neutral helium (Bentz *et al.*, 2010).

This wide range of scales is in stark contrast to the debris disk formed as the result of a tidal disruption, which we schematically illustrate in Figure 6.4. Rather than material spiraling in from parsec scales, material is instead ejected from the nozzle point, which lies at the star's original point of closest approach, and typically has scales on the order of a few AU. As a result, the debris disk forms from the inside out. The ratio of line strengths in a TDE is dependent upon the number of atoms in the photosphere that are in the particular ionization state associated with each line. For PS1-10jh, the lack of an Hα emission line was interpreted by G12 as being attributed to a lack of hydrogen atoms. However, the Balmer series requires neutral hydrogen to be present in sufficient quantities to produce a line in excess of the continuum emission. As shown in our $q = 10^3$ simulation, material is ejected from the nozzle point at approximately the escape velocity, with the fastest moving material traversing a distance $r_{\rm t}[(t-t_{\rm d})/t_{\rm p}]^{2/3}$. *This sets an upper limit on the radial extent of the disk.* Therefore, the lack of an observed emission feature may simply be the result of the disk not being large enough to host the region required for that particular feature's production.

The specifics as to which particular radii contribute the most to the emission strength of each line is complicated to determine, and requires a more-through treatment of the ionization state of the gas as a function of radius, which depends on the geometry of the structure, and the distribution of density and temperature as functions of height and radius. In a tidal disruption, the matter distribution that ensheathes the black hole is established quickly, forming a steady-state structure that is supported by a combination of gas pressure and angular momentum (Loeb and Ulmer, 1997). Accretion then proceeds through the midplane, in which the majority of light is generated within a few r_g at X-ray temperatures. These photons are intercepted by the ensheathing material at higher latitudes. Korista and Goad (2004) determined the equivalent widths of various lines as functions of volume density and ionizing flux, which is not expected to vary much as a function of column density for $10^{23} \leq N \leq 10^{25}$ cm^2 (Ruff, 2012). In Figure

6.5 we show a series of profiles corresponding to our highest-likelihood model for PS1-10jh over the range of times at which spectra were taken of this event. To calculate the density distribution $n(\mathrm{H})$ as a function of r, we once again use the chain rule,

$$n(\mathrm{H}) = \frac{X(\mathrm{H})}{4\pi m_{\mathrm{p}} r^2} \frac{dM}{dE} \frac{dE}{da} \left(\frac{2a}{r_{\mathrm{p}}} \right)^{3/2} \tag{6.27}$$

where $X(\mathrm{H})$ is the mass fraction of hydrogen. and presuming that the radial distribution of mass is determined by the distribution of mass with semi-major axis a, dM/da, set at the time of disruption. Likewise, dM/dr is directly proportional to dM/da, with a scaling factor equal to the ratio of time spent at apocenter versus pericenter, $dM/dr \simeq dM/da(2a/r_{\mathrm{p}})^{3/2}$, where we have assumed that $1-e \to 0$ and thus the apocenter distance $r_{\mathrm{a}} \simeq 2a$.

As a strong dissipation mechanism likely operates at the nozzle point, and this dissipation mechanism is likely to be as dissipative as the commonly invoked MRI mechanism, it stands to reason that the vertical structure of the debris disk formed through the circularization process is similar to that of a steadily-accreting AGN. Therefore, we would expect that the BLR associated with such structures should be similar to the BLR produced by steadily-accreting black holes. Under this assumption, we can use Equation 6.27 to approximate the number density of hydrogen as a function of radius and to determine the equivalent width of various emission lines using the models that have been generated for steadily accreting AGN (Korista and Goad, 2004). Figure 6.5 shows the density profiles calculated from Equation 6.27 as a function of time for our highest-likelihood model of PS1-10jh, with the purple curve corresponding to the time of the first acquired spectrum of PS1-10jh at -22 days, and the red curve corresponding to the last recorded spectrum at +358 days.

From Figure 6.5, it is clear that the equivalent width of HeII $\lambda4686$ is significantly larger than that of Hα, Hβ, and HeI $\lambda5876$, all three of which are not observed in PS1-10jh. The figure does suggest that hydrogen and/or singly-ionized helium emission lines may appear at later times when the ionizing flux has decreased, although this may not ever be observable in PS1-10jh where the flux originating from the TDE has already dropped below that of the host galaxy.

In making this plot, we have made some assumptions that actually would lead to a *decrease* in the strength of the unobserved lines if we performed a more-detailed calculation. Firstly, the models of Korista and Goad (2004) presume that a full annulus of material exists at each radius; this is not the case in an elliptical accretion disks where the inner annuli are closer to full circles than outer annuli (Eracleous *et al.*, 1995). In fact, it is unlikely that the outer material can circularize at all, given that there is significantly less angular momentum in the disk than the angular momentum required to support a circular orbit at the distance at which these lines would be produced (at $r = 10^{16}$ cm, $\sim$30 times more angular momentum would be required to form a circular orbit than what is available at $r_{\rm p}$). Secondly, we have made the assumption that the material that does the reprocessing remains at the distance determined by the energy distribution set at the time of disruption *at all times* (à la Loeb and Ulmer, 1997), when in reality the entire debris structure will shrink onto the black hole due to dissipation at pericenter. It is possible that this shrinkage of the debris could prevent emission features arising from species with lower ionization potentials from ever being observed.

Radiation pressure (which we ignore in this work) may act to push some fraction of

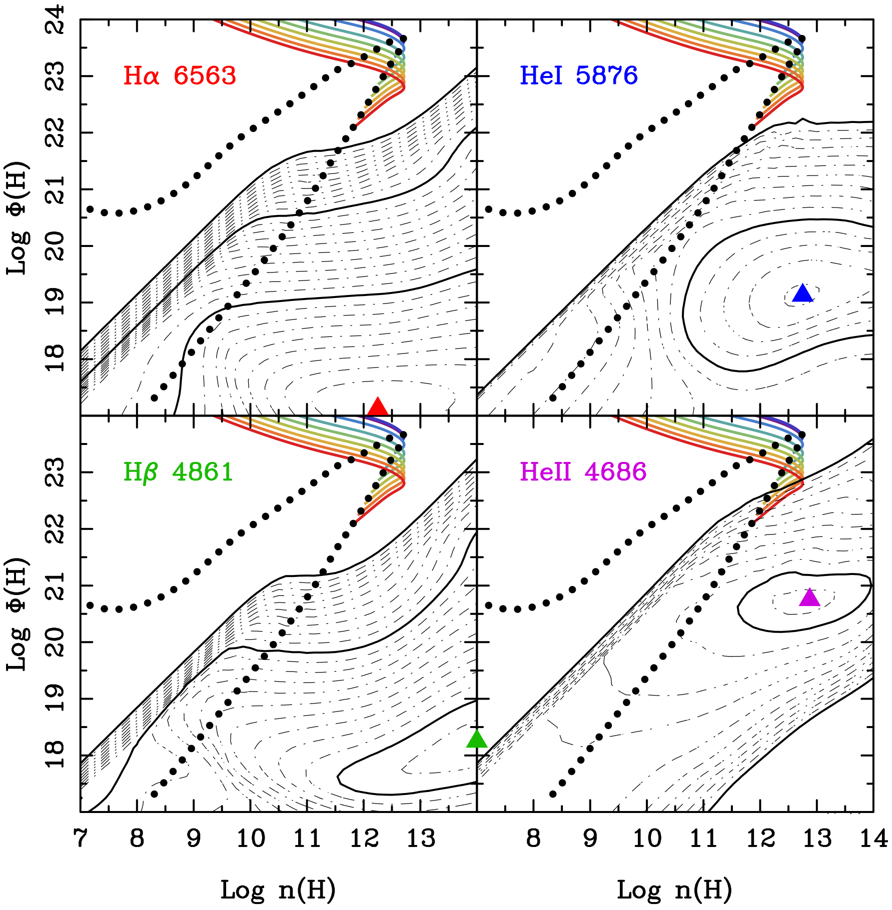

Figure 6.5: Contours of the log of the equivalent width of four emission lines as a function of hydrogen–ionizing flux Φ(H) and hydrogen number density n(H), where the black dashed and solid contours correspond to 0.1 and 1 decade, respectively (Adapted from Figure 1 of Korista and Goad, 2004), with the smallest contour corresponding to 1 Å of equivalent width. The colored triangle within each panel indicates the peak equivalent width for each line. The rainbow-colored curves show the profiles of the debris resulting from the tidal disruption that corresponds to the highest-likelihood fit of PS1-10jh (Section 6.6.3), with the range of curves being shown corresponding to the range between the first and last spectrum taken for the event, with purple being -22 and red being +358 days from peak. The black dotted curve shows the conditions at r_o over the full event duration. Note that Hα, Hβ, and HeI λ5876 would potentially be observable if additional spectra were collected at later times.

the material outwards, which in principle could produce low-energy emission features (Strubbe and Quataert, 2009). However, our highest-likelihood models predict a peak accretion rate that

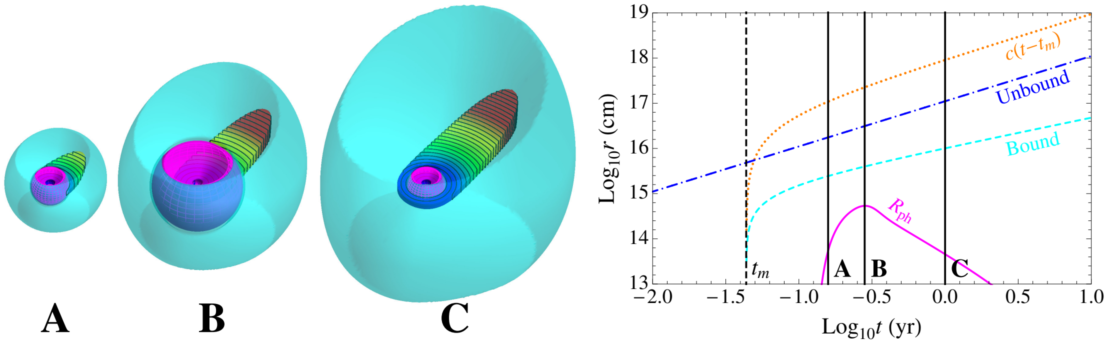

Figure 6.6: Evolution of the size scales relevant to the appearance of TDEs. The left image shows a three-dimensional schematic of the elliptical accretion disk (rainbow-colored surface), the low-density material that ensheaths the disk (cyan surface), and the location of the region interior to which helium is doubly-ionized (magenta surface), at three times labeled A, B, and C. The right plot shows results from the highest-likelihood fit of PS1-10jh, where the solid cyan and dashed magenta curves correspond to the two surfaces in the left image, the dash-dotted blue curve corresponds to the distance to which the unbound material has traveled, and the dotted orange curve corresponds to the distance to which light travels since the time of the accretion of the most-bound material, denoted by the vertical dashed black line. The times to which the images on the left correspond are shown by the labeled vertical black lines.

is sub-Eddington, and thus only a small fraction of the accreted matter is expected to be driven to large distances via radiation. It is unclear whether the amount of mass in this component would be dense enough to produce these features, as the recombination time may be too long.

6.5 A Generalized Model for the Observational Signatures of TDEs

As emphasized in the previous sections, there are many uncertainties relating to how the material circularized when it returns to pericenter, how this returning material radiates its energy when it falls deeper into the black hole's potential well, and in the ionization state of the gas within the debris superstructure. Using the code `TDEFit`, developed for this chapter, we construct a generalized model of the resultant emission from TDEs. In this section, we describe the results of running this fitting procedure, and how PS1-10jh specifically allows us to evaluate some of the other models that have been proposed for modeling TDEs.

6.5.1 Model description and free parameters

Our generalized model for matching TDEs is one in which an accretion disk forms by the disruption of a star of mass M_* by a black hole of mass M_h with impact parameter β and offset time $t_\mathrm{off} \equiv t_0 - t_\mathrm{d}$, where t_0 is the time the first datapoint was collected. This disk spreads both inwards and outwards from r_p, and is ensheathed by a diffuse layer of material that intercepts some fraction of the light. The disk itself is bounded by an inner radius r_i and outer radius r_o, with r_i assumed to be set by the viscous evolution of the material, and r_o being set by the ballistic ejection of material as it leaves the nozzle region, which scales as $r_\mathrm{o} = r_\mathrm{p}(t/t_\mathrm{m})^{2/3}$, where t_m is the time of return of the most-bound material. The fraction of the full annulus θ_f that is covered by the disk varies as a function of time, with $\theta_\mathrm{f} = 0$ when $r = r_\mathrm{o}$, and $= 2\pi$ when $t = t_\mathrm{visc}(r)$, assuming its spread in the azimuthal direction is controlled by the local value of the viscosity. The model is shown pictographically in the left panel of Figure 6.6, with the aforementioned size scales as functions of time being shown in the right panel of the same figure.

The source of this viscosity may be similar to the source of viscosity at the nozzle point (see Section 6.3.2), or it could be the result of the stream-stream collision that occurs when material reaches apocenter (Kochanek, 1994; Kim *et al.*, 1999; Ramirez-Ruiz and Rosswog, 2009). For simplicity, we assume that the same viscous process, parameterized by the free parameter $\mathcal{V}$, applies in both regions.

The emergent emission from the disk is calculated using the prescription of Done *et al.* (2012), which largely follows the original prescription of Shakura and Sunyaev (1973), but amends the no-torque boundary condition to include the effects of the black hole's spin, parameterized by the dimensionless spin parameter $a_{\rm spin}$. The model accounts for a shift in the emergent disk spectrum arising from variations in opacity, resulting in an effective temperature that can be $\sim$2.7 times larger than expected from the fiducial SS model. We do not permit the luminosity L to exceed the Eddington luminosity $L_{\rm Edd} = 4\pi G M_{\rm h} m_{\rm p} c / \kappa_{\rm t}$, and set $L = L_{\rm Edd}$ at times where $\dot{M}$ exceeds this limit. We also include the inclination of the structure relative to the observer ϕ as a free parameter, where $\phi = 0$ is defined to be edge-on, assuming that both the disk's height and the ensheathing layer scale with $\mathcal{V}$ in the same way, with the emergent emission from both components being reduced by a factor $\mathcal{V} + (1 - \mathcal{V}) \cos(\phi)$.

Note that we assume the color correction is intrinsic to the disk emission, and is not the same as the reprocessing that occurs due to the diffuse gas that ensheaths the disk and is ejected from the nozzle region directly. The photosphere of this reprocessing layer, whose size is set by a combination of the mass distribution and the absorption process responsible for intercepting the light, is less constrained. For steadily-accreting AGN with thermal emission, the reprocessing layer has temperatures of several 10^4 K (Koratkar and Blaes, 1999; Lawrence, 2012), and intercepts nearly 100% of the emission from the disk, resulting in an effective photosphere size that can be hundreds of AU in size for SMBHs accreting at the Eddington limit. However, as there are many non-thermal AGN whose spectra are more representative of bare slim-disk models (Walton *et al.*, 2013), it remains unclear how the size of this reprocessing zone and its fractional coverage are set.

In the models of Strubbe and Quataert (2009, 2011), this layer is presumed to arise as the result of ejection via a super-Eddington wind, and scales with this value when $\dot{M}$ exceeds $\dot{M}_{\rm Edd}$. From our hydrodynamical simulations, we find that the material that forms the reprocessing layer may be deposited by a process that does not require the accretion rate to exceed $\dot{M}_{\rm Edd}$, but instead depends on the details of how energy is injected into the material within the nozzle region. The distribution of mass in radius resulting from the ejection from the nozzle maps is directly related to dM/dE, although it is modified somewhat by the additional spread in energy introduced at the nozzle point. However, this spread in energy is local to mass that return at a particular time t, and thus the distribution of mass with radius after leaving the nozzle point will resemble dM/dE with an additional "smear" equal to the spread in energy applied at the nozzle. Therefore, we expect that the mass distribution with radius follows the general shape of dM/dE, and that there will be a density maximum corresponding to the orbital period of the material that constitutes the peak of the accretion. This peak in density that corresponds to the apocenter of the material that determines $\dot{M}_{\rm peak}$ is clearly seen in our hydrodynamical simulations (Figure 6.2).

Thus, the size of the reprocessing layer is likely to be dependent on both the instantaneous value of $\dot{M}$, which determines the amount of ionization radiation produced by the disk and the rate of instantaneous mass loss from the nozzle region, and on the integrated amount of mass that has been ejected from the nozzle region since $t = t_{\rm d}$. The optical depth τ is

$$\tau = \kappa \int_0^\infty \frac{dM}{dr} dr, \tag{6.28}$$

where κ is an opacity that we leave as a free parameter, but is at minimum the Thomson opacity $\kappa_{\rm t} = 0.2(1+X(H))$ cm^2 g^{-1}.

As we described in the derivation of Equation 6.27, the amount of mass at a particular distance r is related to the amount of mass at a particular binding energy E, and thus we can rewrite Equation 6.28 in terms of E,

$$\tau = \kappa \int_{E_{\rm m}}^{E_{\rm o}} \frac{dM}{dE} dE. \tag{6.29}$$

where $E_{\rm m}$ and $E_{\rm o}$ are the binding energy of the most bound material and the material at apocenter at time t respectively.

We presume that the fraction of light C intercepted by the reprocessing layer scales simply with τ,

$$C = 1 - e^{-\tau}, \tag{6.30}$$

but enforce the condition that $C < c(t-t_{\rm d})/R_{\rm ph}$ (where $R_{\rm ph}$ is the size of the photosphere) at all times, otherwise the photon diffusion time would be greater than the time since disruption, and thus L and $\dot{M}$ would not be expected to closely trace one another. In reality, C should have a wavelength dependence, but for the purposes of this work we treat the opacity as being "gray," absorbing all frequencies of light equally.

As the ionization state of the gas (and therefore the opacity) depends on the current luminosity, the size of the photosphere is expected to vary with time. In general, as the Thomson cross-section is significantly smaller than that of bound-free transitions, the photosphere scale is likely to correspond to the first species is not completely ionized, and in the case of PS1-10jh where HeII emission is observed, we speculate that this species is helium (Figure 6.6, magenta region). If we assume that $R_{\rm ph} \propto \dot{M}^l$, $T_{\rm ph} \propto \dot{M}^m$, and $L \propto \dot{M} \propto R_{\rm ph}^2 T_{\rm ph}^4$, then the power law indices of $R_{\rm ph}$ and $T_{\rm ph}$ are simply related,

$$2l + 4m = 1. \tag{6.31}$$

If the opening angle of the reprocessing layer is independent of r, the flux in ionizing photons intercepted is constant, implying $l = 1/2$ and thus $m = 0$, i.e. $T_{\rm ph}$ is independent of time. However, as we find that the geometry may in reality be somewhat more complicated (Figure 6.2), we do not assume the intercepting area necessarily scales as $\dot{M}$, and instead leave l as a free parameter. For any $l \neq 1/2$, the temperature of the photosphere will evolve with time. We leave l as a free parameter and relate m and l through Equation 6.31. The size of the photosphere is then defined to be

$$R_{\rm ph} = R_{\rm ph,0} a_{\rm p} \left(\frac{\dot{M}}{\dot{M}_{\rm Edd}} \right)^l \tag{6.32}$$

$$a_{\rm p} = \left[8GM_{\rm h} \left(\frac{t_{\rm peak} - t_{\rm m}}{\pi} \right)^2 \right]^{1/3}, \tag{6.33}$$

where $a_{\rm p}$ is the semi-major axis of the material that accretes at $t = t_{\rm peak}$, and $R_{\rm ph,0}$ is a dimensionless free parameter.

The amount of reddening in the host galaxy is also an unknown quantity that must be fitted to simultaneously with the parameters of the disruption. For extinction in the IR through the UV, we adopt the reddening law fits of Cardelli *et al.* (1989), in which the amount of reddening is defined by $A(\lambda) = A_{\rm V}[a(\lambda) + b(\lambda)/R_{\rm V}]$, in which $a(\lambda)$ and $b(\lambda)$ are fitted parameters,

$R_{\rm V}$ is a fitted parameter that ranges between 2 and 10 (Goobar *et al.*, 2002), and where we take $N_{\rm h} = 1.8 \times 10^{21} A_{\rm V}$ g cm^{-3}. For the X-rays, we adopt the cross-sections presented in Morrison and McCammon (1983). Extinction in the X-rays is particularly sensitive to metallicity and temperature (Gnat and Ferland, 2012), and the uncertainty in the amount expected for a particular event is large given the environment of a galactic center is likely to have super-solar metallicities (Cunha *et al.*, 2007) and a wide range of temperatures and densities (Quataert, 2002; Cuadra *et al.*, 2006; De Colle *et al.*, 2012).

An advantage of the MCMC method employed here is that it permits the inclusion of discrete parameters that can only assume particular values. This enables us to simultaneously fit multiple physical models, as long as the continuous parameters are shared between the models. We include two discrete free parameters in this work: $\mathcal{A}_*$, which parameterizes the type of object that was disrupted, and $\mathcal{A}_\gamma$, which parameterizes the polytropic model that is assumed. We include two distinct object types, the white dwarf sequence and the main sequence. Within each of these sequences, different mass ranges are characterized by different polytropic γ; we use the $\dot{M}$ functions derived from our hydrodynamical simulations (Guillochon and Ramirez-

Ruiz, 2013) appropriate to each mass range,

$$\dot{M} = \dot{M}_{4/3}(t) \begin{cases} \mathrm{MS} & : \quad 0.3 < M_*/M_\odot < 22 \\ \mathrm{WD} & : \quad M_*/M_\odot > 1.0 \end{cases} \tag{6.34}$$

$$\dot{M} = \dot{M}_{5/3}(t) \begin{cases} \mathrm{MS} & : \quad \begin{matrix} M_*/M_\odot < 1.0 \\ M_*/M_\odot > 22 \end{matrix} \\ \mathrm{WD} & : \quad M_*/M_\odot < 1.0 \end{cases} \tag{6.35}$$

where some overlap is permitted in the mass range $0.3 < M_*/M_\odot < 1.0$ to account for the gradual transition between fully radiative and fully convective stars in this range. It was found that the white dwarf sequence, which is only permits very low mass black holes, is excluded to very high confidence for all of the combinations of parameters that were considered, especially when accounting for the measurement of the black hole's mass presented in G12, which restricts $M > 2 \times 10^6 M_\odot$. For simplicity, we exclude discussion of the white dwarf channel for the rest of this work.

In addition to modifying the emergent disk spectrum, $a_{\rm spin}$ also affects the minimum approach distance of a star on a parabolic trajectory (i.e. the innermost bound circular orbit) $r_{\rm IBCO}$, and the spread in energy across the star at pericenter (Kesden, 2012a). For simplicity in this work we only consider prograde encounters ($a_{\rm spin} > 0$), and apply first-order correction factor to the binding energy,

$$E' = \left(1 - \frac{1}{2}\frac{r_{\rm IBCO}}{r_{\rm p}}\right)^{-1/2} E. \tag{6.36}$$

In general, retrograde and/or orbits in which the orbit's inclination is not equal to the black

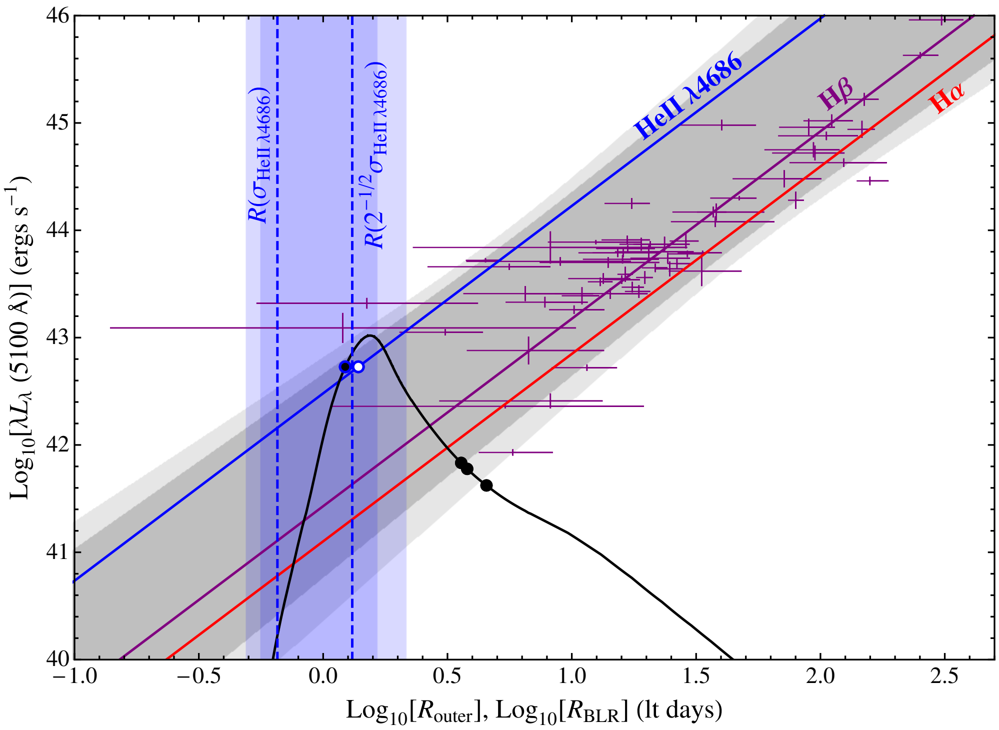

Figure 6.7: Location of BLR in AGN as a function of L at $\lambda = 5100$ Å as compared to the outer radius of the truncated debris disk resulting from a tidal disruption. The purple error bars and purple curve show the data and fit of Peterson (2006) for Hβ, while the red and blue curves show the offsets to the best-fitting Hβ relation as measured by Bentz *et al.* (2010) for Hα and HeII λ4686. The outer radius of the truncated debris disk r_{o} is shown with the black curve, with the time of collection for the four spectra (-22, +227, +254, and +358 restframe days) being denoted by the black points. In all but the last spectrum, in which no lines are apparent, HeII λ4686 was observed and Hα was not observed, which implies that r_{o} must extend beyond the region within which the majority of the flux for HeII λ4686 is produced, but not extend beyond the region within which most of the Hα flux is produced. Thus, the four black points must appear between the red and the blue curves to satisfy this constraint (shaded in gray). Additionally, the velocity dispersion of the HeII λ4686 line (σ_{HeII}) was measured for the first spectrum taken at -22 days. The HeII λ4686 line is assumed to be located along the standard BLR relation, and the velocity of this line predicted by the model is given by matching the luminosity to its associated size on the HeII λ4686 curve (white point). As it is unclear whether the motions being observed are Keplerian or inflow/outflow, the distance implied by the model velocity is constrained between a circular and a parabolic orbit, $GM_{\mathrm{h}}/\sigma^2_{\mathrm{HeII}} < R_{\mathrm{HeII}} < 2GM_{\mathrm{h}}/\sigma^2_{\mathrm{HeII}}$ (dashed vertical blue curves, shaded in blue).

hole's spin inclination would be expected.

AGN show variability from the radio to the X-ray, with variability on the order of a few tenths of a dex being common (Webb and Malkan, 2000). While the photometric errors are small for this event, it is clear that the light curve exhibits some intrinsic variability, as may be expected for an accreting black hole. To model this, we add an additional intrinsic spread $\sigma_{\rm v}$ in quadrature with the observational errors associated with each data point. In addition, the variability has been shown to be dependent on the black hole mass (Uttley and McHardy, 2005). To include this within our modeling, we define a function based on the break in the power spectral density (PSD) of black hole variability using the results of Kelly *et al.* (2011)

$$\begin{aligned}\sigma_{\rm v} &= t_{\rm H}\zeta^2\\ &= 0.0253^{+0.071}_{-0.038} M_7^{-0.19\pm0.78},\end{aligned} \tag{6.37}$$

where $t_{\rm H}$ is the timescale of the break in the PSD, and ζ is the square root of the variability amplitude measured at the break. The quoted error bars are calculated using the fits of Kelly *et al.*.

In total, our fitting procedure includes 15 parameters, 13 of which are continuous (M_*, $M_{\rm h}$, β, $t_{\rm off}$, $a_{\rm spin}$, $\mathcal{V}$, ϕ, κ, l, $R_{\rm ph,0}$, $R_{\rm v}$, $N_{\rm h}$, and $\sigma_{\rm v}$), and 2 of which are discrete ($\mathcal{A}_\gamma$ and $\mathcal{A}_*$).

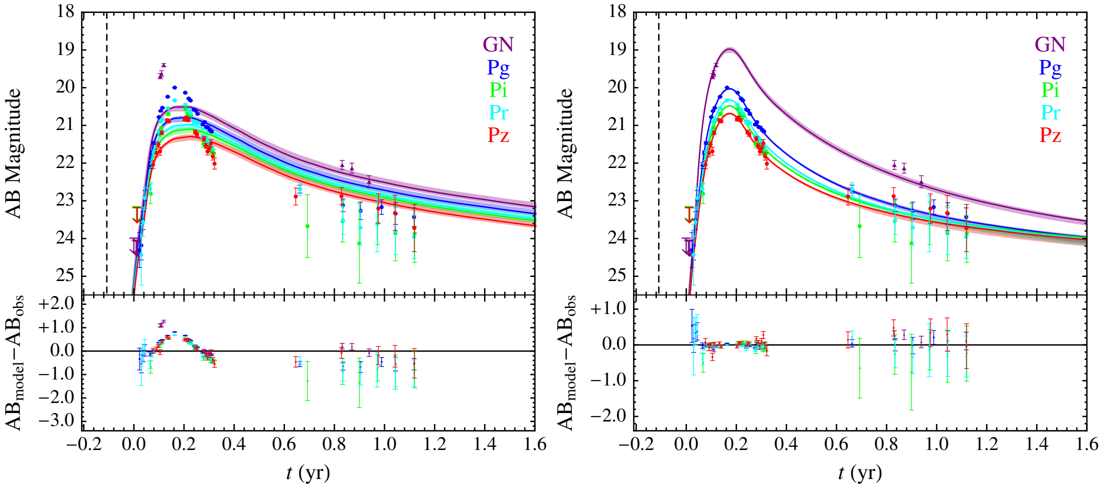

Figure 6.8: Fits of highest likelihood of PS1-10jh for two different models: A bare SS disk (left panel, described in Section 6.6.2), and a disk with a variably-sized reprocessing layer (right panel, described in Section 6.6.3), with the AB magnitude of the data and the models shown in the top panels, and the difference between the highest-likelihood model and the data shown in the bottom panels. The highest-likelihood model found is shown by the solid curves, whereas the 2-σ range in magnitudes encompassed by the full ensemble of walkers is shown by the shaded bands. The five colors correspond to four filters of Pan-STARRS1 system (denoted by Pg, Pi, Pr, and Pz), and the NUV band of the GALEX instrument (denoted as GN).

6.5.2 Using the existence/absence of emission lines and their properties to constrain TDEs

In addition to using the quality of the fit of the model light curves to the data, we also impose additional constraints depending on which lines do or do not exist in spectra taken at various times (Figure 6.7). To do this, we measure the emergent flux at $\lambda = 5100$, which is used in steadily-accreting AGN to measure the continuum, and compare r_{o} to the distance implied by the relationship between $\lambda L_{\lambda}(5100)$ and R_{BLR}, as first determined by Wandel *et al.* (1999) for Hβ. Since then, the relationship between L and R_{BLR} has been more-accurately determined for Hβ (Peterson *et al.*, 2004; Bentz *et al.*, 2013), and for several other emission lines (Bentz *et al.*, 2010). For all lines, it is found that $L \propto R_{\rm BLR}^{0.5}$, indicating that the source of ionizing photons is point-like and that the disk maintains a relatively constant scale-height for a wide range of r, which gives the natural result that the number of ionizing photons $\Phi \propto r^{-2}$.

Our modification to the likelihood function is simple: If a line exists in a spectrum and $r_{\rm o} < R_{\rm BLR}$, or if a line doesn't exist and $r_{\rm o} > R_{\rm BLR}$, we reduce the log-likelihood measured from the light curve alone $\mathcal{L}_{\rm LC}$ by a factor

$$\ln \mathcal{L}_{\rm BLR} = \ln \left[1 - \frac{1}{2}{\rm erfc}\left(\frac{|\ln R_{\rm BLR} - \ln r_{\rm o}|}{2\sigma_{\rm BLR}}\right)\right], \tag{6.38}$$

where $\sigma_{\rm BLR}$ is the error in the measured $L - R_{\rm BLR}$ relation, which we take from Bentz *et al.* (2010).

If a line exists, and a velocity for that line has been measured, we can use that additional information to constrain the event further by relating $R_{\rm BLR}$ to the underlying velocity expected at the position. In steadily-accreting AGN, there is an ambiguity in the velocity measured for the BLR and its location, as it may partially be supported by radiation pressure (Marconi *et al.*, 2008), we ignore this effect here as it only introduces a ∼10% correction (Barth *et al.*, 2011). A greater uncertainty exists in TDE debris disks in that the underlying velocity $v_{\rm BLR}$ can range from Keplerian ($v_{\rm BLR} = v_{\rm K}$) to parabolic ($v_{\rm BLR} = \sqrt{2}v_{\rm K}$), and therefore we cannot constrain the distance implied by $v_{\rm BLR}$ better than a factor of $\sqrt{2}$. Bearing this in mind, our reduction to the log-likelihood assumes the following functional form,

$$\ln \mathcal{L}_v = \begin{cases} v < v_{\rm BLR} & \frac{1}{2}\left(\frac{v-v_{\rm BLR}}{\sigma_{\rm v}}\right)^2 \\ v_{\rm BLR} < v < \sqrt{2}v_{\rm BLR} & 0 \\ v > v_{\rm BLR} & \frac{1}{2}\left(\frac{v-\sqrt{2}v_{\rm BLR}}{\sigma_{\rm v}}\right)^2. \end{cases} \tag{6.39}$$

We show the results of imposing these constraints for PS1-10jh in Figure 6.7, where we plot the distance to which material has traveled $r_{\rm o}$ versus the luminosity at 5100 Å. The specific constraints we have applied are that HeII λ4686 must be produced, and Hα must not be produced, in the four spectra in which the observed light is not dominated by the host galaxy (at -22, +227, +254, and +358 restframe days). We find that $r_{\rm o}$ is sufficiently large to produce HeII λ4686 in all four of these spectra, and that Hα would potentially be observable at later times if the host galaxy did not dominate the observed light (the light is already subdominant to the host galaxy at +254 days). Hβ, which is produced at smaller distances than Hα in steadily-accreting AGN, may potentially be observable in late-time spectra, but its wavelength (4861 Å) notably overlaps with the broad HeII λ4686 feature, and is usually a factor of several weaker than Hα in most AGN (Vanden Berk *et al.*, 2001). We also might expect that Hγ and/or HeI λ5876 may appear at later times, as the distances at which these lines are produced are only slightly larger than the distance at which HeII λ4686 is produced (Bentz *et al.*, 2010). As we had mentioned in Section 6.4.2, we may also be overestimating the size of reprocessing region if it accretes onto the black hole quickly, which would tend to predict the existence of more emission features. Given these uncertainties, we do not impose a constraint on the non-existence of HeI λ5876, Hβ, or Hγ in this work; we note that their inclusion would likely restrict the size of the accretion disk further, which would tend to favor lower-mass black holes.

We note that the constraints we are imposing do not consider the specific luminosity of the lines versus the continuum (see Section 6.4.2), which can strongly affect whether a line is identified within a collected spectrum. This means we also cannot consider in detail the effects of the elliptical accretion disk structure resulting from a tidal disruption on the strengths of the observed lines, which would preferentially reduce the strength of lines originating at large distances as the BLR does not occupy a full 2π in azimuth in the outskirts of the debris structure (Figure 6.2).

6.6 Model Fitting of PS1-10jh, a Prototypical Tidal Disruption

6.6.1 Available Data

For the fitting procedure, we use all of the available data to constrain the event, including four *Pan-STARRS* bands (Pg, Pr, Pi, Pz), the X-ray upper limits from the *Chandra* space-based X-ray telescope (cycle 12), and the spectra taken by the Hectospec instrument on the MMT telescope, all of which are taken from G12. As the data presented in G12 is already corrected for extinction assuming $N_{\rm h} = 7.2 \times 10^{19}$ cm^{-2}, we remove this correction before using the data as an input, as we self-consistently determine the extinction in the model fitting process. We assume a redshift $z = 0.1696$ as is determined in G12 from template fitting to the host galaxy.

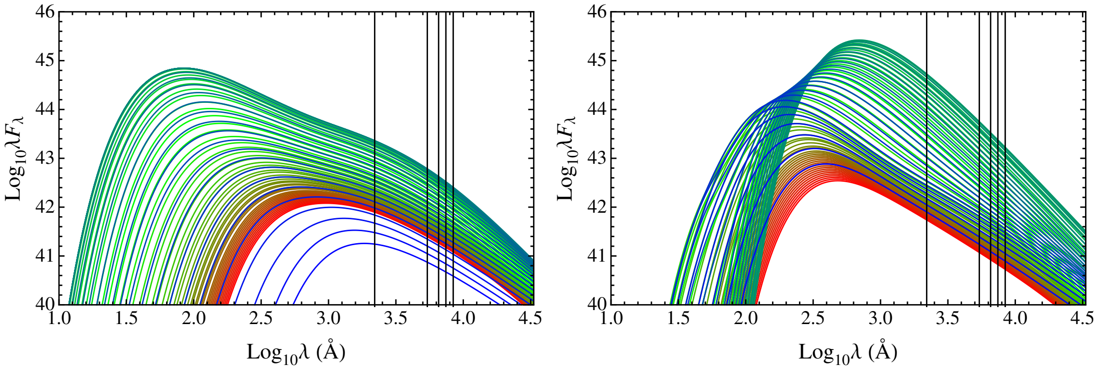

Figure 6.9: Spectral energy distribution of the emergent radiation from the highest-likelihood fits of PS1-10jh as a function of time for the bare disk (left panel) and generalized (right panel) models. The colored curves are spaced equally in $\ln(t-t_\mathrm{d})$, with red corresponding to early times and blue correspond to late times. The vertical black lines show the wavelength of highest transmission for the four *Pan-STARRS* and *GALEX* NUV bands. The bare disk models feature a single component that corresponds to the accretion disk that peaks at $\lambda \sim 10^2$ Å, whereas the generalized model features two components which corresponds to the accretion disk, which peaks at $\lambda \sim 10^2$ Å, and the single-temperature reprocessing component, which peaks at $\lambda \sim 10^3$ Å.

6.6.2 Bare Disk Model

In steadily-accreting AGN disks, the majority of radiation produced by the disk is thought to be intercepted by intervening gas that reprocesses the original emission from the disk. In a TDE, this layer may take some time to form, or may not form at all, depending on the dissipative processes at work. In this case, the light produced as the result of a TDE would resemble a bare Shakura-Sunyaev (SS, Shakura and Sunyaev, 1973) or slim-disk (Abramowicz *et al.*, 1988) model, with peak emission that extends well beyond the tens of eV that is characteristic of AGN spectra. For this model, we do not include the additional constraints imposed by the existence/absence of emission lines.

Fits assuming this "bare" disk model, which are equivalent to our generalized model for TDE debris disks sans the reprocessing layer (cyan region of Figure 6.6), are shown in

Figure 6.8, where it is immediately obvious that a bare disk model is a poor match to PS1-10jh. In order for the bare disk model to closely match the data, the fitting routine settles upon one of two non-ideal solutions: An SED with peak that centers about the range of wavelengths covered by the observed bands, or an SED in which the bands are all within the Rayleigh-jeans tail. In the first case, the luminosity L can closely follow $\dot{M}$, but the color evolves tremendously as the peak of the summed blackbody curves shift into/out of the observed bands. In the latter case, the ratio of fluxes between the observed bands remains constant, but L scales as a much weaker power of $\dot{M}$, $L \propto \dot{M}^{1/4}$ (Figure 6.9).

It has previously been assumed that the size of the disk is controlled by the angular momentum content of the returning material, which is limited to $\sqrt{2GM_{\rm h}r_{\rm t}}$ (see Section 6.3.1 for references). In this case, the disk resembles a bare disk that is "truncated" at $r = 2r_{\rm t}$. We find that these models are an even poorer match to the event.

6.6.3 Fits to Generalized Model With Reprocessing Layer

From the previous section, we know that bare disk models can either reproduce a constant color, or reproduce a luminosity that follows $\dot{M}$, but cannot reproduce both behaviors simultaneously. This suggests that a secondary process is involved that reprocesses a large fraction of the light prior to reaching the observer. In section 6.6.3 we suggested that this mechanism is the absorption of the soft X-ray photons produced primarily at $r \sim r_{\rm g}$ by material deposited at $r \sim a_{\rm p}$.

As can be seen in the right panels of Figures 6.8 and 6.9, these models provide excellent fits to the data; the parameters associated with the fits of highest likelihood are shown in

Table 6.1: Parameters of Highest Likelihood Models

Parameter	Units	Prior	Allowed Range	Value[1]
$\mathrm{Log}_{10} M_*$	$M_\odot$	Flat	$-3 \leq x \leq 2$	$-0.25^{+0.04}_{-0.10}$
$\mathrm{Log}_{10} M_\mathrm{h}$	$M_\odot$	Flat	$4 \leq x \leq 8.6$	$7.04^{+0.08}_{-0.05}$
β	$\cdots$	Flat	$0.5 \leq x \leq 4$	$0.87^{+0.02}_{-0.02}$
t_off	days	Flat	$-700 \leq x \leq 700$	42^{+2}_{-2}
a_spin	$\cdots$	Flat	$0 \leq x \leq 1$	$0.35^{+0.34}_{-0.26}$
$\mathrm{Log}_{10} \mathcal{V}$	$\cdots$	Flat	$-4 \leq x \leq 0$	$-0.0062^{+0.005}_{-0.012}$
ϕ	radians	Flat	$0 \leq x \leq \pi/2$	$0.71^{+0.59}_{-0.52}$
$\mathrm{Log}_{10} \kappa$	$\mathrm{cm}^2\ \mathrm{g}^{-1}$	Flat	$-0.7 \leq x \leq 6$	$-0.31^{+0.27}_{-0.28}$
l	$\cdots$	Flat	$0 \leq x \leq 4$	$0.96^{+0.04}_{-0.04}$
$\mathrm{Log}_{10} R_\mathrm{ph,0}$	$\cdots$	Flat	$-4 \leq x \leq 4$	$-0.77^{+0.05}_{-0.07}$
R_v	$\cdots$	Flat	$2 \leq x \leq 10$	$6.5^{+0.4}_{-0.4}$
$\mathrm{Log}_{10} N_\mathrm{h}$	cm^{-2}	Flat	$17 \leq x \leq 23$	$21^{+0.03}_{-0.03}$
σ_v	$\cdots$	See 6.5.1	$0 \leq x \leq 1$	$0.034^{+0.007}_{-0.007}$

[1] Median value, with ranges corresponding to 1-σ spread from median.

Table 6.1. We immediately caution the reader that the reported medians of the probability distributions, and the small spread in distributions of some parameters, should not be taken at face value. In our generalized model, which is only a simplified realization of the true structure of the debris, we have made many assumptions, and the uncertainty in some of these assumptions is likely to be greater than spread of solutions about the highest-likelihood models presented here. That being said, it is encouraging that such a simple model with relatively few free parameters can provide a reasonable fit to the data, and is highly suggestive of the true values of the underlying parameters.

In the generalized model, we find that the disruption is best matched by the nearly-complete disruption ($\beta = 0.87$) of a low mass star ($M_* = 0.56 M_\odot$) by a $M_\mathrm{h} = 1.1 \times 10^7 M_\odot$ black hole. This combination of parameters is close to the most common sub-Eddington disruption expected (De Colle *et al.*, 2012), but predicts the black hole mass is a factor of a few larger than the black hole mass suggested by G12. Most of this discrepancy is likely to arise not from improper template fitting of the host galaxy, but rather the large intrinsic scatter in the $M_{\rm h}$-L relation, as black holes of mass $10^6 \leq M_{\rm h}/M_{\odot} \leq 10^9$ have been found for other galaxies of similar magnitude (Graham and Scott, 2013). The disruption is predicted to have occurred 42 days prior to the first observation, about 20 days prior to what was originally suggested in G12.

We find that $a_{\rm spin}$ is only loosely constrained, with the main effects of a larger spin being that deeper-β encounters would be permitted (which are disfavored anyway), and an increase in the efficiency of converting mass to light. The inclination ϕ is highly degenerate with this parameter, and shows a strong anti-correlation (i.e. more-slowly spinning black holes tend to be more face-on). We find that the preferred models increase $\mathcal{V}$ to as large a value as possible, and likely this result would be altered given a physical model for $\mathcal{V}$ that accounts for all the various dissipation processes (see Section 6.3.2).

The mass-averaged opacity $\kappa = 0.5$ cm^2 g^{-1} is slightly larger than Thomson, consistent with the expectation that the opacity is dominated by electron scattering with some contribution from bound-free absorption by partially-ionized species heavier than hydrogen (with potentially a large contribution coming from singly-ionized helium). We find that $l = 0.96$, which is larger than $1/2$ and indicates that the photosphere temperature does evolve to some degree during the encounter, with $T \propto \dot{M}^{-0.23}$ (Equation 6.31). The fact that the highest-likelihood models settle on this temperature evolution is a consequence of the increase in flux in the Pz band relative to other bands at late times. A truly isothermal photosphere could be achieved if its location is mediated by the recombination of a single species (acting as a thermostat), in which case $m = 0$. The fact that the highest-likelihood models deviate from this value indicates that either the distribution of matter in radius and height may be non-trivial, or that multiple species may be responsible for setting the observed temperature (Lawrence, 2012). The photosphere scale parameter $R_{\mathrm{ph},0} = 0.17$ corresponds to a physical size of 5.4×10^{14} cm at peak (approximately 50 times larger than pericenter distance $r_{\mathrm{p}} = 1.1 \times 10^{13}$ cm), the time evolution of which is shown in the right panel of Figure 6.6. This distance is approximately the distance at which helium becomes doubly ionized (Figure 6.5).

For the extinction in the host galaxy, we find that a column of $N_{\mathrm{h}} = 10^{21}$ cm^{-2} is preferred, with a reddening parameter $R_{\mathrm{v}} = 6.5$. This value is somewhat higher than what is typically observed within the Milky Way ($R_{\mathrm{v}} = 3.1$), and is more representative of "gray" dust in which all wavelengths are absorbed equally. Such values of R_{v} have been observed outside of the Milky Way (see e.g. Falco *et al.*, 1999), and are typical of dense molecular clouds (Draine, 2003). Another possibility that our generalized model simply does not produce enough UV photons, necessitating a gray opacity law to compensate.

Lastly, we find that the model requires $\sigma_{\mathrm{v}} = 0.034$ magnitudes of intrinsic variability, well within the expected range given a black hole mass of $10^7 M_\odot$ (Equation 6.37), and surprisingly small given the potentially chaotic nature of the accretion process. This strongly suggests that the accretion process is smooth and regular, with no major changes in global structure over short timescales.

We find that our highest-likelihood models with and without the BLR constraints are very similar to one another. In Figure 6.10, we present the posteriors of four parameters that showed the most change (M_{h}, M_*, a_{spin}, and $R_{\mathrm{ph},0}$) when the BLR constraints are removed, and find that difference in the posteriors is on the same order as the scatter about the median. This

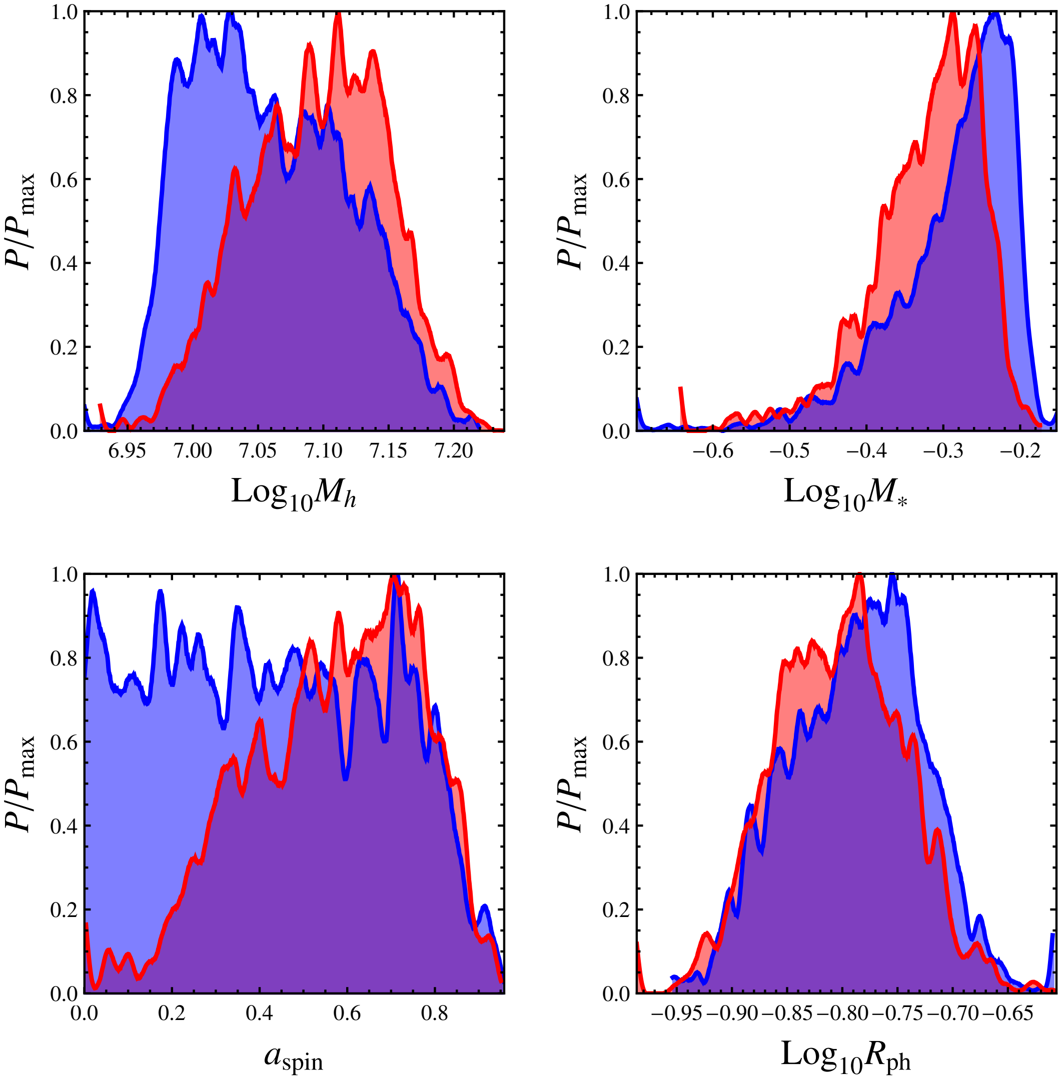

Figure 6.10: Posterior distributions of $M_{\rm h}$, M_*, $a_{\rm spin}$, and $R_{\rm ph,0}$ for PS1-10jh. Within each panel are the probability P scaled to the maximum probability $P_{\rm max}$, with the red curves showing the posteriors when the BLR constraints are not included, and the blue curves showing the posteriors when they are included. With the constraints, slightly smaller $M_{\rm h}$ and slightly larger M_* are preferred, leading to a slightly larger photosphere scaling parameter $R_{\rm ph,0}$ to compensate.

suggests that the timescale, luminosity, and color of PS1-10jh are sufficient to constrain most of the physical parameters of an event, whereas the BLR constraints can be used as a sanity check to ensure there is no discrepancy between the existent BLR emission regions and the observed spectra.

6.7 Discussion

6.7.1 Arguments against the helium star interpretation

The discovery of a flare with no noticeable hydrogen features certainly hints at the possibility that the disrupted star may have been relatively devoid of hydrogen. Aside from the hypothesis presented in the previous sections, there are other reasons to believe why the helium-rich progenitor scenario might be unlikely.

Firstly, helium-rich stars are rare in the universe. The known candidates are SdB/SdO stars ($\sim 10^6$ in the MW, Han *et al.*, 2003), helium WDs ($\sim 10^7$ in the MW, Nelemans *et al.*, 2001b), and WR stars ($\sim 10^4$ in the MW, van der Hucht, 2001). While there is some evidence that the mass function around SMBHs is not well-represented by a canonical IMF (Bartko *et al.*, 2010), it seems unlikely that the numbers of these stars could be increased by the factor of $\sim 10^4$–10^7 required to plausibly explain why the first well-resolved TDE happened to be a helium-rich star.

A second possibility is that the helium-rich star comes as the result of the previous interaction of a giant star with the SMBH, or potentially through a collision between the giant and a more compact stellar object (Davies *et al.*, 1991). However, in both of these cases, hydrogen is not completely removed from the star. In fact, even for deep tidal encounters, the core tends to retain an atmospheric mass of hydrogen comparable to its own mass (MacLeod *et al.*, 2012). Additionally, giant stars do not frequently get deposited into highly-bound orbits in which the core itself is likely to be disrupted, as the densities of their cores are $\gtrsim 10^3$ times larger than their envelopes, and their orbital migration into the loss-cone is largely dictated by diffusion (Wang and Merritt, 2004; MacLeod *et al.*, 2012).

We can thus conclude that while helium-rich disruptions will occur occasionally, they will not be the dominant contributor to the rate, and as a result, it is highly unlikely by chance that these disruptions would be among the first to be observed.

6.7.2 Inclusion of priors

In this work, we do not make any assumptions about the distribution of any of our input parameters, with the exception of our intrinsic variability parameter $\sigma_{\rm v}$ (see Section 6.5.1). For example, the distribution of stars around SMBHs is likely to possess a current mass function (CMF) that is strongly related to the initial mass function (IMF), which would suggest that the most likely stars to be disrupted are those with $M_* \sim 0.1 M_\odot$ (Kroupa, 2001). Additionally, we might expect that that grazing encounters (e.g. small β) should outnumber deep encounters (Frank and Rees, 1976), and the black hole mass should follow established $M_{\rm h}$-L relations (Graham and Scott, 2013).

This prior information could be used to further constrain the parameters of any given event. However, each of these priors has a great deal of uncertainty associated with it. In our own galactic center, it is not clear if the distribution of stars is similar to the general IMF observed in the field, especially given the prevalence of short-lived B-stars within several lt-days of the black hole (Gillessen *et al.*, 2009). These stars may have been deposited through binary disruption (Ginsburg and Loeb, 2006), or through a disk (Madigan *et al.*, 2011), both of which would lead to different distribution in β than what would be produced by a steady-state, spherically symmetric cluster around the black hole (à la Wang and Merritt, 2004). Lastly, while a clear trend has been demonstrated between the luminosity of the host galaxy and the mass of its black hole, there is significant scatter about this trend (Gültekin *et al.*, 2009). In principle, once a significant number of TDEs have been identified, these distributions can be determined from the collection of fits to all disruptions, which could potentially improve the accuracy of parameter estimations of future events.

6.7.3 How BLRs can help us understand TDEs

The (non-)existence of various lines in spectra acquired of TDEs can be used to great effect to constrain the parameter space of allowed encounters for any particular event. These features enable one to place a time-dependent size constraint on the size of the debris structure resulting from a tidal disruption, which is directly related to the combination of three parameters: $M_{\rm h}$, M_*, and β (Equation 6.9). In this chapter, we have focused specifically on HeII λ4686 and Hα in regards to PS1-10jh, but our technique could be used in general with other emission lines. PS1-10jh appears to originate from a moderately-massive SMBH, but disruptions of stars by more or less massive black holes would respectively produce larger or smaller structures from which emission lines could be produced. As an example, the disruption of the same star by a $10^8 M_\odot$ may show Hβ and HeI λ5876 features early, with Hα appearing later, whereas a disruption by a $10^6 M_\odot$ black hole may never show any helium or hydrogen emission lines.

In the optical at $z = 0$, the number of strong emission lines is limited, but many more emission lines are available in the UV and X-ray where metals with larger ionization potentials begin to lose their electrons. These lines, which would be produced nearer to the SMBH, could potentially be used to constrain the size scale at early times, and would provide a spatial map of the accretion disk as it grows. It is critical that TDEs are identified early and followed up spectroscopically to obtain this valuable information.

6.7.4 How TDEs can help us understand BLRs

The BLR has long been used to measure the masses of black holes from the lag times observed in the response of various emission lines, which are thought to lie at various distances. However, there remains much uncertainty in these models, namely the form of the BLR itself. If the dissipation mechanism within the debris disks resulting from tidal disruptions is similar to the dissipation mechanism that controls angular momentum transport in steadily-accreting AGN, it is reasonable to expect that the two structures should have many similarities in terms of their density and temperature profiles, velocity structures, and in the components of the structure that conspire to produce the emergent light.

In this chapter, we have made direct comparisons to BLRs in order to understand the emission features that are observed in a particular event. As we have shown, the dependence between the distance at which a particular emission line is produced and the flux originating from the central engine is even more exaggerated than in the case of steadily-accreting AGN, as some line-emitting regions do not exist at all due to the absence of mass beyond a certain distance. With a larger catalogue of TDEs, we can reverse the arguments presented here to learn more about the structure of the BLR present in TDE debris disks.

6.7.5 Caveats and future directions

At the time of this writing, PS1-10jh is the only event that is claimed to be a TDE and also captures the rise, peak, and decay of the flare. By capturing all three phases, and with the addition of spectroscopic information, this event provides significantly more information on the underlying mechanisms than the small number of poorly sampled UV/optical TDEs that only capture the decay phase and may have no spectroscopic data (Gezari *et al.*, 2006, 2008; Cappelluti *et al.*, 2009; van Velzen *et al.*, 2011; Cenko *et al.*, 2012). While the models presented here provide compelling evidence of the similarities between steadily-accreting AGN and luminous flares resulting from the tidal disruptions of stars, there are many aspects that can be improved upon. Some uncertainties in the generalized model presented here, such as details on the viscous processes that govern accretion and how matter light is reprocessed, could potentially be resolved with a more-complete collection of well-sampled TDEs.

It is clear from our purely hydrodynamical simulations that mere gas dynamics is incapable of generating the necessary dissipation for high mass-ratio encounters, as we described in Section 6.3.3. This suggests that magnetohydrodynamical simulations that focus on the nozzle region need to be performed to examine the growth of the MRI, which by our estimate may be capable of providing the required dissipation. If this mechanism is incapable of operating, then it is possible that only deeply-penetrating encounters in which $r_{\rm p} \sim r_{\rm g}$ will yield rapidly-rising light curves.

A second critical uncertainty is our treatment of the reprocessing layer, which is inextricably linked to the BLR of TDE debris disks. In this work, we have presumed that this reprocessing layer is spherical, parameterized the amount of light absorbed by an average gray opacity, and have ignored potentially complex radiation transport and line-of-sight effects. It is also unlikely that the BLR relations we compare to here are identical for debris disks resulting from disruption, given their elliptical geometry and different radial mass distributions. While the scaling relations determined for steadily-accreting AGN are likely to be similar to TDE scaling relations, meaningful constraints on individual events can only be obtained by revising these relations to account for the differences.

Given a more-accurate prescription of how the viscous and reprocessing mechanisms operate, `TDEFit` can easily be improved to include these additional aspects of the problem, which can potentially yield very accurate estimates of the parameters associated with individual disruption events. With a large library of TDEs, which will likely exist in the LSST era when potentially thousands of TDEs may be detected (van Velzen *et al.*, 2011), it should be possible to obtain detailed demographics of the stellar clusters that surround SMBHs.

6.7.6 Lessons Learned

For the readers convenience, we summarize the main findings of this chapter below.

1. The unbound material, while ejected at high velocity from pericenter after a disruption, is gravitationally confined in the two directions transverse to its motion. This constricts the debris to a thin stream that presents a negligible surface area as compared to the emitting surface generated by the return of the stream to pericenter, and is unlikely to affect the flare’s appearance.

2. When material returns to pericenter, it is heated via hydrodynamical shocks, but this dissipation is likely insufficient to explain the tight relationship between L and $\dot{M}$ for large-q encounters. Additional dissipation via an MRI-like mechanism or through general relativistic precession is probably required to explain this observed relationship.

3. A disk that is truncated at $2r_{\rm t}$ fails drastically in explaining the observed flare, and cannot match the observed shape of the light curves without extreme color evolution.

4. The light curve of PS1-10jh is well modeled by a single blackbody whose temperature evolves weakly in time, and whose size is tens of times larger than $r_{\rm t}$. We speculate that this distance is roughly co-spatial with the distance at which helium is doubly-ionized.

5. The fact that HeII emission lines are observed, but Hα and Hβ are not, is consistent with the size constraint on the bound debris that is ejected from the nozzle point upon returning to pericenter. In general, the presence or absence of various emission lines can be used as a probe of the size of the elliptical debris disk.

6. The parameters for PS1-10jh of our highest-likelihood fits indicate that a $0.56M_{\odot}$ main-sequence star was partially disrupted by a $1.1 \times 10^{7}M_{\odot}$ black hole. As this involves the disruption of a common star by a common SMBH with an impact parameter near the expected average, TDEs of the kind we associate with PS1-10jh are likely to be among the most common sub-Eddington disruption events. However, given that we are analyzing a single event in this chapter, we cannot eliminate the possibility that an event of this type was among the first observed due to observational bias. Once more well-sampled TDEs are available, a joint analysis of many events similar to what we perform here is required

for a complete understanding of the demographics of tidal disruption.

Bibliography

Abramowicz, M. A.; Czerny, B.; Lasota, J. P. and Szuszkiewicz, E. Slim accretion disks. ApJ **332**, 646 (1988).

Aizenman, M. L. The Equilibrium and the Stability of the Roche-Riemann Ellipsoids. ApJ **153**, 511 (1968).

Alexander, T. Stellar processes near the massive black hole in the Galactic center. Phys. Rep. **419**, 65 (2005).

Alsubai, K. A.; Parley, N. R.; Bramich, D. M.; West, R. G.; Sorensen, P. M.; Collier Cameron, A.; Latham, D. W.; Horne, K.; Anderson, D. R.; Brown, D. J. A.; Buchhave, L. A.; Esquerdo, G. A.; Everett, M. E.; Fürész, G.; Hellier, C.; Miller, G. M.; Pollacco, D.; Quinn, S. N.; Smith, J. C.; Stefanik, R. P. and Szentgyorgyi, A. Qatar-1b: a hot Jupiter orbiting a metal-rich K dwarf star. *ArXiv* **arXiv:1012.3027** (2010).

Antonini, F.; Faber, J.; Gualandris, A. and Merritt, D. Tidal Breakup of Binary Stars at the Galactic Center and Its Consequences. ApJ **713**, 90 (2010).

Antonini, F.; Lombardi, J. C. J. and Merritt, D. Tidal Breakup of Binary Stars at the Galactic Center. II. Hydrodynamic Simulations. ApJ **731**, 128 (2011).

Antonucci, R. Unified models for active galactic nuclei and quasars. A&A Rev. **31**, 473 (1993).

Arras, P. and Socrates, A. Thermal Tides in Fluid Extrasolar Planets. ApJ **714**, 1 (2010).

Bakos, G. Ã.; Hartman, J.; Torres, G.; Latham, D. W.; Kovács, G.; Noyes, R. W.; Fischer, D. A.; Johnson, J. A.; Marcy, G. W.; Howard, A. W.; Kipping, D.; Esquerdo, G. A.; Shporer, A.; Béky, B.; Buchhave, L. A.; Perumpilly, G.; Everett, M.; Sasselov, D. D.; Stefanik, R. P.; Lázár, J.; Papp, I. and Sári, P. HAT-P-20b-HAT-P-23b: Four Massive Transiting Extrasolar Planets. *ArXiv* **arXiv:1008.3388** (2010).

Balbus, S. A. and Hawley, J. F. Instability, turbulence, and enhanced transport in accretion disks. *Reviews of Modern Physics* **70**, 1 (1998).

Band, D. L.; Grindlay, J. E.; Hong, J.; Fishman, G.; Hartmann, D. H.; Garson, A.; Krawczynski, H.; Barthelmy, S.; Gehrels, N. and Skinner, G. EXIST's Gamma-Ray Burst Sensitivity. ApJ **673**, 1225 (2008).

Barnes, S. A. On the Rotational Evolution of Solar- and Late-Type Stars, Its Magnetic Origins, and the Possibility of Stellar Gyrochronology. ApJ **586**, 464 (2003).

Barnes, S. A. and Kim, Y.-C. Angular Momentum Loss from Cool Stars: An Empirical Expression and Connection to Stellar Activity. ApJ **721**, 675 (2010).

Barth, A. J.; Nguyen, M. L.; Malkan, M. A.; Filippenko, A. V.; Li, W.; Gorjian, V.; Joner, M. D.; Bennert, V. N.; Botyanszki, J.; Cenko, S. B.; Childress, M.; Choi, J.; Comerford,

J. M.; Cucciara, A.; da Silva, R.; Duchêne, G.; Fumagalli, M.; Ganeshalingam, M.; Gates, E. L.; Gerke, B. F.; Griffith, C. V.; Harris, C.; Hintz, E. G.; Hsiao, E.; Kandrashoff, M. T.; Keel, W. C.; Kirkman, D.; Kleiser, I. K. W.; Laney, C. D.; Lee, J.; Lopez, L.; Lowe, T. B.; Moody, J. W.; Morton, A.; Nierenberg, A. M.; Nugent, P.; Pancoast, A.; Rex, J.; Rich, R. M.; Silverman, J. M.; Smith, G. H.; Sonnenfeld, A.; Suzuki, N.; Tytler, D.; Walsh, J. L.; Woo, J.-H.; Yang, Y. and Zeisse, C. Broad-line Reverberation in the Kepler-field Seyfert Galaxy Zw 229-015. ApJ **732**, 121 (2011).

Bartko, H.; Martins, F.; Trippe, S.; Fritz, T. K.; Genzel, R.; Ott, T.; Eisenhauer, F.; Gillessen, S.; Paumard, T.; Alexander, T.; Dodds-Eden, K.; Gerhard, O.; Levin, Y.; Mascetti, L.; Nayakshin, S.; Perets, H. B.; Perrin, G.; Pfuhl, O.; Reid, M. J.; Rouan, D.; Zilka, M. and Sternberg, A. An Extremely Top-Heavy Initial Mass Function in the Galactic Center Stellar Disks. ApJ **708**, 834 (2010).

Beloborodov, A. M. Accretion Disk Models. *High Energy Processes in Accreting Black Holes* **161**, 295 (1999).

Bentz, M. C.; Denney, K. D.; Grier, C. J.; Barth, A. J.; Peterson, B. M.; Vestergaard, M.; Bennert, V. N.; Canalizo, G.; De Rosa, G.; Filippenko, A. V.; Gates, E. L.; Greene, J. E.; Li, W.; Malkan, M. A.; Pogge, R. W.; Stern, D.; Treu, T. and Woo, J.-H. The Low-Luminosity End of the Radius-Luminosity Relationship for Active Galactic Nuclei. *arXiv* (2013).

Bentz, M. C.; Walsh, J. L.; Barth, A. J.; Yoshii, Y.; Woo, J.-H.; Wang, X.; Treu, T.; Thornton, C. E.; Street, R. A.; Steele, T. N.; Silverman, J. M.; Serduke, F. J. D.; Sakata, Y.; Minezaki, T.; Malkan, M. A.; Li, W.; Lee, N.; Hiner, K. D.; Hidas, M. G.; Greene, J. E.; Gates, E. L.;

Ganeshalingam, M.; Filippenko, A. V.; Canalizo, G.; Bennert, V. N. and Baliber, N. The Lick AGN Monitoring Project: Reverberation Mapping of Optical Hydrogen and Helium Recombination Lines. ApJ **716**, 993 (2010).

Benz, W.; Cameron, A. G. W.; Press, W. H. and Bowers, R. L. Dynamic mass exchange in doubly degenerate binaries. I - 0.9 and 1.2 solar mass stars. ApJ **348**, 647 (1990).

Bicknell, G. V. and Gingold, R. A. On tidal detonation of stars by massive black holes. ApJ **273**, 749 (1983).

Bildsten, L.; Shen, K. J.; Weinberg, N. N. and Nelemans, G. Faint Thermonuclear Supernovae from AM Canum Venaticorum Binaries. ApJ **662**, L95 (2007).

Bodenheimer, P.; Lin, D. N. C. and Mardling, R. A. On the Tidal Inflation of Short-Period Extrasolar Planets. ApJ **548**, 466 (2001).

Brassart, M. and Luminet, J. P. Shock waves in tidally compressed stars by massive black holes. A&A **481**, 259 (2008).

Bryan, G. L.; Norman, M. L.; Stone, J. M.; Cen, R. and Ostriker, J. P. A piecewise parabolic method for cosmological hydrodynamics. *Computer Physics Communications* **89**, 149 (1995).

Cannizzo, J. K.; Lee, H. M. and Goodman, J. The disk accretion of a tidally disrupted star onto a massive black hole. ApJ **351**, 38 (1990).

Cappelluti, N.; Ajello, M.; Rebusco, P.; Komossa, S.; Bongiorno, A.; Clemens, C.; Salvato, M.;

Esquej, P.; Aldcroft, T.; Greiner, J. and Quintana, H. A candidate tidal disruption event in the Galaxy cluster Abell 3571. A&A **495**, L9 (2009).

Cardelli, J. A.; Clayton, G. C. and Mathis, J. S. The relationship between infrared, optical, and ultraviolet extinction. ApJ **345**, 245 (1989).

Carter, B. and Luminet, J. Pancake detonation of stars by black holes in galactic nuclei. Nature **296**, 211 (1982).

Carter, B. and Luminet, J. Tidal compression of a star by a large black hole. I Mechanical evolution and nuclear energy release by proton capture. A&A **121**, 97 (1983).

Carter, B. and Luminet, J. P. Mechanics of the affine star model. MNRAS **212**, 23 (1985).

Cartwright, D. E. *Tides: A Scientific History*. Cambridge University Press (1999).

Caughlan, G. R. and Fowler, W. A. Thermonuclear Reaction Rates V. *Atomic Data and Nuclear Data Tables* **40**, 283 (1988).

Celotti, A. and Rees, M. J. Reprocessing of radiation by multiâĂŘphase gas in lowâĂŘluminosity accretion flows. MNRAS **305**, L41 (1999).

Cenko, S. B.; Bloom, J. S.; Kulkarni, S. R.; Strubbe, L. E.; Miller, A. A.; Butler, N. R.; Quimby, R. M.; Gal-Yam, A.; Ofek, E. O.; Quataert, E.; Bildsten, L.; Poznanski, D.; Perley, D. A.; Morgan, A. N.; Filippenko, A. V.; Frail, D. A.; Arcavi, I.; Ben-Ami, S.; Cucchiara, A.; Fassnacht, C. D.; Green, Y.; Hook, I. M.; Howell, D. A.; Lagattuta, D. J.; Law, N. M.; Kasliwal, M. M.; Nugent, P. E.; Silverman, J. M.; Sullivan, M.; Tendulkar, S. P. and Yaron,

O. PTF10iya: a short-lived, luminous flare from the nuclear region of a star-forming galaxy. MNRAS **420**, 2684 (2012).

Champagne, A. E. and Wiescher, M. Explosive Hydrogen Burning. *Annual Review of Nuclear and Particle Science* **42**, 39 (1992).

Chandrasekhar, S. *An Introduction to the Study of Stellar Structure*. The University of Chicago Press (1939).

Chandrasekhar, S. Hydrodynamic and hydromagnetic stability. *International Series of Monographs on Physics* (1961).

Chandrasekhar, S. Ellipsoidal figures of equilibrium. *The Silliman Foundation Lectures* (1969).

Clausen, D. and Eracleous, M. Probing Intermediate-mass Black Holes with Optical Emission Lines from Tidally Disrupted White Dwarfs. ApJ **726**, 34 (2011).

Colella, P. and Woodward, P. R. The Piecewise Parabolic Method (PPM) for Gas-Dynamical Simulations. *Journal of Computational Physics* **54**, 174 (1984).

Cowling, T. G. The non-radial oscillations of polytropic stars. MNRAS **101**, 367 (1941).

Cuadra, J.; Nayakshin, S.; Springel, V. and di Matteo, T. Galactic Centre stellar winds and Sgr A* accretion. MNRAS **366**, 358 (2006).

Cunha, K.; Sellgren, K.; Smith, V. V.; Ramirez, S. V.; Blum, R. D. and Terndrup, D. M. Chemical Abundances of Luminous Cool Stars in the Galactic Center from High-Resolution Infrared Spectroscopy. ApJ **669**, 1011 (2007).

Dan, M.; Rosswog, S. and Brüggen, M. Mass transfer dynamics in double degenerate binary systems. *Journal of Physics: Conference Series* **172**, 2034 (2009).

Davies, M. B.; Benz, W. and Hills, J. G. Stellar encounters involving red giants in globular cluster cores. ApJ **381**, 449 (1991).

De Colle, F.; Guillochon, J.; Naiman, J. and Ramirez-Ruiz, E. The Dynamics, Appearance, and Demographics of Relativistic Jets Triggered by Tidal Disruption of Stars in Quiescent Supermassive Black Holes. ApJ **760**, 103 (2012).

Diener, P.; Frolov, V. P.; Khokhlov, A. M.; Novikov, I. D. and Pethick, C. J. Relativistic Tidal Interaction of Stars with a Rotating Black Hole. ApJ **479**, 164 (1997).

Diener, P.; Kosovichev, A. G.; Kotok, E. V.; Novikov, I. D. and Pethick, C. J. Non-linear effects at tidal capture of stars by a massive black hole - II. Compressible affine models and tidal interaction after capture. MNRAS **275**, 498 (1995).

Dobbs-Dixon, I.; Lin, D. N. C. and Mardling, R. A. Spin-Orbit Evolution of Short-Period Planets. ApJ **610**, 464 (2004).

Done, C.; Davis, S. W.; Jin, C.; Blaes, O. and Ward, M. Intrinsic disc emission and the soft X-ray excess in active galactic nuclei. MNRAS **-1**, no (2012).

Draine, B. T. Interstellar Dust Grains. A&A Rev. **41**, 241 (2003).

D'Souza, M. C. R.; Motl, P. M.; Tohline, J. E. and Frank, J. Numerical Simulations of the Onset and Stability of Dynamical Mass Transfer in Binaries. ApJ **643**, 381 (2006).

Durney, B. R.; De Young, D. S. and Roxburgh, I. W. On the generation of the large-scale and turbulent magnetic fields in solar-type stars. Sol. Phys. **145**, 207 (1993).

Eggleton, P. P.; Kiseleva, L. G. and Hut, P. The Equilibrium Tide Model for Tidal Friction. ApJ **499**, 853 (1998).

Eracleous, M.; Livio, M.; Halpern, J. P. and Storchi-Bergmann, T. Elliptical accretion disks in active galactic nuclei. ApJ **438**, 610 (1995).

Evans, C. R. and Kochanek, C. S. The tidal disruption of a star by a massive black hole. ApJ **346**, L13 (1989).

Faber, J. A.; Rasio, F. A. and Willems, B. Tidal interactions and disruptions of giant planets on highly eccentric orbits. *Icarus* **175**, 248 (2005).

Fabian, A. C.; Iwasawa, K.; Reynolds, C. S. and Young, A. J. Broad Iron Lines in Active Galactic Nuclei. PASP **112**, 1145 (2000).

Fabrycky, D. and Tremaine, S. Shrinking Binary and Planetary Orbits by Kozai Cycles with Tidal Friction. ApJ **669**, 1298 (2007).

Falco, E. E.; Impey, C. D.; Kochanek, C. S.; Lehar, J.; McLeod, B. A.; Rix, H. W.; Keeton, C. R.; Munoz, J. A. and Peng, C. Y. Dust and Extinction Curves in Galaxies with z>0: The Interstellar Medium of Gravitational Lens Galaxies. ApJ **523**, 617 (1999).

Fink, M.; Hillebrandt, W. and Röpke, F. K. Double-detonation supernovae of sub-Chandrasekhar mass white dwarfs. A&A **476**, 1133 (2007).

Foley, R. J.; Chornock, R.; Filippenko, A. V.; Ganeshalingam, M.; Kirshner, R. P.; Li, W.; Cenko, S. B.; Challis, P. J.; Friedman, A. S.; Modjaz, M.; Silverman, J. M. and Wood-Vasey, W. M. SN 2008ha: An Extremely Low Luminosity and Exceptionally Low Energy Supernova. AJ **138**, 376 (2009).

Ford, E. B. and Rasio, F. A. Origins of Eccentric Extrasolar Planets: Testing the Planet-Planet Scattering Model. ApJ **686**, 621 (2008).

Foreman-Mackey, D.; Hogg, D. W.; Lang, D. and Goodman, J. emcee: The MCMC Hammer. PASP **125**, 306 (2013).

Fortney, J. J.; Marley, M. S. and Barnes, J. W. Planetary Radii across Five Orders of Magnitude in Mass and Stellar Insolation: Application to Transits. ApJ **659**, 1661 (2007).

Foucart, F. and Lai, D. Evolution of spin direction of accreting magnetic protostars and spin-orbit misalignment in exoplanetary systems - II. Warped discs. MNRAS p. 234 (2011).

Frank, J.; King, A. and Raine, D. J. Accretion Power in Astrophysics: Third Edition. *Accretion Power in Astrophysics* (2002).

Frank, J. and Rees, M. J. Effects of massive central black holes on dense stellar systems. MNRAS **176**, 633 (1976).

Frolov, V. P.; Khokhlov, A. M.; Novikov, I. D. and Pethick, C. J. Relativistic tidal interaction of a white dwarf with a massive black hole. ApJ **432**, 680 (1994).

Fryxell, B.; Olson, K.; Ricker, P.; Timmes, F. X.; Zingale, M.; Lamb, D. Q.; MacNeice, P.;

Rosner, R.; Truran, J. W. and Tufo, H. FLASH: An Adaptive Mesh Hydrodynamics Code for Modeling Astrophysical Thermonuclear Flashes. ApJS **131**, 273 (2000).

Garaud, P. What happened to the other Mohicans? Realistic models of metallicity dilution by fingering convection and observational implications. *ArXiv* **arXiv:1011.3452** (2010).

Gaskell, C. M. Accretion Disks and the Nature and Origin of AGN Continuum Variability. *The Nuclear Region, Host Galaxy and Environment of Active Galaxies* **32**, 1 (2008).

Gaskell, C. M. What broad emission lines tell us about how active galactic nuclei work. New A Rev. **53**, 140 (2009).

Geha, M.; Guhathakurta, P. and van der Marel, R. P. Internal Dynamics, Structure, and Formation of Dwarf Elliptical Galaxies. I. A Keck/Hubble Space Telescope Study of Six Virgo Cluster Dwarf Galaxies. AJ **124**, 3073 (2002).

Gezari, S.; Basa, S.; Martin, D. C.; Bazin, G.; Forster, K.; Milliard, B.; Halpern, J. P.; Friedman, P. G.; Morrissey, P.; Neff, S. G.; Schiminovich, D.; Seibert, M.; Small, T. and Wyder, T. K. UV/Optical Detections of Candidate Tidal Disruption Events by GALEX and CFHTLS. ApJ **676**, 944 (2008).

Gezari, S.; Chornock, R.; Rest, A.; Huber, M. E.; Forster, K.; Berger, E.; Challis, P. J.; Neill, J. D.; Martin, D. C.; Heckman, T.; Lawrence, A.; Norman, C.; Narayan, G.; Foley, R. J.; Marion, G. H.; Scolnic, D.; Chomiuk, L.; Soderberg, A.; Smith, K.; Kirshner, R. P.; Riess, A. G.; Smartt, S. J.; Stubbs, C. W.; Tonry, J. L.; Wood-Vasey, W. M.; Burgett, W. S.; Chambers, K. C.; Grav, T.; Heasley, J. N.; Kaiser, N.; Kudritzki, R.-P.; Magnier, E. A.; Morgan,

J. S. and Price, P. A. An ultraviolet–optical flare from the tidal disruption of a helium-rich stellar core. Nature **485**, 217 (2012).

Gezari, S.; Heckman, T.; Cenko, S. B.; Eracleous, M.; Forster, K.; Gonçalves, T. S.; Martin, D. C.; Morrissey, P.; Neff, S. G.; Seibert, M.; Schiminovich, D. and Wyder, T. K. Luminous Thermal Flares from Quiescent Supermassive Black Holes. ApJ **698**, 1367 (2009).

Gezari, S.; Martin, D. C.; Milliard, B.; Basa, S.; Halpern, J. P.; Forster, K.; Friedman, P. G.; Morrissey, P.; Neff, S. G.; Schiminovich, D.; Seibert, M.; Small, T. and Wyder, T. K. Ultraviolet Detection of the Tidal Disruption of a Star by a Supermassive Black Hole. ApJ **653**, L25 (2006).

Ghez, A. M.; Salim, S.; Weinberg, N. N.; Lu, J. R.; Do, T.; Dunn, J. K.; Matthews, K.; Morris, M. R.; Yelda, S.; Becklin, E. E.; Kremenek, T.; Milosavljevic, M. and Naiman, J. Measuring Distance and Properties of the Milky Way's Central Supermassive Black Hole with Stellar Orbits. ApJ **689**, 1044 (2008).

Gillessen, S.; Eisenhauer, F.; Trippe, S.; Alexander, T.; Genzel, R.; Martins, F. and Ott, T. Monitoring Stellar Orbits Around the Massive Black Hole in the Galactic Center. ApJ **692**, 1075 (2009).

Ginsburg, I. and Loeb, A. The fate of former companions to hypervelocity stars originating at the Galactic Centre. MNRAS **368**, 221 (2006).

Gnat, O. and Ferland, G. J. Ion-by-ion Cooling Efficiencies. ApJS **199**, 20 (2012).

Gokhale, V.; Peng, X. M. and Frank, J. Evolution of Close White Dwarf Binaries. ApJ **655**, 1010 (2007).

Goobar, A.; Bergström, L. and Mörtsell, E. Measuring the properties of extragalactic dust and implications for the Hubble diagram. A&A **384**, 1 (2002).

Goodman, J. and Weare, J. Ensemble samplers with affine invariance. *CAMCoS* **5**, 65 (2010).

Gough, D. O. and McIntyre, M. E. Inevitability of a magnetic field in the Sun's radiative interior. Nature **394**, 755 (1998).

Graham, A. W. and Scott, N. The M BH-L spheroid Relation at High and Low Masses, the Quadratic Growth of Black Holes, and Intermediate-mass Black Hole Candidates. ApJ **764**, 151 (2013).

Grindlay, J. E. Hard X-ray Timing with EXIST. *X-ray Timing 2003: Rossi and Beyond. AIP Conference Proceedings* **714**, 413 (2004).

Grover, R. and Hardy, J. W. The Propagation of Shocks in Exponentially Decreasing Atmospheres. ApJ **143**, 48 (1966).

Guerrero, J.; García-Berro, E. and Isern, J. Smoothed Particle Hydrodynamics simulations of merging white dwarfs. A&A **413**, 257 (2004).

Guillochon, J. and Ramirez-Ruiz, E. Hydrodynamical Simulations to Determine the Feeding Rate of Black Holes by the Tidal Disruption of Stars: The Importance of the Impact Parameter and Stellar Structure. ApJ **767**, 25 (2013).

Guillochon, J.; Ramirez-Ruiz, E. and Lin, D. Consequences of the Ejection and Disruption of Giant Planets. ApJ **732**, 74 (2011).

Guillochon, J.; Ramirez-Ruiz, E.; Rosswog, S. and Kasen, D. Three-dimensional Simulations of Tidally Disrupted Solar-type Stars and the Observational Signatures of Shock Breakout. ApJ **705**, 844 (2009).

Guillot, T.; Stevenson, D. J.; Hubbard, W. B. and Saumon, D. The interior of Jupiter. *In: Jupiter. The planet* p. 35 (2004).

Gültekin, K.; Richstone, D. O.; Gebhardt, K.; Lauer, T. R.; Tremaine, S.; Aller, M. C.; Bender, R.; Dressler, A.; Faber, S. M.; Filippenko, A. V.; Green, R.; Ho, L. C.; Kormendy, J.; Magorrian, J.; Pinkney, J. and Siopis, C. The M-ÏČ and M-L Relations in Galactic Bulges, and Determinations of Their Intrinsic Scatter. ApJ **698**, 198 (2009).

Haas, R.; Shcherbakov, R. V.; Bode, T. and Laguna, P. Tidal Disruptions of White Dwarfs from Ultra-close Encounters with Intermediate-mass Spinning Black Holes. ApJ **749**, 117 (2012).

Hamilton, D. P. and Burns, J. A. Orbital stability zones about asteroids. II - The destabilizing effects of eccentric orbits and of solar radiation. *Icarus* **96**, 43 (1992).

Han, Z.; Podsiadlowski, P.; Maxted, P. F. L. and Marsh, T. R. The origin of subdwarf B stars - II. MNRAS **341**, 669 (2003).

Hawley, J. F.; Gammie, C. F. and Balbus, S. A. Local Three-dimensional Simulations of an Accretion Disk Hydromagnetic Dynamo. ApJ **464**, 690 (1996).

Hayasaki, K.; Stone, N. and Loeb, A. Finite, Intense Accretion Bursts from Tidal Disruption of Stars on Bound Orbits. *arXiv* p. 1333 (2012).

Hayes, W. D. Self-similar strong shocks in an exponential medium. *Journal of Fluid Mechanics* **32**, 305 (1968).

Hebb, L.; Collier-Cameron, A.; Triaud, A.; Lister, T.; Smalley, B.; Maxted, P.; Hellier, C.; Anderson, D.; Pollacco, D.; Gillon, M.; Queloz, D.; West, R.; Bentley, S.; Enoch, B.; Haswell, C.; Horne, K.; Mayor, M.; Pepe, F.; Segransan, D.; Skillen, I.; Udry, S. and Wheatley, P. WASP-19b: The Shortest Period Transiting Exoplanet Yet Discovered. ApJ **708**, 224 (2010).

Hellier, C.; Anderson, D. R.; Collier-Cameron, A.; Miller, G. R. M.; Queloz, D.; Smalley, B.; Southworth, J. and Triaud, A. H. M. J. On the Orbit of the Short-period Exoplanet WASP-19b. ApJ **730**, L31 (2011).

Hills, J. G. Hyper-velocity and tidal stars from binaries disrupted by a massive Galactic black hole. Nature **331**, 687 (1988).

Hjellming, M. S. and Webbink, R. F. Thresholds for rapid mass transfer in binary systems. I - Polytropic models. ApJ **318**, 794 (1987).

Hou, F.; Goodman, J.; Hogg, D. W.; Weare, J. and Schwab, C. An Affine-invariant Sampler for Exoplanet Fitting and Discovery in Radial Velocity Data. ApJ **745**, 198 (2012).

Hubbard, W. B. Planetary interiors. *New York* (1984).

Hut, P. Stability of tidal equilibrium. A&A **92**, 167 (1980).

Ida, S. and Lin, D. N. C. Toward a Deterministic Model of Planetary Formation. II. The Formation and Retention of Gas Giant Planets around Stars with a Range of Metallicities. ApJ **616**, 567 (2004).

Ida, S. and Lin, D. N. C. Toward a Deterministic Model of Planetary Formation. V. Accumulation Near the Ice Line and Super-Earths. ApJ **685**, 584 (2008).

Irwin, J. and Bouvier, J. The rotational evolution of low-mass stars. *IAU Symposium* **258**, 363 (2009).

Ivanov, P. B. and Chernyakova, M. A. Relativistic cross sections of mass stripping and tidal disruption of a star by a super-massive rotating black hole. A&A **448**, 843 (2006).

Ivanov, P. B.; Chernyakova, M. A. and Novikov, I. D. The new model of a tidally disrupted star: further development and relativistic calculations. MNRAS **338**, 147 (2003).

Ivanov, P. B. and Novikov, I. D. A New Model of a Tidally Disrupted Star. ApJ **549**, 467 (2001).

Ivanov, P. B. and Papaloizou, J. C. B. Inertial waves in rotating bodies: a WKBJ formalism for inertial modes and a comparison with numerical results. MNRAS **407**, 1609 (2010).

Jackson, B.; Barnes, R. and Greenberg, R. Observational Evidence for Tidal Destruction of Exoplanets. ApJ **698**, 1357 (2009).

Jiang, Y.-F.; Belyaev, M.; Goodman, J. and Stone, J. M. A new way to conserve total energy for Eulerian hydrodynamic simulations with self-gravity. New A **19**, 48 (2013).

Jurić, M. and Tremaine, S. Dynamical Origin of Extrasolar Planet Eccentricity Distribution. ApJ **686**, 603 (2008).

Kasen, D. and Ramirez-Ruiz, E. Optical Transients from the Unbound Debris of Tidal Disruption. ApJ **714**, 155 (2010).

Kasen, D.; Röpke, F. K. and Woosley, S. E. The diversity of type Ia supernovae from broken symmetries. Nature **460**, 869 (2009).

Katz, B.; Budnik, R. and Waxman, E. Fast radiation mediated shocks and supernova shock breakouts. *ArXiv* **0902**, 4708 (2009).

Kelly, B. C.; Sobolewska, M. and Siemiginowska, A. A Stochastic Model for the Luminosity Fluctuations of Accreting Black Holes. ApJ **730**, 52 (2011).

Kesden, M. Black-hole spin dependence in the light curves of tidal disruption events. Phys. Rev. D **86**, 064026 (2012a).

Kesden, M. Tidal-disruption rate of stars by spinning supermassive black holes. Phys. Rev. D **85**, 24037 (2012b).

Khokhlov, A.; Novikov, I. D. and Pethick, C. J. Strong Effects during Close Encounters of a Star with a Massive Black Hole. ApJ **418**, 181 (1993a).

Khokhlov, A.; Novikov, I. D. and Pethick, C. J. Weak Tidal Encounters of a Star with a Massive Black Hole. ApJ **418**, 163 (1993b).

Khokhlov, A. M.; Oran, E. S. and Wheeler, J. C. Deflagration-to-Detonation Transition in Thermonuclear Supernovae. ApJ **478**, 678 (1997).

Kim, S. S.; Park, M.-G. and Lee, H. M. The Stream-Stream Collision after the Tidal Disruption of a Star around a Massive Black Hole. ApJ **519**, 647 (1999).

Kippenhahn, R. and Weigert, A. Stellar Structure and Evolution. *Stellar Structure and Evolution* (1990).

Kobayashi, S.; Laguna, P.; Phinney, E. S. and Mészáros, P. Gravitational Waves and X-Ray Signals from Stellar Disruption by a Massive Black Hole. ApJ **615**, 855 (2004).

Kochanek, C. S. The dynamical evolution of tidal capture binaries. ApJ **385**, 604 (1992).

Kochanek, C. S. The aftermath of tidal disruption: The dynamics of thin gas streams. ApJ **422**, 508 (1994).

Komossa, S. and Greiner, J. Discovery of a giant and luminous X-ray outburst from the optically inactive galaxy pair RX J1242.6-1119. A&A **349**, L45 (1999).

Komossa, S.; Halpern, J.; Schartel, N.; Hasinger, G.; Santos-Lleo, M. and Predehl, P. A Huge Drop in the X-Ray Luminosity of the Nonactive Galaxy RX J1242.6-1119A, and the First Postflare Spectrum: Testing the Tidal Disruption Scenario. ApJ **603**, L17 (2004).

Koratkar, A. and Blaes, O. The Ultraviolet and Optical Continuum Emission in Active Galactic Nuclei: The Status of Accretion Disks. PASP **111**, 1 (1999).

Korista, K. T. and Goad, M. R. What the Optical Recombination Lines Can Tell Us about the Broad-Line Regions of Active Galactic Nuclei. ApJ **606**, 749 (2004).

Kormendy, J. and Ho, L. C. Coevolution (Or Not) of Supermassive Black Holes and Host Galaxies. *ArXiv* (2013).

Kozai, Y. Secular perturbations of asteroids with high inclination and eccentricity. AJ **67**, 591 (1962).

Kroupa, P. On the variation of the initial mass function. MNRAS **322**, 231 (2001).

Kroupa, P.; Tout, C. A. and Gilmore, G. The distribution of low-mass stars in the Galactic disc. *Royal Astronomical Society* **262**, 545 (1993).

Krumholz, M. R.; McKee, C. F. and Klein, R. I. Embedding Lagrangian Sink Particles in Eulerian Grids. ApJ **611**, 399 (2004).

Kumar, P. and Goodman, J. Nonlinear Damping of Oscillations in Tidal-Capture Binaries. ApJ **466**, 946 (1996).

Laguna, P.; Miller, W. A.; Zurek, W. H. and Davies, M. B. Tidal disruptions by supermassive black holes - Hydrodynamic evolution of stars on a Schwarzschild background. ApJ **410**, L83 (1993).

Lai, D.; Rasio, F. A. and Shapiro, S. L. Equilibrium, stability, and orbital evolution of close binary systems. ApJ **423**, 344 (1994).

Laine, R.; Lin, D. and Dong, S. Interaction of Close-in Planets with the Magnetosphere of Their

Host Stars. I. Diffusion, Ohmic Dissipation of Time-dependent Field, Planetary Inflation, and Mass Loss. ApJ **685**, 521 (2009).

Larson, R. B. Cloud fragmentation and stellar masses. MNRAS **214**, 379 (1985).

Lawrence, A. The UV peak in active galactic nuclei: a false continuum from blurred reflection? MNRAS **423**, 451 (2012).

Lee, W. H. and Ramirez-Ruiz, E. The progenitors of short gamma-ray bursts. *New Journal of Physics* **9**, 17 (2007).

Lee, W. H.; Ramirez-Ruiz, E. and van de Ven, G. Short Gamma-ray Bursts from Dynamically Assembled Compact Binaries in Globular Clusters: Pathways, Rates, Hydrodynamics, and Cosmological Setting. ApJ **720**, 953 (2010).

Li, S.-L.; Miller, N.; Lin, D. N. C. and Fortney, J. J. WASP-12b as a prolate, inflated and disrupting planet from tidal dissipation. Nature **463**, 1054 (2010).

Lin, D. N. C.; Bodenheimer, P. and Richardson, D. C. Orbital migration of the planetary companion of 51 Pegasi to its present location. Nature **380**, 606 (1996).

Liu, S.-F.; Guillochon, J.; Lin, D. N. C. and Ramirez-Ruiz, E. On the Survivability and Metamorphism of Tidally Disrupted Giant Planets: The Role of Dense Cores. ApJ **762**, 37 (2013).

Livio, M. The Progenitors of Type Ia Supernovae. *Type Ia Supernovae* p. 33 (2000).

Lodato, G.; King, A. R. and Pringle, J. E. Stellar disruption by a supermassive black hole: is the light curve really proportional to t-5/3? MNRAS **392**, 332 (2009).

Lodato, G. and Rossi, E. M. Multiband light curves of tidal disruption events. MNRAS **410**, 359 (2010).

Loeb, A. and Ulmer, A. Optical Appearance of the Debris of a Star Disrupted by a Massive Black Hole. ApJ **489**, 573 (1997).

Lorén-Aguilar, P.; Isern, J. and García-Berro, E. High-resolution smoothed particle hydrodynamics simulations of the merger of binary white dwarfs. A&A **500**, 1193 (2009).

Lubow, S. H. and Shu, F. H. Gas dynamics of semidetached binaries. ApJ **198**, 383 (1975).

Lubow, S. H. and Shu, F. H. Gas dynamics of semidetached binaries. II - The vertical structure of the stream. ApJ **207**, L53 (1976).

Luminet, J. and Marck, J.-A. Tidal squeezing of stars by Schwarzschild black holes. MNRAS **212**, 57 (1985).

Luminet, J. P. and Carter, B. Dynamics of an affine star model in a black hole tidal field. ApJS **61**, 219 (1986).

MacLeod, M.; Guillochon, J. and Ramirez-Ruiz, E. The Tidal Disruption of Giant Stars and their Contribution to the Flaring Supermassive Black Hole Population. ApJ **757**, 134 (2012).

Madigan, A.-M.; Hopman, C. and Levin, Y. Secular Stellar Dynamics near a Massive Black Hole. ApJ **738**, 99 (2011).

Maeder, A. Analytical studies in stellar evolution. II - On the evolution of rotating stars in the log Tc-log rhoC plane from main sequence to pre-supernova stage. A&A **34**, 409 (1974).

Magorrian, J. and Tremaine, S. Rates of tidal disruption of stars by massive central black holes. MNRAS **309**, 447 (1999).

Magorrian, J.; Tremaine, S.; Richstone, D.; Bender, R.; Bower, G.; Dressler, A.; Faber, S. M.; Gebhardt, K.; Green, R.; Grillmair, C.; Kormendy, J. and Lauer, T. The Demography of Massive Dark Objects in Galaxy Centers. AJ **115**, 2285 (1998).

Malmberg, D.; Davies, M. B. and Heggie, D. C. The effects of fly-bys on planetary systems. MNRAS **411**, 859 (2011).

Marconi, A.; Axon, D. J.; Maiolino, R.; Nagao, T.; Pastorini, G.; Pietrini, P.; Robinson, A. and Torricelli, G. The Effect of Radiation Pressure on Virial Black Hole Mass Estimates and the Case of Narrow-Line Seyfert 1 Galaxies. ApJ **678**, 693 (2008).

Mardling, R. A. The Role of Chaos in the Circularization of Tidal Capture Binaries. I. The Chaos Boundary. ApJ **450**, 722 (1995a).

Mardling, R. A. The Role of Chaos in the Circularization of Tidal Capture Binaries. II. Long-Time Evolution. ApJ **450**, 732 (1995b).

Marsh, T. R.; Nelemans, G. and Steeghs, D. Mass transfer between double white dwarfs. MNRAS **350**, 113 (2004).

Matsumura, S.; Takeda, G. and Rasio, F. A. On the Origins of Eccentric Close-In Planets. ApJ **686**, L29 (2008).

Matsumura, S.; Thommes, E. W.; Chatterjee, S. and Rasio, F. A. Unstable Planetary Systems Emerging Out of Gas Disks. ApJ **714**, 194 (2010).

Matzner, C. D. and McKee, C. F. The Expulsion of Stellar Envelopes in Core-Collapse Supernovae. ApJ **510**, 379 (1999).

Maupertuis, P. L. M. d. *The figure of the earth, determined from observations made by order of the French King, at the polar circle*. London: T. Cox, 1738 (1738).

Mayor, M. and Queloz, D. A Jupiter-mass companion to a solar-type star. Nature **378**, 355 (1995).

McKee, C. F. and Ostriker, E. C. Theory of Star Formation. A&A Rev. **45**, 565 (2007).

Merritt, D. and Ferrarese, L. The M*-ÏČ Relation for Supermassive Black Holes. ApJ **547**, 140 (2001).

Miesch, M. S. and Toomre, J. Turbulence, Magnetism, and Shear in Stellar Interiors. *Annual Review of Fluid Mechanics* **41**, 317 (2009).

Miller, N.; Fortney, J. J. and Jackson, B. Inflating and Deflating Hot Jupiters: Coupled Tidal and Thermal Evolution of Known Transiting Planets. ApJ **702**, 1413 (2009).

Morrison, R. and McCammon, D. Interstellar photoelectric absorption cross sections, 0.03-10 keV. ApJ **270**, 119 (1983).

Motl, P. M.; Frank, J.; Tohline, J. E. and D'Souza, M. C. R. The Stability of Double White Dwarf Binaries Undergoing Direct-Impact Accretion. ApJ **670**, 1314 (2007).

Murray, C. D. and Dermott, S. F. Solar system dynamics. *Solar system dynamics by Murray* (1999).

Nagasawa, M.; Ida, S. and Bessho, T. Formation of Hot Planets by a Combination of Planet Scattering, Tidal Circularization, and the Kozai Mechanism. ApJ **678**, 498 (2008).

Napiwotzki, R. The galactic population of white dwarfs. *Journal of Physics: Conference Series* **172**, 2004 (2009).

Napiwotzki, R.; Karl, C. A.; Nelemans, G.; Yungelson, L.; Christlieb, N.; Drechsel, H.; Heber, U.; Homeier, D.; Koester, D.; Leibundgut, B.; Marsh, T. R.; Moehler, S.; Renzini, A. and Reimers, D. Binary White Dwarfs in the Supernova Ia Progenitor Survey. *15th European Workshop on White Dwarfs ASP Conference Series* **372**, 387 (2007).

Nauenberg, M. Analytic Approximations to the Mass-Radius Relation and Energy of Zero-Temperature Stars. ApJ **175**, 417 (1972).

Nelemans, G.; Portegies Zwart, S. F.; Verbunt, F. and Yungelson, L. R. Population synthesis for double white dwarfs. II. Semi-detached systems: AM CVn stars. A&A **368**, 939 (2001a).

Nelemans, G.; Yungelson, L. R.; Portegies Zwart, S. F. and Verbunt, F. Population synthesis for double white dwarfs . I. Close detached systems. A&A **365**, 491 (2001b).

New, K. C. B. and Tohline, J. E. The Relative Stability against Merger of Close, Compact Binaries. ApJ **490**, 311 (1997).

Niemeyer, J. C. and Woosley, S. E. The Thermonuclear Explosion of Chandrasekhar Mass White Dwarfs. ApJ **475**, 740 (1997).

Nolthenius, R. A. and Katz, J. I. The passage of a star by a massive black hole. ApJ **263**, 377 (1982).

Noyola, E.; Gebhardt, K. and Bergmann, M. Gemini and Hubble Space Telescope Evidence for an Intermediate-Mass Black Hole in ÏL' Centauri. ApJ **676**, 1008 (2008).

Ogilvie, G. I. and Lin, D. N. C. Tidal Dissipation in Rotating Giant Planets. ApJ **610**, 477 (2004).

Ostriker, J. On the Oscillations and the Stability of a Homogeneous Compressible Cylinder. ApJ **140**, 1529 (1964).

Pancoast, A.; Brewer, B. J.; Treu, T.; Barth, A. J.; Bennert, V. N.; Canalizo, G.; Filippenko, A. V.; Gates, E. L.; Greene, J. E.; Li, W.; Malkan, M. A.; Sand, D. J.; Stern, D.; Woo, J.-H.; Assef, R. J.; Bae, H.-J.; Buehler, T.; Cenko, S. B.; Clubb, K. I.; Cooper, M. C.; Diamond-Stanic, A. M.; Hiner, K. D.; Hönig, S. F.; Joner, M. D.; Kandrashoff, M. T.; Laney, C. D.; Lazarova, M. S.; Nierenberg, A. M.; Park, D.; Silverman, J. M.; Son, D.; Sonnenfeld, A.; Thorman, S. J.; Tollerud, E. J.; Walsh, J. L. and Walters, R. The Lick AGN Monitoring Project 2011: Dynamical Modeling of the Broad-line Region in Mrk 50. ApJ **754**, 49 (2012).

Perets, H. B.; Gal-Yam, A.; Mazzali, P.; Arnett, D.; Kagan, D.; Filippenko, A. V.; Li, W.; Cenko, S. B.; Fox, D. B.; Leonard, D. C.; Moon, D. S.; Sand, D. J.; Soderberg, A. M.; Foley, R. J.; Ganeshalingam, M.; Anderson, J. P.; James, P. A.; Ofek, E. O.; Bildsten, L.; Nelemans, G.; Shen, K. J.; Weinberg, N. N.; Metzger, B. D.; Piro, A. L.; Quataert, E.; Kiewe, M. and Poznanski, D. A new type of stellar explosion. *ArXiv* **0906**, 2003 (2009).

Peterson, B. M. The broad-line region in active galactic nuclei. *Physics of Active Galactic Nuclei at all Scales* pp. 77–100 (2006).

Peterson, B. M.; Ferrarese, L.; Gilbert, K. M.; Kaspi, S.; Malkan, M. A.; Maoz, D.; Merritt, D.; Netzer, H.; Onken, C. A.; Pogge, R. W.; Vestergaard, M. and Wandel, A. Central Masses and Broad-Line Region Sizes of Active Galactic Nuclei. II. A Homogeneous Analysis of a Large Reverberation-Mapping Database. ApJ **613**, 682 (2004).

Peterson, B. M. and Wandel, A. Keplerian motion of broad-line region gas as evidence for supermassive black holes in active galactic nuclei. *The Astrophysical Journal Letters* **521**, L95 (1999).

Phinney, E. S. Manifestations of a Massive Black Hole in the Galactic Center. *The Center of the Galaxy: Proceedings of the 136th Symposium of the International Astronomical Union* **136**, 543 (1989).

Press, W. H.; Flannery, B. P. and Teukolsky, S. A. Numerical recipes. The art of scientific computing. *Cambridge: University Press* (1986).

Press, W. H. and Teukolsky, S. A. On formation of close binaries by two-body tidal capture. ApJ **213**, 183 (1977).

Pringle, J. E. and Rees, M. J. Accretion Disc Models for Compact X-Ray Sources. A&A **21**, 1 (1972).

Proga, D.; Ostriker, J. P. and Kurosawa, R. Dynamics of Rotating Accretion Flows Irradiated by a Quasar. ApJ **676**, 101 (2008).

Quataert, E. A Thermal Bremsstrahlung Model for the Quiescent X-Ray Emission from Sagittarius A*. ApJ **575**, 855 (2002).

Ramirez-Ruiz, E. and Rosswog, S. The Star Ingesting Luminosity of Intermediate-Mass Black Holes in Globular Clusters. ApJ **697**, L77 (2009).

Rasio, F. A. and Shapiro, S. L. Hydrodynamics of binary coalescence. 2: Polytropes with gamma = 5/3. ApJ **438**, 887 (1995).

Rathore, Y. Resonant excitation of white dwarf oscillations in compact object binaries. *Proquest Dissertations And Theses 2005. Section 0037* p. 23 (2005).

Rees, M. J. Tidal disruption of stars by black holes of 10 to the 6th-10 to the 8th solar masses in nearby galaxies. Nature **333**, 523 (1988).

Robertson, B. E.; Kravtsov, A. V.; Gnedin, N. Y.; Abel, T. and Rudd, D. H. Computational Eulerian hydrodynamics and Galilean invariance. MNRAS **401**, 2463 (2010).

Roos, N. Gas clouds from tidally disrupted stars in active galactic nuclei. ApJ **385**, 108 (1992).

Röpke, F. K.; Woosley, S. E. and Hillebrandt, W. Off-Center Ignition in Type Ia Supernovae. I. Initial Evolution and Implications for Delayed Detonation. ApJ **660**, 1344 (2007).

Rosenblum, E.; Garaud, P.; Traxler, A. and Stellmach, S. Turbulent Mixing and Layer Formation in Double-diffusive Convection: Three-dimensional Numerical Simulations and Theory. ApJ **731**, 66 (2011).

Rosswog, S.; Kasen, D.; Guillochon, J. and Ramirez-Ruiz, E. Collisions of White Dwarfs as a New Progenitor Channel for Type Ia Supernovae. ApJ **705**, L128 (2009a).

Rosswog, S.; Ramirez-Ruiz, E. and Hix, W. R. Atypical Thermonuclear Supernovae from Tidally Crushed White Dwarfs. ApJ **679**, 1385 (2008a).

Rosswog, S.; Ramirez-Ruiz, E. and Hix, W. R. Tidal Disruption and Ignition of White Dwarfs by Moderately Massive Black Holes. ApJ **695**, 404 (2009b).

Rosswog, S.; Ramirez-Ruiz, E.; Hix, W. R. and Dan, M. Simulating black hole white dwarf encounters. *Computer Physics Communications* **179**, 184 (2008b).

Ruff, A. J. *The broad emission line region of quasars and gravitational lensing by early-type galaxies*. Ph.D. thesis, The University of Melbourne (2012).

Sakurai, A. On the problem of a shock wave arriving at the edge of a gas. *Communications on Pure and Applied Mathematics* (1960).

Sari, R.; Kobayashi, S. and Rossi, E. M. Hypervelocity Stars and the Restricted Parabolic Three-Body Problem. ApJ **708**, 605 (2010).

Schlaufman, K. C. Evidence of Possible Spin-orbit Misalignment Along the Line of Sight in Transiting Exoplanet Systems. ApJ **719**, 602 (2010).

Schlaufman, K. C.; Lin, D. N. C. and Ida, S. A Population of Very Hot Super-Earths in Multiple-planet Systems Should be Uncovered by Kepler. ApJ **724**, L53 (2010).

Schönberg, M. and Chandrasekhar, S. On the Evolution of the Main-Sequence Stars. ApJ **96**, 161 (1942).

Segretain, L.; Chabrier, G. and Mochkovitch, R. The Fate of Merging White Dwarfs. ApJ **481**, 355 (1997).

Seitenzahl, I. R.; Meakin, C. a.; Townsley, D. M.; Lamb, D. Q. and Truran, J. W. Spontaneous Initiation of Detonations in White Dwarf Environments: Determination of Critical Sizes. ApJ **696**, 515 (2009).

Shakura, N. I. and Sunyaev, R. A. Black holes in binary systems. Observational appearance. A&A **24**, 337 (1973).

Shen, Y. and Turner, E. L. On the Eccentricity Distribution of Exoplanets from Radial Velocity Surveys. ApJ **685**, 553 (2008).

Shields, G. A. Thermal continuum from acretion disks in quasars. Nature **272**, 706 (1978).

Shu, F. H. Physics of Astrophysics, Vol. II. *Physics of Astrophysics* (1992).

Springel, V. E pur si muove: Galilean-invariant cosmological hydrodynamical simulations on a moving mesh. MNRAS **401**, 791 (2010).

Stone, J. M.; Hawley, J. F.; Gammie, C. F. and Balbus, S. A. Three-dimensional Magnetohydrodynamical Simulations of Vertically Stratified Accretion Disks. ApJ **463**, 656 (1996).

Stone, N.; Sari, R. and Loeb, A. Consequences of Strong Compression in Tidal Disruption Events. *arXiv* p. 3374 (2012).

Strubbe, L. E. and Quataert, E. Optical flares from the tidal disruption of stars by massive black holes. MNRAS **400**, 2070 (2009).

Strubbe, L. E. and Quataert, E. Spectroscopic signatures of the tidal disruption of stars by massive black holes. MNRAS **415**, 168 (2011).

Swesty, F. D.; Wang, E. Y. M. and Calder, A. C. Numerical Models of Binary Neutron Star System Mergers. I. Numerical Methods and Equilibrium Data for Newtonian Models. ApJ **541**, 937 (2000).

Takeda, G. and Rasio, F. A. High Orbital Eccentricities of Extrasolar Planets Induced by the Kozai Mechanism. ApJ **627**, 1001 (2005).

Tasker, E. J.; Brunino, R.; Mitchell, N. L.; Michielsen, D.; Hopton, S.; Pearce, F. R.; Bryan, G. L. and Theuns, T. A test suite for quantitative comparison of hydrodynamic codes in astrophysics. MNRAS **390**, 1267 (2008).

Thomas, H. C. Consequences of Mass Transfer in Close Binary Systems. A&A Rev. **15**, 127 (1977).

Thompson, S. E.; Everett, M.; Mullally, F.; Barclay, T.; Howell, S. B.; Still, M.; Rowe, J.; Christiansen, J. L.; Kurtz, D. W.; Hambleton, K.; Twicken, J. D.; Ibrahim, K. A. and Clarke, B. D. A Class of Eccentric Binaries with Dynamic Tidal Distortions Discovered with Kepler. ApJ **753**, 86 (2012).

Timmes, F. X. Integration of Nuclear Reaction Networks for Stellar Hydrodynamics. ApJS **124**, 241 (1999).

Timmes, F. X.; Brown, E. F. and Truran, J. W. On Variations in the Peak Luminosity of Type Ia Supernovae. ApJ **590**, L83 (2003).

Timmes, F. X.; Hoffman, R. D. and Woosley, S. E. An Inexpensive Nuclear Energy Generation Network for Stellar Hydrodynamics. ApJS **129**, 377 (2000).

Timmes, F. X. and Swesty, F. D. The Accuracy, Consistency, and Speed of an Electron-Positron Equation of State Based on Table Interpolation of the Helmholtz Free Energy. ApJ **126**, 501 (2000).

Tout, C. A.; Pols, O. R.; Eggleton, P. P. and Han, Z. Zero-age main-seqence radii and luminosities as analytic functions of mass and metallicity. MNRAS **281**, 257 (1996).

Treister, E.; Urry, C. M. and Virani, S. The Space Density of Compton-Thick Active Galactic Nucleus and the X-Ray Background. ApJ **696**, 110 (2009).

Trentham, N. and Tully, R. B. The faint end of the galaxy luminosity function. MNRAS **335**, 712 (2002).

Triaud, A.; Collier Cameron, A.; Queloz, D.; Anderson, D.; Gillon, M.; Hebb, L.; Hellier, C.; Loeillet, B.; Maxted, P.; Mayor, M.; Pepe, F.; Pollacco, D.; Ségransan, D.; Smalley, B.; Udry, S.; West, R. and Wheatley, P. Spin-orbit angle measurements for six southern transiting planets. New insights into the dynamical origins of hot Jupiters. A&A **524**, 25 (2010).

Truelove, J. K.; Klein, R. I.; McKee, C. F.; Holliman, J. H. I.; Howell, L. H. and Greenough, J. A. The Jeans Condition: A New Constraint on Spatial Resolution in Simulations of Isothermal Self-gravitational Hydrodynamics. ApJ **489**, L179 (1997).

Trump, J. R.; Impey, C. D.; Kelly, B. C.; Civano, F.; Gabor, J. M.; Diamond-Stanic, A. M.; Merloni, A.; Urry, C. M.; Hao, H.; Jahnke, K.; Nagao, T.; Taniguchi, Y.; Koekemoer, A. M.;

Lanzuisi, G.; Liu, C.; Mainieri, V.; Salvato, M. and Scoville, N. Z. Accretion Rate and the Physical Nature of Unobscured Active Galaxies. *ArXiv* **1103**, 276 (2011).

Ulmer, A. Flares from the Tidal Disruption of Stars by Massive Black Holes. ApJ **514**, 180 (1999).

Usami, M. and Fujimoto, M. Tidal Effects on Rotating Gaseous Ellipsoids Revolving around a Central Massive Object. ApJ **487**, 489 (1997).

Uttley, P. and McHardy, I. M. X-ray variability of NGC 3227 and 5506 and the nature of active galactic nucleus 'states'. MNRAS **363**, 586 (2005).

Valsecchi, F.; Farr, W. M.; Willems, B.; Deloye, C. J. and Kalogera, V. Tidally Induced Apsidal Precession in Double White Dwarfs: A New Mass Measurement Tool with LISA. ApJ **745**, 137 (2012).

van der Hucht, K. A. The VIIth catalogue of galactic Wolf-Rayet stars. New A Rev. **45**, 135 (2001).

van Velzen, S.; Farrar, G. R.; Gezari, S.; Morrell, N.; Zaritsky, D.; Östman, L.; Smith, M.; Gelfand, J. and Drake, A. J. Optical Discovery of Probable Stellar Tidal Disruption Flares. ApJ **741**, 73 (2011).

Vanden Berk, D. E.; Richards, G. T.; Bauer, A.; Strauss, M. A.; Schneider, D. P.; Heckman, T. M.; York, D. G.; Hall, P. B.; Fan, X.; Knapp, G. R.; Anderson, S. F.; Annis, J.; Bahcall, N. A.; Bernardi, M.; Briggs, J. W.; Brinkmann, J.; Brunner, R.; Burles, S.; Carey, L.; Castander, F. J.; Connolly, A. J.; Crocker, J. H.; Csabai, I.; Doi, M.; Finkbeiner, D.; Friedman, S.;

Frieman, J. A.; Fukugita, M.; Gunn, J. E.; Hennessy, G. S.; Ivezic, Z.; Kent, S.; Kunszt, P. Z.; Lamb, D. Q.; Leger, R. F.; Long, D. C.; Loveday, J.; Lupton, R. H.; Meiksin, A.; Merelli, A.; Munn, J. A.; Newberg, H. J.; Newcomb, M.; Nichol, R. C.; Owen, R.; Pier, J. R.; Pope, A.; Rockosi, C. M.; Schlegel, D. J.; Siegmund, W. A.; Smee, S.; Snir, Y.; Stoughton, C.; Stubbs, C.; SubbaRao, M.; Szalay, A. S.; Szokoly, G. P.; Tremonti, C.; Uomoto, A.; Waddell, P.; Yanny, B. and Zheng, W. Composite Quasar Spectra from the Sloan Digital Sky Survey. AJ **122**, 549 (2001).

Verbunt, F. Origin and Evolution of X-Ray Binaries and Binary Radio Pulsars. A&A Rev. **31**, 93 (1993).

Wagner, R. L. Theoretical Evolution of Extremely Metal-Poor Stars. ApJ **191**, 173 (1974).

Walton, D. J.; Nardini, E.; Fabian, A. C.; Gallo, L. C. and Reis, R. C. Suzaku observations of 'bare' active galactic nuclei. MNRAS **428**, 2901 (2013).

Wandel, A.; Peterson, B. M. and Malkan, M. A. Central Masses and Broad-Line Region Sizes of Active Galactic Nuclei. I. Comparing the Photoionization and Reverberation Techniques. ApJ **526**, 579 (1999).

Wang, J. and Merritt, D. Revised Rates of Stellar Disruption in Galactic Nuclei. ApJ **600**, 149 (2004).

Watson, C. A.; Littlefair, S. P.; Diamond, C.; Collier Cameron, A.; Fitzsimmons, A.; Simpson, E.; Moulds, V. and Pollacco, D. On the alignment of debris disks and their host stars’ rotation axis -implications for spin-orbit misalignment in exoplanetary systems. *ArXiv* **arXiv:1009.4132** (2010).

Webb, W. and Malkan, M. Rapid Optical Variability in Active Galactic Nuclei and Quasars. ApJ **540**, 652 (2000).

Yoon, S.-C.; Podsiadlowski, P. and Rosswog, S. Remnant evolution after a carbon/oxygen white dwarf merger. MNRAS **380**, 933 (2007).

Zakamska, N. L.; Pan, M. and Ford, E. B. Observational biases in determining extrasolar planet eccentricities in single-planet systems. MNRAS p. 1566 (2010).

Zel’Dovich, Y. B. and Raizer, Y. P. Physics of Shock Waves and High-Temperature Hydrodynamic Phenomena, Volume I. *New York: Academic Press* **I** (1967).

Zhou, J.-L.; Lin, D. N. C. and Sun, Y.-S. Post-oligarchic Evolution of Protoplanetary Embryos and the Stability of Planetary Systems. ApJ **666**, 423 (2007).

Appendix A

Modified PPM Gravity Algorithm

Because the binding energy of a planet on a disruptive orbit is comparable to the planet self-binding energy, the conservative properties of a code used to investigate planetary disruption are important. As the simulation of a partially-disruptive encounter involves the simultaneous resolution of both a compact core and two debris tails which are hundreds of time larger than the core, we found that the standard methods used to calculate the gravitational potential in a tidal disruption are too computationally expensive given the required accuracies.

Our approach was to improve upon the gravity solver found within the FLASH hydrodynamics code (Fryxell *et al.*, 2000) such that it is better suited to investigating the problem of tidal disruption, a pictorial representation of the algorithm described below is shown in Figure

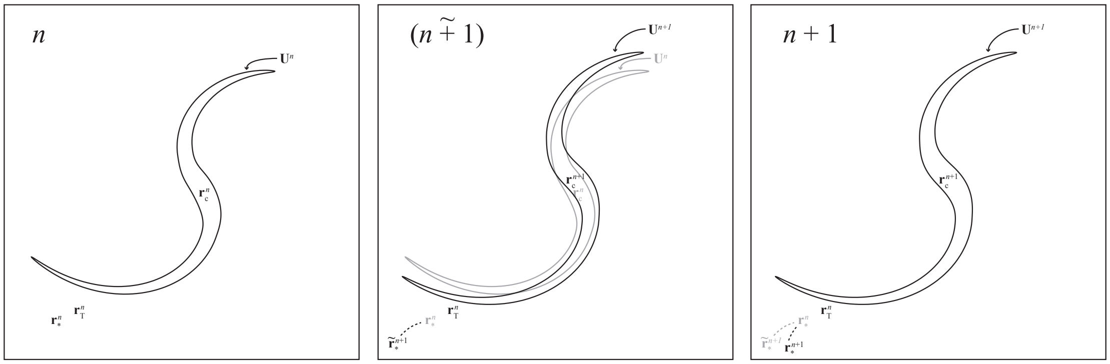

Figure A.1: Cartoon showing the sequence of states used to compute the evolution over a single a time-step using our modified gravity solver. The initial state m is showing in the left panel, the middle panel shows the intermediate state $(m \widetilde{+} 1)$, and the last panel shows the final state $m+1$. $\mathbf{r}_*$ is the position of the point mass representing the star, $\mathbf{r}_c$ is the planetary core's true center of mass, $\mathbf{r}_T \equiv (M_P \mathbf{r}_t + M_* \mathbf{r}_*)/(M_J + M_*)$ is the center of mass of the complete system. The variable vector field $\mathbf{U}(\mathbf{r}) \equiv [\rho, \rho \mathbf{v}, e, X]$ represents the value of all the conserved quantities in a given state. Differences between the states are exaggerated for illustrative purposes.

A.1. Two centers of mass are calculated at each time-step, which are defined as

$$\mathbf{r}_t = \frac{\sum_i m_i r_i}{\sum_i m_i} \tag{A.1}$$

$$\mathbf{r}_c = \frac{\sum_{i,\, \rho(i) > f \rho_{\max}} m_i r_i}{\sum_{i,\, \rho(i) > f \rho_{\max}} m_i}, \tag{A.2}$$

where $\mathbf{r}_t$ is the "true" center of mass and $\mathbf{r}_c$ is the "core" center of mass, which only includes matter above a density cut-off $\rho > f \rho_{\max}$, where f is set to 0.1. The planet's virtual particle is fixed to spatially coincide with the $\mathbf{r}_c$ vector at all times. The planet's self-gravity is calculated using a multipole expansion of the planet's mass about $\mathbf{r}_c$ instead of $\mathbf{r}_t$, which allows us to better approximate the planet's potential using less terms in the multipole expansion.

Our algorithm is particularly well-suited for investigating tidal disruptions. If the expansion were performed about $\mathbf{r}_t$ after large tidal tails have formed within the simulation,

$\mathbf{r}_{\mathrm{t}}$ would be mostly determined by the position of material that is far away from the core, and the region with the best resolution of the potential may lie in empty space. We can estimate the number of terms required to represent the core's potential if the expansion is carried out about $\mathbf{r}_{\mathrm{t}}$ instead of $\mathbf{r}_{\mathrm{c}}$. Assume the core has a radius r_{c}, and that the core lies a distance $d \equiv |\mathbf{r}-\mathbf{r}_{\mathrm{c}}|$ from the true center of mass. The angular scale of a lobe corresponding to a spherical harmonic of degree l is simply π/l, which means that even a first-order approximation of the core's potential requires an expansion with $l_{\max} \geq \pi d/r_{\mathrm{c}}$. Assuming $\sim 10\%$ of a planet's mass is lost during an encounter and this material lies an average distance $\sim 10^3 R_{\mathrm{J}}$ from the core at apocenter, d is on order $100 R_{\mathrm{J}}$, meaning that the multipole expansion must be carried out to $l \gtrsim 300$. This is highly impractical, and thus it is much more efficient to carry out the multipole expansion about the planet's core, whose position is associated with the densest material in the simulation and is where the potential gradients are largest.

The potential ϕ calculated from the multipole expansion about $\mathbf{r}_{\mathrm{c}}$ is used both to apply forces to the fluid in the simulation domain and to the virtual star and planet particles. A consequence of not expanding about the true center of mass is that there exists a non-zero force that is applied to the core. These forces are associated with the odd-l multipole terms that usually cancel when the expansion is carried out about the true center of mass. Our multipole expansion does not discard these odd-l terms, which allows us to confidently represent the fluid's potential using an expansion of relatively low order.

In the FLASH code's split PPM formalism, the equations used for coupling hydrodynamics and the gravitational field for a cell i along each of the three cartesian directions are

(Bryan *et al.*, 1995)

$$(\rho v)_i^{m+1} = (\rho v)_i^m + \frac{\Delta t^m}{2} g_i^{m+1} \left(\rho_i^m + \rho_i^{m+1}\right) \tag{A.3}$$

$$(\rho E)_i^{m+1} = (\rho E)_i^m + \frac{\Delta t^m}{4} g_i^{m+1} \left(\rho_i^m + \rho_i^{m+1}\right) \left(v_i^m + v_i^{m+1}\right). \tag{A.4}$$

The acceleration g_i^{m+1} is calculated by extrapolating ϕ_i^{m-1} and ϕ_i^m to obtain an estimate for ϕ_i^{m+1}

$$\tilde{\phi}_i^{m+1} = \phi_i^m \left(1 + \frac{\Delta t^m}{\Delta t^{m-1}}\right) - \phi_i^{m-1} \frac{\Delta t^m}{\Delta t^{m-1}}. \tag{A.5}$$

This is in turn used to calculate g_i^{m+1}

$$g_i^{m+1} = \frac{1}{2\Delta x_i} \left[\tilde{\phi}_{i+1}^{m+1} - \phi_{i-1}^{m+1} + \frac{1}{12} \left(\tilde{\phi}_{i+1}^{m+1} - 2\phi_i^{m+1} + \phi_{i-1}^{m+1} \frac{\delta \rho_i}{\rho_i}\right)\right], \tag{A.6}$$

where $\delta\rho_i$ is defined as

$$\delta\rho_i = \min\left(\left|\rho_{i+1}^m - \rho_{i-1}^m\right|, 2\left|\rho_i^m - \rho_{i-1}^m\right|, 2\left|\rho_i^m - \rho_{i+1}^m\right|\right) \times \operatorname{sign}\left(\rho_{\mathrm{i+1}}^{\mathrm{m}} - \rho_{\mathrm{i-1}}^{\mathrm{m}}\right) \tag{A.7}$$

to enforce monotonicity in ρ.

Because the potential of the star in our simulations is approximated by an analytical expression (for our simulations, a monopole potential), we can implement the following modification such that the component of the acceleration attributed to the star can be calculated to much higher accuracy. We first make the assumption that the matter distribution remains fixed over the course of the time-step, and then integrate the virtual particle positions forward in time from m to $m+1$. This allows us to calculate

$$\tilde{\phi}^{m+1}_{*,i} = \frac{GM_* \rho^m_{\mathrm{P},i}}{|\mathbf{r}_i - \mathbf{r}^{m+1}_*|}, \tag{A.8}$$

an estimate of the star's contribution to the potential based on the star's approximate final position. This estimate should be much closer to the true value than simple extrapolation as the potential at a given location has a non-trivial time-dependence. Splitting ϕ_i into two components $\phi_{*,i}$ (star) and $\phi_{\mathrm{P},i}$ (planet), Equation (A.5) becomes

$$\tilde{\phi}^{m+1}_i = \phi^m_{\mathrm{P},i}\left(1 + \frac{\Delta t^m}{\Delta t^{m-1}}\right) - \phi^{m-1}_{\mathrm{P},i}\frac{\Delta t^m}{\Delta t^{m-1}} + \tilde{\phi}^{m+1}_{*,i}. \tag{A.9}$$

Additionally, a correction must be made to Equation (A.6)

$$g^{m+1}_{i,\mathrm{cor}} = g^{m+1}_i - g^{m+1}_{\mathrm{c}}, \tag{A.10}$$

where g^{m+1}_{c} is the acceleration experienced by the core due to the presence of odd-l terms in the multipole expansion. Using $g^{m+1}_{i,\mathrm{cor}}$ instead of g^{m+1}_i, a hydrodynamical step is performed according to Equations (A.3) and (A.4), which yields ρ^{m+1}_i and thus the true contribution at $m+1$ of the planet to the potential, $\phi^{m+1}_{\mathrm{P},i}$. The positions of the virtual particles are then re-integrated from m to $m+1$, but this time using a linear interpolation of the time-evolving potential over the time-step.

As mentioned previously, a complication introduced by this method is that the net force applied to the point about which the multipole expansion is carried out is non-zero. This

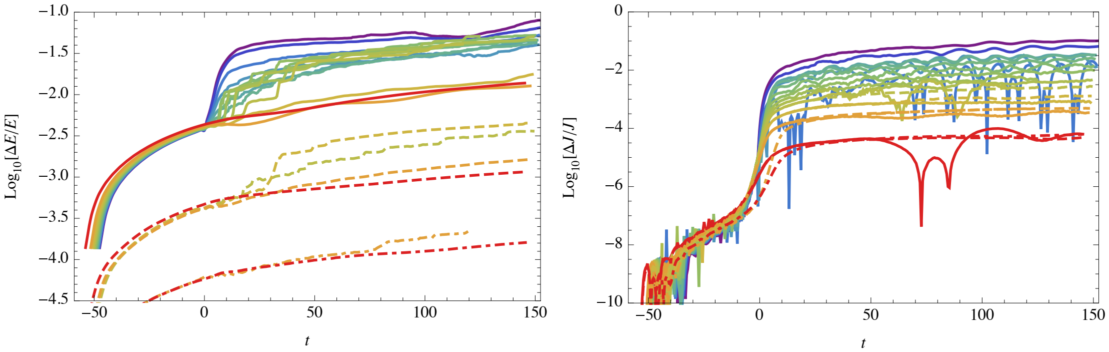

Figure A.2: Accumulation of numerical error in the total energy E and angular momentum J for the simulations ran to compare with the results of FRW. The solid lines show simulations for which $s = 0.02R_{\mathrm{J}}$, the dashed lines show simulations where $s = 0.01R_{\mathrm{J}}$, and the dash-dotted lines show simulations where $s = 5 \times 10^{-3} R_{\mathrm{J}}$. Note that the rate of error accumulation is greatest shortly after periastron when the planet's self-potential is rapidly varying as a function of time. As the planet returns to a state of quasi-equilibrium, the rate of error accumulation asymptotes to the original rate.

is because we do not cancel out the acceleration applied to the extended object's true center of mass $\mathbf{r}_{\mathrm{t}}$, but rather the center of mass defined by the densest material, $\mathbf{r}_{\mathrm{c}}$. While our correction to the gravitational acceleration (Equation (A.10)) mitigates the problem somewhat, the mass density within the simulation domain varies as a function of time, and thus the total mass that satisfies the density criteria to be included when calculating $\mathbf{r}_{\mathrm{c}}$ also changes as a function of time. This leads to small, but measurable, changes in the reference point over the course of a simulation which are not entirely corrected by simply subtracting off the force applied at $\mathbf{r}_{\mathrm{c}}$. To ensure that angular momentum and energy are conserved, a correction is made to virtual particle positions over the course each time-step when re-integrating from m to $m+1$,

$$\mathbf{x}_{*,cor}(t) = \mathbf{x}_{*}(t) - \frac{t - t^{m}}{t^{m+1} - t^{m}} \left(\mathbf{r}_{\mathrm{c}}^{m+1} - \mathbf{r}_{\mathrm{c}}^{m} \right). \tag{A.11}$$

In practice, $\mathbf{r}_{\mathrm{c}}^{m}$ and $\mathbf{r}_{\mathrm{c}}^{m+1}$ are very nearly equal, with a substantial difference only arising when the extended object is close to being destroyed. Typical corrections are significantly smaller than the size of individual grid cells in the most highly-resolved regions.

The accumulation of error for our single passage encounters is shown in Figure A.2. In the deepest encounters where the self-potential changes rapidly, we find that the rate of relative error accumulation in total energy and angular momentum is no larger than 10^{-4} per dynamical time for our simulations with the lowest maximum-resolution, with the planet's initial diameter being resolved by 50 grid cells at $t = 0$. Most of this error arises from the ejected tidal tails, which are resolved at lower resolution out of necessity because of the large volume they occupy. For encounters in which all the matter within the simulation is always resolved at highest resolution (i.e. those that do not have significant mass loss), the relative error accumulation is only 10^{-6} per dynamical time.

We also tested the error accumulation for two sets of simulations with higher maximum resolutions, with the planet's initial diameter being resolved by 100 and 200 grid cells. These simulations show an accumulation of fractional error of $\sim 10^{-7}$ and 10^{-8} per dynamical time, respectively.

Appendix B

Fitting Parameters for Main-Sequence Star Disruptions

For convenience, we have calculated fitting parameters for four characteristic quantities: The peak accretion rate $\dot{M}_{\rm peak}$, the time of peak accretion $t_{\rm peak}$, the amount of mass lost by the star ΔM, and the asymptotic decay power-law index n_{∞}. These parameters can be used to constrain observed tidal disruption events based on measurable characteristics of their light curves (see Section 5.4.1):

$$\dot{M}_{\rm peak} = A_\gamma \left(\frac{M_{\rm h}}{10^6 M_\odot}\right)^{-1/2} \left(\frac{M_*}{M_\odot}\right)^{2} \left(\frac{R_*}{R_\odot}\right)^{-3/2} M_\odot/{\rm yr} \tag{B.1}$$

$$t_{\rm peak} = B_\gamma \left(\frac{M_{\rm h}}{10^6 M_\odot}\right)^{1/2} \left(\frac{M_*}{M_\odot}\right)^{-1} \left(\frac{R_*}{R_\odot}\right)^{3/2} {\rm yr} \tag{B.2}$$

$$\Delta M = C_\gamma M_* \tag{B.3}$$

$$n_\infty = D_\gamma. \tag{B.4}$$

In these expressions are four functions of β alone: A_γ, B_γ, C_γ, and D_γ. The forms of these functions are derived by fitting rational functions to the outputs produced by the numerical simulations presented in this chapter. These functions are derived separately for two polytropic γ, $\gamma = 4/3$ and $\gamma = 5/3$, which are appropriate for high- and low-mass main sequence stars, respectively.

$$A_{5/3} = \mathrm{Exp}\left[\frac{10-17\beta+6.0\beta^2}{1-0.47\beta-4.5\beta^2}\right], \qquad 0.5 \le \beta \le 2.5 \tag{B.5}$$

$$A_{4/3} = \mathrm{Exp}\left[\frac{27-28\beta+3.9\beta^2}{1-3.3\beta-1.4\beta^2}\right], \qquad 0.6 \le \beta \le 4.0 \tag{B.6}$$

$$B_{5/3} = \frac{-0.31+1.2\sqrt{\beta}-1.2\beta}{1.0+1.3\sqrt{\beta}-4.2\beta}, \qquad 0.5 \le \beta \le 2.5 \tag{B.7}$$

$$B_{4/3} = \frac{-0.39+0.57\sqrt{\beta}-0.31\beta}{1-1.3\sqrt{\beta}-0.9\beta}, \qquad 0.6 \le \beta \le 4.0 \tag{B.8}$$

$$C_{5/3} = \mathrm{Exp}\left[\frac{3.2-6.4\beta+3.2\beta^2}{1-3.4\beta+2.5\beta^2}\right], \qquad 0.5 \le \beta \le 2.5 \tag{B.9}$$

$$C_{4/3} = \mathrm{Exp}\left[\frac{12-28\beta+11\beta^2}{1-5.1\beta+5.9\beta^2}\right], \qquad 0.6 \le \beta \le 4.0 \tag{B.10}$$

$$D_{5/3} = \frac{-0.94+11\beta-38\beta^2+50\beta^3-23\beta^4}{1-8.6\beta+26\beta^2-32\beta^3+14\beta^4}, \qquad 0.5 \le \beta \le 2.5 \tag{B.11}$$

$$D_{4/3} = \frac{-2.7+6.9\beta-3.3\beta^2-0.85\beta^3+0.56\beta^4}{1-2.4\beta+0.48\beta^2+0.96\beta^3-0.38\beta^4}, \qquad 0.6 \le \beta \le 4.0 \tag{B.12}$$